

**Imaging technology for digital image based
motion detection in the DIET breast cancer
screening system**

Amer S Kashif

A thesis presented for the degree of
Doctor of Philosophy
in
Mechanical Engineering
at the
University of Canterbury,
Christchurch, New Zealand

8 July 2013

ACKNOWLEDGEMENTS

This research is dedicated to my two sisters, Farah Tajali (1964-2005), who was a victim of breast cancer and proved to be a consistent motivation behind this research, and Talat Kokab, who has recently been diagnosed with infiltrating lobular carcinoma.

First of all, I want to express my gratitude to the Almighty, who has been very kind to me throughout my life. A massive gratitude to my supervisors, Geoff Chase and Thomas Lotz. Thomas was a constant guiding and motivating presence, and proved to be an untiring mentor and a great friend. Geoff, despite his consistently busy state has always been there, showing commitment and support during the entire production of this thesis. I salute him for his work ethics and time management skills.

I am very grateful to visiting research assistants who have directly or indirectly contributed towards the accomplishment of this thesis, especially, Thomas Tirschler, Sheng Feng, Yohann Denais, Pierrick Biret, Damien Lottin, Guillaume Leclancher, Maikel Heeren, Robert Collier, Thibaut Lesueur, Hugo Stalder, Jennifer Dickson and Jens Glasbrenner. Thanks are also due to Dr Tom Botterill, who is still associated with DIET research. Finally, thanks are also due to the “world’s oldest post-doc” Dr Richard Wien for his highly valued support and advice. It has been great working with all of you, as part of the DIET team. I am also indebted to the technical staff who have always been welcoming, supportive and guiding. Thank you Julian Phillips, Julian Murphy, Rodney Elliot, Kevin Stobbs, Ken Brown, David Read and Scott Amies.

Many thanks to my wonderful family, who have been a source of continuous encouragement, as always. Thank you Sumreen, for your love and support, you are the best wife I could have ever hoped for and I couldn’t have done it without you. Thank you Tabeer and Ahmed, you have been a source of great pleasure, joy and refreshment to Papa during all those years. Thanks to my extended family and friends for all your well wishes, encouragement and prayers.

Special thanks to National University of Science and Technology (NUST), Islamabad, Pakistan and NZi3, New Zealand, for providing scholarship for this research.

CONTENTS

1 Introduction	1
1.1 Background	1
1.2 Breast cancer and tissue stiffness	2
1.3 Breast cancer detection	4
1.4 Elasticity imaging	4
1.5 Elastography	5
1.6 Digital Imaged Elasto Tomography (DIET)	6
1.7 Research Scope	7
1.8 Research objectives	8
1.8.1 Optical imaging array	8
1.8.2 Strobe illumination system	8
1.8.3 Vibration actuation system	9
1.8.4 Actuator positioning system	9
1.8.5 Ergonomics, design and integration.....	10
1.8.6 Imaging software and GUI.....	10
1.8.7 DIET IDS LiveVIEW.....	11
1.8.8 Anthropomorphic breast phantoms for elastographic imaging evaluation.....	11
1.8.9 Diagnostic software and system evaluation.....	11
1.9 Thesis organisation	11
2 Optical imaging array	13
2.1 Background	13
2.2 Identified areas of improvement	15

2.3 Important parameters of optical system	16
2.4 Application Specific Parameters	18
2.4.1 Working Distance (WD)	18
2.4.2 Field of View (FOV)	18
2.4.3 Depth of Field (DOF)	19
2.4.4 Focal Length (FL)	19
2.4.5 Aperture (F#)	20
2.5 Specifications for the test camera	20
2.6 Shortlisted camera models	21
2.7 First test camera	22
2.8 Initial trial results	22
2.9 Hardware Modification of the Test Camera	24
2.10 Selected Camera and specifications	25
2.11 Camera lenses	26
2.12 Initial Lens trials	28
2.13 Camera installation	29
2.14 Camera programming	30
2.14.1 Basic steps of <i>uEye</i> programming	32
2.14.2 Implementing Multithreading - DIET IDS imaging software	33
2.14.3 DIET IDS LiveVIEW	35
2.15 Summary	36
3 Strobe Illumination System	39
3.1 Background	39
3.2 Previous Work	39
3.3 Areas needing improvement	41
3.3.1 Time Lag	41
3.3.2 Fuzzy Images	42

3.3.3 Glare patterns from reflective surface	42
3.4 Initial Research	43
3.5 Design concept	45
3.6 Testing and calibration	49
3.7 Discussion	51
3.8 Summary	53
4 Vibration Actuation System	55
4.1 Introduction and prior work	55
4.2 Rationale	56
4.3 Development Approach	56
4.3.1 Design considerations	57
4.3.2 Concept Justification	57
4.4 Dimensioning of voice coils	60
4.4.1 Voice coil concept	60
4.4.2 Mechanical model of the breast and actuation unit.....	61
4.4.3 Spring Effect	65
4.4.4 Selection of voice coil.....	66
4.5 Actuation control system integration	69
4.5.1 Controller	70
4.5.2 Motor Drive.....	70
4.5.3 Motor	71
4.5.4 Feedback Position sensor - LVDT.....	71
4.6 Actuator design and assembly	72
4.7 Damping solution for vibration isolation	75
4.8 Calibration of LVDT position sensor	79
4.8.1 Bit Volts Relationship	80
4.8.2 Absolute accuracy of NI 9215.....	81
4.8.3 Verification of actuation signal and feedback control	82

4.9 Summary	83
5 3-Axes positioning	85
5.1 Background	85
5.2 System Specifications	86
5.3 Linear motion solutions	87
5.3.1 Linear Motors	87
5.3.2 Rack and pinion	87
5.3.3 Nut and screw system	88
5.3.4 Cylinders actuators	88
5.4 Initial design concept	88
5.5 Analysis of the initial design	89
5.6 Final design concept for the actuator positioning system	90
5.6.1 2-axis positioning system	91
5.6.2 Z-axis positioning system	93
5.7 Hardware control concept	96
5.8 Summary	100
6 Ergonomic design and Integration	103
6.1 Background	103
6.2 Previous work and identified areas of improvement	104
6.3 Initial research	106
6.4 DIET design specifications	107
6.4.1 Ergonomic specifications	107
6.4.2 General specifications	108
6.4.3 Technical specifications	108
6.5 Functional analysis of design	110
6.5.1 Primary functions	110
6.5.2 Constraint functions	110

6.6 Initial design concept	110
6.7 Evaluation - initial design	111
6.8 Final design concept	112
6.8.1 Construction of ergonomic frame	113
6.8.2 Ergonomic trial	116
6.9 Reduction of headrest segment	121
6.10 Hardware installation and integration	122
6.11 Connections and cabling	124
6.12 External design	127
6.13 Summary	131
7 Imaging software and GUI	133
7.1 Background	133
7.2 Previous work and scope of current research	134
7.3 Integrated imaging control software	135
7.3.1 Image capturing code	137
7.3.2 Hardware and software interaction	137
7.3.3 Socket communication for FPGA control through TCP/IP	141
7.3.4 Message interpretation	144
7.4 DIET IDS LiveVIEW	148
7.4.1 Initial design concept	148
7.4.2 Final software design	149
7.5 Graphical user interface (GUI) and user manual	150
7.6 Test mode	156
7.7 Summary	158
8 Silicone breast phantoms for elastographic imaging evaluation	159
8.1 Background	159
8.1.1 Breast phantom materials	160

8.1.2 Design of anthropomorphic breast phantom	161
8.2 Materials and Methods	161
8.2.1 Phantom specifications and tissues to model	161
8.2.2 Elastomers used:	162
8.2.3 Selected compositions for dynamic mechanical analysis.....	163
8.2.4 Dynamic mechanical analysis	163
8.2.5 DMA testing procedure	164
8.2.6 Phantom moulding	165
8.2.7 Phantom imaging	169
8.3 Results	170
8.3.1 Elastic properties of tested materials	170
8.3.2 Phantom application	172
8.4 Discussion	175
8.5 Summary	177
9 Diagnostic evaluation through Surface motion reconstruction	179
9.1 Background	179
9.2 Elimination of fiducial markers	179
9.2.1 Model based segmentation	180
9.2.2 3D surface reconstruction	181
9.2.3 Optical flow (OF) computation.....	181
9.2.4 Surface motion reconstruction in 3D	182
9.3 Data acquisition	183
9.4 Tumour detection methodology	183
9.5 Diagnostic outcome	184
9.6 Discussion	185
9.7 Summary	188
10 Diagnostic evaluation through seperate modal analysis	189
10.1 Background	189

10.2 Data acquisition	190
10.3 Modal parameter estimation	192
10.4 Statistical diagnostic analysis	195
10.5 Outcome of the separate modal analysis	196
10.6 Separate modal analysis as a diagnostic tool	200
10.7 Summary	202
11 Conclusions	205
12 Future work	211
12.1 A large scale clinical trail	211
12.2 Optimisation of illumination	211
12.3 Upgradation of the Host-PC	212
12.4 More realistic breast phantoms	212
12.5 Further research in tumour detection through separate modal analysis	213
12.6 Robust reconstruction of 3D skin surface	213
References	215
Appendix A	225
Appendix B	226
Appendix C	227
Appendix D	228

LIST OF FIGURES

Figure 1.1: Key steps of the DIET Imaging procedure: (1) Excite the breast at low frequencies [left], (2) Image surface motion with digital cameras [middle] and (3) Calculate motion disturbance for diagnostic analysis [right]. Embedded in this breast phantom is 20 mm stiffer inclusion at 6-7 o'clock which can be easily identified	7
Figure 2.1: (A) WD dimensions estimated at 200mm, (B) FOV measurements in vertical dimension (170 mm) and (C) FOV measurements in horizontal dimension (160 mm)	19
Figure 2.2: Sequence of images taken at different exposure times at 20 Hz flash frequency. At 300ms and 350ms the effect of partial exposure seemed to be minimum, while showing more uniform brightness at 350ms. But with the change in imaging frequency a new value of optimum exposure time had to be established.....	23
Figure 2.3: Showing the pin configuration extended as a result of hardware modification in the test camera providing a control signal for exposure. The objective was to convert rolling shutter into global start rolling shutter	25
Figure 2.4: Evolution process of digital cameras for DIET, starting from left Canon G5, Canon G9, IDS UI 1465 LE-C, IDS UI-2250 SE-C with C mount lens	26
Figure 2.5: Lens trial, exposure series of UI-2250 SE-C at 0.2m distance using C3M0814 at F8 aperture (top), CY0813 at F8 aperture (centre) and B3M8018S12 at F1.3 aperture (bottom)	28
Figure 2.6: Subcomponents of the custom built camera mount, (A) base plate (B) side bracket and (C) top plate	29
Figure 2.7: (A) Exploded view of the camera mount and heat sink (B) assembled camera with strobe light and PCB ready to be mounted on the main frame Programming IDS UI 2250 SE-C	30
Figure 2.8 : Flow chart of image capturing Code after implementing multithreading	34
Figure 2.9: Picture of a silicone phantom under actuation taken with IDS UI 2250 SE-C.....	35
Figure 2.10: Actuator positioning window showing the real time video. Control of the 3-axis positioning system is also provided in the interface to facilitates the operator in positioning the actuator with respect to the size of the breast.....	36
Figure 3.1: Schematic of camera exposure and strobing (Peters, 2007).....	41
Figure 3.2: Stage-1 DIET prototype image showing specular reflections from the highly reflective surface of the silicone breast phantom during in vitro trials	42

Figure 3.3: LED Strobe ring mounted on top of the camera in the stage-1 DIET prototype	45
Figure 3.4: Circuit diagram of LED drive PCB with XRE Cree Star LED	46
Figure 3.5: CAD image of circuit board layout, collimators are the black cylinders sitting on top of the LEDs, 30mm cut-out in the centre of the board is for the camera lens. The capacitor board is shown in transparent.....	47
Figure 3.6: Solidworks drawing of the heat sink (a base plate for LED circuit board)	48
Figure 3.7: (A) The front view showing the strobe illumination system in operation with light passing through a circular polarizing filter and (B) side view showing strobe flash system mounted on camera UI2250 SE-C	48
Figure 3.8: (A) Images showing effective use of polarizer for glare reduction, captured at 50 ms exposure time, without polarizer and (B) with polarizer using only one strobe light.....	48
Figure 3.9: Showing calibration test settings with a photodiode and luxmeter applied in the darkroom environment. LED strobe system is in operation	49
Figure 3.10: (A) New strobe system (with polarizer) at 5 volts, 0.17 amp, showing illumination peak ~20000 lux (B) New strobe system (without polarizer) at 5 volts, 0.17 amp showing illumination peak ~47,500 lux (C) New strobe system (with polarizer) at 12 volts, 0.7 amp showing illumination peak showing ~51000 lux (D) New strobe system (without polarizer) at 12 volts, 0.7 amp showing illumination peak showing ~68000 lux. The X-scale is shows time (s) and Y-scale shows illumination (Lux). Note that Y-scale in A to C is 0-55,000, while in D Y-scale is 0-100,000.	50
Figure 3.11: (A) Output of the old strobe system (B) Output of the new strobe system showing a pulse peak sustainability using 6800 μ F charging capacitor, at 12 V, 1.7 Amp (without polarization).....	50
Figure 3.12: LED pulse generation loop in the FPGA VI. The loop was timed to execute at 10 μ s.	52
Figure 3.13: Image of the silicone breast phantom captured in the new light environment with clinical DIET prototype.....	52
Figure 4.1: (A) Showing cross section of actuator design (Jason Fincher, 2005) and (B) First actuator employed in the lab environment surrounded by cameras	56
Figure 4.2: (A) Simplified schematic sketch of the breast, (B) mechanical model of the breast, and (C) mechanical model of the breast including actuator	61
Figure 4.3: Mechanical model of the actuator	64
Figure 4.4: (A) Sinusoidal behaviour of displacements of actuator (x_A) and breast (x_B) at $f = 20$ Hz, (B) The driving force required by the actuator at $f = 20$ Hz	65

Figure 4.5: Requirement of max force depending upon the frequency f and spring constant k_a , X-axis represents frequency f , Y-axis showing the spring constant, colours represent the value of force in Newtons (N).....	65
Figure 4.6: (a) Showing design of concentric spring, (b) springs of the actuator connected by a shaft.....	66
Figure 4.7: Graphical representation of feedback controlled integrated actuation system for DIET	70
Figure 4.8: (A) Showing location of the applied load for stiffness test of the coil bone during simulation, (B) final design of the coil bone.....	73
Figure 4.9: (A) Displacement distribution of the spring having a spring constant of 10 kN/m, (B) Solidworks representation of the spring with a spring constant of 10 kN/m, and (C) Spring geometry with a spring constant of 20 kN/m.....	74
Figure 4.10: From left (a) Design concept of main frame (b) moving parts with concentric springs and (c) internal view of the assemble actuator with LVDT.....	74
Figure 4.11: Showing experimental set up for testing silicone padding as vibration isolation solution	76
Figure 4.12: Showing three different locations where Laser Doppler Vibrometer testing were performed for optimising the vibration isolation.....	77
Figure 4.13: Measured vibrations over the range of operational frequencies for all three products under evaluation at all three locations. AlphaGel SF-10 (top), AlphaGel SF-2 (middle) and Paulstradyn (bottom).....	77
Figure 4.14: Plots showing measurements of vibration for each damping product under evaluation at location-3	78
Figure 4.15: Showing design changes made in the base plate of the actuator to accommodate the damping feet (left), and the Solidworks representation of actuator after being mounted on the damping feet	79
Figure 4.16: Schematic of the bit_to_mm conversion VI	81
Figure 4.17: Plots showing number of bits required for a set value of amplitude (μm), (A) before calibration and (B) after calibration	83
Figure 5.1: Schematic illustration showing overall position of the patient during DIET screening process (top) and actuator positioning underneath a breast phantom (bottom).....	85
Figure 5.2: Solidworks representation of lift table concept; fully retracted (left) and fully extended (right).....	89
Figure 5.3: Showing blocked FOV or blind (red dotted) area, when positioning system is extended	90
Figure 5.4: Performance curve of MDrive-14 (Schneider Electric)	91

Figure 5.5: Showing positions of the rail, limit switches and stepper motors (top left), final design of the 2-axis positioning system (top right), and Solidworks representation of 2-axis positioning system with actuator mounted on the damping feet (bottom)	93
Figure 5.6: Showing the concept of generating motion in Z-axis in order to maximize FOV of the optical system	93
Figure 5.7: Showing drive and the motor used for generating motion in Z-axis position system (Haydon Motion Solutions)	94
Figure 5.8: Cut out of the final design of the actuator after implementing the z-axis positioning capability. Green colour shows the parts which required modification and the red colours shows addition to the original design	95
Figure 5.9: Block diagram of the chopper control loop in Labview. Pin Configuration on NI 9403: DO 17 enables and disables the drive; DI 5 and DI 6 are the inputs for the limit switches. DO 4 controls the speed and DO 2 controls the direction.	96
Figure 5.10: Schematic diagram of circuit to control the 24 V DC direction input of one motor with a digital 5V TTL signal (Glasbrenner, 2012)	98
Figure 5.11: Pulse signal generation loop for enabling MDrive stepper motor in X-axis. The pulse signal (DO 8) is connected to the step clock input of the motor. The case structure is executed from left to right; in the left case digital output is enabled and in the right it is disabled	98
Figure 5.12: Direction and limit switch control loop for MDrive providing motion in X-axis. The loop is timed to execute on a 200 ms interval.	99
Figure 5.13: Inside view of the DIET clinical prototype, showing the actuator installed on the 2 – axis positioning system, while the breast interface mounted on the z-axis positioning motor can also be seen.	100
Figure 6.1: (A) DIET equipment layout in the lab during concept validation trials (top left) and (B) DIET stage-1 prototype (bottom left)	104
Figure 6.2: Ergonomic design of Signa HDxt 3.0T (GE) used for MRI imaging at Hagley Radiology which was the source of inspiration of design considerations for DIET clinical prototype	106
Figure 6.3: Comfort angles between legs and torso and between arms and shoulders defined as results of initial research on MRI machines	107
Figure 6.4: Octopus diagram for functional analysis of main frame of DIET clinical prototype	109
Figure 6.5: CAD representation - Concept-1 of ergonomics design of DIET clinical prototype.....	111
Figure 6.6: Wooden mock up device constructed to evaluate general space requirements and functionality	112

Figure 6.7: CAD representation of final design concept for DIET clinical prototype	113
Figure 6.8: CAD drawings of main frame along with quantity and measurements as sent to AutoLine (MayTec’s local suppliers) for profile sizing. The lengths shown in colour have different angles required to meet the criteria of ergonomics defined in the functional analysis [FP2, FC3]	114
Figure 6.9: CAD drawings showing different ergonomic angles of various parts. Part 15 shown in Figure 6.8 had the same angle as part 11.....	115
Figure 6.10: Installation of headrest on the main frame	115
Figure 6.11: The setup used for ergonomic trials.....	116
Figure 6.12: Ergonomic trial setup explaining how various anthropometric dimensions were recorded	117
Figure 6.13: Ethnic representation of ergonomic trials for DIET clinical prototype	119
Figure 6.14: Mean, μ , and standard deviation, δ , values of different anthropometric dimensions of DIET ergonomic trial cohort	120
Figure 6.15: Modification to reduce the overall length of headrest segment carried out as a result of ergonomics trials	122
Figure 6.16: Internal view of DIET clinical prototype showing positioning of various hardware components required for optical imaging; Feet side (left), Head side (right).....	124
Figure 6.17: Principal wiring schematic of clinical DIET prototype	125
Figure 6.18: Terminal connection diagram of clinical DIET prototype.....	126
Figure 6.19: Top plate (left), armrest (centre) and triangular shape for light obstruction (right)	128
Figure 6.20: Showing breast adapter (in blue) and two cavity inserts applied for comfort of inactive breast	128
Figure 6.21: Showing positioning of arm and leg supports. These sheets can be extended at any desired angle during operation (left) and folded for transportation (right) though lockable hinges.	129
Figure 6.22: Transportation bar fixed to the actuator and sides of the frame to avoid damage to actuator’s damping feet. The actuator has to be in “Home” position before fixing this bar	130
Figure 6.23: DIET clinical prototype (A) transportation mode, (B) extended mode and (C) operational mode	130
Figure 7.1: Flow diagram of DIET imaging procedure	136
Figure 7.2: Block diagram of key hardware and software components of clinical DIET system	138
Figure 7.3: Control panel of the LabVIEW VI showing desired value of actuation amplitude (set point =0.5mm) and the measured value from LVDT (process variable =0.499mm)	139

Figure 7.4: Block diagram of the PID controller LabVIEW VI	140
Figure 7.5: Block diagram of TCP/IP communication loop showing flat sequence structure and messaging loop. Red dotted circle shows the sub-case-structure for amplitude settings.	142
Figure 7.6: Block diagram of the TCP listen VI	143
Figure 7.7: Block diagram of 'TCP String Interpretation' sub-VI. This VI splits up the messages into characters and numbers	143
Figure 7.8: Block Diagram of the case-structure 'Pos' and three corresponding sub-case-structures for each X, Y and Z direction.....	145
Figure 7.9: Block diagram of case structure handling LS control messages incoming (upper) and outgoing (lower). Incoming messages (limit reached) stops the motors to move actuator further while outgoing messages to prompt the operator.....	147
Figure 7.10: Graphical user interface of initially developed DIET IDS LiveVIEW software, displaying real time video from all 5 cameras.....	149
Figure 7.11: LiveVIEW window of GUI displaying real-time video from two cameras to present the operator with an internal view of the system during imaging. LiveVIEW enables the operator to reposition the actuator remotely in 3-axis depending upon the size dimensions of the breast under screening	150
Figure 7.12: LabVIEW controller VI required to be running in the background during calibration process ...	151
Figure 7.13: The first window of GUI displaying various control options. The operator needs to press 'Subject Imaging' button. The test mode and control settings have been provided to be handled by the service engineer for maintenance purposes	152
Figure 7.14: Patient's details and actuation parameters are fed into this form	153
Figure 7.15: Calibration window displaying images of the calibration cube	154
Figure 7.16: Actuator positioning window presenting real-time video (LiveVIEW) from 2 cameras installed 72° apart. The operator can reposition the actuator according to the size dimensions of the breast using this interface.	154
Figure 7.17: 'Form_Imaging' interface which enables the operator to start actual imaging session	156
Figure 7.18: Manual actuator control interface provided to facilitate the service staff to monitor performance of different DIET breast cancer screening systems.	157
Figure 7.19: User interface to make quick changes in the software in order to change the path to base directory and number to be captured on each motion frequency.....	157
Figure 8.1: Drawings of phantom mould (A) cavity, (B) core and (C) complete assembly showing 1mm gap between cavity and core	165

Figure 8.2: Depth locations of inclusions (A) 5mm, (B) 10mm and (C) 20mm, and (D) 6-o' clock position when the breast is viewed from front.....	166
Figure 8.3: Moulding procedure of silicone breast phantoms: (A) process of core extraction (B) procedure of placing a stiff tumour into the healthy tissue, (C) cured healthy tissue, (D) circular disc with bolts, (E) method of applying a circular disk during moulding of pectoral muscle, (F) the moulded breast phantom.	168
Figure 8.4: (A) Mean values, μ , and (B) Coefficient of variation ($C_v = \sigma/\mu$) for the storage Modulus E' , of the measured compositions.....	171
Figure 8.5: (A) Mean values, μ , and (B) coefficient of variation ($C_v = \sigma/\mu$) for the damping ratios, ζ , of the measured compositions.....	171
Figure 8.6: Bode plot of healthy and tumour inclusion phantom data set showing shift in the first natural frequency	173
Figure 8.7: Result of t -test for phantoms (A) healthy and (B) having a 20mm tumour at 6 o' clock. The thresholded outcome $1-p$ [hypothesis rejected (red) or accepted (blue)] is shown in each case, indicating a (lower) second natural frequency and thus a stiffer inclusion at the red area.	173
Figure 8.8: MRE Reconstruction of a phantom with composition A background and two inclusions: composition C on the left and composition A on the right. A subset of slices from the full volume data read shown: (A) is a $T2^*$ weighted image, (B) is the storage modulus (kPa), (C) is the loss modulus (kPa) and (D) is the damping ratio.	174
Figure 9.1: (A) Stage-1 of motion reconstruction, where the breast is segmented and the actuator interface position is identified, (B) Stage-2, showing 3D surface profiling of the breast, and (C) Stage-3, output of the dense optical flow (OF) computation	180
Figure 9.2: Surface motion disruption measured in terms of phase delay in the direction of actuation in the inclusion areas, identifying the presence and location of tumour. Left panel shows results of phantoms with 5mm tumour, the middle panel shows results of phantoms with 10 mm tumours and the right panel shows results from the phantoms with 20 mm tumours. The result of a healthy phantom (with no inclusion) is displayed at the bottom. These results were processed for input frequencies between 31-33 Hz.	185
Figure 9.3: Tumour signatures as a function of input frequencies, in the range of second resonance, 31-33 Hz. (top) A phantom with 5 mm inclusion at location B, (centre) A phantom with 10 mm inclusion at location B, and (bottom) A phantom with 20 mm inclusion at location B	187
Figure 10.1: Silicone breast phantom with examples of stiffer inclusions embedded inside	190

Figure 10.2: Defining angle α and ϑ . Angle α is the elevation angle with 0° at the chest wall and 90° at the bust-point, and ϑ is the rotational angle, starting with 0° at 12-o'clock position when viewed from the front, rotating clockwise.	191
Figure 10.3: A typical Bode diagram for one of the segments of an imaged breast showing the first two natural frequencies.....	192
Figure 10.4: An example of the used segments, overlaid upon a triangulation of the tracked fiducial markers	195
Figure 10.5: A typical example of the fitting results. Measurement data is shown in dashed black, fit of the first natural frequency in dash-dotted red, fit of the second natural frequency in dotted magenta and the combined fit is shown in solid blue.	197
Figure 10.6: Segmented healthy breast phantom viewed from the front with a colour-map of second natural frequency, ω_{02} , in Hz	197
Figure 10.7: Segmented breast phantoms with inclusions viewed from the front with a colour-map of second natural frequency, ω_{02} , in Hz. Left column shows results of phantoms with 5 mm tumour, middle column shows results of phantoms with 10 mm tumours, and the right column shows results of phantoms with 20 mm tumours, at locations A-D. Blank (white) segments indicate bad model fits due to noise and gaps in the data.	198
Figure 10.8: Probability density functions for the normal distributions in two different segments of the breast phantom with a 10 mm tumour. The solid red line represents the data in the segment $160^\circ < \vartheta < 220^\circ$ and the dashed red line corresponds to data outside this segment. Similarly, the solid black line show data in the segment $300^\circ < \vartheta < 360^\circ$ and the dashed black line considers the data outside this range.	199
Figure 10.9: Result of the t -test for a healthy phantom (no inclusion), showing that the hypothesis was accepted in all 126 segments across the surface and no difference in second natural frequency was observed.....	199
Figure 10.10: Results of the t -test for phantoms with different tumour sizes: 5 mm [A-D] (left), 10 mm [A-D] (centre), and 20 mm [A-D] (right). The threshold outcome $1-p$ (hypothesis rejected (red) or accepted (blue)) is shown in each case, indicating a lower second natural frequency and thus a stiffer inclusion at the red areas.....	200

LIST OF TABLES

Table 2.1: Processes involved in DIET imaging and time taken (in seconds) for each process using the Canon PowerShot G9 Cameras, numbers of images captured by all 5 cameras are shown in parenthesis.....	16
Table 2.2: Characteristics defining the performance of an imaging device	17
Table 2.3: Camera models and specifications shortlisted for induction in the initial DIET imaging research ..	21
Table 2.4: Comparisons of cameras specifications used during the initial research of DIET system.....	27
Table 2.5: Shortlisted lenses and their technical characteristics	27
Table 2.6: Comparison of time required for each process at one frequency during a standard imaging session of DIET stage-1 and clinical prototype	35
Table 3.1: Comparison of various illumination techniques vis-à-vis suggested applications ((EO), Joinson, MCHUGH)	43
Table 4.1: Actuation systems evaluation matrix.....	59
Table 4.2: Comparison of characteristics of shortlisted voice coils	67
Table 4.3: Important formulas used motor rating selection and power supply requirements	68
Table 4.4: Continuous force requirement from a single voice coil motor for different frequencies and spring constants.....	69
Table 4.5: Important characteristics of the three shortlisted vibration damping solutions.....	76
Table 4.6: Calibration data of LVDT position sensor	79
Table 6.1: Grading chart of reported comfort levels in various areas of body	121
Table 6.2: Mounting dimensions of DIET imaging hardware	123
Table 6.3: Peak current requirements of various hardware components used for DIET imaging	125
Table 7.1: List of digital control signals vis-a-vis pin assignment on DIO module NI-9304 (mod3)	141
Table 7.2: TCP/IP messages and their interpretation	144
Table 7.3: Number of cases for each sub-case structure for XYZ-axis positioning.....	146
Table 7.4: Depiction of each integer value for respective positioning system	146
Table 8.1: Materials used for mimicking breast tissues and the measured values of Young's modulus by previous investigators.....	160

Table 8.2: Description of tumour location (depth) in heterogeneous breast phantoms	167
Table 8.3: Materials used for mimicking different tissues in DIET anthropomorphic breast phantoms	172
Table 8.4: Materials used for mimicking background and inclusions in the MRE phantom	175

ABSTRACT

Breast cancer is a major health problem across the globe. Many incidences in the underdeveloped nations go unreported, due to non-availability or lack of access to breast screening programs. Mammography, the current gold standard for breast screening, comes with several inherent limitations in terms of cost, radiation exposure, and associated discomfort. The cost of equipment and personnel alone puts mammography out of reach for most developing nations. Hence, there is a great and growing need for an adjunct breast screening modality, within reach of general masses, especially in the overpopulated, underdeveloped countries.

Digital Image Elasto Tomography (DIET) is intended to be a low cost, radiation free, noninvasive and portable breast cancer screening modality that will be accessible to the general population and will encourage more women to undergo breast screening. The DIET imaging concept induces mechanical vibrations into a breast and its surface motion is captured with digital cameras and reconstructed in 3D, for elastic characterization of the breast tissues. Ex-vivo trials and limited in-vivo trials show promise in breast cancer diagnostic evaluation.

The current DIET system is, as noted, functional, but not suitable for wide scale screening. There are significant development issues in hardware, software and algorithms required to improve its speed of testing and quality of diagnostic results. The main aim of this thesis is to overcome these issues taking the DIET system from the lab to a more directly useful and usable system.

This thesis presents a complete design development and analysis of the DIET clinical system, developing a prototype suitable for large-scale in-vivo trials, to establish the sensitivity and specificity of this novel technology. The major components of this research are development, of the imaging array to capture surface motion, strobe illumination for reliable image capture, actuation system to vibrate the breast harmonically, remote positioning of the actuator,

ergonomic design of the imaging device, and the development of a graphical interface for easy operation of the system. Moreover, anthropomorphic silicone breast phantoms suitable for diagnostic evaluation of elastographic imaging modalities, including DIET and MRE are also presented. A new approach in software based DIET diagnosis through separate modal analysis, focusing on the second natural frequency of the breast, is also presented. Finally, the new DIET technology developed is validated ex-vivo, using two different diagnostic techniques. The trials results are positive and demonstrate viability of this new technology for commercialization. All of these aspects have advanced the clinical and technological future of this overall DIET system concept.

The overall thesis makes several technical advances necessary to advance the DIET concept from a purely research concept to clinical feasibility. These advances are coupled within an advanced design to create an all new clinical prototype system. The final, validated result shows the clinical potential, both ex-vivo and in-vivo, and clinical feasibility of the DIET concept and this research.

Chapter 1

1 INTRODUCTION

1.1 Background

Breast cancer is a major health problem. It is estimated that every year, one million women are diagnosed with breast cancer, and more than 410,000 die from this deadly disease worldwide (Coughlin and Ekwueme, 2009). Previously, the significance of the disease was not being realized to warrant allocation of health care budget in low and middle income countries (Porter, 2008). However, more recently, breast cancer has become an urgent public health issue, even in low resource regions (Anderson et al., 2008). It has now been recognised as the most common cancer among women, both in developed and developing nations (Ferlay et al., 2010).

Breast cancer is the second most common reported malignancy among women, accounting for nearly one in three cancers diagnosed in USA (Society). Approximately 230,000 new cases of invasive breast cancer and 40,000 breast cancer deaths were expected to occur in the USA during 2011 (DeSantis et al., 2011). Breast cancer is also the number one cancer killer of New Zealand (NZ) women, with more than 2,700 cases diagnosed every year, and losing more than 600 women to the disease annually. The 2,565 breast cancer cases in NZ, during year 2007, represented 28% of all female cancer registrations, the highest proportion of any cancer among NZ women (Foundation, 2009/2010, 2002, 2004a, 2004b).

The breast is a modified skin gland consisting of several duct systems, each containing lobules (milk producing gland). The surrounding tissue is called adipose and consists of mainly fats along

with blood vessels and lymphatic vessels (Kopans, 2007). Like any other cancer, breast cancer is an uncontrolled overgrowth of abnormal cells. Unlike other healthy cells of body, the cancer cells do not undergo apoptosis, a process which causes cell death, and, as a result, cancer cells keep on growing to form new abnormal cells. As cancer cells grow, they acquire mutate and spread to axilla and eventually affect distant organs. The spread of breast cancer through the human body is characterised into eight stages.

Stage-0 is a pre-cancerous condition, where benign abnormal cells are formed in ducts or lobules. Ductal carcinoma *in situ* (DCIS) is a non-invasive condition affecting the lining of breast ducts. Lobular carcinoma *in situ* (LCIS) is the next stage, in which abnormal cells are formed inside lobules. The next stage is invasive cancers. Though it is not assured that all DCIS and LCIS become invasive cancer, but it is not possible to predict which carcinomas *in situ* will turn into invasive carcinoma. At the last stage the cancerous cells have spread to other organs of body, most often, the lungs, liver, bones or brain (Kopans, 2007). The women whose cancer is diagnosed early have a 95 % five year survival rate (Kopans, 1998), whereas, if cancer is detected at the last stage, the 5 year survival rate drops to 15% (Society).

1.2 Breast cancer and tissue stiffness

Cancer alters the elastic properties of biological tissue depending upon the structural organization of the tissues in that region of human body (Fung Y.C., 1993). Pathological changes, such as development of different types of carcinomas, alter the elastic properties of human tissues resulting in stiffness contrasts of 5:1 or more between cancerous tissue and healthy tissues (Krouskop, 1998, Samani, 2007, Samani A, 2003, Sarvazyan, 1995). This high contrast provides a potential diagnostic avenue (Peters, 2004, Peters, 2005, Peters, 2006, Peters, 2007, Peters, 2008a, Peters, 2008b, Peters, 2009).

Despite extensive characterization of the elastic properties of structural materials, mechanical properties of many biological materials remain unknown or uncertain. This uncertainty is due in part to the technical difficulty of measuring visco-elastic tissues (Fung Y.C., 1993), particularly in vivo, and intersubject variation for a given tissue type. However, the stiffness of healthy and cancerous breast tissues have been investigated, and stiffness contrasts of 200-1500% have been reported for carcinomas [1-2, 14-15, 18-22].

Krouskop et al. (Krouskop, 1998) used dynamic compression testing to measure the elastic modulus of excised breast tissues. Testing was performed at frequencies of 1 & 4 Hz at 5% and 20% pre-compression using 30mm diameter cylindrical samples. Samani et al. (Samani, 2007) presented elastic moduli of normal and pathological human breast tissues, where 169 human breast tissue samples were measured by applying a sinusoidal motion indentation with peak to peak amplitude of 0.5 mm and a frequency of 0.1 Hz. The elastic properties were then calculated using a finite element inverse solution. The sample size of dissected breast tissue from reduction mammoplasties was a 15x15x10 mm³ block.

Sinkus et al. (Sinkus, 2005) tested 15 patients with different pathologies, six breast cancer cases, six fibroadenoma (benign lumps with no malignant potentials) cases and three mastopathy (benign tumours with malignant potential) cases to validate their results by using MR elastography. Srivastava et al. used OCT elastography to measure the elastic properties of 12 normal, benign and malignant resected breast tissue samples (Srivastava, 2011). Egorov and Sarvazyan (Egorov and Sarvazyan, 2008) presented clinical data of six patients each with a different type of breast cancer, using Breast Mechanical Imager (BMI), a device for real time imaging of breast pathologies. The method mimics Clinical Breast Examination, which palpates the breast tissue and is based on reconstructing the internal structure of soft tissues using the data obtained by a force sensor array pressed against the examined site. The results of these studies have been consolidated in Table 1.1 (*Appendix A*).

1.3 Breast cancer detection

For breast cancer detection, palpation or clinical breast examination (CBE) remains the most common procedure to date with its inherent limitations of subjectivity and low sensitivity (Kopans, 2007, McDonald, 2004). Manual palpation, often the only available diagnosis, is not recommended for screening in the western world due to poor and variable, performance and its high dependence on operator skill and experience (McDonald et al., 2004). Other detection modalities include mammography, ultrasound, CT and MRI.

Mammography is the only modality currently approved for screening applications, due to its relatively low cost and short duration, despite the invasiveness from the induced radiation. X-Ray mammography is the current gold standard screening method and is widely used in most developed nations, but a high non-compliance rate is observed due to the expected and/or experienced discomfort associated with the required breast compression (Asghari and Nicholas, 2004, Kashikar-Zuck et al., 1997) and limited access to screening in remote or rural areas (Elting et al., 2009). There are no other modalities currently recommended for screening applications. More accurate diagnostics, such as MRI are too costly (Sarvazyan, 2008).

Thus, there is a great need for an adjunct screening modality to improve screening performance and delivery with a low cost and non-invasive system. Such a system able to deliver these features is not yet available.

1.4 Elasticity imaging

The contrast between healthy and cancerous tissues has given rise to continued research in the field of elastic parameter estimation of human tissues (Weaver et al., 2001, McKnight et al., 2002, Ernest et al., 2005, Krouskop, 1998, Samani, 2007, Egorov, 2008, Chu and Rutt, 1997, Hall et al., 2003, Madsen, 2006, Muthupillai et al., 1995, Muthupillai et al., 1996, Plewes et al., 1995,

Siegmann et al., 2010, Sinkus et al., 2005, Zhu and Hall, 2002, Parker et al., 2011), resulting in the development of various elastographic imaging techniques. Elasticity Imaging is based on the general principle of palpation or compression. Images are taken with and without compression (mechanical or vibrational) and compared for strain and displacement measure.

There are three primary types of elasticity imaging:

- Tracking the motion during compression called 'Strain Imaging' (Skovoroda et al., 1995).
- Tracking of shear wave propagation through tissue to obtain the elastic modulus" (Pickerell, 2010, Imaging, 2005).
- Elastography: generates an image of tissue movement in response to external vibration or compression. Elastography involves measurement of elastic properties of tissues and can detect abnormal tissue by their firmness (Ophir, 2001).

1.5 Elastography

Increased survival with early detection provides the motivation for effective, wide-scale screening programmes (2006). This outcome led to continued development of imaging techniques, with a primary focus on contrast mechanism of biological tissues, introducing several modalities collectively known as Elastography (Plewes, 2007). Currently, elastography is primarily used in breast, thyroid, and liver imaging. Elastography for breast cancer detection is done using several modalities including Magnetic Resonance Elastography (MRE), Ultrasound Elastography (USE) and Digital Image Elasto-tomography (DIET). DIET relies on high contrast difference in elastic properties of 300% to 1500% between cancerous tissues and healthy fatty or fibro-glandular tissue in breast (Samani, 2007, Krouskop, 1998, Kopans, 1998). This contrast is an order of magnitude larger than the 5-10% radio density contrast imaged in x-ray mammography (Kopans, 1998), offering a potentially much higher resolution screening target.

1.6 Digital Imaged Elasto Tomography (DIET)

A new breast cancer screening system called Digital Image Elasto Tomography (DIET) is being developed that is non-invasive, works well on denser tissue, is less painful, quicker, and low cost. The goal is to improve screening performance and compliance. The diagnosis is primarily software based, and thus could be automated and systematic. It also would not require specialist operator and radiologist skills, further reducing operational costs (Peters, 2004, Peters, 2005, Peters, 2006, Peters, 2007, Peters, 2008a, Peters, 2008b, Peters, 2009, Brown, 2007, Brown, 2008b, Brown, 2008a, Brown, 2010, Brown et al., 2012, Hann, 2007, Hann, 2009, Lotz, 2010, Lotz, 2011a, Lotz, 2012, Lotz, 2011b).

The DIET concept relies on measuring tissue stiffness instead of radio-density, providing a much higher contrast, as cancerous tissue has been shown to be 200 – 1400% stiffer than the surrounding fibroglandular or fat tissue (Samani, 2007). The technique is based on machine vision and motion tracking to measure surface motion on a vibrating breast and analyse this data to identify a stiffer mass within the breast. The initial goal is to detect a 10mm mass, which in a screening application is clinically significant. A tumour size of 10-14mm at first detection has been shown to lead to 15-year survival rates of over 85% (Michaelson, 2002).

The DIET imaging procedure consists of three fundamental steps, which are also shown in the schematic in Figure 1.1.

- **Excitation** of the breast at low frequencies (10-100Hz)
- **Motion tracking** of breast surface motion by digital images of the breast surface
- **Software analysis** of this motion to detect disturbances caused by a stiffer inclusion

The DIET system has been tested in vitro on silicone phantom breasts with comparable elastic properties to human tissue (Lotz, 2010, Chase, 2009). Limited human trials have also been

performed with promising initial results. The imaging results observed *in vivo* match the behaviour seen *in vitro*, validating the DIET concept approach.



Figure 1.1: Key steps of the DIET Imaging procedure: (1) Excite the breast at low frequencies [left], (2) Image surface motion with digital cameras [middle] and (3) Calculate motion disturbance for diagnostic analysis [right]. Embedded in this breast phantom is 20 mm stiffer inclusion at 6-7 o'clock which can be easily identified

1.7 Research Scope

Previous work during DIET concept validation, system showed promising results (Peters, 2004, Peters, 2005, Peters, 2006, Peters, 2007, Peters, 2008a, Peters, 2008b, Peters, 2009, Brown, 2007, Brown, 2008b, Brown, 2008a, Brown, 2010, Brown et al., 2012, Lotz, 2010). A DIET stage-1 prototype was developed and tested *in-vitro* on silicone breast phantoms with limited *in-vivo* trials to establish requirements for the clinical prototype (Lotz, 2010).

The initial trials revealed a number of limitations, restricting the employment of DIET system in a large scale clinical trial. These limitations needed to be addressed to better establish the sensitivity and specificity of DIET breast cancer screening technology based on results from larger clinical trials. Development of a DIET clinical prototype thus required major improvements in image quality, imaging speed, robust vibration actuation, ergonomics, imaging procedures and diagnostic software, all of which would improve performance as well as adding robustness.

1.8 Research objectives

The main aim of this research was to develop a DIET clinical prototype system suitable for large scale clinical trials. The next main focus is on safety, speed of the imaging procedure, robustness of the electronics, ergonomic design for patient comfort, control integration, ease of use, and more robust diagnostic software. The compactness of the system, portability and cost effectiveness also remained priority objectives from conception till the development. All sub-systems were designed, built, programmed and tested in the lab, before final integration into the DIET clinical prototype (Lotz, 2011a). This thesis addresses all aspects of development for this DIET clinical prototype.

The following sections outline the specific needs and gaps that the new design needed to satisfy.

1.8.1 Optical imaging array

The DIET imaging array consists of 5 digital cameras and synchronized strobes to capture breast surface motion with high accuracy. To carry out clinical validation trials on a screening population, an imaging procedure should be completed in less than 10 minutes. This target was not possible with the existing stage-1 system, as it required 4 minutes and 12 sec for each imaging sequence acquisition, thus requiring about 2 hour and 20 minutes for a sweep of 35 actuation frequencies. The objective was to develop an optical imaging system for clinical DIET with reduced imaging time while improving its performance.

1.8.2 Strobe illumination system

The luminous intensity required for superior quality images needed to be increased to ensure precise exposures. Illumination system of stage-1 DIET prototype consisted of five strobe lights, each comprising of 127 low power LEDs and provided illumination of the order of 10 kcd, with all

five lights flashing at one time. This illumination intensity was not enough to implement the further narrowing of the pulse signal required to significantly reduce the overall imaging time. The slow flashing system also affected the image quality causing blurriness at lower frequencies and producing specular reflections on the surface of the imaged breast leading the loss of surface motion information in that particular region.

The objective was thus to improve luminescence and enable shorter imaging times while improving image quality.

1.8.3 Vibration actuation system

During DIET screening, a particular frequency in the range of 10-100 Hz induced in the breast and the sinusoidal harmonic surface motion is optically captured for further diagnostic analysis. The mechanical actuator is thus a very important sub-system of the DIET technology, as the surface motion patterns provide the main diagnostic avenue. The DIET stage-1 actuator used a vertical mechanical actuator with limitations in size and performance.

A compact and robust actuation system, capable of producing uniform and repeatable harmonic actuations at all the desired frequencies and amplitudes was another main need and objective. In addition, for greater range of adjustment and positioning was required to provide more precise actuation.

1.8.4 Actuator positioning system

In the stage-1 DIET prototype there was no mechanism to position the vibration actuation system according to varying size dimensions of the breast under screening. During the limited *in vivo* trials the breast interface of the actuator used to be manually adjusted causing discomfort

to both subject and operator. Hence, developing a 3-axis positioning system that could produce a 40mm stroke of motion in XY-stack and 100 mm in Z-axis was also an objective of this research.

1.8.5 Ergonomics, design and integration

During the conception of DIET stage-1 proof of concept prototype human anatomy had not been significantly considered and almost all subjects undergoing limited clinical trials reported discomfort and unease. The physical dimensions of the device restricted its portability and its non-ergonomic design ensured it could not be used for larger clinical trials. Finally, its weight and size rendered it unsuitable for use in a multi-storey building, without a reasonably sized elevator.

The clinical DIET prototype needs to be designed ergonomically, while also ensuring portability.

1.8.6 Imaging software and GUI

The DIET imaging procedure involves calibrating cameras in 3D, positioning the actuator according to the breast being screened, inducing a range of vibration frequencies into the breast, and freezing breast surface motion at different phases of the harmonic sinusoidal vibration by synchronising image capture with strobe light flashing. It thus requires development of integrated client-server software to control cameras, strobe lights, vibration actuator and actuator positioning system that were lacking in the original system, which required an external computer.

Therefore, a user friendly graphical users interface (GUI) and improved software systems for image capture and system operation provided further design objectives.

1.8.7 DIET IDS LiveVIEW

DIET stage-1 prototype did not account for providing a real time motion video to facilitate the operator during DIET imaging. To ensure ease of use during positioning of the actuator with respect to the breast size, a run time motion video was required to be presented to the operator.

1.8.8 Anthropomorphic breast phantoms for elastographic imaging evaluation

Currently, there is increased research interest in a wide range of elastographic soft-tissue imaging techniques based on the correlation between pathology and mechanical stiffness. Anthropomorphic breast phantoms are critical for ex-vivo validation of emerging elastographic technologies. Hence, a further need and objective was the development of realistic, repeatable phantoms made from materials that do not degrade significantly over time. Such outcomes would benefit DIET development, as well as several other research groups.

1.8.9 Diagnostic software and system evaluation

To remove human error from diagnosis, a DIET system requires software and methods for direct vibration analysis of the surface. The goal is to identify areas of higher stiffness within the areas of normal fatty adipose based on the observed tissue motion and simple models.

1.9 Thesis organisation

Each chapter of this thesis addresses a fairly distinct subcomponent of clinical DIET system and the objectives broadly defined here. The relevant prior work related to each subsystem and initial research is discussed at the beginning of each chapter, where appropriate, rather than in a separate overall introductory thesis chapter.

Chapter 2 of this thesis describes the development of optical imaging array using latest CCD industrial cameras. Chapter 3 provides details of strobe illumination system developed to avoid the requirement of expensive high frame rate cameras. Chapter 4 describes development of vibration actuation system for DIET clinical prototype, required for vibrating the breast. Chapter 5 details the development and integration of 3-axis positioning system for the actuator. Chapter 6 explains the ergonomic design and overall integration of the clinical DIET prototype. Chapter 7 describes the development of integrated imaging software and graphical user interface (GUI), and also provides a simple user manual for easy assimilation by an operator.

Chapter 8 describes the methodology for construction of realistic, anthropomorphic heterogeneous breast phantoms required for system evaluation of various elastographic imaging modalities including DIET (Amer et al., 2013). Chapter 9 and Chapter 10, respectively, present elastographic tissue characterisation through surface vibration phase response, and separate modal analysis, using DIET breast cancer screening system. Finally, Chapters 11 and 12 present overall conclusions and avenues for further work in future.

Chapter 2

2 OPTICAL IMAGING ARRAY

2.1 Background

The DIET system relies on tracking surface motion of the optically imaged breast under sinusoidal actuation. Measured surface motion is used to infer the internal stiffness distribution of the breast, where tumours are identified by their high stiffness contrast to normal breast tissue. Thus the diagnostic quality will be a function of imaging quality.

A computer vision system is used for accurately measuring the three-dimensional (3D) surface motion of the actuated breasts. Model-based segmentation is used to identify the profile of the breast and then a 3D surface is reconstructed by fitting a model to the profiles. The surface motion is measured using a modern optical flow implementation, which is customised to this application. The motion of points on the surface is reconstructed by fusing the optical flow with the reconstructed surfaces. The disruption in motion of the breast surface is used to detect presence and angular location of a tumour (Lotz, 2010).

The images of the breast under harmonic sinusoidal motion are captured by an array of 5 digital cameras. Images are captured by freezing motion with the help of a strobe illumination system (Hann, 2009), which flashes at every 36° of phase angle relative to the sinusoidal input. Thus, 10 images are captured over one cycle of a particular input frequency for each camera. The camera shutter remains open for a certain amount of time (250 ms) and the strobe illumination system, which is synchronised with the actuation frequencies, provides 10 bursts of light during each

cycle. The duration of the light burst depends upon the selected frequency and the chosen duty cycle for the light strobes (Peters, 2007).

Each point on the breast surface is captured by at least two cameras at 10 different phases of harmonic oscillation relative to the actuation input to capture the full harmonic response. The end use is to reconstruct a 3D model of the breast and analyse its surface motion behaviour for post processing (Peters, 2004). The image capturing process consists of 5 main steps. Before the examination starts, the cameras are initialized and calibrated. These images are necessary to identify the position of the cameras, by comparing the images with a known pattern and sized calibration cube (Brown, 2008a). In step three, the captured calibration images are sent to the hard disk from camera's internal memory. The patient is then positioned and steady state sinusoidal actuations are applied to the breast. The actual imaging then starts over a predefined range of frequencies, called a frequency sweep.

The strobe lights and the actuator are controlled by a LabVIEW system that runs on the real time controller. The Host PC communicates with the controller through a TCP-IP connection. The phase is set by the program controlling the actuator, the strobe lights, and the cameras. The first image is captured and saved to the hard disk. Then the next phase is set and the same cycle is repeated, thereby capturing 10 images at different phase angles relative to the actuator input (phase = 0) and saved to the hard disk sequentially (Peters, 2007).

Most consumer cameras are capable of delivering images of sufficiently high quality. However, a few brands allow their non-DSLR (3rd Gen) cameras to be controlled by third party software. Canon TM is one of those camera manufacturers that provide a Software Development Kit (SDK) for some of its non-DSLR products, such as the G series. The Stage-1 DIET prototype was equipped with 5 Canon PowerShot G5 Cameras. The G5 is a 5MP, CCD, USB1.1 camera with low processor speed (DGIC I) and low image transfer rate (1.5 MB/s). The slow transfer rate of the

G5 restricted its use for a parallel research study on Tissue Modal Analysis (Feng, 2010a, Feng, 2010b). Later, the DIET optical system was upgraded to Canon PowerShot-G9 cameras.

2.2 Identified areas of improvement

During the in vitro trials of the DIET stage-1 prototype, the capture process of the G9 cameras was found to be of acceptable quality (Feng, 2010b, Feng, 2010a). The G9 had a superior processor (DIGIC III) with a USB 2.0 interface and provided better imaging time. However, Canon had discontinued manufacturing G9 cameras and dropped SDK support for its non-DSLR products, thus constraining the replicability of the DIET imaging system. Moreover, there were difficulties associated with embedding these cameras into a portable more commercial ready medical imaging unit. Alternative imaging devices had to be introduced so that future clinical prototypes could easily be replicated and upgraded.

One obvious solution would have been to employ DSLR cameras, which are versatile and have relatively longer life cycles. However, these cameras are more expensive and each model requires a different SDK. In contrast, industrial cameras are becoming more affordable, very compact, and come with a universal SDK. Although these industrial cameras carry similar price tags compared to DSLR cameras, they are specifically designed to be embedded into other applications. In addition, a SDK is generally applicable to all cameras of a specific brand and already written software can be recycled for upgraded camera systems.

With G9 cameras, the DIET imaging time improved compared to the previous G5 cameras but was still not up to the standard necessary for the DIET application. In particular, DIET imaging involved 5 basic steps. The time taken for each of these steps with the upgraded G9 cameras is shown in Table 2.1.

Table 2.1: Processes involved in DIET imaging and time taken (in seconds) for each process using the Canon PowerShot G9 Cameras, numbers of images captured by all 5 cameras are shown in parenthesis

Process	Duration (sec)
Initialization	32
Capturing calibration Images (5)	12
Transfer calibration images (5)	12
Capturing motion images (50)	78
Transfer motion images (50)	110

Calibration is a onetime, pre-procedure process. However, the initialization of the cameras has to be done for each imaging frequency. Thus, the total time to image motion at one input frequency was 4:04 (minutes). At this stage, it was intended to image approximately 20 frequencies to have a detailed analysis of the breast surface motion. Hence, the overall time required for screening of one patient (two breasts) would have been approximately 2:30 hrs, which was not acceptable for a medical device intended for breast screening. This time cost was the main reason that only a very few subjects could be screened during the limited DIET stage-1 in vivo trials. Moreover, total numbers of imaged frequencies, during these trials were not adequate for a detailed analysis. Thus, the following areas for improvement were identified during the in vitro and limited in vivo trials of the DIET stage-1 prototype:

- Imaging time was far too high
- Cameras had to be initialized manually after each restart
- Short life cycle due to being consumer cameras
- Gradual depletion of cameras and parts from the market
- Lack of manufacturer’s technical support for commercial cameras
- Limited SDK
- Physical dimensions (107 x 72 x 50) mm³ with extended lens
- Weight 320 g

2.3 Important parameters of optical system

The cameras are characterized by a number of attributes. The significance of each attribute varies depending upon the nature of the application and the environment where the optical system is going to be used. Some attributes are interrelated and can be compensated by adjusting different components of the overall optical system.

Table 2.2: Characteristics defining the performance of an imaging device

Attribute	Options	Description and Influence
Interface	<ul style="list-style-type: none"> • GigE • USB • Firewire 	<p>Interface defines connection of the camera to PC. It affects the transfer speed (bandwidth), cable length and Power Supply (e.g. USB-powered)</p>
Sensor	<ul style="list-style-type: none"> • CCD • CMOS 	<p>Image sensor converts the optical information into an electrical signal. CMOS sensors are Active Pixel Sensors (APS), less light sensitive, faster, available in higher resolution and are cheaper than CCD sensors. CCD sensors use global shutter (simultaneous read out of all pixels) while CMOS use rolling shutters (line to line read out). Some CMOS sensors come with global start rolling shutter, a latest technology in optical imaging.</p>
Shutter	<ul style="list-style-type: none"> • Global • Rolling • Global-start-rolling shutter 	<p>The shutter is either mechanical or electrical and controls the way in which the sensor lines are exposed. Industrial cameras operate with electrical shutter i.e. global, rolling and global start rolling. A rolling shutter can cause skew, blurred, or partial exposed image.</p>
Resolution	≤ 10 MP	<p>Resolution is defined by number of pixels on the sensor. More the resolution, higher the definition of details of captured image. The sensor resolution must be supported by the lens being used.</p>
Exposure Time	0-5 s	<p>It is the time for which the sensor is exposed to light. Possible exposure times are different for each camera model. The required exposure time is influenced by brightness of object, aperture setting, light sensitivity of the sensor and the desired illumination level. A longer exposure time leads to brighter images, slower frame rate and can cause noisy images.</p>
Frame Rate	Usually ≤ 30 fps	<p>Frame rate commonly known as fps defines that how many images can be captured in one second. Each camera has adjustable fps which is influenced by pixel clock, exposure time, resolution and bandwidth of the interface. For this application this value can be as low as 1 fps as the motion is frozen by the strobe lights.</p>
Pixel Clock	5-30 MHz (adjustable), some frame grabbers are available with as high as 100 MHz	<p>Sets the frequency to read out image data from the sensor called as pixel clock frequency. Dictates maximum and minimum values of fps and exposure time. Due to an excessive pixel clock for USB cameras, images may get lost during the transfer.</p>
Sensor Size	<ul style="list-style-type: none"> • 1/3" (4.8mm x 3.6mm) • 1/2" (6.4mm x 4.8mm) • 1/1.8" (7.176mm x 5.319) 	<p>The light capturing area of sensor with pixels. This area is defined by FOV together with focal length. The designation of the sensor size does not define the diagonal of the sensor area. There are different aspect ratios; 4 (horizontal): 3 (vertical) is most common aspect ratio.</p>
Pixel Size	In microns	<p>Pixel size measured in micro meters describes the length of one side of the square shaped pixel. Bigger pixels can capture more light and provide a higher light sensitivity. Sensors with less pixel density i.e. fewer pixels per mm of the sensor, are usually less noisy.</p>
Lens Mount	<ul style="list-style-type: none"> • C-Mount • S-Mount • CS-Mount 	<p>The lens mount is the thread of the camera into which the lens is mounted. Although it defines which lens can be used on the camera, it is possible to attach other lenses with suitable adapter rings.</p>

The whole design of the optical system has to be considered, including the imaging devices, lenses and illumination system. In particular, cameras are defined by resolution, sensor type and sensor size, pixel clock and pixel size, technology used for pixel readout, shutter speed, frame rate, data interface and lens mount. Table 2.2 defines the specifically important parameters that were considered before short listing the imaging system components for the clinical DIET prototype (GMBH, 2012, (EO), MCHUGH, Joinson). The application specific parameters are Field of View (FOV), Working Distance (WD), requirement of Depth of Field (DOF) and illumination. All these cameras attributes and application specific parameters are influenced by one another. The FOV, for example, is dependent on camera's sensor size, but can also be adjusted by varying the focal length of the lens or by changing the WD.

2.4 Application Specific Parameters

2.4.1 Working Distance (WD)

WD is the space between the front of the lens and the object. It is dependent upon the space available and overall FOV required to be captured. WD for the DIET stage-1 prototype was 250mm. As it was intended to make the overall system more compact, while keeping the same or larger FOV, the WD for the new DIET clinical prototype was estimated at 200mm, as shown in Figure 2.1 (A).

2.4.2 Field of View (FOV)

The FOV is the area required to be captured by the camera in horizontal and vertical directions. FOV is influenced by WD, Focal Length (FL) and sensor size. DIET stage-1 FOV settings were 125mm (V) X 167mm (H), but it was desirable to increase the vertical dimension to accommodate larger breast sizes. Thus, FOV measurements of 170mm (V) X 160mm (H) were estimated, as shown in Figure 2.1 (B & C).

2.4.3 Depth of Field (DOF)

DOF is the range of distance around the point of focus where the image is acceptably sharp. It is influenced by aperture size (smaller aperture size (F#) leads to larger DOF), focusing distance, and acceptable circle of confusion (fuzziness). It is also a trade-off between focal length, WD, FOV and sensor size. For this DIET clinical prototype it was desirable to have a higher DOF with a minimal circle of confusion to maximize image area and overlap between cameras. A minimum requirement of close to 20 mm was estimated.

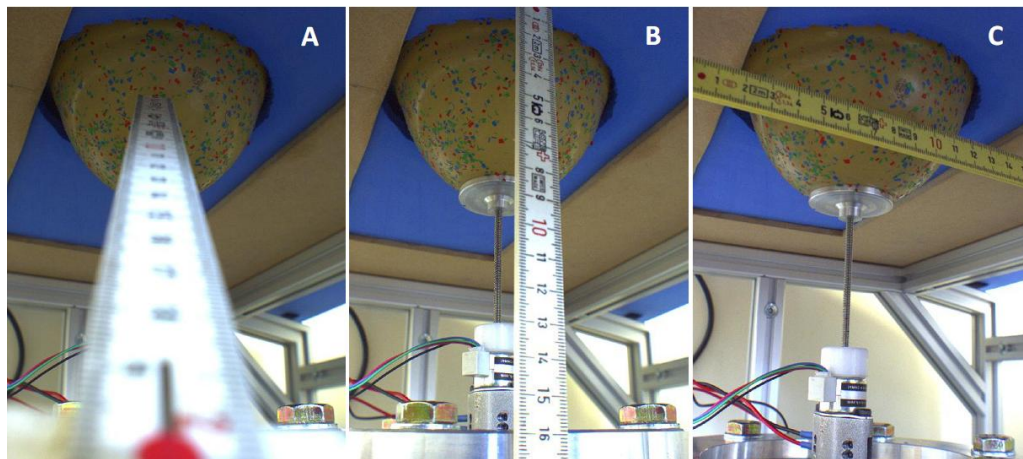


Figure 2.1: (A) WD dimensions estimated at 200mm, (B) FOV measurements in vertical dimension (170 mm) and (C) FOV measurements in horizontal dimension (160 mm)

2.4.4 Focal Length (FL)

FL is a lens attribute that can be defined as the distance from the optical centre of the lens, to the sensor, if an object at infinity is focused. Shorter FL provides a wider view angle. Equation 2.1 explains the relationship between focal length, WD, FOV and sensor size. In particular, 8mm FL lenses were used with stage-1 DIET prototype, and there was no significant change in the rest of the parameters. Thus, it was decided to use the same FL lenses for DIET clinical prototype.

$$f = \frac{WD * \text{sensor size } (h \text{ or } v)}{FOV (h \text{ or } v) + \text{sensor size } (h \text{ or } v)} \quad (2.1)$$

where h and v stand for horizontal and vertical dimension.

2.4.5 Aperture (F#)

The size of the opening in the lens through which the light passes defines the aperture size. F# is the ratio of focal length to aperture diameter. Higher F# means smaller opening of the aperture and less light incident on sensor. Higher F# provides better DOF and, consequently, a smaller circle of confusion. Canon G9 lenses were F8 and provided acceptably sharper images with adequate DOF. Therefore, it was decided to use the same aperture size for the DIET clinical prototype. Most of the lenses come with adjustable F#. Thus, depending upon overall illumination and the adopted exposure time, there is the potential to aim for higher F# for better noise filtration.

2.5 Specifications for the test camera

Overall, the following specifications were finalised for the first industrial test cameras for the DIET clinical prototype:

- Image Sensor: CCD or CMOS with global start rolling shutter
- 1 Pixel on sensor \approx 0.1 mm on object FOV
- Working Distance (WD) = 200-210 mm
- FOV: 170mm (V) X 160mm (H)
- Interface: USB 2.0 or GigE or Firewire
- Adjustable Focus (lockable)
- Adjustable aperture (F8 or F16)
- High DOF to enable sharp images for different breast sizes
- Suitable lenses thread, preferably C mount
- Control interface (SDK) programmable in C#, C++ or LabVIEW

2.6 Shortlisted camera models

Based on the specifications created, a questionnaire was prepared and sent to a number of major camera manufactures along with a brief description of the DIET system. The firms provided detailed responses with case studies and recommendations. On the basis of these case studies, their recommendations, and a cost analysis, four camera cameras models were short listed as the first test cameras for DIET imaging. An overview of the shortlisted cameras is given in Table 2.3 and a list of the firms initially approached includes:

- Imaging Development Systems, GmbH, Germany: <http://www.ids-imaging.com>
- New Electronic Technology, GmbH, Germany: <http://www.net-gmbh.com>
- The Imaging Source Europe, GmbH, Germany: <http://www.theimagingsource.com>
- Adept Electronic Solutions, Pty Ltd, Australia: <http://www.adept.net.au>
- Teledyne Dalsa Inc, ON, Canada: <http://www.dalsa.com>
- Basler, AG, Germany: <http://www.baslerweb.com>
- Mightex Systems, CA, USA: <http://www.mightexsystems.com>
- RMA Electronics, Inc. MA, USA: <http://www.rmassa.com>
- Lumenera Corporation, Ottawa, Canada: <http://www.lumenera.com>
- Scitech Pty Ltd, Victoria, Australia: <http://www.scitech.com.au>
- Point Grey Research Inc. BC, Canada: <http://www.ptgrey.com>

Table 2.3: Camera models and specifications shortlisted for induction in the initial DIET imaging research

Manufacturer	Web Address	Camera Model	Specifications
IDS (Germany)	www.ids-imaging.com	USB UI-1465LE	USB2.0, ½" CMOS, 3.1MP, 11fps rolling shutter
Imaging Source (Taiwan)	www.theimagingsource.com	DFK 72BUC02	USB2.0, 1/2.5" CMOS, 5MP, rolling shutter
Mightex (Canada, USA)	www.mightexsystems.com	BCE-C030-U	USB2.0, ½" CMOS, 3.1 MP, 8 fps, rolling shutter
SciTech (Australia)	www.scitech.com.au	Lumenera Lu375C	USB2.0, ½" CMOS, 3.1 MP, 11 fps, rolling shutter

2.7 First test camera

The specification of these cameras were studied in conjunction with their use in a medical application, technical support provided by the manufacturers, stipulated life cycle, possibilities of depletion of spare parts, and their cost effects. For a low cost breast screening device like DIET, the price tag was a dominant selection criterion. IDS UI-1465LE-C (Imaging Development Systems (IDS), GmbH, Germany) was selected as the first test camera. It was 3.1 MP, 1/2" CMOS rolling shutter camera provided with both C mount and S mount lens threads (GMBH, 2012). This camera had advantages in terms of price and space requirements, and there was a possibility to opt for a sensor-chip version (frame grabber), if the initial trial proved successful.

2.8 Initial trial results

The IDS UI-1465LE-C is a CMOS camera with rolling shutter, and thus pixel read out is done sequentially. The first pixel line (top of sensor) starts the exposure read out first, and rest of the lines read out sequentially one after the other with a short delay. As each line operates with same exposure time the first finishes exposure a small fraction of time before the last line does.

This phenomena proved to be critical for capturing motion in the DIET application, as motion was captured with the help of a strobe illumination system (Hann, 2009, Peters, 2007). Strobing was done at 2% (duty cycle) of the imaging frequency. Thus, at higher frequencies, flash durations were very short. Sequential read out of the CMOS sensor failed to expose the whole sensor area at one time when the strobe pulses were very short. This outcome resulted in black lines in those areas that were still in the process of exposure when the strobe lights went off. For example, at 50 Hz, strobe pulse (flash duration) would be 0.4 ms at 2% duty cycle, and given a fixed exposure time the last few pixel lines on the camera sensor, still in the process of exposure, would miss the flash, resulting in an image with the top few lines getting more light compared

to the last few lines. The result is partial exposure and the pixel lines missing out on part or all of the illumination appeared darker on the image.

An image series of these distorted motion capture at different exposure times is shown in Figure 2.2. As can be seen from the exposure series, the effect of darker lines was different at different exposure times. Trials were conducted to find out the optimum value of the exposure time, but, as the DIET system runs over a sweep of frequencies, different exposure times had to be set for different frequencies, which was not possible. One option could have been to trigger the camera exposure through hardware, synchronised with the actuation motion and the strobe lights. However, hardware triggering was not available with this camera.

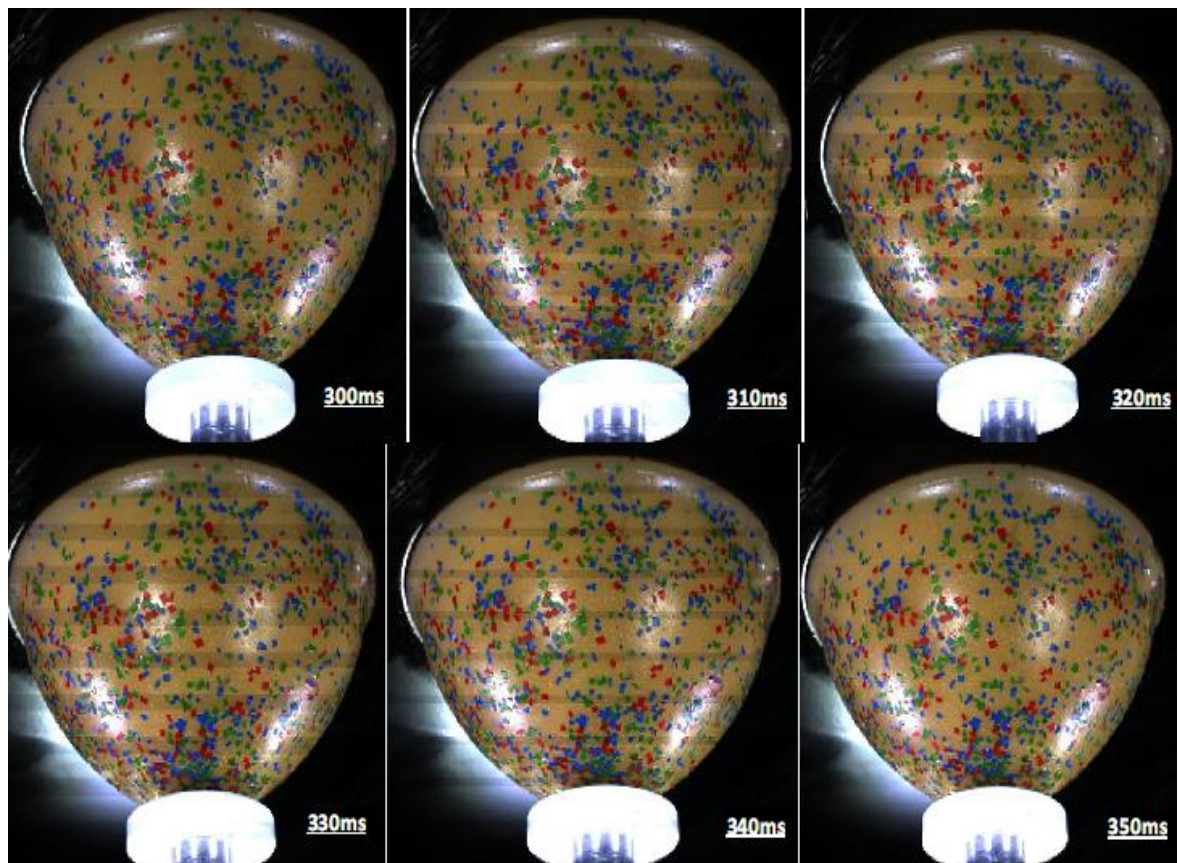


Figure 2.2: Sequence of images taken at different exposure times at 20 Hz flash frequency. At 300ms and 350ms the effect of partial exposure seemed to be minimum, while showing more uniform brightness at 350ms. But with the change in imaging frequency a new value of optimum exposure time had to be established.

2.9 Hardware Modification of the Test Camera

Image recording in the sensor of the camera involves four phases:

- Reset pixels of the rows to be exposed
- Exposure of pixel rows
- Charge transfer to sensor
- Data readout

In CCD cameras, the image is projected through a lens onto the capacitor array, causing each capacitor to accumulate an electric charge proportional to the light intensity at that location. CCD, also known as passive pixel sensors (PPS), technology is implemented as shift registers that move electric charge between capacitive bins, to an area where the charge can be manipulated. It is done after converting it to a digital value with the shift, allowing for the transfer of charge between the bins. In contrast to active pixel sensors (APS), CMOS sensors consist of ICs. Hence, solving the processing speed and scalability issues of the PPS.

However, there is a trade-off, as CCD cameras come with global shutters whereas most of CMOS cameras normally have the rolling shutters. Rolling shutter sensors expose and read out each line of pixels sequentially with a delay between each line, a blocked read out of several hundred microseconds. A global shutter possesses a storage element allowing the pixel to dump the storage charge into a shielded area, which can be read out during the exposure of the next frame. Therefore, there are no discontinuities or image artefacts associated with global shutter.

The IDS UI 1465 LE-C comes with a 3 MP CMOS sensor having an electronic rolling shutter, the pixel rows are reset and exposed one after another. At the end of the exposure, the lines are read out sequentially. As it results in time delay between the exposure of the first and last sensor rows, captured images of moving objects are distorted. To counteract this effect, some rolling start shutters also provide a global flash window providing exposure of all rows

simultaneously during a defined time period. This exposure is obtained by providing a trigger signal. However, IDS UI 1465 LE-C did not have this option.

Therefore, as shown in Figure 2.3, a hardware modification was carried out to provide a 5 volts TTL trigger signal to the camera sensor to start exposure. A cut was made in the camera's external body and the pins were extended to provide the control signal to the chip to start exposure. The idea was to provide a global flash window, triggering the camera only for a desired interval of time to synchronize it with the strobe flash using LabVIEW. This modification also did not solve the problem and some under exposed areas were still observed. This outcome necessitated selection of a CCD camera for the DIET clinical prototype that could provide a global shutter method.



Figure 2.3: Showing the pin configuration extended as a result of hardware modification in the test camera providing a control signal for exposure. The objective was to convert rolling shutter into global start rolling shutter

2.10 Selected Camera and specifications

The reason for selecting a CMOS camera with rolling shutter was mainly its cost and also that industrial CCD cameras with resolution as high as 1600 x 1200 pixel were not available till the end 2010. As a result of continuous correspondence with the technical support team of IDS GmbH, Germany due to the distorted image capture by the first test camera, it was reported

that IDS had launched a new USB 2.0 CCD camera, UI-2250 SE-C, with 2 MP resolution. Other specifications also matched the criteria for the DIET application.

After an initial feasibility study, it was quickly decided to purchase a single camera for testing. The trials proved successful, and the UI-2250 SE-C was selected for inclusion in the DIET clinical prototype. Figure 2.4 shows pictures of all the cameras involved in the gradual evolution of imaging technology in DIET prototypes. Table 2.4 contains a comparison of the important attributes of the selected camera, the IDS UI 2250 SE-C, with three earlier models used for capturing surface motion of the breast during the initial research of DIET concept.



Figure 2.4: Evolution process of digital cameras for DIET, starting from left Canon G5, Canon G9, IDS UI 1465 LE-C, IDS UI-2250 SE-C with C mount lens

2.11 Camera lenses

Lenses are an important component of the imaging system. Most lenses comprise several elements, each of which directs the path of light rays to recreate the image on a digital sensor as accurately as possible. The goal is to minimize the aberrations and artefacts. Optical aberrations occur when points in the image do not translate back onto single points after passing through the lens, causing blurring and reduced contrast, or resulting in misalignment of colours (chromatic aberration). Lenses may also suffer from radially decreasing image brightness

(vignetting) or distortion. These issues are present to some extent with any lens. When a lens is referred to as having a lower optical quality than another, it is manifested as some combination of these effects.

Table 2.4: Comparisons of cameras specifications used during the initial research of DIET system

Camera models	Canon G5	Canon G9	IDS UI-1465 LE-C	IDS UI-2250 SE-C
Interface	USB 1.1	USB 2.0	USB 2.0	USB 2.0
Lens	Built in	Built in	C & S mount	C & S mount
Sensor technology	1/1.8" CCD	1/1.7" CCD	½ " CMOS (Aptina)	1/1.8" CCD (Sony)
Resolution	5MP (1600x1200 used)	12 MP (1600x1200 used)	2048 x 1536 (1600x1200 used)	1600 x 1200
Pixel Pitch (µm)	2.8	1.9	3.2 µm	4.4
Resolution depth	12	12	8	8
Shutter technology	global	global	rolling	global
Frame rate (fps)	11	15	11	12
Exposure Time	0.05ms – 15s	0.04ms – 15s	57 µs – 1.75s	94 µs – 1.57s
Dimensions (mm ³)	121x75x70 mm ³	106 x 72 x 43	44x44x25	34x32x41
Mass	410	320 g	32 g	74g
Power Supply	Li-Ion battery / AC adapter	Li-Ion battery /AC adapter	USB	USB

Table 2.5: Shortlisted lenses and their technical characteristics

	Lensagon B3M8018S12	Lensagon CY0813	Lensagon C3M0814
Mount	S-mount	C-mount	C-mount
Max image format	½ "	2/3"	1/1.8"
Focal length	8mm	8mm	8mm
Aperture	F1.8 (fixed)	F1.3 - F16 (adjustable)	F1.4 – F16 (adjustable)
Minimum operating distance (MOD)	-	0.2 m	0.2
Angle of view	35.° x 46.5°	45° x 57.8°	36.4° x 48.3°
Dimensions (mm ²)	22 x 24	29 x 34	29 x 38
Mass (g)	18	60	65

There is always a tradeoff between image quality, size and cost of the lens. Canon G5 & G9 cameras came with built in lenses. However, for IDS industrial cameras, an appropriate lens had to be chosen. Three different lenses from Lensation GmbH, Germany were earmarked and tested. The nomenclature of the shortlisted lenses and their specifications are shown in Table 2.5.

2.12 Initial Lens trials

The simplest way to estimate the image quality of a lens is by imaging a checker board. This method clearly shows aberrations including contrast problems, vignetting and blur (Kumler and Bauer, 2000, Stein, 1995).

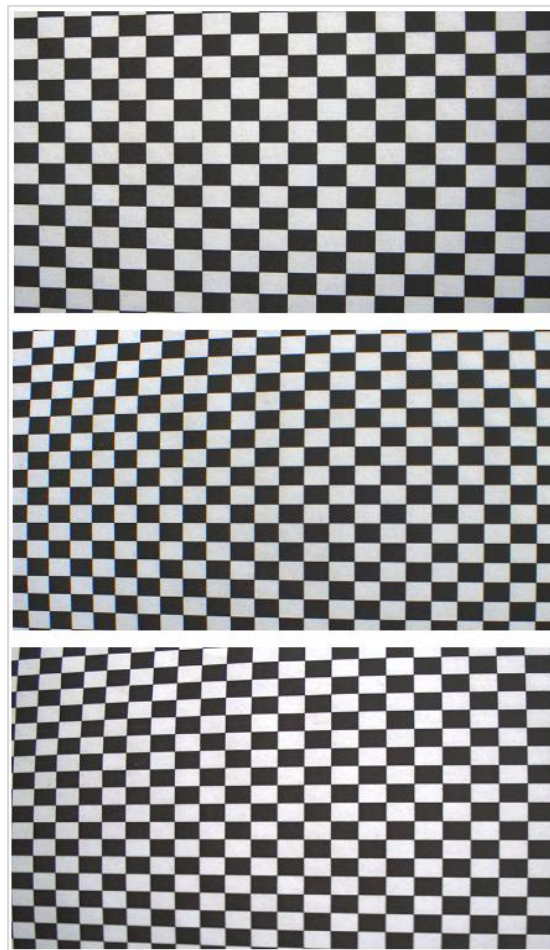


Figure 2.5: Lens trial, exposure series of UI-2250 SE-C at 0.2m distance using C3M0814 at F8 aperture (top), CY0813 at F8 aperture (centre) and B3M8018S12 at F1.3 aperture (bottom)

A checker board pattern having black and white squares of 5mm x 5mm was printed on a paper and extensively imaged from different angles and distances to finalize the lens selection for the DIET. Figure 2.5 provides a series of exposures captured with different lenses using the IDS UI-2250 SE-C camera from a minimum working distance of 0.2 m at F8 and an exposure of 210 ms. As expected, none of the lenses provided a 100% perfect image. However, best quality images with the least aberration in terms of pattern size, blur, distortion and barrel effects were captured using C3M0814, and it was finalized for selection (Lensation).

2.13 Camera installation

To install the cameras on the main frame of the device, a custom built mount was designed as a 3D CAD model and CNC milled out of aluminium. The camera mount consisted of three subcomponents each having a 4mm thickness:

- A base plate to fix the camera to the main frame, allowing the flexibility of panning the camera through 180° in the horizontal plane and flexibility to move cameras closer or away from the object thus increasing or decreasing the WD by up to 20mm [Fig. 2.6(A)]
- Two side brackets with curving slots allowing the flexibility of tilting the camera 20° up or down. These brackets would hold the cameras from sides and mount them onto the base plate [Fig. 2.6(B)].
- A top plate to hold strobe light's heat sink and PCB [Fig. 2.6 (C)].

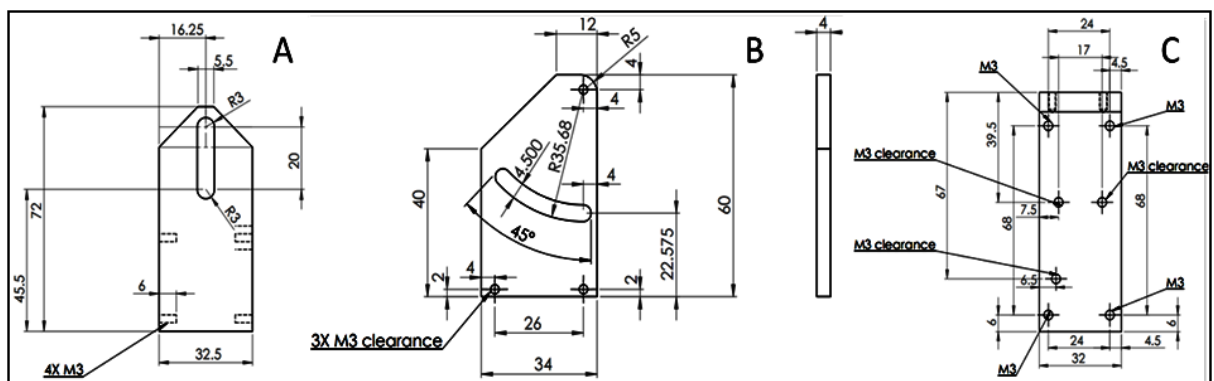


Figure 2.6: Subcomponents of the custom built camera mount, (A) base plate (B) side bracket and (C) top plate

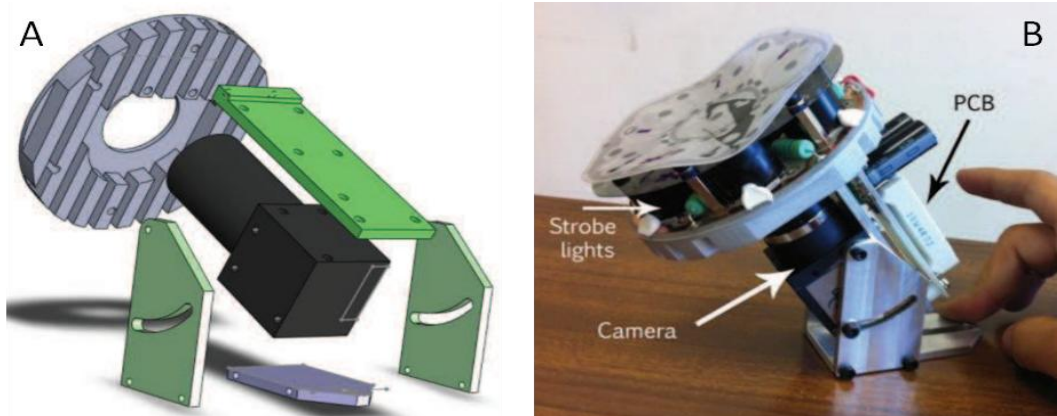


Figure 2.7: (A) Exploded view of the camera mount and heat sink (B) assembled camera with strobe light and PCB ready to be mounted on the main frame Programming IDS UI 2250 SE-C

Figure 2.7 shows the exploded view of the camera mount with heat sink (A) and the assembled camera with heat sink, strobe light and PCB ready to be installed on the main frame of the device through an M6 screw.

2.14 Camera programming

One of the main aims of evolving the camera array was to improve overall timing of the DIET imaging procedure, apart from space requirements, image quality and long life cycle of the imaging devices. During a DIET examination, the woman lies horizontally face down with one breast hanging downwards through a hole in the examination table. Every imaging session is executed over a sweep of different frequencies depending upon the fundamental frequencies of the breast and the post processing algorithms being used. Each camera captures 10 images at each frequency with the help of a strobe light system, which is synchronised with the actuation frequencies and flashes at controlled pulse duration.

The camera aperture remains open for a certain amount of time (~250 ms) and motion is frozen by strobing the lights on and off in the dark room environment, at a very small interval of time (~0.4 ms at 50 HZ and 2% duty cycle). Before the examination can start, the camera system needs to be initialized and calibrated to be able to reconstruct the motion in 3D during the post

processing (Brown, 2008b, Brown, 2008a). The strobe light's pulse duration is synchronised with the actuation frequency, such that it flashes at every 36° phase, thus capturing 10 images during one cycle of motion (Hann, 2009). These images are subsequently transferred to the Host-PC.

The strobe lights and the actuator are controlled by a LabVIEW-VI, which runs on a real time FPGA. This program allows the user to control the actuator amplitude and the frequency and also the phase and duty cycle of the strobe lights. The C-programme that runs on the Host-PC has access to these parameters via TCP. At first, the phase is set, after which the C-programs sends the image capturing command to the cameras, which starts the exposure.

Cameras temporarily store the captured images on their internal SD card and when the image capture is completed, it saves those images on the Host-PC using threading. Following this process, the actuation and imaging step move onto the next frequency and repeat these steps for all the specified frequencies.

The IDS Imaging software was initially written in C++ using the MS Visual Studio 2010 Professional platform and subsequently converted to C# for better adaptation to Graphical User Interface (GUI). For programming with the *uEye* API, IDS suggest using the C++ programming language. This programming language offers efficient access to all functions of the *uEye* API. Enabling access to image memory contents through pointers, C++ is especially suitable for image processing applications. Most of the *uEye* sample programs are also created in Microsoft Visual Studio using the C++ programming language. After installing the drivers, the following files from the SDK are required to be included in the project:

- Header file : *uEye.h*
- Lib file : *uEye.h*
- Function library (DLL) : *uEye_Api.dll*

Functions that refer to an initialized camera have the camera handle (HIDS hCam) as the first parameter. All parameters that are set using these functions remain valid for as long as the handle is valid, until the corresponding camera is closed or the program is exited.

2.14.1 Basic steps of *uEye* programming

The main functions were provided with the IDS SDK and accessible by including the DLL function library to the user defined project. There were six basic steps involved in the programming of *uEye* cameras (Systems).

2.14.1.1 Initialize camera

The *is_InitCamera()* function initialized the *uEye* camera. The cameras were assigned unique handles through which these were accessed in subsequent function calls.

2.14.1.2 Set display mode

The *uEye API* provides two different modes to display images on the Host-PC: 1) Direct3D mode to quickly show live image under Windows without allocating any memory, and 2) Direct Bitmap (DIB) mode. To use DIB mode, first memory for all the 5 cameras had to be allocated and then by using the memory buffer, the images are displayed. The *is_SetDisplayMode()* function is called to select the display mode.

2.14.1.3 Adjust Parameters

All function calls to change camera settings start with *is_Set*. To change the frame rate, for example, *is_SetFrameRate()* is called. Image brightness is adjusted through the exposure time set with *is_SetExposureTime*. User defined control parameters were implemented using *is_LoadParameters()* from an *ini* (configuration) file which is read through in real time during the process of imaging. Pixel clock (read out frequency in MHz), Frame Rate (fps) and Exposure Time

are 3 dominating parameters defining the image quality in a certain illumination environment. Other parameters like, image size, colour correction, white balance, gamma correction, hot pixel removal, and Area of Interest (AOI) can be defined in the *ini* file.

2.14.1.4 Capture Images

To capture single frames, function *is_FreezeVideo()* is called, however for capturing a live video *is_CaptureVideo()* is called. Cameras are controlled externally through cameras server software by calling *is_SetExternalTrigger()*.

2.14.1.5 Save Images

The *is_SaveImageEx()* function is used to save the current image as a BMP file.

2.14.1.6 Close Camera

The camera and the allocated memory are automatically released by calling *is_ExitCamera()*. All previously set camera parameters are lost if the cameras are closed. However, *is_SaveParameters()* is used to save settings and loading them using *is_LoadParameters()*, on next initialization.

2.14.2 Implementing Multithreading - DIET IDS imaging software

After finalizing the imaging code with the new IDS cameras, a stop watch was implemented to measure the timing for each process individually. The image capture and image saving at one particular frequency (10 images each from all five cameras) would take 12s, which was relatively long with respect to the set exposure time and transfer rate of USB 2.0 bandwidth. The time loss was attributed to the sequential imaging by all 5 cameras one after the other.

The *UEye* API is thread-safe, so the API can be accessed by multiple threads simultaneously. IDS recommends to call three basic functions, *is_Init_Camera()*, *is_SetDisplayMode()* and

is_Exit_Camera(), only from a single thread so that simultaneous attempts to call the same function are recognised and prevented by driver.

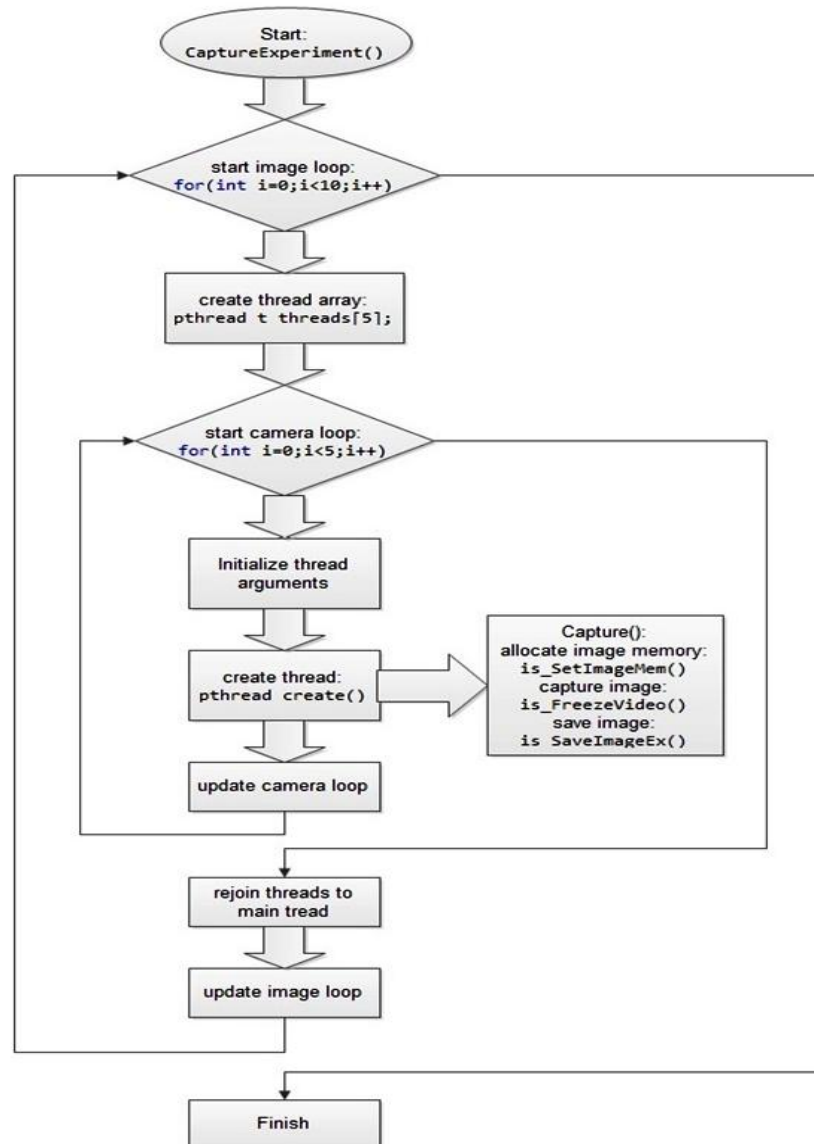


Figure 2.8 : Flow chart of image capturing Code after implementing multithreading

Therefore, for more efficient imaging, multithreading was implemented in the DIET control software (C#), allocating a single thread to each camera from initialization to saving the image. This approach reduced the overall imaging time for one cycle from 12s to 6.4s. Figure 2.8 shows the flow chart of implementation of multithreading in the imaging code.

Table 2.6 shows a comparison of time required for each process during a standard DIET imaging session required to run the trial at one particular frequency. Figure 2.9 shows a single shot captured by IDS UI 2250 SE-C (cam2) at 31 Hz, where the actuation amplitude was 0.5mm. The new prototype results in a 93% reduction in the imaging time from the initial prototype.



Figure 2.9: Picture of a silicone phantom under actuation taken with IDS UI 2250 SE-C

Table 2.6: Comparison of time required for each process at one frequency during a standard imaging session of DIET stage-1 and clinical prototype

Process	Time Taken (all five cameras)	
	DIET stage-1 prototype	DIET clinical prototype
Initialization	32s	8.6s
Capturing Calibration Images	12s	2.4s (combined for image capturing and saving)
Transfer Calibration Images	11s	
Capturing Motion Images	1:27 min (for 10 phases)	6.4s (combined for image capturing and saving)
Transfer Motion Images	1:50 min (for 10 phases)	
Total time (for one frequency)	4:12 min	17.4s (multithreaded)

2.14.3 DIET IDS LiveVIEW

One of objectives of DIET clinical prototype was that a nurse/operator should be able to operate the system with least technical skills and the positioning of the breast actuator should be done remotely. To achieve this goal, it was necessary to present the operator with a real time video

from at least 2 cameras, one positioned at the x-axis and one positioned at y-axis of the device.

The IDS manual suggests using C# for visualization applications, using the *uEye.cs* header file.

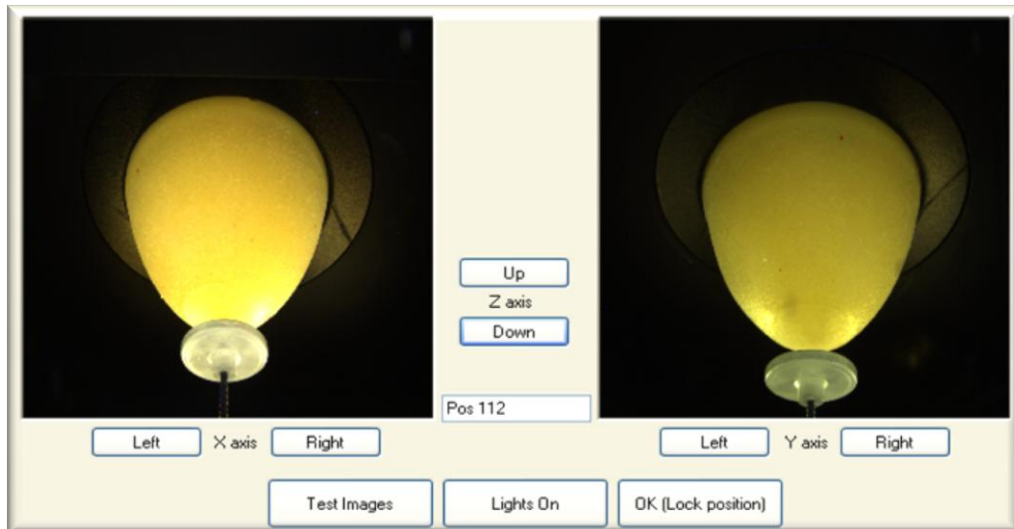


Figure 2.10: Actuator positioning window showing the real time video. Control of the 3-axis positioning system is also provided in the interface to facilitates the operator in positioning the actuator with respect to the size of the breast

A program was written in C# providing LiveVIEW from cam1 (reference camera at 12' o'clock) and cam5 (reference camera at 9' o'clock). The messages for xyz-positioning of the actuator were also implemented in the program providing control of the 3-axis positioning unit to the operator. Figure 2.10 shows the real time video required to control the 3-axis positioning of the actuator.

2.15 Summary

Ideally, to conduct clinical trials on a screening population the imaging procedure should not take more than 30 minutes and preferably much less. This goal was not possible with the DIET stage-1 prototype, as it required approx three minutes for each acquisition (capturing and transferring ten motion images at a particular frequency). An array of five robust (industrial), high speed (USB-2) CCD cameras with 2MP resolution was developed, programmed and integrated with high powered strobe illumination system to eliminate the requirement of very

high frame rate cameras (fps=50-100). The overall objective was to develop an optical imaging system for clinical DIET with reduced imaging time while improving its performance.

The overall imaging capturing time has been reduced to 17.4 s at one frequency, a 93% reduction. The imaging array consisting of five IDS UI 2250 SE-C cameras synchronized with the strobe illumination system was designed to capture breast surface motion with high accuracy and in a shortest possible time. Adequate lenses were selected and integrated. Cameras were programmed for the DIET imaging session as well as to provide a real time video to facilitate the operator in positioning the breast actuator. The cameras were integrated into the system synchronised with the strobe illumination system to avoid the requirement of high cost cameras with high frame rates. The overall imaging time for acquisition of images at one frequency was reduced from over 4 minutes to 17 seconds, which would enable a screening of 10-20 frequencies in 3-6 minutes far faster than 30 minutes.

Chapter 3

3 STROBE ILLUMINATION SYSTEM

3.1 Background

Choosing the correct illumination in an optical system is as important as choosing the right camera. Often, the desired image quality can be met by improving system illumination, rather than investing in higher resolution detectors, imaging lenses or software. Improper illumination can cause a variety of image problems, such as blooming, hot spots, shadowing and low signal to noise ratio, which subsequently can lead to difficulties in edge detection and thresholding. The imaging lens aperture (F#) impacts the amount of light incident on the camera, so illumination should be increased as the lens aperture is closed, switching to a higher F#. Higher power lenses usually require more illumination, as smaller areas viewed reflect less light back into lens. The camera's minimum sensitivity is also important in determining the minimum amount of light required in the system. Finally, camera settings such as pixel clock, shutter speed, exposure time and gain adjustments also affect the decision of choosing the right light intensity of the system. Hence, illumination is a relatively complex problem in many variables, and can significantly impact overall system performance.

3.2 Previous Work

One major challenge with DIET imaging is to capture a large number of images (normally - 10) during one cycle of the actuation frequency, such as 50 Hz, which entails capturing images at the rate of 500 frames per second. The frequency sweep in a DIET system may also use higher

actuation frequencies of up to 80 Hz in some cases. High resolution cameras with frame rates in this range are either not available or are highly expensive. CMOS technology has developed to the point, that the cameras can now capture images at the frame rate of 500 images per second at a resolution of 1280x 1024. However, this resolution is rather limited for DIET. High resolution CCD cameras with high frame rate to match DIET system requirements are not available.

To offset this issue an innovative approach was adopted. A strobe flash system was devised to provide flashes of illumination with the same frequency as actuation but with an offset phase angle. The system thus uses precision controlled strobe lighting to capture sinusoidal response at different points in the sinusoidal response cycle. Because the breast is actuated sinusoidally, the steady state motion of the surface is sinusoidal at the actuation frequency. Therefore, the image capture can be solved by using a strobe light running at the same frequency as the actuator to obtain static images of the actuated breast.

To use the LEDs as a strobe, a stream of narrow pulses, synchronised with the linear variable differential transformer (LVDT) position sensor of the actuator was used as input (Hann, 2009, Peters, 2007, Brown, 2008a). The strobe system is controlled by NI-cRIO and runs on real time FPGA. The LabVIEW program allows the user to control the phase and duty cycle of the strobe. The C++ program that runs on the Host-PC has access to these parameters via TCP-IP. The number of different phases for capture can be set by the user.

In the stage-1 DIET prototype, the camera aperture was set to remain open for 2 sec. The flash duration was kept at 2% duty cycle of the frequency of actuation. Finally, a total of 10 images were captured during one cycle of a typical frequency at 10 different phase angles.

Five strobe rings each containing 127 X 5mm white (ZD 1999x) were installed in parallel to the cameras. The illumination intensity provided by each LED was 16 candelas at a viewing angle of 15°. Thus, each ring of the strobe lights provided a total of 2000 candelas. Each camera has its

own strobe ring but the timing is controlled so that all five strobe lights flash at one time for the flash duration set by the user. Hence, each camera sensor gets illumination intensity of the order of 10,000 candelas for each capture. A schematic diagram explaining the synchronization of camera exposure and light strobing is shown in Figure 3.1.

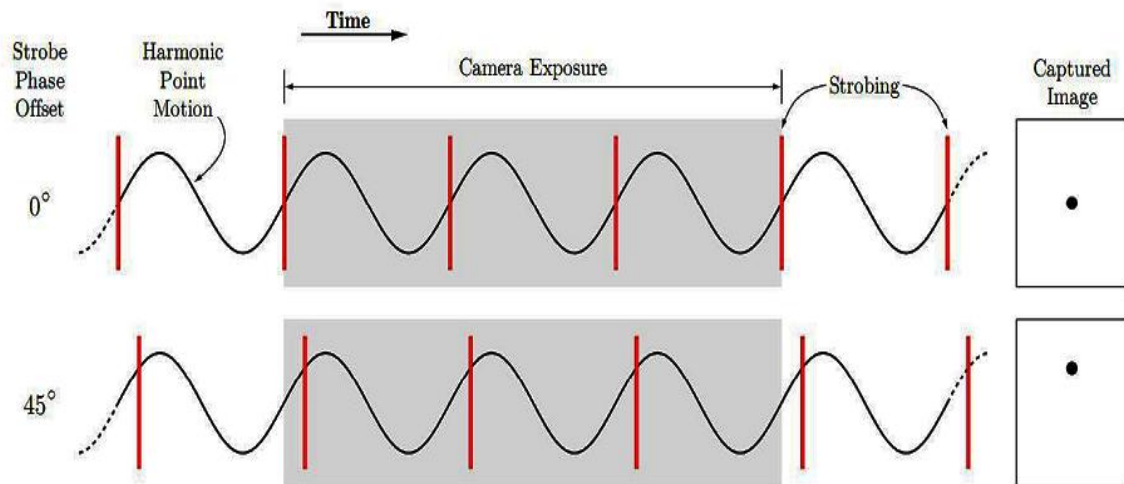


Figure 3.1: Schematic of camera exposure and strobing (Peters, 2007)

3.3 Areas needing improvement

During the limited trials of DIET stage-1 prototype following areas of improvement were identified:

3.3.1 Time Lag

The time required to capture one motion imaging data set was 4 minutes 12 seconds at a single frequency. For a sweep of 10-50 Hz with a step rate of 2 Hz, the patient would have to remain in position for more than one hour. Limited in vivo trials showed the need to minimize this time for patient comfort, imaging speed and throughput. However, increased shutter speed, reduced exposure time required higher illumination intensity of at least 2x of the initial DIET configuration.

3.3.2 Fuzzy Images

It was also noticed during the initial trials that at lower frequencies with 2 seconds of exposure and 2% duty cycle for strobe flash system, the motion images were fuzzy. The motion tracking software was unable to accurately process these images for 3-D reconstruction in the SEER algorithm (Brown, 2008a). This issue required reducing the duty cycle to 1% to get sharper images and led to increasing the light intensity by at least (another) factor of 2x.

3.3.3 Glare patterns from reflective surface

The in vitro validation trials used silicone breast phantoms, which have a greater index of reflectivity compared to real human skin. Specular reflection from the silicone surface caused circular glare patterns on the motion images, distorting the image. Thus, motion information in those regions was lost. As the feature tracking was done fiducially (Brown, 2008a), with markers having a wide colour contrast, it was still possible to process the motion reconstruction with gaps in the areas of higher brightness.



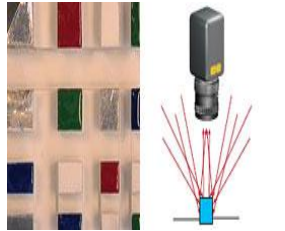
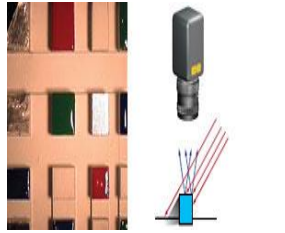
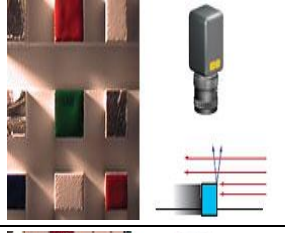
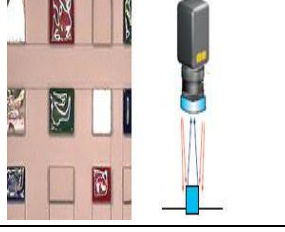
Figure 3.2: Stage-1 DIET prototype image showing specular reflections from the highly reflective surface of the silicone breast phantom during in vitro trials

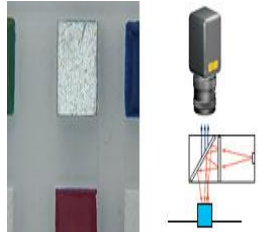
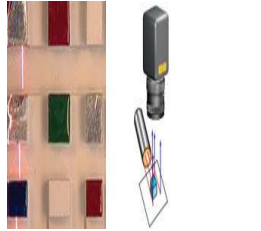
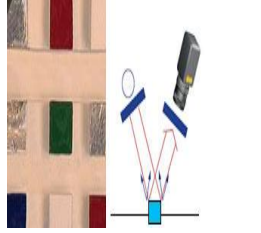
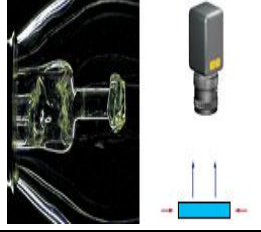
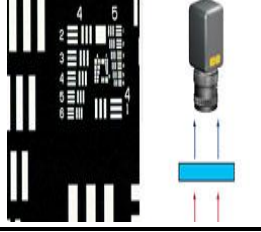
Figure 3.2 shows an image from the stage-1 DIET prototype having regions of high specular reflection. However, as future DIET systems seek to track bare skin using a modern optical flow technique, it was necessary to remove the higher reflective glare from the images.

3.4 Initial Research

Several illumination techniques were evaluated to assess if they provided enough light. A comparison of illumination techniques currently being used, their advantages and limitations in a certain application are given in Table 3.1.

Table 3.1: Comparison of various illumination techniques vis-à-vis suggested applications ((EO), Joinson, MCHUGH)

Illumination Techniques	Sources	Advantages	Dis-advantages	Applications	Visual Representation
Diffused Illumination	extended source	Reduces glare and provides even illumination	Large and difficult to fit in confined spaces	Best for imaging shiny objects with large WD	
Directional Illumination	Point source (single or multiple)	Bright and flexible	Shadowing and Glare	Inspections and measurements	
Glancing Illumination	Point source illumination at a sharp angle of incidences	enhances object topography	Hot spots and extreme shadowing	Examining finish of opaque objects & defect detection	
Ring Light	Coaxial illumination mounted on lens	Reduced shadowing & even illumination	Circular glare patterns, works only in short WD	Inspection and measurement systems with matt objects	

Diffused Axial Illumination	Coaxial to imaging axis, beam-splitter reflects light	Even & diffused, reduced shadowing	Larger in size, limited WD, low throughput	Measurements and inspection of shiny objects	
Structured Light (Line Generators)	Typically laser projected lines, spots, grids or circles	Enhanced surface features, intense light over small area	Blooming and absorption of some colours	Inspection of 3-D objects, Topography measurements	
Polarized Light	Directional illumination making use of polarized light	Even illumination, reduced glare, features more discernible	Overall intensity is reduced after polarization of source and/or lens	Measurements and inspections of shiny objects	
Dark-field	Light enters transparent objects through the edge perpendicular to the lens	High contrast of internal and surface details	Poor edge contrast, Not useful for opaque objects	Glass and plastic inspections	
Bright-field or Backlight	Object is lit from behind, used to silhouette opaque objects	High contrast for edge detection	Eliminates surface details	Targets and test patterns, edge detection, measurement of opaque objects	

DIET requires intense but even illumination for 3D shape profiling of the breast for further image processing. Reduced shadowing and low specularly, for in vitro trials on silicone phantoms with highly reflective surfaces, were primary considerations given the optical flow (OF) algorithms used to track skin surface motion. Thus, the environment required needs to be a combination of intense, diffused, structured, ring and polarized illumination. The specific design criteria involved compact overall size with high flash intensity and high flash rate (approx 100Hz).

3.5 Design concept

The previous strobe light consisted of 127, low power, 5mm White LEDs. The LEDs were installed in ring fashion to provide uniform lighting with a small on-board PCB for power conversion. Each strobe light was mounted on top of the camera lens as shown in Figure 3.3 and was supplied with 7.5 V DC through a bench top regulated power supply. The diameter of the ring was 130 mm. With the on-board electronic circuitry, the total span of the strobe light was 175 mm. The illumination intensity of each LED was 16 candelas. Thus, one strobe light provided a combined illumination of approx 2,000 candelas. There were no arrangements for heat dissipation and a considerable number of LEDs would fail due to overheating.

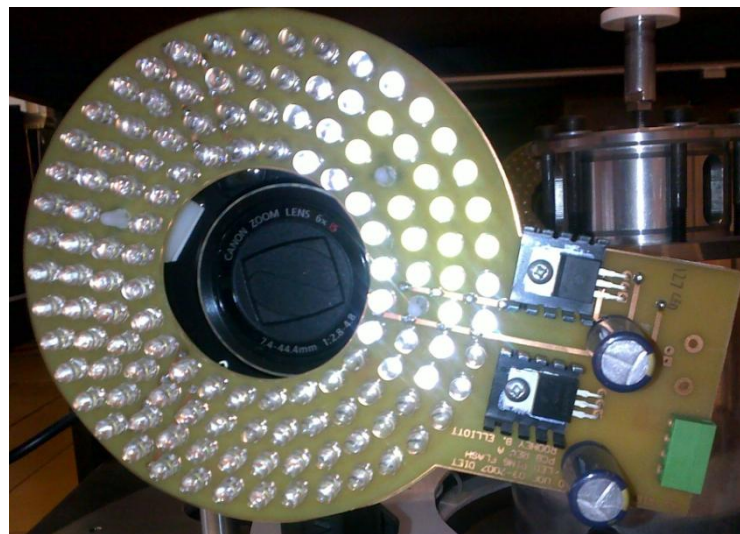


Figure 3.3: LED Strobe ring mounted on top of the camera in the stage-1 DIET prototype

The illumination intensity of the LEDs used in the previous strobe lights was specified in Candela and most high power LEDs considered are specified in Lumens. Converting Candelas to Lumens shows that high power LEDs with 250 Lumens and a 24° beam angle yield 5x greater intensity of the prior strobe lights.

Once the type and number of LED's required were known, the electrical drive circuit could be designed. It was decided to use a capacitive discharge circuit to drive the LED's at several times their normal operating current, increasing the peak light output, and a current limiting resistor to establish a lower steady-state current to charge the capacitor. The LED's chosen were 6 XRE Cree Star modules, with an operating current of 1A and output of 250 lumens (Cree, 2011). In the circuit shown in Figure 3.4, the peak current was of the order of 4 Amps per LED. This current was set by a combination of LED operating voltage at the peak current level, the LED series resistor (0.47 Ohm) and the capacitor charge voltage. It was relatively easy to alter the peak current by changing the supply voltage, and the normal range was 5 to 12 V. The time constant of the LED series resistor/capacitor (C0/C1) combination, which determines the time taken to discharge to 63% of the initial voltage, was 3.1ms not taking into account the internal resistance of the LED chip. The charge time to 90% of full charge of the capacitor was 5x the time constant of the R1/R0-C0/C1 combination, or 77.5ms. Q1 is a MOSFET switch that switches current through the LED's when 5 volts is applied to its gate.

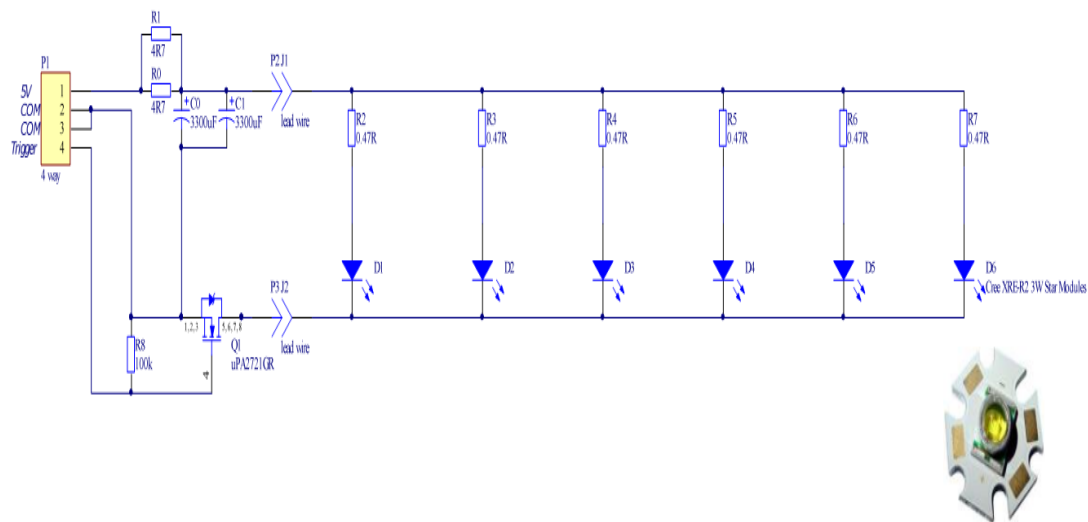


Figure 3.4: Circuit diagram of LED drive PCB with XRE Cree Star LED

The six LEDs were installed in ring fashion to be mounted around the camera lens. The PCB also included a small circuitry for the charge capacitor. The diameter of the ring was 100 mm and the

size of the charge capacitor PCB was $90 \times 40 \text{ mm}^2$, but it was meant to sit on the back of the camera as shown in Figure 3.7. Therefore, the total space requirement for the strobe light was only 100 mm (circular) and should provide 5x more light compared to the previous system. Figure 3.5 shows the CAD image of the circuit board layout with applied collimators sitting on top of the LEDs and the capacitor board. Five such LED strobe light rings were constructed and mounted on each of the five cameras. To allow heat dissipation of the high power LEDs, a linear fin aluminium heat sink was designed and attached to the PCB using thermally conductive adhesive. Holes were made in the heat sink base plate to fix the LED PCB ring such that no LED sat on the attachment screw, to avoid heat transfer through the screws. A Solidworks representation of the heat sink base plate, developed to house the LED strobe lights is shown in Figure 3.6.

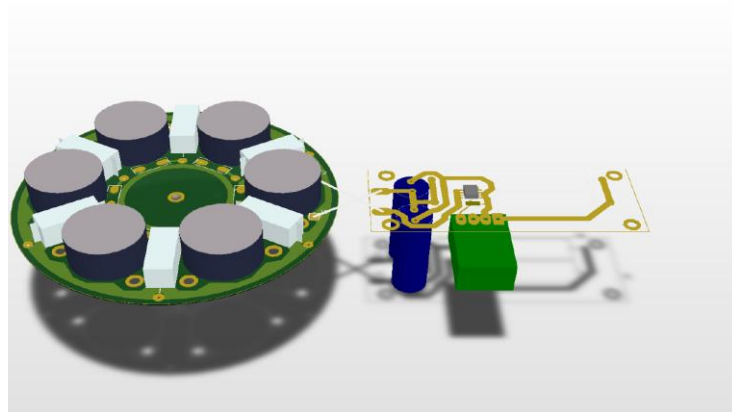


Figure 3.5: CAD image of circuit board layout, collimators are the black cylinders sitting on top of the LEDs, 30mm cut-out in the centre of the board is for the camera lens. The capacitor board is shown in transparent

To reduce glare from shiny surfaces a circular polarising filter was applied on the ring LED strobe light. Thus, light transmitted by the LED would be polarized twice. Once when incident on the object and again when entering the camera lens. Although polarized light is significantly attenuated through the filter, it increases the saturation of colors by eliminating some of the light reflected from the shiny surfaces. A circular polarizer not only blocks or allows circularly polarized light, but it is also sensitive to linear polarization.

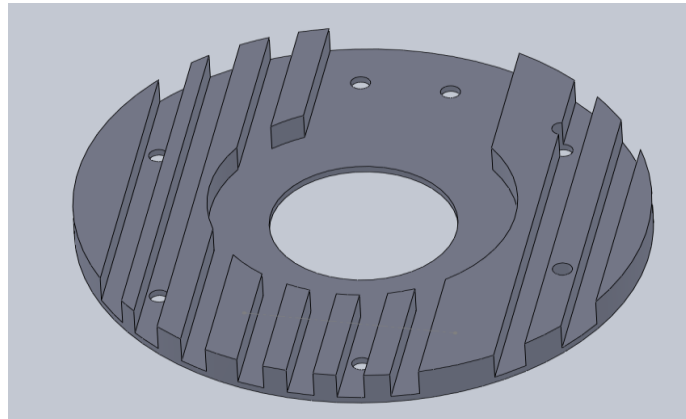


Figure 3.6: Solidworks drawing of the heat sink (a base plate for LED circuit board)

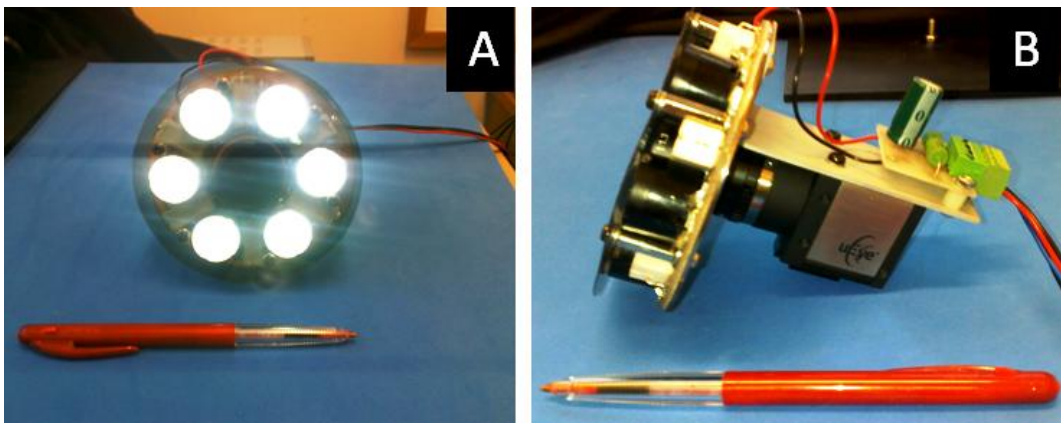


Figure 3.7: (A) The front view showing the strobe illumination system in operation with light passing through a circular polarizing filter and (B) side view showing strobe flash system mounted on camera UI2250 SE-C

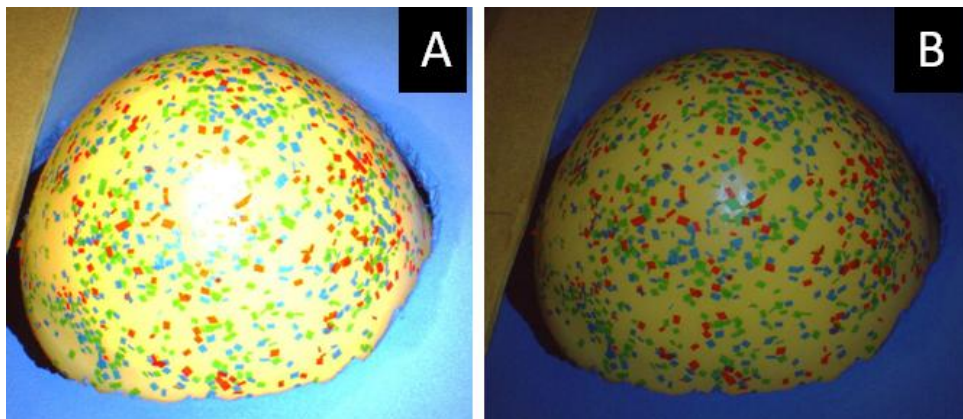


Figure 3.8: (A) Images showing effective use of polarizer for glare reduction, captured at 50 ms exposure time, without polarizer and (B) with polarizer using only one strobe light

Figure 3.7(A) shows the front-view of the strobe illumination system in operation and Figure 3.7(B) shows side-view of the developed strobe illumination system after mounting on the camera. Figure 3.8 (A&B) show the effective use of circular polarizing filter to kill the glare.

3.6 Testing and calibration

To ensure the desired illumination intensity was achieved, a photodiode calibration test was conducted and light intensity measured. A program was written in LabVIEW to measure the light intensity detected by a photodiode as a result of operation of a single strobe light in a darkroom environment. A pulse of 2 ms was provided using cRIO NI-9403 and intensity measurements were counter-checked using a Luxmeter, as shown in Figure 3.9. A comparison of the light intensity of the developed strobe system was done with the strobe system of the initial DIET prototype.



Figure 3.9: Showing calibration test settings with a photodiode and luxmeter applied in the darkroom environment. LED strobe system is in operation

Figure 3.10 (A-D) shows comparison of output of the new strobe illumination system at different power settings during the calibration process. Figure 3.11 (A & B) shows comparison of output of the old and the new strobe system. The comparison shows a 90% gain in the output illumination from the new strobe system (without polarization) compared to the old system. This output is from a single LED strobe ring, on power settings as used in the real-time environment.

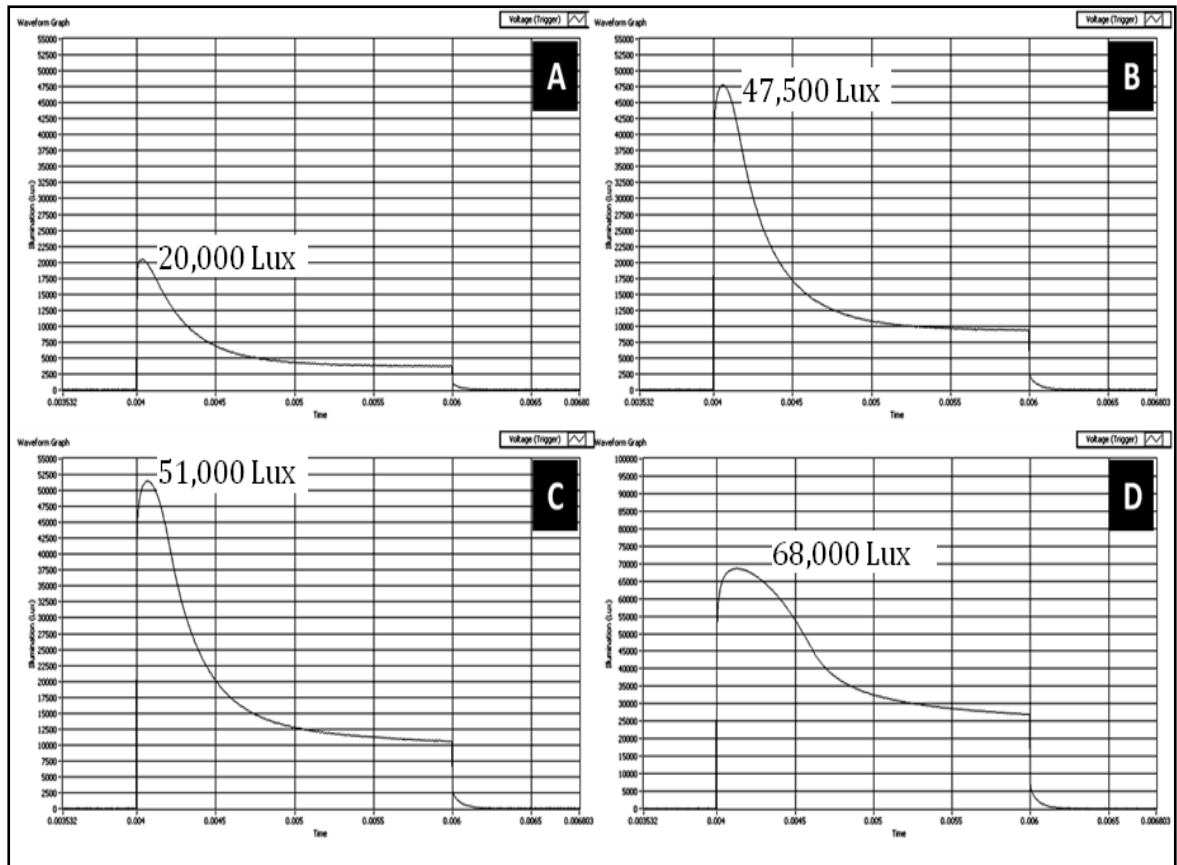


Figure 3.10: (A) New strobe system (with polarizer) at 5 volts, 0.17 amp, showing illumination peak $\sim 20,000$ lux (B) New strobe system (without polarizer) at 5 volts, 0.17 amp showing illumination peak $\sim 47,500$ lux (C) New strobe system (with polarizer) at 12 volts, 0.7 amp showing illumination peak showing $\sim 51,000$ lux (D) New strobe system (without polarizer) at 12 volts, 0.7 amp showing illumination peak showing $\sim 68,000$ lux. The X-scale is shows time (s) and Y-scale shows illumination (Lux). Note that Y-scale in A to C is 0-55,000, while in D Y-scale is 0-100,000.

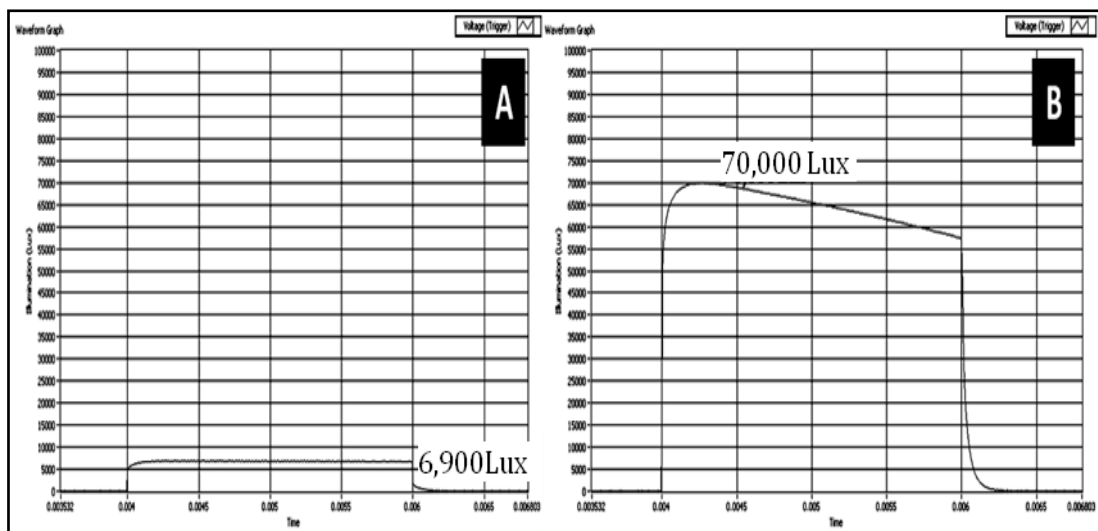


Figure 3.11: (A) Output of the old strobe system (B) Output of the new strobe system showing a pulse peak sustainability using $6800 \mu\text{F}$ charging capacitor, at 12 V, 1.7 Amp (without polarization)

3.7 Discussion

Calibration testing shows that the new strobe illumination system with six high power LEDs provides more than 6x higher illumination peak and more than 2x average real time illumination at 25% lesser input current. By supplying a higher operating voltage and current at 12 V DC and a 1.7 A, the increase in peak illumination was more than 10x as compared to the previous system and the average real time illumination intensity was increased by 90%. However, application of the circular polarizer on the new strobe system caused more than 40% illumination attenuation. Thus, with the new strobe system, the net effect was more than 50% increase in illumination, after using the circular polarizer for glare reduction.

Calibration testing also revealed that there was a significant exponential decay in the peak illumination, after a small transition of time (0.5 ms), with the new system. To achieve pulse peak sustainability a charging capacitor of 6800 μ F was applied across the LEDs, which provided significantly stable and sustained output as can be seen in Figure 3.11 (B). There was still some decay but it was much lower and more linear, and the transition time was much higher. After the application of this charge capacitor there was a total of 12000 lux drop over the pulse duration of 2 ms as compared to a drop of 35000 lux over 1 ms.

In summary, the total increase in the light intensity of the new strobe system without applying the polarizing filter was 10x the previous one. The total gain after applying the polarizer was still more than 5x. Hence, the objective of increasing the light intensity of more than 4x was achieved. It was also noted that the luxmeter reading was very much comparable to the measurements done with photodiode, validating the overall approach.

After the testing it was decided to implement the 6800 μ F charge capacitor and to run the strobe illumination system at 12 V DC. However, most of the electronics of the DIET system operate at 24 V DC. Therefore, the LED strobe system was powered by an existing 24 VDC power

supply and a step down (24 V to 12 V) circuit was designed and implemented. Figure 3.12 shows the pulse generation control signal implemented in LabVIEW. The application of circular polarizer reduced the illumination almost 40% but also virtually eliminated specular reflections.

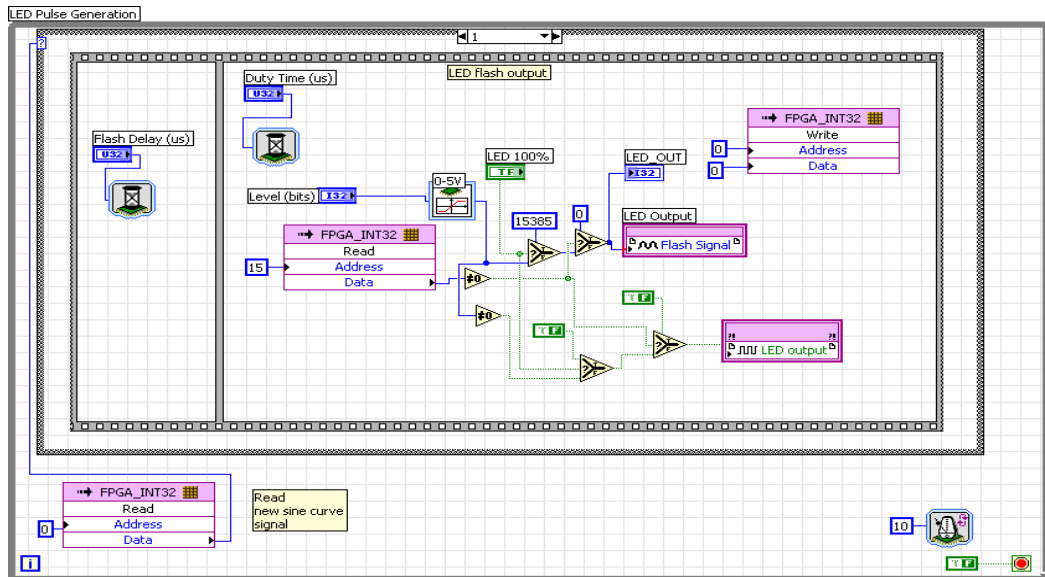


Figure 3.12: LED pulse generation loop in the FPGA VI. The loop was timed to execute at 10 μ s.



Figure 3.13: Image of the silicone breast phantom captured in the new light environment with clinical DIET prototype

From this level, effectively A 100% removal of the glare patterns from the shiny surface of the silicone breast phantoms was achieved by the simple application of chalk powder. Figure 3.13 shows an image captured with the clinical DIET prototype in new lighting environment. The

image was captured at 18 Hz with 0.5% duty cycle as the trigger pulse, with camera exposure time of 300 ms.

3.8 Summary

To avoid very high cost CCD industrial cameras with high frame rates in the range of 50-100 fps, a novel strobe flash system was implemented. The original prototype system provided less illumination than required and caused longer imaging times. The lower illumination also entailed higher duty cycle (2 %), and produced glare patterns on shiny surfaces of the silicone phantoms.

To address these issues, a new strobe flash system was designed and implemented using 6 high power LEDs, which provided approximately 10x more illumination. A circular polarizer was applied, which eliminated the glare but reduced intensity. However, the overall objective of 4-5 times more illumination was achieved and the duty cycle for pulse generation was reduced from 2% to 0.5%. These changes removed the blurriness from images at lower frequencies and also helped in optimizing the total imaging time. The imaging time to capture 10 phases at a particular frequency using the previous cameras and the strobe illumination system was reduced to 17.4 s from 252, a factor of $\sim 15x$.

Chapter 4

4 VIBRATION ACTUATION SYSTEM

4.1 Introduction and prior work

To obtain the imaging results for motion reconstruction, the breast is actuated with a steady state sinusoidal vibration over a range of frequencies depending upon the resonant frequencies of the breast. The amplitude of the sine wave depends on any pre-compression and breast density. The typical frequency range is between 10-70 Hz and the amplitude is 1-2 mm peak to peak. The input is defined:

$$U(t) = A \sin(\omega t + \varphi) \quad (4.1)$$

The phase φ observed is affected by the elastic properties of the breast. Stiffer cancerous tumours having a higher storage modulus (E') cause reduction in phase delays in that specific region of interest. Z-direction phase, φ_z , is thus well suited for detection of tumours, being in line with the direction of actuation.

A previous version of the actuator was designed with target specifications of applying 3mm amplitude at 50Hz and 1mm at 100 Hz with a peak force of 20N. These specifications were evaluated using a finite element model of the breast and a voice coil technology was adopted after detailed consideration of parameter evaluation (Jason Fincher, 2005). Figure 4.1 (a) shows the cross section of the design and Figure 4.1 (b) shows the actuator employed in the lab environment during in vitro trials.

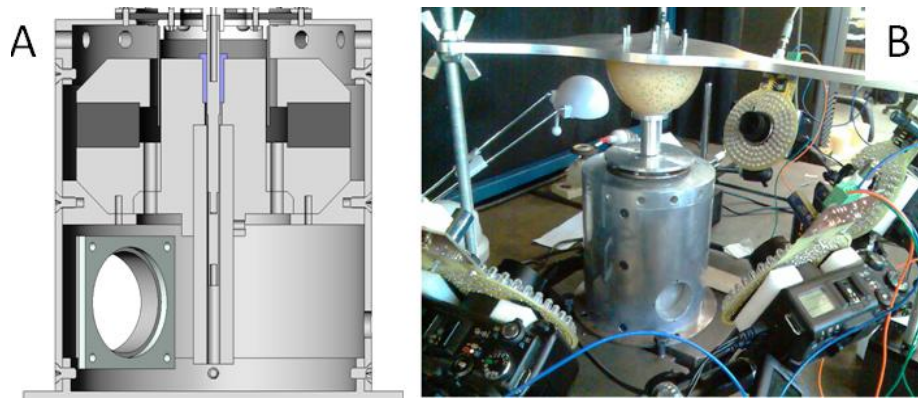


Figure 4.1: (A) Showing cross section of actuator design (Jason Fincher, 2005) and (B) First actuator employed in the lab environment surrounded by cameras

4.2 Rationale

The first prototype actuator was tested in vitro and during limited in vivo trials. A new actuation system was needed due to the physical dimensions of the existing actuator and its manual positioning underneath the breast. In particular, its size did not allow its use in a portable clinical device. Its dimensions were:

- Outer diameter: 150 mm
- Vertical height: 220 mm
- Total mass > 12 Kgs

This prototype actuator also did not allow flexibility in (X, Y, Z) positioning with respect to different breast sizes, and it could only be adjusted vertically. Hence, a new device with automated (X, Y, Z) positioning was realised.

4.3 Development Approach

Research was conducted to evaluate available actuation systems. Four major types of actuation systems were studied and parametric evaluation was carried out to design the DIET actuator following design considerations outlined.

4.3.1 Design considerations

To estimate the breast weight in the system a compression test was performed on three different breast phantoms. The mass of the breast was thus estimated at 200 g under a vertical pre-compression not exceeding 10mm. The resulting design specifications comprised:

- Outer diameter < 150 mm
- Vertical height \approx 110 mm
- Total mass \approx 5 kgs
- Capable of providing 2 mm peak to peak amplitude over range of frequencies 10-100 Hz
- Capable of allowing flexibility of automatic remote positioning in 3-axis
- Implementation of Linear Variable Differential Transformer (LVDT) position sensor for PID feedback loop control
- Implementation of energy efficient springs to ensure smooth operation

4.3.2 Concept Justification

Research was conducted to determine the types of actuators that could meet the specifications. Four main methods of actuation showed promise: 1) linear motor actuators; 2) piezoelectric actuators; 3) voice coil actuators; and 4) integration of 3 low power voice coils into a customised actuation unit. All four methods were analysed. In particular:

- **Piezoelectric:** Solid state actuators that convert electrical energy directly into high precision displacement. These actuators are made of ceramics. The high resolution of these actuators makes them ideal for precise positioning. However, it comes at the cost of very low amplitudes of \sim 1-100 μ m at high voltages (Jason Fincher, 2005).
- **Voice coils:** Voice coils offer excellent control characteristics where linear actuation is required over short distances. A voice coil actuator is simple in construction consisting of a permanent magnet, an iron core and a wound coil configuration. However, the vertical size of the strong voice coil required to meet the desired specifications is too large for the compact design intended for DIET. Moreover, the running noise is too loud due to


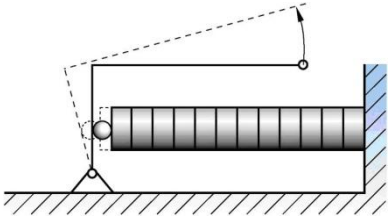
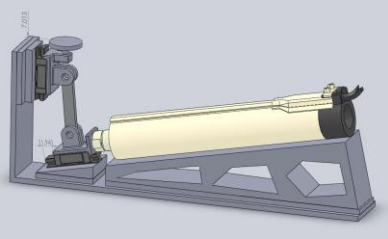
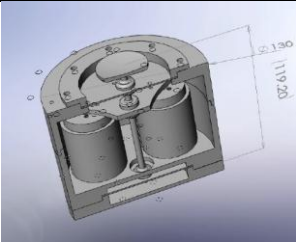
the linear bearing used, and integration of the position sensor to control motion would add vertical height and mass of the moving parts.

- **Linear motor actuators:** These actuators convert rotational motion into linear motion. They can be quite simple mechanisms, capable of high displacement and high force. However, their resolution and controllability can be limited. The main disadvantage of this concept is the requirement of a linkage system to obtain vertical motion, which introduces many moving parts. It could also introduce unwanted, additional vibrations because of manufacturing tolerances.
- **3 Voice coil solution:** Integrating 3 low power voice coils into a compact actuation unit using a double spring system as a linear guide works with effectively no friction and reduces the running noise significantly. Integration of a LDVT position sensor for the PID control loop is easy and workable.

From the feasibility study conducted for each actuator type, the characteristics of each actuator were judged and an evaluation matrix constructed. The parameters used in the evaluation matrix are defined along with their suggested importance rating shown in parentheses (5 is the most important and 1 is the least important):

- **Linear motion (5):** The ability of the concept to deliver sinusoidal output motion
- **Displacement (5):** The ability and ease with which the system can deliver the required displacement
- **Force (5):** The ability and certainty for the system to deliver the required force
- **Controllability (5):** The degree of simplicity in integrating a control system to the concept
- **Simplicity (2):** How simple the concept will be to take from concept to manufacturing stage in terms of technical analysis and modelling
- **Manufacturing (2):** The ease at which the concept can be manufactured
- **Cost (2):** The total cost of manufacturing
- **Friction (2):** How friction free the actuation system is going to be after manufacturing
- **Noise (3):** How noise free the final product is going to be
- **Dimensions (4):** Overall compactness of the actuator
- **Position sensor (4):** How easily a position sensor can be integrated into the system for feed back
- **Number of Parts (3):** How many number of moving and static parts are involved in the final design

Table 4.1: Actuation systems evaluation matrix

Actuator Design Concepts	Requirements	Score
 <p>Linear Voice Coil Motors (LVCM)</p>	<i>Linear motion</i>	25
	<i>Displacement</i>	15
	<i>Force</i>	15
	<i>Controllability</i>	20
	<i>Simplicity</i>	10
	<i>Manufacturing</i>	10
	<i>Cost</i>	10
	<i>Friction</i>	6
	<i>Noise</i>	6
	<i>Dimensions</i>	12
	<i>Position sensor</i>	8
	<i>Number of Parts</i>	12
	Total Score	
 <p>Piezoelectric</p>	Linear motion	15
	Displacement	25
	Force	25
	Controllability	20
	Simplicity	4
	Manufacturing	2
	Cost	2
	Friction	6
	Noise	9
	Dimensions	8
	Position sensor	8
	Number of Parts	9
	Total Score	
 <p>Linear motor concept</p>	Linear motion	25
	Displacement	25
	Force	25
	Controllability	15
	Simplicity	2
	Manufacturing	2
	Cost	2
	Friction	4
	Noise	9
	Dimensions	8
	Position sensor	8
	Number of Parts	3
	Total Score	
 <p>3 voice coil solution</p>	Linear motion	25
	Displacement	13
	Force	20
	Controllability	20
	Simplicity	8
	Manufacturing	8
	Cost	8
	Friction	8
	Noise	12
	Dimensions	20
	Position sensor	20
	Number of Parts	9
	Total Score	

The concept evaluation matrix shown in Table 4.1, assigns a score to each design concept based on importance rating of the required parameters. The evaluation matrix was achieved by multiplying the importance ratings with a scale of 1 to 5 depending upon the effectiveness of that characteristic in each design concept. The evaluation matrix determined that the best concept was an integrated 3 voice coil actuation solution. Its score was 16-35% larger than any other system concept.

4.4 Dimensioning of voice coils

Voice coils are commonly used in loud speakers and in automation applications where linear proportional servo control is required. They are highly accurate and fast with a low moving mass. Voice coil actuators are direct drive devices and have relatively limited motion. They are made of two main components, a magnet and a coil. By driving current through the coil a magnetic field is produced, causing the coil to react to the magnetic field and producing force. The produced force is proportional to the current signal applied as input to the coil.

4.4.1 Voice coil concept

The Lorentz Force Principle governs the electro-mechanical conversion of a voice coil actuator. The value of the acting force (F) is determined by the magnetic flux density (B), the input current (I), the orientation of the field, the number of turns in the coil (N) and the length (L) of conductor:

$$F = kBLIN \tag{4.2}$$

where k is a constant.

Once a conductor moves through a magnetic field, an additional voltage can be realised across the conductor. This additional voltage (E) depends of the magnetic flux density (B), the length (L), the speed (v) and the number of conductors (N):

$$E = kBLvN \quad (4.3)$$

Equations (4.2) and (4.3) are for a device that contains a permanent magnetic field and the coil winding moving in that field will produce a force proportional to the current carried in the coil and a voltage proportional to the velocity of the coil.

4.4.2 Mechanical model of the breast and actuation unit

To estimate the force and stroke requirements, the mechanical response of the breast was modelled. Figure 4.2 (A) shows simplified sketch of the breast, the input $u(t)$ is the excitation of the breast by the actuator. The breast response is modelled by a single spring-mass-damper system, as shown in Figure 4.2 (B).

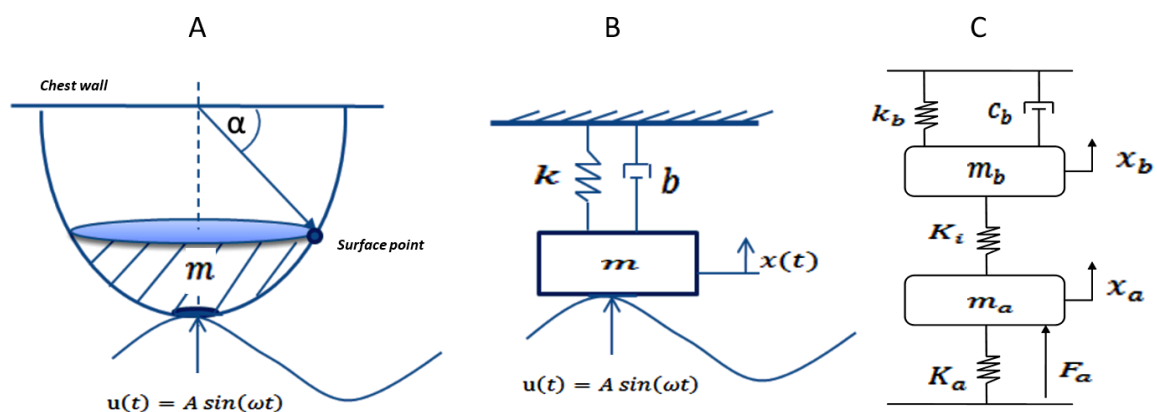


Figure 4.2: (A) Simplified schematic sketch of the breast, (B) mechanical model of the breast, and (C) mechanical model of the breast including actuator

The schematic shown in Figure 4.2 (C) represents the mechanical behaviour of the breast and actuator which can be used for the dynamic analysis of the whole system. Different parameters are:

K_b	spring constant of breast
c_b	damping constant of breast
k_i	spring constant between the breast and the actuator
k_a	spring constant of the actuator
m_a	mass of the actuator
m_b	mass of the breast
x_a	displacement of the actuator
x_b	displacement of the breast
F_a	actuator's driving force

For initial studies, the mass of the breast was assumed to be 200g and the mass of the moving parts in the actuator was taken to be 300g, for a total moving mass of 500g. Gravity for the actuator and the breast were neglected as it can be accounted as a constant affect. However, spring forces, the actuator's driving force, and the damping forces were modelled to find the requirement of force from the voice coils, yielding in full:

$$m_b \ddot{x}_b = -(k_b + k_i)x_b - c_b \dot{x}_b + k_i x_a - m_b g \quad (4.4)$$

$$m_a \ddot{x}_a = F_a - (k_a + k_i)x_a + k_i x_b - m_a g \quad (4.5)$$

Forces of gravity $m_b g$ and $m_a g$ were neglected:

$$m_b \ddot{x}_b + (k_b + k_i)x_b + c_b \dot{x}_b - k_i x_a = 0 \quad (4.6)$$

$$m_a \ddot{x}_a + (k_a + k_i)x_a - k_i x_b = F_a \quad (4.7)$$

Laplace transformation of Equations 4.6 and 4.7 yield:

$$(m_b s^2 + c_b s + k_b + k_i)X_1(s) - k_i X_2(s) = 0 \quad (4.8)$$

$$(m_a s^2 + k_a + k_i)X_2(s) - k_i X_1(s) = F_a(s) \quad (4.9)$$

which can be expressed in matrix form:

$$\begin{bmatrix} (m_b s^2 + c_b s + k_b + k_i) & -k_i \\ -k_i & (m_a s^2 + k_a + k_i) \end{bmatrix} \begin{bmatrix} X_1(s) \\ X_2(s) \end{bmatrix} = \begin{bmatrix} 0 \\ F_a(s) \end{bmatrix} \quad (4.10)$$

The transfer functions $\frac{X_1(s)}{F_a(s)}$ and $\frac{X_2(s)}{F_a(s)}$ can be found from Equation (4.10) and solving for the ratios

with Cramer's method as follows:

$$T_1(s) = \frac{X_1(s)}{F_a(s)} = \frac{k_i}{(m_b s^2 + c_b s + k_b + k_i)(m_a s^2 + k_a + k_i) - k_i^2} \quad (4.11)$$

$$T_2(s) = \frac{X_2(s)}{F_a(s)} = \frac{(m_b s^2 + c_b s + k_b + k_i)}{(m_b s^2 + c_b s + k_b + k_i)(m_a s^2 + k_a + k_i) - k_i^2} \quad (4.12)$$

An analytical solution was difficult to obtain in this case, as it was a fourth order system.

However, numerical solution methods can readily simulate the system behaviour using Matlab

for sinusoidal inputs, where damping c_b is defined:

$$c_b = 2\xi\sqrt{m_b(k_b + k_i)} \quad (4.13)$$

where ξ is the damping ratio, an estimated value for breast tissue ($\xi = 5\%$) was used. This

numerical method was used to find the force required from the voice coils.

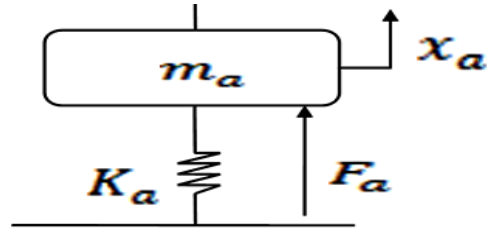


Figure 4.3: Mechanical model of the actuator

To minimise overall size and enhance the portability of the clinical device, it was desired to choose the voice coils with the minimum possible size. Accordingly, the force estimation was done. The smallest force is required when the frequency of the movement is the natural frequency of the overall system. A range of forces required was calculated with different spring constant, k_a . Figure 4.3 shows the mechanical model of the actuator.

Again applying Newton's second law, neglecting gravity and using Equation 4.1, yields:

$$F_a = A \sin(\omega t) (k_a - \omega^2 m_a) \quad (4.14)$$

Assuming $F_a F_a = 0$ to find the range of K_a and noting $A \sin(\omega t) \neq 0$ and $\omega = 2\pi f$, yields:

$$k_a - \omega^2 m_a = 0 \Rightarrow k_a = 4m_a \pi^2 f^2 \quad (4.15)$$

The range of f chosen was 10-100 Hz and k_a is thus:

$$2 \times 10^3 < k_a < 2 \times 10^5 \text{ N/m} \quad (4.16)$$

Figure 4.4 (A) shows the sinusoidal behaviour of displacement of the actuator, x_A and displacement of the breast, x_B during one second at an operating frequency $f = 20$ Hz. Figure 4.4 (B) shows the driving force for the actuator.

Figure 4.5 shows maximum force required as a function of frequency and spring constant. This plot was used to size the voice coils for the actuator and to choose the springs requiring the least amount of force to operate within the frequency range of interest.

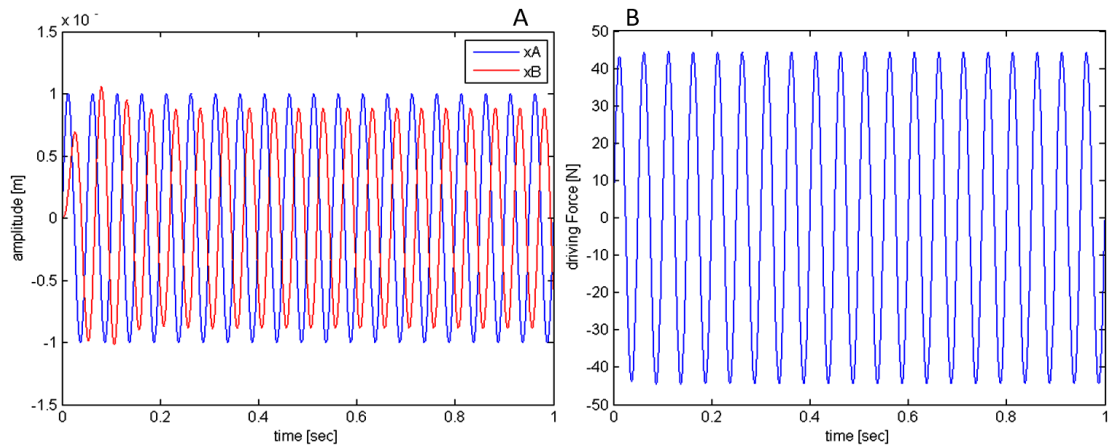


Figure 4.4: (A) Sinusoidal behaviour of displacements of actuator (x_A) and breast (x_B) at $f = 20$ Hz, (B) The driving force required by the actuator at $f = 20$ Hz

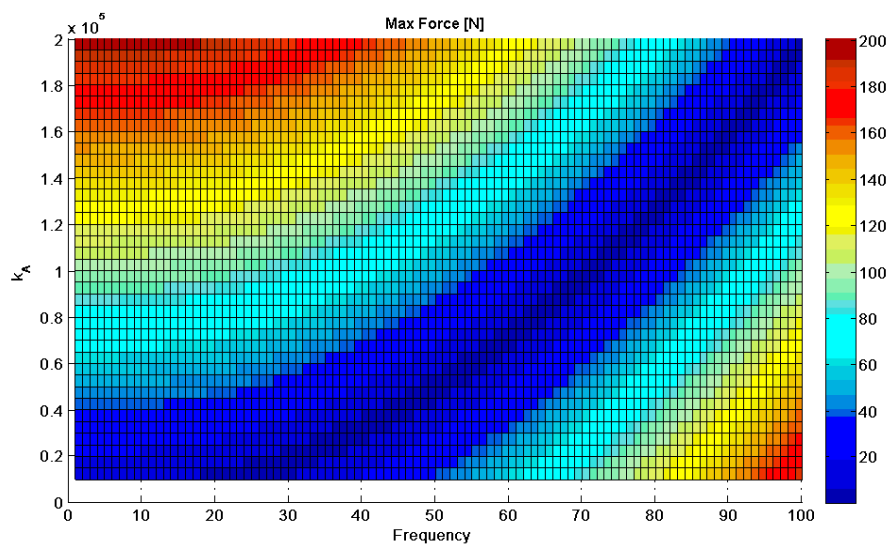


Figure 4.5: Requirement of max force depending upon the frequency f and spring constant k_a , X-axis represents frequency f , Y-axis showing the spring constant, colours represent the value of force in Newtons (N)

4.4.3 Spring Effect

The most important criteria for the voice coils is the linearity. For DIET, the vertical movement needs to be accurate, and friction and noise need to be minimized. Two circular flexure springs

were used to achieve these aims [Figure 4.6 (A)]. One was installed at the top of the system and the other one at the bottom. Both springs are concentric and a shaft connects them in parallel in the middle, as shown in Figure 4.6 (B).

The spring constant is a variable and is used in equations to calculate the force of the actuator. The range of spring constant k_a was evaluated in Equation 4.16. In fact, k_a in this model corresponds to the addition of the two spring constants of both the concentric springs. As the two springs are linked rigidly in parallel:

$$k_a = k_1 + k_2 = 2 k_1 \quad (4.17)$$

where the two springs have equal characteristics and $k_1 = k_2$.

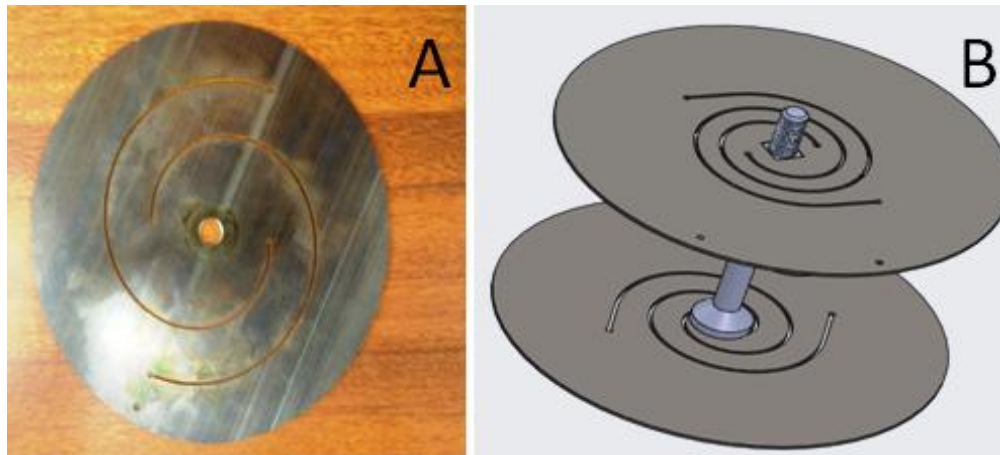


Figure 4.6: (a) Showing design of concentric spring, (b) springs of the actuator connected by a shaft

4.4.4 Selection of voice coil

Using the maximum possible force required, the voice coil was selected by a comparison of available voice coil specifications, including:

- Peak Force (N): Force generated by the motor at 10% duty cycle
- Continuous Force (N): Force generated by the motor at 100% duty cycle

- Force Constant (N/A): A constant used to detect the current through the motor
- Back EMF constant (v/m/s): The constant of proportionality which describes the relationship between coil velocity and reverse acting electromagnetic forces
- Stroke (mm): Max displacement of the moving parts
- Coil resistance (Ω): Coil's internal resistance
- Max continuous power (W): Max power a voice coil can handle

Profiles of various voice coils motor manufacturers were studied and Moticont, CA, USA (Moticont) was selected as the potential supplier. Table 4.2 compares the different Linear Voice Coil Motors (LVCM) considered. Max continuous current requirements for three voice coils were calculated on the basis of the max power output and coil's internal resistance ($I_{max} = \sqrt{P_{max}/R}$).

Table 4.2: Comparison of characteristics of shortlisted voice coils

(LVCM)	044-32-02	044-051-01	044-051-02	051-051-01	051-064-01	051-089-01
Peak Force @ 10% duty cycle (N)	70.4	68.4	70.4	88.6	92.9	82.7
Continuous Force (N)	22.2	21.6	22.3	28.0	29.4	26.2
Force constant (N/A)	12.3	10.3	6.9	8.0	9.6	10.1
Back EMF constant (v/m/s)	12.3	10.3	6.9	8.0	9.6	10.1
Stroke (mm)	12.7	31.8	31.8	19.1	31.8	57.2
Coil assy mass (g)	64	165	90	120	150	195
Body mass (g)	320	405	497	685	850	1155
Physical Dimensions (mm x mm)	44.5 x 44.5	72.8 x 44.5	72.8 x 44.5	73.4 x 50.8	92.5 x 50.8	130.6 x 50.8
Resistance (R) (Ω)	6.1	6.3	2.7	2.7	3.9	6.0
Max Continuous Power (Pmax) (W)	20.0	28.0	28.0	33.0	36.0	40.0
Imax (A)	1.8	2.1	3.2	3.5	3.0	2.6
3*Imax (A)	5.4	6.3	9.6	10.5	9.0	7.8

The voice coil motor should be able to generate the force to move the required moving mass over the range of desired frequencies (10-100 Hz). The continuous force of the motor specified by the voice coil manufacturers is the force that motor generates at 100% duty cycle. If the required force is not required all the time as in the case of DIET actuation system, a smaller motor should be selected. The average power dissipated by the motor should not exceed the motor rating.

For selection of motor, associated power electronics, and power supplies, certain formulas were provided by the voice coil suppliers (Moticont) which are summarized in Table 4.3, where, R (Ω) is the internal motor resistance, I (A) current through the motor, P (W) power consumed by the motor, K_f (N/A) motor force constant, K_e (v/m/s) the induced back EMF and v (m/s) is the linear velocity.

Based on these formulas, the simulation results from Figure 4.5 were grouped in an excel sheet and continuous force values capable of producing 1mm amplitude for different spring constants over a range of frequencies (10-100 Hz) were calculated to finalise the selection.

Table 4.3: Important formulas used motor rating selection and power supply requirements

$$\begin{aligned}
 F &= ma \\
 a(t) &= -A\omega^2 \sin(\omega t) \\
 F &= -A\omega^2 \sin(\omega t) * m \\
 F_{peak} &= mA\omega^2 \\
 F_{rms} &= 0.7 mA\omega^2 \\
 I &= F/K_f \\
 P &= R * I^2 \\
 V_{ps} &= R * I + K_e * v \\
 v(t) &= A\omega * \cos(\omega * t)
 \end{aligned}$$

Table 4.4 shows the measured force requirements for different spring constants over the range of frequencies to achieve 1mm amplitude. F_{rms} is the total continuous force required which is further divided by 3 to obtain the force requirements from a single voice coil motor in desired 3 voice coil actuator. Depending upon the force requirements, stroke provided, body mass and

physical dimensions of the shortlisted voice coils, the LVCM-044-032-02 from Moticont, CA, USA (Moticont) was selected.

Table 4.4: Continuous force requirement from a single voice coil motor for different frequencies and spring constants

f(Hz)	10	20	30	40	50	60	70	80	90	100
v (m/s)	0.063	0.126	0.188	0.251	0.314	0.377	0.440	0.503	0.565	0.628
$K_a = 0.1 \times 10^5 \text{ N/m}$										
F_{peak} (N)	15	12	8	15	40	60	80	110	145	180
F_{rms} (N)	10.5	8.4	5.6	10.5	28	42	56	77	101.5	126
F_{rms} /3 (N)	3.5	2.8	1.87	3.5	9.33	14	18.67	25.67	33.83	42
$K_a = 0.2 \times 10^5 \text{ N/m}$										
F_{peak} (N)	18	15	10	10	40	55	80	110	145	175
F_{rms} (N)	12.6	10.5	7	7	28	38.5	56	77	101.5	122.5
F_{rms} /3 (N)	4.20	3.50	2.33	2.33	9.33	12.83	18.67	25.67	33.83	40.83
$K_a = 0.4 \times 10^5 \text{ N/m}$										
F_{peak} (N)	40	35	25	10	10	30	65	90	130	155
F_{rms} (N)	28	24.5	17.5	7	7	21	45.5	63	91	108.5
F_{rms} /3 (N)	9.33	8.17	5.83	2.33	2.33	7.00	15.17	21.00	30.33	36.17
$K_a = 0.6 \times 10^5 \text{ N/m}$										
F_{peak} (N)	50	45	40	30	15	20	35	75	100	130
F_{rms} (N)	35	31.5	28	21	10.5	14	24.5	52.5	70	91
F_{rms} /3 (N)	11.67	10.50	9.33	7.00	3.50	4.67	8.17	17.50	23.33	30.33
$K_a = 0.8 \times 10^5 \text{ N/m}$										
F_{peak} (N)	80	70	60	50	35	10	20	40	80	110
F_{rms} (N)	56	49	42	35	24.5	7	14	28	56	77
F_{rms} /3 (N)	18.67	16.33	14.00	11.67	8.17	2.33	4.67	9.33	18.67	25.67
$K_a = 1 \times 10^5 \text{ N/m}$										
F_{peak} (N)	95	90	80	70	50	30	10	30	50	90
F_{rms} (N)	66.5	63	56	49	35	21	7	21	35	63
F_{rms} /3 (N)	22.17	21.00	18.67	16.33	11.67	7.00	2.33	7.00	11.67	21.00
$K_a = 1.2 \times 10^5 \text{ N/m}$										
F_{peak} (N)	110	105	90	85	80	60	30	10	20	70
F_{rms} (N)	77	73.5	63	59.5	56	42	21	7	14	49
F_{rms} /3 (N)	25.67	24.50	21.00	19.83	18.67	14.00	7.00	2.33	4.67	16.33
$K_a = 1.4 \times 10^5 \text{ N/m}$										
F_{peak} (N)	140	130	120	110	90	80	50	30	10	40
F_{rms} (N)	98	91	84	77	63	56	35	21	7	28
F_{rms} /3 (N)	32.67	30.33	28.00	25.67	21.00	18.67	11.67	7.00	2.33	9.33

4.5 Actuation control system integration

The LVCM actuators are used and feedback control is implemented to control position and stroke. Figure 4.7 shows the graphical representation of the integrated actuation system. The

entire actuation system is controlled through an external computer (Host-PC) that communicates to the controller through TCP-IP sockets using an external LVDT sensor for feedback.

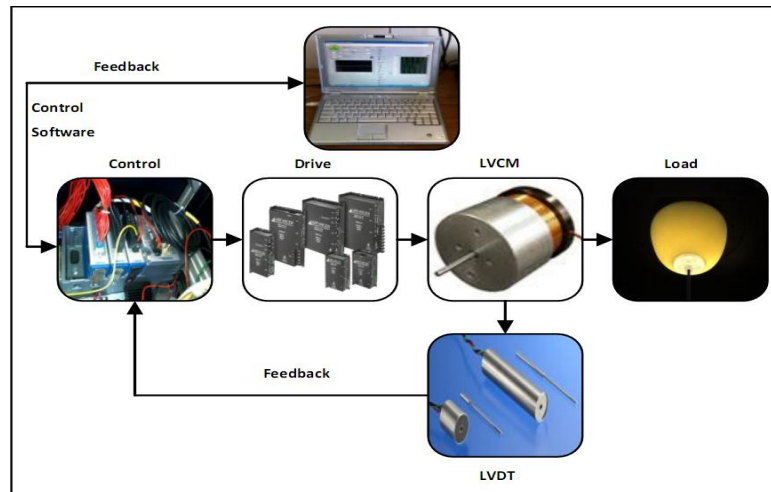


Figure 4.7: Graphical representation of feedback controlled integrated actuation system for DIET

4.5.1 Controller

The controller is responsible for generating the input motion and for reacting to changes. A real time controller, NI cRIO – 9012 was selected from National Instruments (NI) (National Instruments), and was programmed in LabVIEW. This real-time input output (RIO) system communicates to the Host-PC via TCP/IP Socket. The RIO system controls the analogue and digital IO's and also synchronises the strobe flash system discussed in Chapter 3 with the actuator. The stepper motors of the 3-axis positioning system (discussed later), are also controlled through this controller.

4.5.2 Motor Drive

The servo drive or amplifier translates the low energy reference signal from the controller into a high energy signal to the motor. The controller signal from the cRIO ranges over ± 10 V, whereas the input signal to the selected voice coils ranges over ± 24 V. After researching various

manufacturers, a 25A8 PWM from Advanced Motion Controls, CA, USA (Controls) was selected. The amplifier is designed to drive brush type DC motors at high switching frequency and provides full protection against over voltage, under voltage, over current, overheating and short circuiting. It can output up to 25A of peak current and provide 12.5A as continuous current at 950 W continuous power.

4.5.3 Motor

As discussed in Section 4.4, the actuation motor consisted of 3 parallel, spring loaded LVCMs for increased power in a smaller vertical height. LVCM-044-032-02 were purchased from Moticont, USA (Moticont).

4.5.4 Feedback Position sensor - LVDT

Linear Variable Differential Transformer (LVDT), also referred to as a linear displacement transducer, is an absolute feedback device and is known for its accuracy and precision. It works like a voice coil, in which three coils are placed around a tube. The magnitude of the output voltage is proportional to the distance moved by the core. The phase of the voltage indicates direction of movement. The LVDT is a highly reliable device which produces clean data, infinite resolution, and exhibits excellent repeatability.

Precision feedback is important as the prototype is intended to be used in clinical trials. As the stroke provided by the voice coils is not intended to be more than 2mm peak to peak, 4mm was chosen as the measurement range. The cRIO controller would read output signal from LVDT using a 16 bit analogue input module NI 9215 with a ± 10 V signal range. To maximise the signal resolution, an LVDT with an output signal close to ± 10 V was desirable. Size considerations were also important to avoid unnecessary addition to the vertical height.

Based on these factors, an LVDT 0241-0000 from Trans-Tek, Inc. USA (TRANS-TEK) was selected. This LVDT covers a linear range of ± 2.54 mm, body length is 28.5 mm, and has a body mass of 28 g. It comes with a 19.1 mm long core, but to suit the overall design of the actuator a rod was designed and attached to the core.

4.6 Actuator design and assembly

Owing to the weight and size requirements discussed in Section 4.2, it was important to minimise the mass of the moving parts and maximise stiffness for durability and precise operation. To ensure linearity of motion and avoid induced friction between the moving parts it was necessary to ensure zero play between the moving parts and the main body. With the help of dynamic force calculations and coil dimensioning described in Section 4.4, three voice coils were used in parallel, to generate the vibration motion, and the system was designed in Solidworks in two main parts (the moving parts and the main frame). The moving parts generate linear motion, whereas the main frame was to fix the moving parts and to protect them from outside interference. The moving parts included a shaft, three coils, a coil bone and a breast interface. The coil bone was meant to transmit the motion from the coils to the shaft and further to the breast interface and a due consideration was given to its design. The shaft was attached to two springs. As discussed in Section 4.4.3, the springs had an important role to play concerning the motion and its axial guide.

The main frame consisted of a housing to isolate the moving parts, 3 magnets of the voice coils, two concentric springs, and a case for the LVDT. The housing consisted of top and bottom plate and a cylinder and the two springs were fitted between top and bottom plates and the cylinder, respectively, with the use of six screws.

To ensure straight linear motion, reduce the risk of bending, and avoid friction in the coils, the design of the coil bone was critical. Solidworks tool SimulationXpress Analysis Wizard was used

to test different versions of the part with different shapes and aluminium alloys. All results were regrouped in an excel table with details of stress and displacement distribution in the model. The safety factor and mass were also accounted for in each case. The tests were performed by applying a desired load where the coils were attached as shown in Figure 4.8 (A). Restraint was applied where the coil bone was supposed to be locked on the shaft and then the software calculated the stress distribution, the displacement distribution, the safety factor and the mass.

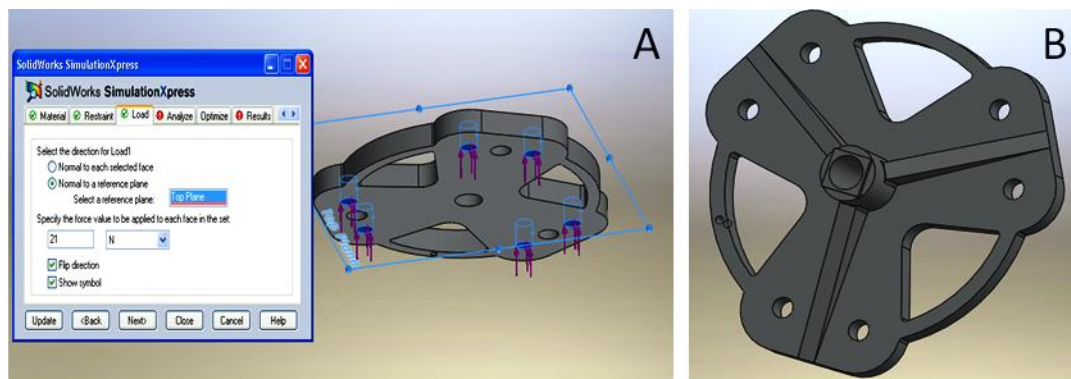


Figure 4.8: (A) Showing location of the applied load for stiffness test of the coil bone during simulation, (B) final design of the coil bone

When these tests were performed the design of the coil bone was not definitive and many improvements were made based on the simulation results. The safety factor in worst case scenario i.e. with $F_{rms} = 126$ was calculated to be ~ 5 , meaning that maximum stress in the part was 5 times smaller than the yield strength of the material. The final version of the coil bone matching all the criteria of design including stiffness and mass is shown in Figure 4.8 (B).

The two concentric springs were also designed using Solidworks and its simulation tool, SimulationXpress. The aim was to design the spring geometry to obtain the desired spring constant. A 20N load was placed and the geometry was changed to achieve the desired displacement. Two pairs of springs were designed and manufactured with two different spring constants. The one with 10 KN/m spring constant produced a displacement of 2mm and the other with 20KN/m produced 1mm displacement. Figure 4.9 (A) shows displacement distribution

of the a concentric spring with a spring constant of 10 kN/m as a result of Solidworks simulation, and Figure 4.9 (B) and (C) show Solidworks geometry of springs having a spring constant of 10 kN/m and 20 kN/m, respectively.

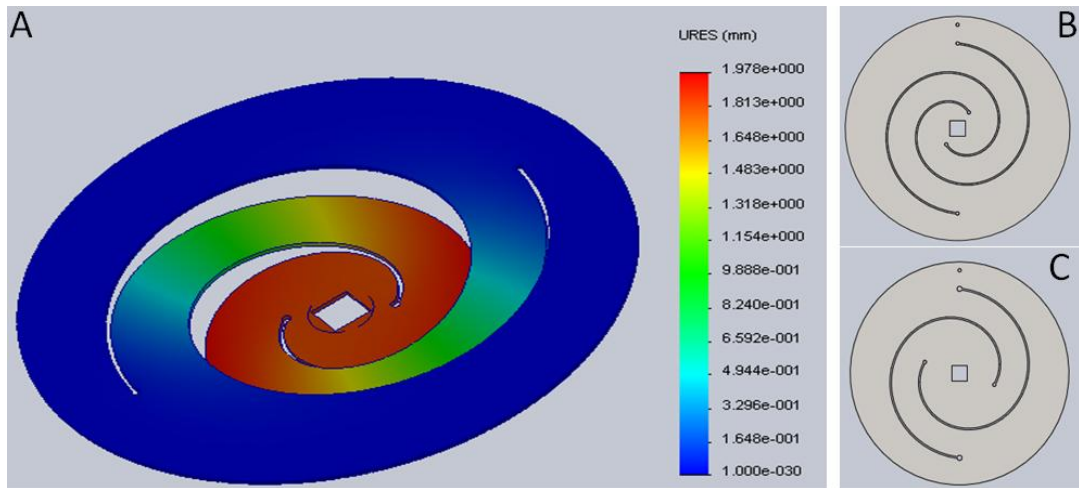


Figure 4.9: (A) Displacement distribution of the spring having a spring constant of 10 kN/m, (B) Solidworks representation of the spring with a spring constant of 10 kN/m, and (C) Spring geometry with a spring constant of 20 kN/m

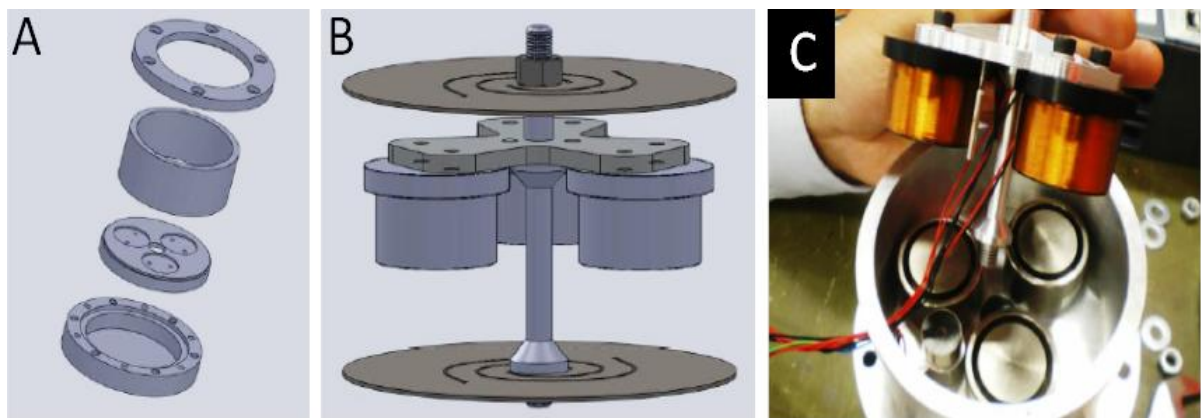


Figure 4.10: From left (a) Design concept of main frame (b) moving parts with concentric springs and (c) internal view of the assemble actuator with LVDT

The design also had to integrate the LVDT position sensor, a case for LVDT was accommodated in the base plate designed to house the magnets as part forms the part of main frame. Figure 4.10 shows the design concept of individual components of main frame, the moving parts and internal view of the final actuator after assembly. The housing for LVDT sensor was added to the

base plate of the main frame and the core of LVDT was mounted on the coil bone with an extension rod as can be seen in Figure 4.10 (C).

4.7 Damping solution for vibration isolation

To implement the actuator in the DIET breast cancer screening clinical prototype it was very important to isolate the vibrations produced to avoid transmission to the DIET system's main frame and subsequently to the cameras. This vibration, if transmitted to the cameras, would result in blurry image capture and failing of the image reconstruction software to reproduce motion behaviour from the breast surface. Therefore, it was required to isolate all vibrations.

The requirements for a vibration isolation solution were:

- Be economical
- Easy to implement
- Small in size and weight, as possible
- Minimum design changes required to install the actuator in the main frame

Initial experiments were carried out on introducing silicone padding underneath the actuation unit to provide a flexible base to damp vibration transmission. Three different silicone compositions with known damping ratios were tested, as shown in Figure 4.11. The details of the three tested elastomers are:

- Composition1: 50% Softgel 341C + 50% DC 200 Silicone fluid 50 cs, with storage modulus, $E' \approx 10$ kPa and damping ratio, $\zeta \approx 10\%$
- Composition2: 50% Elastosil P7600 RTV-2 + 50 % DC 200 Silicone Fluid 50 cs, with storage modulus, $E' \approx 10$ kPa and damping ratio, $\zeta \approx 40\%$
- Composition3: 100% Elastosil P7600 RTV-2, with storage modulus, $E' \approx 100$ kPa and damping ratio, $\zeta \approx 25\%$

The idea was practical and showed promise in terms of damping performance. However, it required complicated design changes and might have resulted in an increase in the size of the actuation unit. Therefore, to maintain the portability of the clinical prototype of the DIET

system, this idea was dropped and off-the-shelf damping solutions were evaluated for induction. Three damping feet from two different manufacturers were shortlisted for evaluation, as summarised in Table 4.5.



Figure 4.11: Showing experimental set up for testing silicone padding as vibration isolation solution

Table 4.5: Important characteristics of the three shortlisted vibration damping solutions

Dampers	Alfagel SF – 10	Alfagel SF -2	Paulstradyn
Source	Taica corporation (Corporation)	Taica corporation (Corporation)	RS components (RS-Components)
Load capacity (daN)	10	3	4
Resonance frequency (HZ)	9-12	10-15	7-10
Resonance magnification (dB)	19-21	12-13	10-12

These three products were tested by measuring vibration at three different locations on the DIET system: 1) on tip of the actuator; 2) on upper surface of the top plate of actuator; and 3) at the main frame of DIET system, as shown in Figure 4.12. The main focus was on detection of vibration at location (3) because the maximum impact of the damping the solution was experienced at this location and the optical system of DIET would subsequently be fixed on the main frame near location (3). Vibration was measured using a laser Doppler vibrometer.

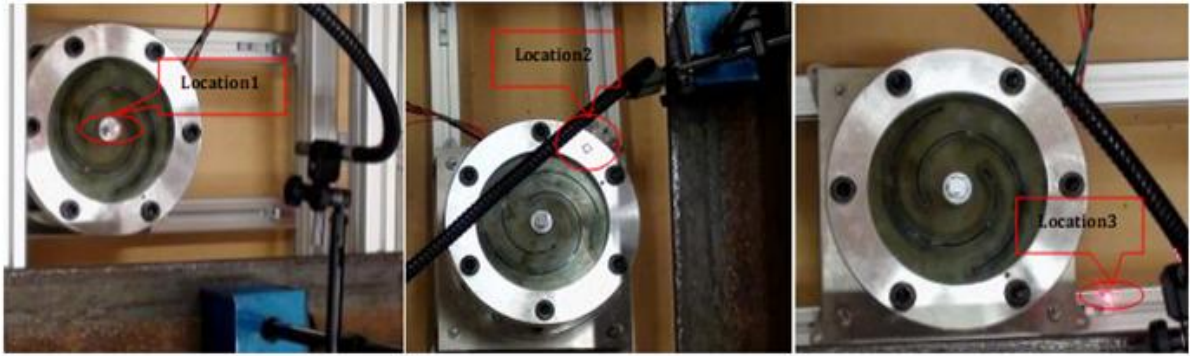


Figure 4.12: Showing three different locations where Laser Doppler Vibrometer testing were performed for optimising the vibration isolation

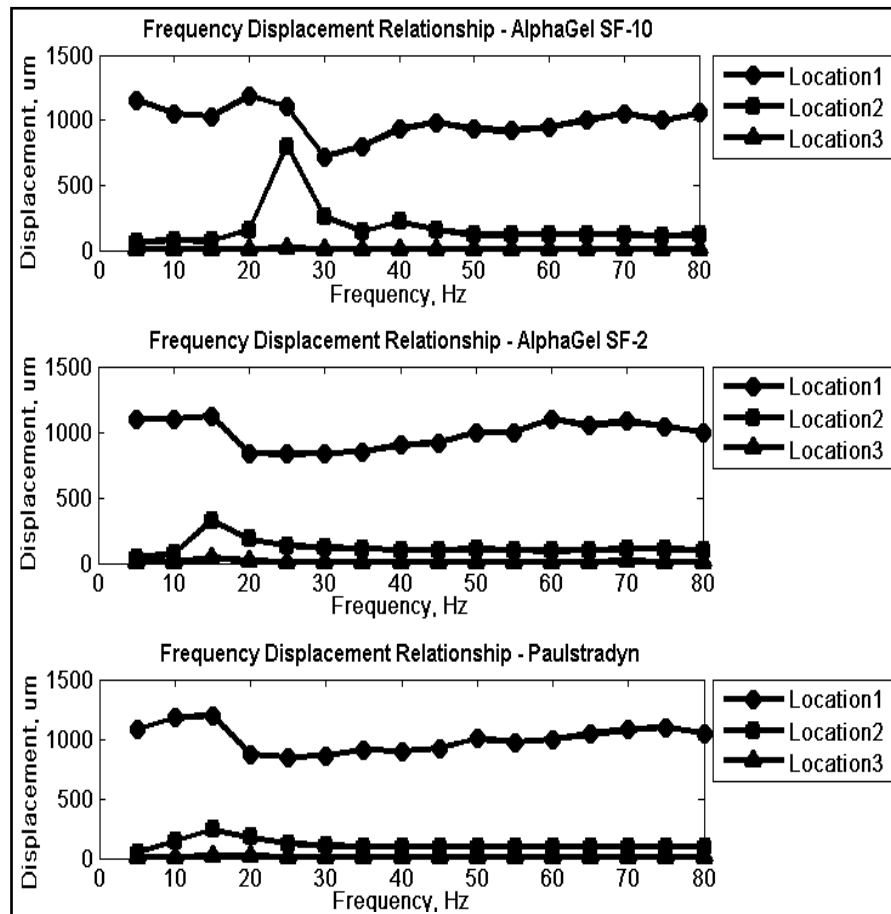


Figure 4.13: Measured vibrations over the range of operational frequencies for all three products under evaluation at all three locations. AlphaGel SF-10 (top), AlphaGel SF-2 (middle) and Paulstradyn (bottom)

Four damping feet from each shortlisted category were applied on four corners of a base plate and fixed to the main frame of the DIET system. The actuation unit was then fixed on that base plate with the help of six screws, as shown in Figure 4.12. Laser Doppler vibrometer was set up

and the actuation unit was operated to generate a sinusoid of 1mm (peak to peak) over 5-80 Hz. Measurement of steady state vibration was done with a resolution of 5 Hz and the test was repeated at all three locations. The results were plotted separately for all three products showing amplitude of displacement measured in (μm) against all the operational frequencies, at all three locations as shown in Figure 4.13.

As discussed earlier, location (3) was most critical for vibration isolation, so plots for all three products at location (3) are combined together and presented on a larger scale in Figure 4.14. Some nonlinear behaviour was observed for lower frequencies, which could be an accumulated effect of the resonant frequencies of the actuator and damping feet. This nonlinear behaviour ranged from 15-20 Hz in case of SF-2 and Paulstradyn but was more prevalent in case of SF-10 and ranged from 5-30 Hz at location (1).

It may also be noted here that the output amplitude of the sinusoid measured is not exactly 1mm, the likely reasons for this issue could be noise in the laser measurements as the top surface of the tip of the actuator (location1) was not 100% plane. Moreover, the LVDT position sensor providing the PID feedback control was not calibrated at that point in time.

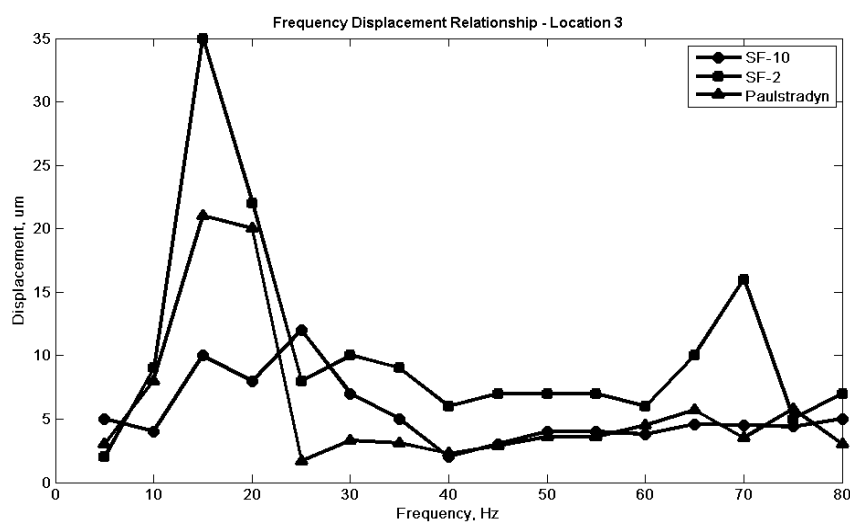


Figure 4.14: Plots showing measurements of vibration for each damping product under evaluation at location-3

The laser testing in fact served a dual purpose. It helped in finalising the choice of Paulstradyn damping feet, which exhibited best response by producing a maximum of 20 (μm) displacements at critical frequencies, and also pointed out that the LVDT position sensor needed calibration.

Based on these results, Paulstradyn damping feet were chosen as vibration isolation solution for the DIET actuation system and the design of base plate of the actuator discussed in Section 4.6 was adapted to accommodate three Paulstradyn damping feet, as shown in Figure 4.15.

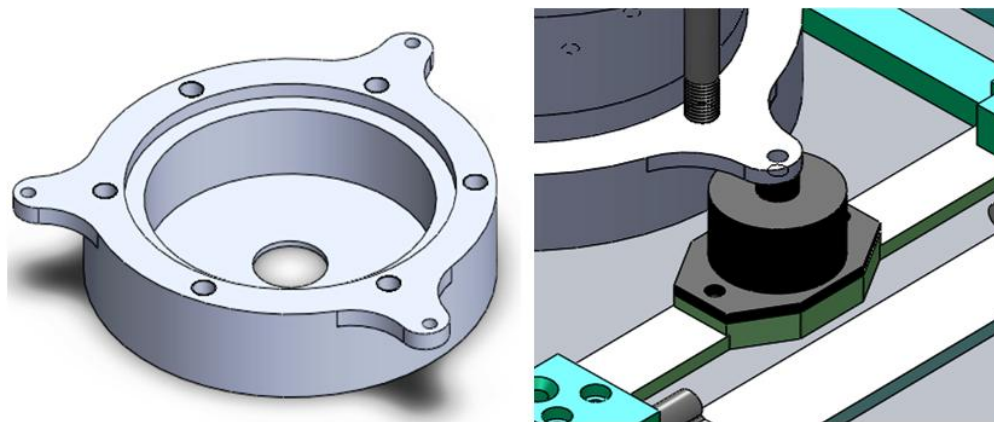


Figure 4.15: Showing design changes made in the base plate of the actuator to accommodate the damping feet (left), and the Solidworks representation of actuator after being mounted on the damping feet

4.8 Calibration of LVDT position sensor

The manufacturers, Trans-Tek, had provided calibration record for the LVDT model number: 0241-0000 (TRANS-TEK). The calculation method adopted was Best Fit Straight Line through Zero and the calculated slope of the line was defined:

$$Y = 103.5708 X + 0.0000 \quad (4.18)$$

The calibration data pertaining to the DIET application to produce 2mm peak to peak output is presented in Table 4.6.

Table 4.6: Calibration data of LVDT position sensor

Position		Output VDC		Error
inch(es)	mm	data	Zero adjusted	% F.S.
-0.04	-1.016	-4.1828	-4.1614	0.090
-0.02	-0.508	-2.1138	-2.0923	0.101
0.00	0.00	-0.0214	0.0000	0.000
0.02	0.508	2.0729	2.0943	0.110
0.04	1.016	4.1762	4.1977	0.265

4.8.1 Bit Volts Relationship

In the DIET actuation control system, the feedback signal (VDC) from the position sensor is fed to NI-9215 (16 bit, analogue input module), which is capable of handling a voltage signal in the range of ± 10.4 volts. So the input span of the NI 9215 is 20.8 and analogue to digital converter resolution (ADC resolution) is 16. The relationship used to convert binary analogue input to calibrated engineering units is defined:

$$\text{Input engineering units} = (\text{Binary value} \times \text{LSB weight} - \text{offset error}) \quad (4.19)$$

where offset error of NI-9215 is negligible (0.014%) and the value of input signal which the least significant bit of this module can handle is called LSB weight. LSB weight for NI-9215 was calculated:

$$\text{LSB weight} = \text{typical input} \frac{\text{span}}{2^{\text{ADC resolution}}} \quad (4.20)$$

The calculated LSB weight was 0.31738 mV. Software was written in LabVIEW for this bit to volts conversion and in the host VI bit value of the peak to peak signal was divided by 3150.769

(inverse of LSB weight), scaled down to convert the standard units of voltage and length to μv and mm, respectively.

Then the peak to peak signal was divided by 2 to get the set value of the amplitude signal in mm. After multiplying by the LVDT scaling factor the signal was fed to the actuation unit. The LVDT scaling factor of 0.0254 was required for conversion from inches to m. The LabVIEW schematic of the host VI is shown in Figure 4.16.

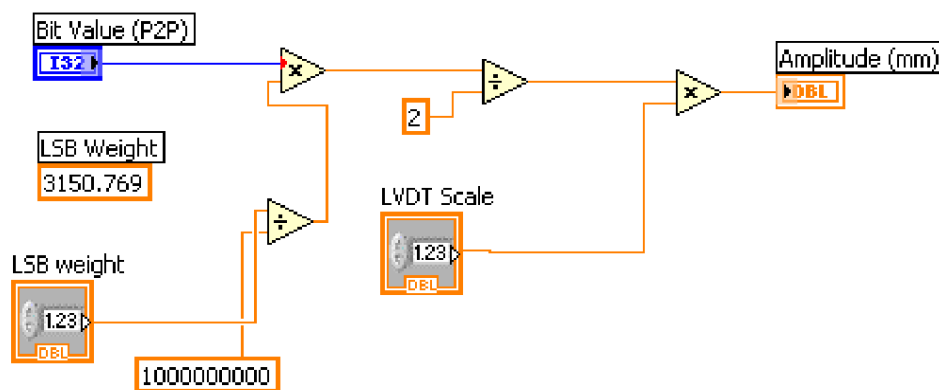


Figure 4.16: Schematic of the bit_to_mm conversion VI

4.8.2 Absolute accuracy of NI 9215

To determine overall possible error of measurements it was also important ascertain the absolute accuracy of the NI 9215. The following relationship defines the absolute accuracy of this device:

$$Accuracy = Voltage + Device\ range \times offset\ error + system\ noise + temp\ drift \quad (4.21)$$

where the voltage reading is specific to system requirement and in case of DIET actuation control the range is ± 4.1828 or 8.36 V to produce a maximum peak to peak signal of 2.032 mm.

Gain error for NI 9215 is 0.02% and the offset error 0.014%. The device is calibrated at 25 ± 5 °C, so temperature drift at room temperature is negligible (National Instruments). Now for system noise calculations, the value of RMS input noise for NI 9215 is 1.2 LSB and LSB is worth about 0.305175 mV, so averaging over 100 points:

$$\text{Noise uncertainty} = \frac{\text{InputNoise} * 3}{\sqrt{100}} \quad (4.22)$$

So the noise uncertainty was calculated to be 0.1098 mV and the overall absolute uncertainty expected from NI 9215 for DIET actuation control system was 3.23 mV.

4.8.3 Verification of actuation signal and feedback control

To analyse the magnitude of the actuation signal and verify performance of the feedback control mechanism, Laser Doppler testing was carried out. The amplitude signal to the actuator was varied from 0.1 mm to 0.9 mm, on a range of frequencies over 10-90 Hz with a resolution of 10 Hz. Displacement values obtained by the Laser Doppler vibrometer were compared to the set values and relationship of bit to mm conversion was established.

The overall results, showing actuator displacement for a set value of actuation amplitude along with the corresponding binary values (bits) are presented in Table 4.7 (*Appendix B*). It was established that on average 10050 bits were required to transmit a displacement signal of 1mm. Some outliers were found due to the involvement of noise in the laser motion detection. However, slopes were small and the offsets were very close to the set values and the plotted values showed a reasonably tight scatter. Figure 4.17 (A & B) illustrate a comparison of the scatter of bit-displacement relationship before and after the LVDT calibration.

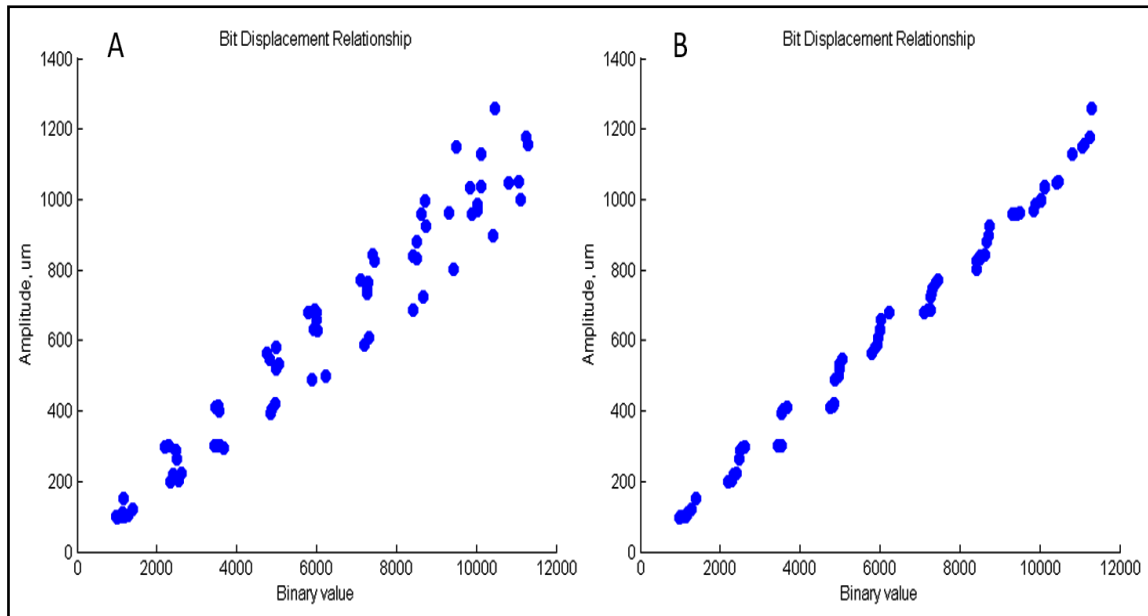


Figure 4.17: Plots showing number of bits required for a set value of amplitude (μm), (A) before calibration and (B) after calibration

4.9 Summary

Steady state sinusoidal actuation of the breast is a very important process of DIET imaging. Typical frequency range of this actuation is between 10-70 Hz and at amplitudes between 1-2 mm peak to peak. Surface motion reconstruction of this applied actuation indicates the presence of a stiffer inclusion inside the healthy breast tissue. A previous version of the actuator was tested in vitro and during limited in vivo trials which showed limitations in its use for a portable clinical device, particularly in terms of its size dimensions and positioning.

The mechanical response of the breast was modelled, and the actuation stroke and force requirements were estimated. To obtain precise and accurate linear motion and to minimise overall size, 3-voice coils were integrated in actuation system. A real-time controller was programmed to communicate with an external machine (Host-PC) through TCP/IP, using an LVDT sensor for feedback. To optimise linear motion and a sustained output over time, two concentric springs were integrated in the overall design. Vibration analysis was conducted and damping

feet were implemented to provide vibration isolation to the cameras. Calibration of LVDT position sensor was done for precise feedback.

Overall, a compact and accurate actuation system with automated positioning was designed and implemented in the DIET clinical prototype.

Chapter 5

5 3-AXES POSITIONING

5.1 Background

In DIET clinical imaging the patient would lie on the top surface, torso facing down, with one breast hanging pendent through a hole. The vibration actuator that transfers a vertically oscillating sinusoid into the breast is positioned at the nipple. Varying breast anatomy makes it impossible to define a generic centred, and thus fixed, position for the actuator underneath the breast.

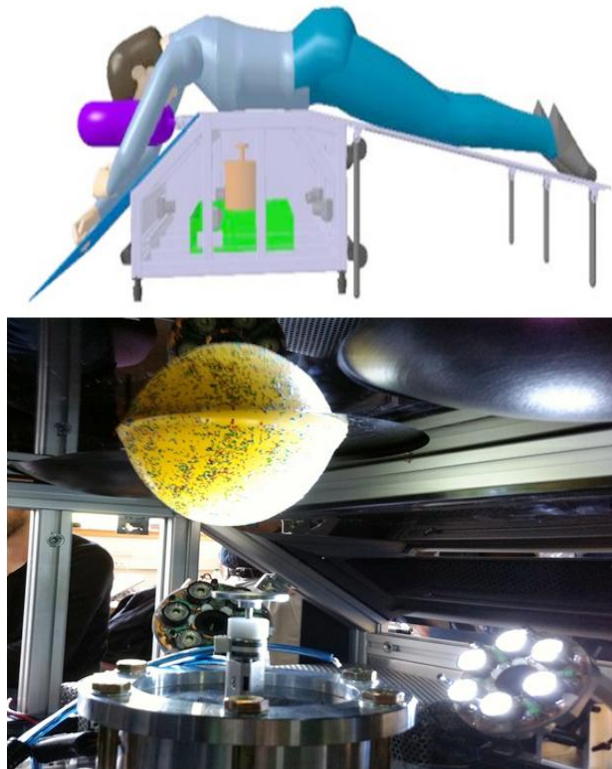


Figure 5.1: Schematic illustration showing overall position of the patient during DIET screening process (top) and actuator positioning underneath a breast phantom (bottom)

Depending upon the size and volume of the breast, the positioning of the actuator varies from subject to subject. This positioning of the patient and the actuator is illustrated in Figure 5.1. In the previous prototype, this positioning was done manually. Positioning involved a time cost and caused unease/discomfort, not only for the patient, but also for the nursing staff responsible for screening. During the initial limited clinical trials, it was determined that an automated positioning system to position the actuator underneath the breast would be more useful. In particular, it would make the system more users friendly, and ensure automated imaging with minimal operator skills.

Variable anatomy of the human breast requires manoeuvrability of the actuator in (X, Y and Z). An automated and remote controlled 3-axis positioning system was implemented in the clinical prototype capable of positioning the breast interface of the actuator. It works using visual feedback through a built-in optical system.

5.2 System Specifications

The 3-axis positioning system had to be a mechanical device capable of moving the DIET actuation system within a given space in three dimensions. These types of subsystems are common in industrial use, mainly in the production lines. Positioning systems are characterized by several features including number of motion axes, relative motion of one axis to another, and the required stroke on each axis. For the DIET application, the actuator positioning system needed to have three orthogonal axes (X, Y and Z), and depending upon availability of space and requirement of manoeuvrability in relation to the anatomy of the human breast, a motion stroke of 40 mm in the X and Y dimensions and 100 mm in the vertical dimension (Z axis) was required. Moreover, it was desired to keep its size and weight, as small as possible. The system requirements were thus defined:

- Allow flexibility to position the actuator below the patient's breast 40 mm in X-axis, 40 mm in Y-axis and 100 mm in Z-axis
- Repeatable linear motion
- Speed and limit control
- Respects the physical dimensions and weight restrictions of DIET breast screening system
- Ease of mounting in the new frame
- Electrically powered and real time control through software, preferably LabVIEW
- Resists transmission of vibration from actuator to the optical system
- Operable with low skill levels
- Simple design and easily machined (manufactured)
- Self-lubricating (no maintenance)

5.3 Linear motion solutions

Linear motion can be generated in many ways, the majority of which were either too bulky or too expensive. For DIET being a low cost and portable screening system, cost, weight and dimensions constraints were of top priority.

5.3.1 Linear Motors

Linear motors generate linear motion without involvement of any means of motion translation as is the case with rotary motors. The load is directly applied, allowing reduction of inertia and clearance of the system. Linear motors are very suitable for high speed range and better positioning accuracy. They typically have a longer service life and lower maintenance needs. Their only disadvantage is cost.

5.3.2 Rack and pinion

The input of this system is a rotary motion provided by a motor and the output is linear motion. They can provide very accurate positioning, but are bulky and not recommended for delicate and critical loads. This option was discarded from the outset.

5.3.3 Nut and screw system

The screw and nut arrangement also transforms rotary motion from a motor into a linear motion and when used in conjunction with a stepper motor its positioning accuracy is good. They are not typically recommended when high speed is of priority. A precision ball screw system is a similar option, which is more efficient, allows high speed range and requires less clearance, but it is more expensive.

5.3.4 Cylinders actuators

They are of three different types: 1) hydraulic; 2) pneumatic; and 3) electric. They can provide a large range of strokes and can handle large range of loads. The first two types require additional hydraulic or pneumatic cylinders, adding weight and mass to the system. However, the electric cylinders could be one option for the DIET application.

5.4 Initial design concept

The initial design concept involved one integrated positioning system providing motion in all 3-axes. The design concept was based on three main components each responsible for motion in a particular axis using three different stepper motors and lead-screws.

For the Z-axis (up/down motion) a scissor jack lift table was designed to move the actuator up and down with the help of an electrical cylinder. The lift table consisted of top and bottom plates and a four scissors jack. The scissors jack was subsequently replaced by a level arm system to avoid the use of a powerful electrical cylinder and instead a third stepper motor was in place to provide power required for vertical motion. Figure 5.2 shows a Solidworks representation of the initial design concept (Lottin, 2011).

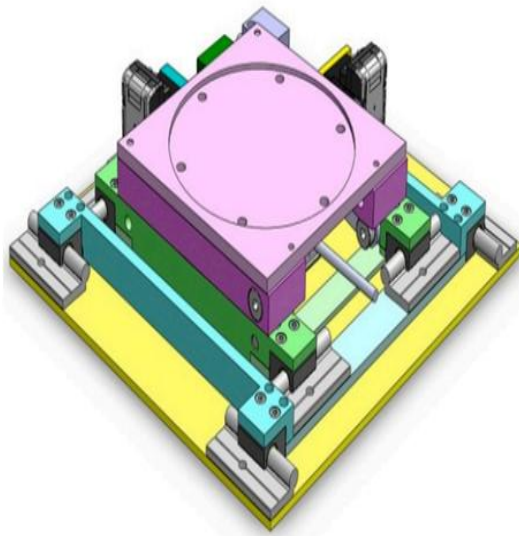


Figure 5.2: Solidworks representation of lift table concept; fully retracted (left) and fully extended (right)

5.5 Analysis of the initial design

This design was able to provide the required stroke in all three dimensions, but was not considered feasible for DIET application for two reasons:

- The total internal vertical height for the DIET clinical prototype was planned to be ≈ 230 mm. The height of this system was to be ~ 30 mm when fully retracted and the height of the actuator with damping feet (discussed in Chapter 4) was 125 mm. Now, accounting for another 70 mm for vertical height of an average human breast, the internal available vertical space was not enough to allow flexibility for a larger breast. So, opting for this design would have necessitated increasing the planned overall vertical height of the DIET system, reducing its portability.
- The most important reason for not implementing this design was that once the positioning system was extended in the vertical dimension, the width of the actuator was going to block the FOV of the optical system thereby leaving some blind spots, as

shown in Figure 5.3. Creating a platform for the cameras would have induced extra imaging error, as well as adding weight complexity and cost.

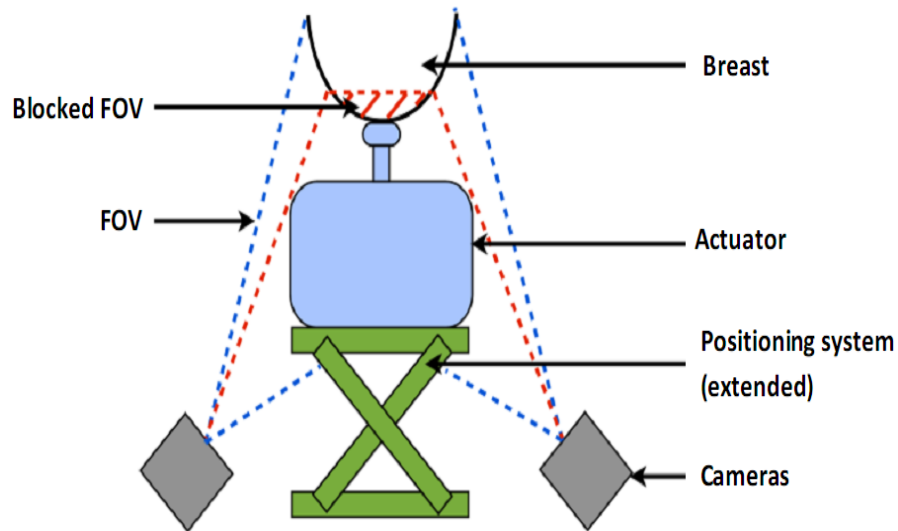


Figure 5.3: Showing blocked FOV or blind (red dotted) area, when positioning system is extended

5.6 Final design concept for the actuator positioning system

The simplest solution to this design problem was to keep the XY stack as conceived in the initial design, but to modify the vertical positioning mechanism (Z-axis) by implementing a more practical solution. Therefore, this subsystem was divided into two main components from a design perspective, comprising a 2-axis positioning system (XY stack) and Z-axis positioning system for up and down movement.

For the Z-axis the idea was to implement a motorised lead screw inside the actuator to move the breast interface up and down. This concept was more practical in all respects. On one hand it would allow the cameras a consistent and clear FOV during the whole imaging process and also moving a 5 kg of actuator mass for every imaging session could be avoided thereby increasing the life span of the moving parts of positioning system.

5.6.1 2-axis positioning system

5.6.1.1 Selection of motors for 2-axis positioning

A stepper motor converts electronic pulses into proportional mechanical movement. Each rotation of the stepper motor shaft is made of a series of discrete individual steps. A step is defined as the angular rotation produced by the output shaft each time the motor receives a step pulse. Each step causes the shaft to rotate a certain number of degrees. The most common type of stepper motor is the permanent magnet (PM) and variable reluctance (VR) motor. Depending on the shaft configuration, these are normally available in three different types: captive, non-captive and external linear actuators.

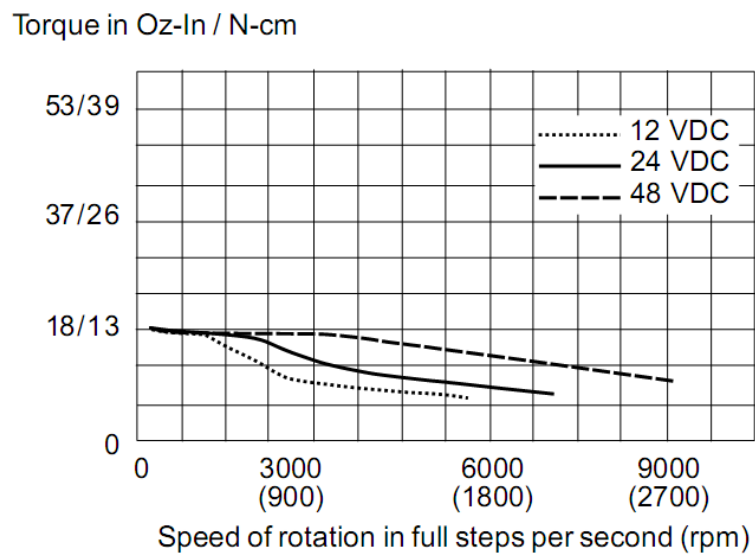


Figure 5.4: Performance curve of MDrive-14 (Schneider Electric)

The captive actuators have a built-in anti-rotation mechanism through the use of a splined output shaft that allows it to extend and retract as a unit with no requirements for additional anti-rotation mechanism, and are designed for short strokes. Non captive actuators have the lead screw going through the motor and have no reasonable stroke limits, but must be attached to an assembly that does not rotate. The external linear actuator uses a lead screw and a nut

combination that extends out from the motor. Linear motion is created by the nut traversing back and forth as the lead screw turns.

For DIET, a XY stack external linear actuator MDrive-14 from Schneider Electric, USA (Schneider Electric) was selected. This actuator is a high torque 2-phase motor and comes with step/direction input control. Its step size is 1.8° and the step /direction signals from controller are directly converted into motion with the help of on-board control electronics. It can be operated on 12-48 VDC with a max power supply current of 1 A. Like most of the other electronics in DIET, this stepper motor was powered at 24 VDC and it moved 5 kg actuator at a reasonable speed. The performance curve of the motor is shown in Figure 5.4. Two motors were applied to provide motion in each of the two axis in the XY stack.

To stop the motor operation at the extremities of the required stroke two limit switches were applied on each end of the forward and reverse direction. The motion was controlled through National Instruments (NI) Compact Reconfigurable Input Output (cRIO) using LabVIEW.

5.6.1.2 Implementation of XY-axis positioning

The idea was to position the actuator in such a way to save as much space as possible. Stress simulations were done in Solidworks to work out the actuator load in different design options. Lubrication free rails, Drylin W range, from IGUS (Germany) (IGUS) were used to move the actuator in XY stack.

The stepper motors were fixed on the side of the rails to save vertical space. Motors and guides were positioned beside the actuator to save space and the actuator was made to sink into the main frame. Figure 5.5 shows the basic assembly.

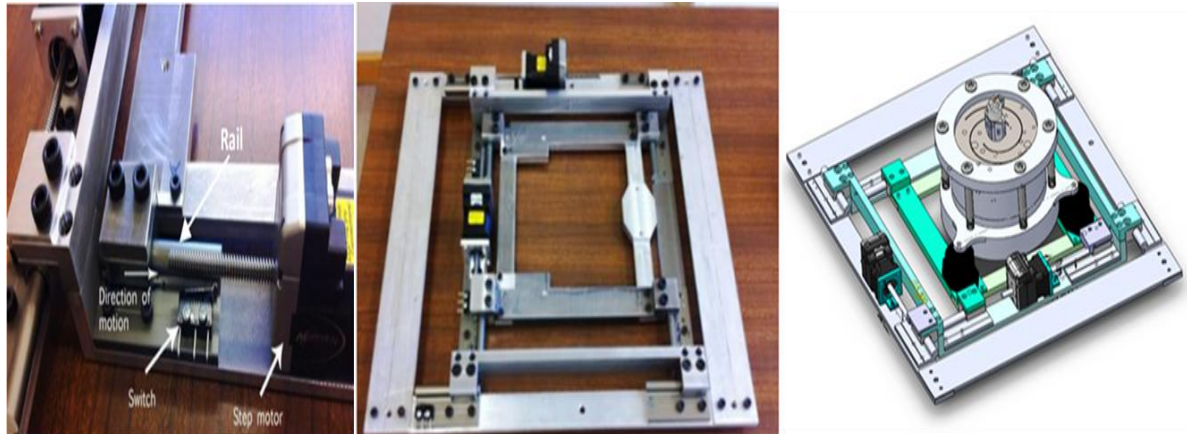


Figure 5.5: Showing positions of the rail, limit switches and stepper motors (top left), final design of the 2-axis positioning system (top right), and Solidworks representation of 2-axis positioning system with actuator mounted on the damping feet (bottom)

5.6.2 Z-axis positioning system

5.6.2.1 Selection of motor for Z-axis positioning

To maximize camera FOV and to provide the motion in Z-axis (up and down) a motorised interface was incorporated in the design of the actuator discussed in Chapter 4. This way instead of moving the entire actuator vertically, only the breast interface (a small circular plate) sitting on top of a lead screw will be adjusted. Once the interface reaches the breast and required pre-stress is applied, the actuator will start vibrating the breast at the required frequency and amplitude. This concept is illustrated in Figure 5.6.

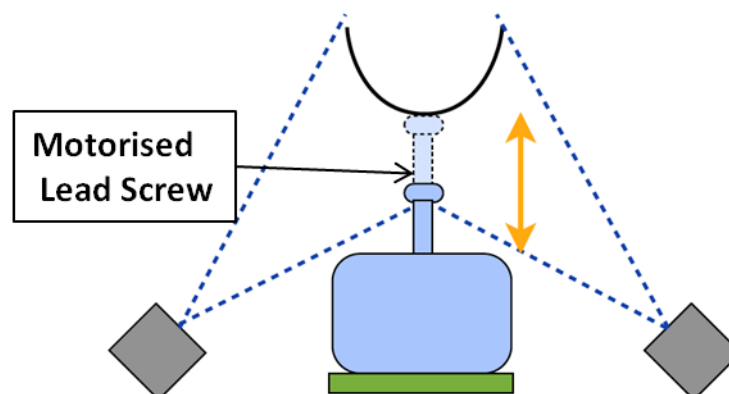


Figure 5.6: Showing the concept of generating motion in Z-axis in order to maximize FOV of the optical system

A captive can-stack linear actuator of 15000 series from Haydon Motion Solutions, USA (Haydon Motion Solutions) was selected to generate motion in the Z-axis through a lead screw. These stepper motors provide high force to size ratios and are most suitable in applications with space constraints. They come with 15° and 7.5° adjustable step resolution and multiple sized screw-leads. Body dimension of this motor were 15 mm (length) x 20 mm (diameter). The motor came with 12.7 mm stroke lead screw which was subsequently replaced with a 110 mm stroke lead screw. The max linear step size was 20 microns and the motor provided a max force of 7 N.

To power up this motor a bipolar chopper drive DCS-4020 was also purchased from the same manufacturer (Haydon Motion Solutions). The chopper drives allow a stepper motor to maintain a greater torque at higher speeds. Body dimensions of the drive were 113 x 78 x 33 mm³, but it was not an issue as it could be fixed anywhere in the main frame. This drive provided all basic motor controls including full or half stepping and also the direction control. The drive was powered by 24 VDC and a 5 V TTL logic external signal was provided for enabling and controlling step size and direction control via NI 9403 using LabVIEW. For the extent of the stroke, two hinge-leaf-lever type limit switches D2MQ-4L were incorporated at extreme positions on top and bottom. Figure 5.7 shows pictures of the stepper motor and chopper drive.



Figure 5.7: Showing drive and the motor used for generating motion in Z-axis position system (Haydon Motion Solutions)

5.6.2.2 Implementation of Z-axis positioning

Initial testing of the stepper motor was done in the lab environment by providing 24 VDC to the drive through a bench-top power supply and a 5V TTL enable control signal was provided by NI 9403 (National Instruments). The redesigning of the actuator involved increase in the internal diameter of the 'main shaft' and the 'coil bone' meant to transfer vibrations to the breast (Chapter 4). This increase was necessary to accommodate the 3.5 mm lead screw of the stepper motor.

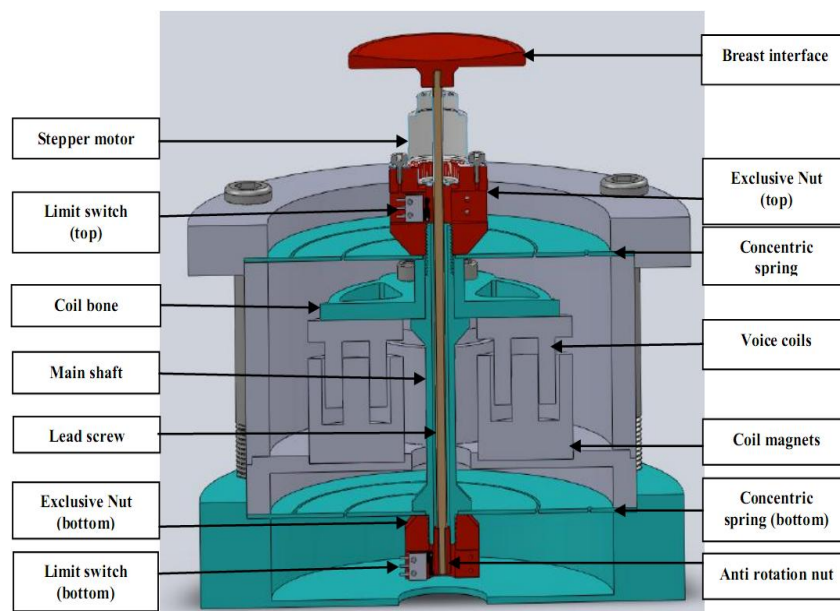


Figure 5.8: Cut out of the final design of the actuator after implementing the z-axis positioning capability. Green colour shows the parts which required modification and the red colours shows addition to the original design

An anti-rotation nut was applied to the lead screw to lock the rotation and to make sure that the lead screw moves accurately through the shaft without play and also to actuate the top and bottom limit switches. A breast interface (40mm circular disk) was thread-fixed on top of the lead-screw to shake the breast. Three breast interfaces (20mm, 40mm, & 60mm) were developed for different anatomical sizes. Figure 5.8 shows the cut out models of the final design of the actuator implementing the changes.

5.7 Hardware control concept

As described earlier, the 3-axis positioning system was split into two sub-systems. For the Z-axis, an external bipolar chopper drive powering and controlling the motor with all basic motor controls including direction (up and down) and speed (half and full stepping) was realized within the main frame. This drive was remotely controlled by a cRIO controller by National Instruments (NI) via digital inputs (National Instruments). Two limit switches control excursion.

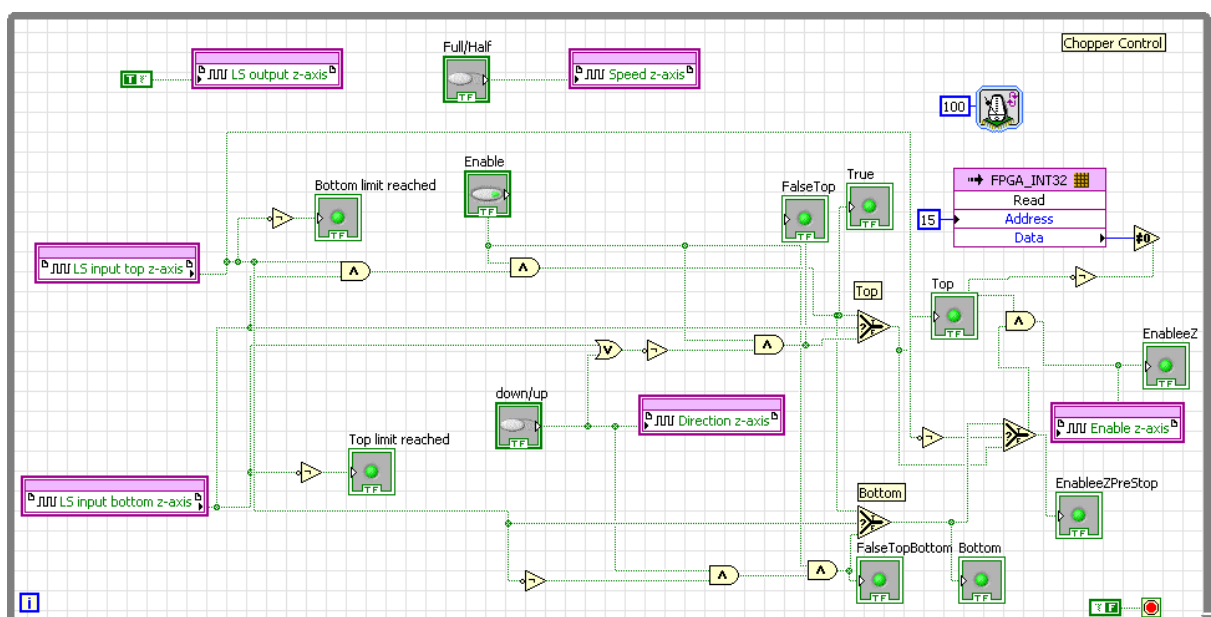


Figure 5.9: Block diagram of the chopper control loop in Labview. Pin Configuration on NI 9403: DO 17 enables and disables the drive; DI 5 and DI 6 are the inputs for the limit switches. DO 4 controls the speed and DO 2 controls the direction.

The XY-axis control was designed to enable a movement of the actuator for 20 mm in both directions from the centre. This movement is accomplished by two MDrive stepper motors. These motors are powered by an external 24 V DC power supply and require 0-24 VDC analogue input to control the direction. The maximum output current of the NI 9263 analogue output module used in the system for actuation control, is ± 1 mA per channel. This was not possible to control the stepper motors of XY stack via this module due to low level of output current. A

small circuit was designed to create a 24 V DC potential coming from the power supply, by triggering it with a digital 5 V TTL logic signal from cRIO controller (Glasbrenner, 2012).

Figure 5.9 shows the block diagram of the chopper control software which was written in LabVIEW. The loop is timed to execute at a 0.1 Hz rate.

The required 24 V DC potential was connected to a high-voltage transistor which switches the 24V when it gets a digital 5V high signal from cRIO controller. Thus, it was possible to control the motors with digital signals instead of analogue signals. This circuit was printed on a PCB and mounted inside the frame of the device near the MDrive stepper motors. The 5V TTL signal was connected to the base of the transistor, the 24 V DC potential to the collector and the emitter was grounded. If a tension over roughly 0.7 V is applied to the base, the transistor interconnects the 24 V DC signal. As a consequence, the circuit is zero active, which means 24V output is enabled when a low signal is supplied and vice versa. The connected drive runs counter-clockwise if the direction input is high and clockwise if the direction input is low. NPN transistor MPSA42 with a DC current gain (h_{FE}) of 40 was used. The maximum current of the drive is 15 mA (I_c) at 24 V DC. The control voltage from the cRIO controller V_b is 5 V, so if the base current (I_b) equals:

$$I_b = \frac{I_c}{h_{FE}} = \frac{0.015 A}{40} = 0.000375 A \quad (5.1)$$

At the base emitter junction there is a voltage drop of 0.7 V from 5 V control voltage signal (V_b). Thus the base resistor was calculated as under:

$$R_b = \frac{V_b - 0.7}{I_b} = \frac{4.3 V}{0.000375 A} = 11466.66 \Omega \quad (5.2)$$

The resulting required resistance was rounded off to 10 K Ω to ensure a reliable switching behaviour of the transistor. The schematic diagram of the designed control circuit is shown in Figure 5.10.

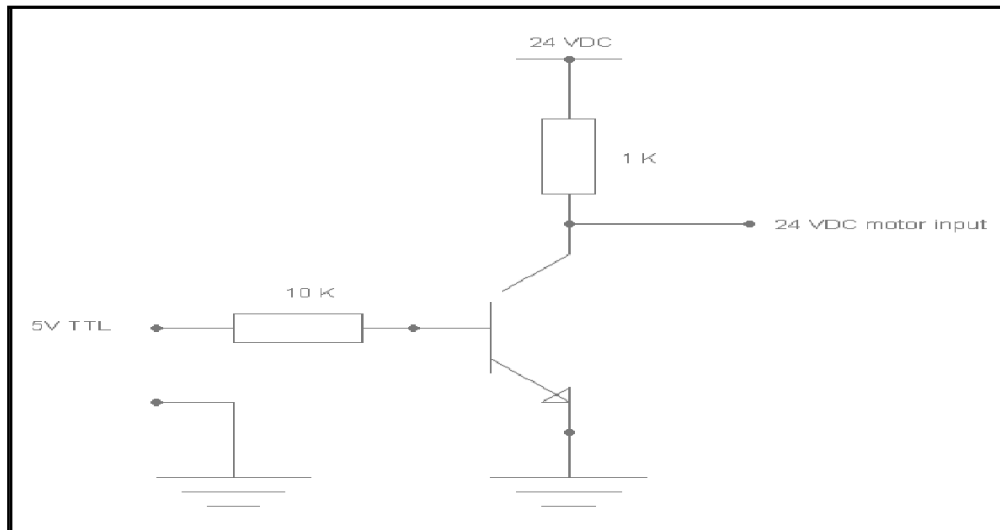


Figure 5.10: Schematic diagram of circuit to control the 24 V DC direction input of one motor with a digital 5V TTL signal (Glasbrenner, 2012)

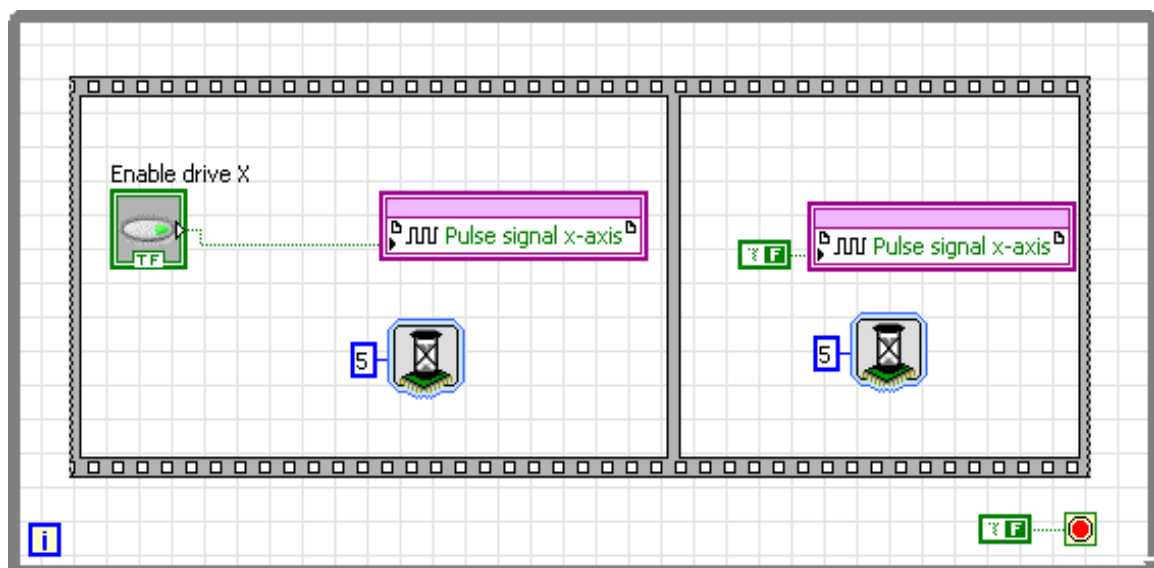


Figure 5.11: Pulse signal generation loop for enabling MDrive stepper motor in X-axis. The pulse signal (DO 8) is connected to the step clock input of the motor. The case structure is executed from left to right; in the left case digital output is enabled and in the right it is disabled

In order to enable the drive it is necessary to supply a step frequency to the step clock input of the motor, basically a digital pulse signal. This pulse signal is generated by simply disabling and enabling the digital output channel of the digital I/O module at a specified time which was kept 5 μ s. Generating the pulse signal is a time-critical process. Its generation is, therefore, done in a separate loop without a sleep mode. A time-critical loop without any sleep time will monopolize the CPU resources which is important at timing such as 5 μ s. Figure 5.11 shows how the step clock signal for the MDrive stepper motor is generated.

Similar to the Z-axis control, both the XY-axis direction controls have the limit switches for each direction which stop the stepper motor when triggered. The motors are provided with an enable/disable input from the cRIO. By supplying a digital high signal to this input the drive is disabled, consequently this input is zero active. Once one limit switch is triggered closing a contact, it is perceived by the cRIO controller and it sets the digital input to the stepper motor to high, thereby stopping further movement.

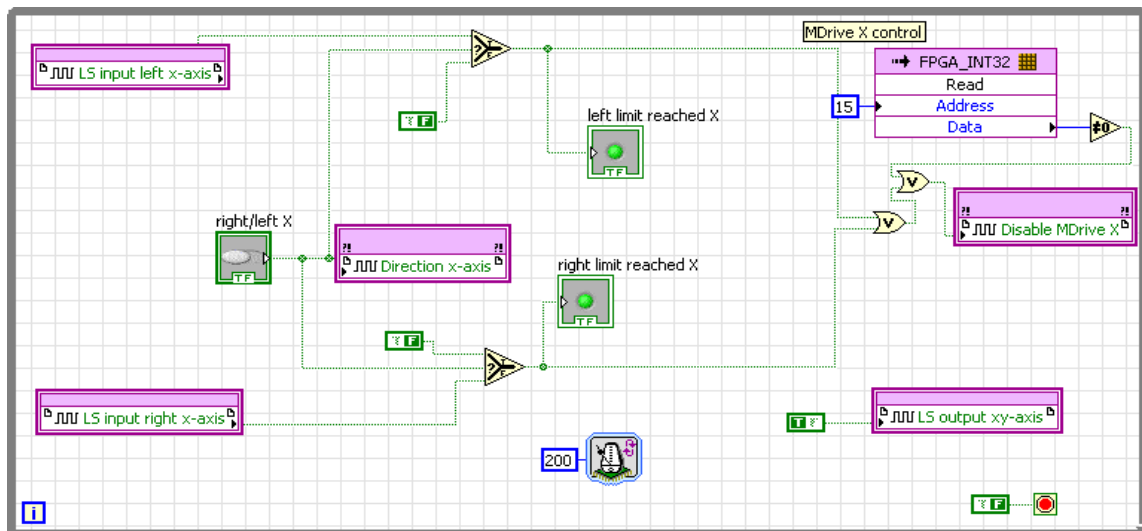


Figure 5.12: Direction and limit switch control loop for MDrive providing motion in X-axis. The loop is timed to execute on a 200 ms interval.

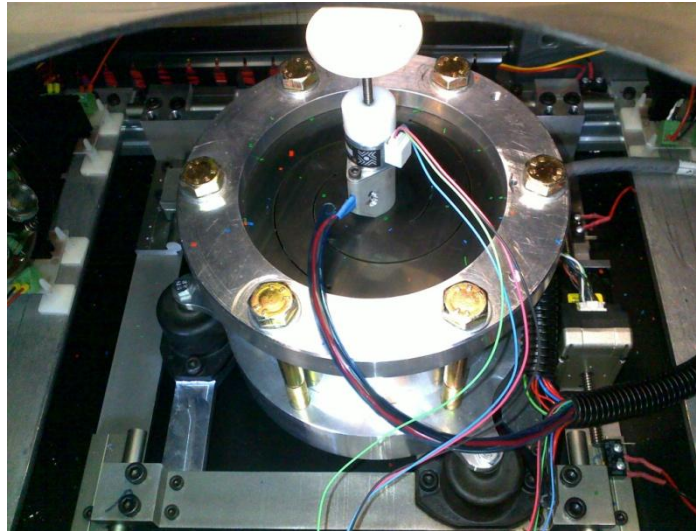


Figure 5.13: Inside view of the DIET clinical prototype, showing the actuator installed on the 2 – axis positioning system, while the breast interface mounted on the z-axis positioning motor can also be seen.

As a result of the time critical step clock frequency the limit control could not be realized in the same loop by enabling and disabling the pulse signal, as in case of the Z-axis control. Therefore the Limit switches for XY-positioning were implemented in a separate loop timed with a loop timer to execute on a 200ms interval. Otherwise, the generation of the pulse signal for the step clock input of the drives would have been slowed down. The direction control loop for the MDrive, implemented in X-axis is shown in Figure 5.12. Figure 5.13 shows the inside view of the DIET actuation unit mounted on the 2–axis positioning system. The breast interface, which is guided through a lead screw by the Z-axis positioning system, can also be seen in the picture.

5.8 Summary

During the initial clinical trials of the DIET breast cancer screening system there was a need for repositioning of the actuator during each imaging session, depending upon the breast size of the subject. This necessitated implementation of an automated positioning system capable of providing the motion in all X, Y and Z directions. A positioning system was designed that was subdivided into two components providing motion in XY stack and in the Z-axis independently. Two stepper motors with limit switches were implemented for positioning in X and Y direction.

For positioning along the Z-axis, the design changes were implemented in the actuation unit to accommodate the a chopper motor, two limit switches and the main shaft through which the lead screw moved the breast interface in up and down direction. The motors providing motion in 3-axis were programmed to be controlled remotely using a Field Programmable Gate Array (FPGA).

Chapter 6

6 ERGONOMIC DESIGN AND INTEGRATION

6.1 Background

In a standard DIET imaging session, the subject lies down on the top surface of imaging device with one breast hanging pendant through a hole. The actuation unit is repositioned according to breast size, such that the actuator interface is compressing the breast at the bust-point. Once the subject is positioned the actual imaging starts and loops through the whole range of frequencies selected for a particular imaging session.

The breast is vibrated under a sinusoidal harmonic actuation and normally ten optical images are captured by an array of digital cameras, at each frequency. These images are subsequently processed to analyse the breast surface motion in 3D. Disruptions in surface motion indicate the presence and location of much stiffer tumour tissue inside the healthy adipose tissue (Brown, 2007, Brown, 2008b, Brown, 2008a, Brown, 2010, Brown et al., 2012). During the whole imaging session, the subject has to remain in position (unmoving) or the motion reconstruction either fails or loses significance.

Imaging session time varies depending upon the range of frequencies to be imaged and image capture time of the cameras. The imaging time of the DIET stage-1 prototype was far too high at ~70 minutes for 20 frequencies. Thus, discomfort was reported by subjects undergoing examination during limited in vivo trials. Hence, image capture time must be fast enough to enable comfort, compliance and good throughput.

Moreover, the bulky size of the device restricted its mobility. The system was not suitable for frequent moves and did not pass through narrow doors. One aspect of the first prototype size was the need for a large imaging area to handle the large actuator and cameras used. Thus, a further requirement was created to develop an ergonomically designed clinical prototype according to improve comfort and portability for a multi-site breast screening program.

6.2 Previous work and identified areas of improvement

DIET concept validation was initially done on silicone phantoms in vitro, using the cameras, strobe lights, and actuator in the lab environment, as shown in Figure 6.1 (A) (Peters, 2004, Peters, 2005, Peters, 2007). Later, the subcomponents were integrated into a frame and the DIET stage-1 prototype was realised to carry out limited clinical trials, at Canterbury Breastcare, St. George's hospital (Christchurch, NZ).

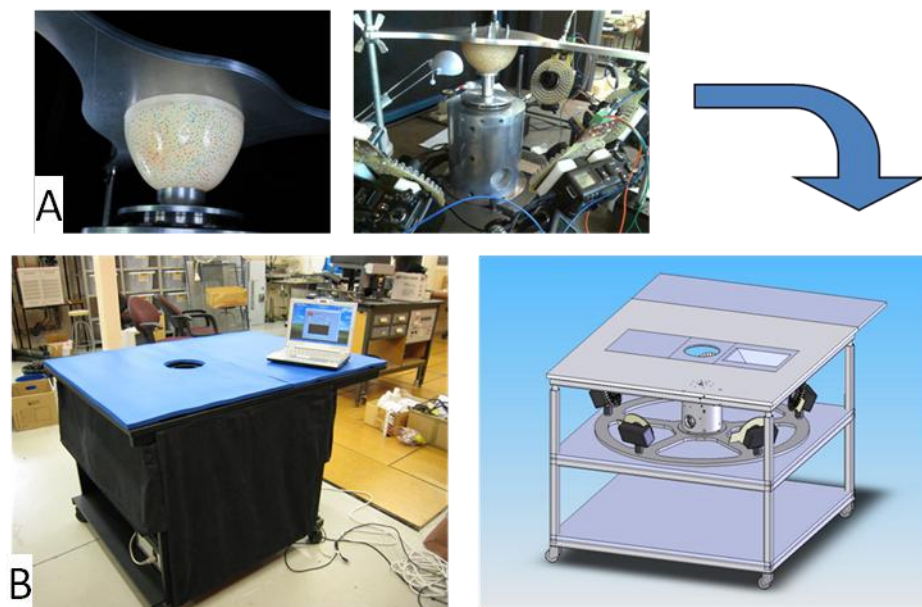


Figure 6.1: (A) DIET equipment layout in the lab during concept validation trials (top left) and (B) DIET stage-1 prototype (bottom left)

During the design of the DIET stage-1 prototype, human physiology and breast anatomy had not been significantly considered and pain in the neck and overall discomfort was reported by all

eight subjects who underwent initial pilot clinical trials. The non-ergonomic design voided its use for large scale clinical trials and physical dimensions of the device restricted its portability. In particular, this prototype measured 850mm in height, 1200 mm in length and 900 mm in width and its total weight exceeded 80 Kg, and it could only be used in vivo in conjunction with a surgical bench. Figure 6.1 shows different stages of the DIET prototype, which evolved over a period of last few years.

Though this stage-1 prototype was on wheels, its weight and size dimensions hindered its portability rendering its use totally unsuitable in a multi-storey building, without a suitable elevator. Due to the bulky design a 4x4 vehicle with two men crew was required to transport the prototype. The vibration isolation between the actuator and cameras was provided by using a separate steel stand that had to be decoupled every time the prototype had to be transported. Dimensions were too wide to fit through doors. During the trials it had to be attached to a longer examination table to provide more space for the woman to lie on it. The top surface was flat and not aligned to the shape of the body. There was no support for the head, which led to neck pain after some time. There was no support to rest the arms and no space had been provided to account for the comfort of the second breast. Black curtains were drawn on all four sides in order to provide the dark room environment to the optical system.

Hence, the ergonomics of the DIET system had to be completely redeveloped. Key elements of the new design included:

- Shape of the top surface was required to be adapted to female physiology
- Device size and weight needed to be reduced to make it more portable
- There was a requirement to integrate a headrest and armrest

Overall, the new design needed to be more comfortable, modular and adaptive in changing environment, making it suitable for mobile screening applications.

6.3 Initial research

During the initial phase, internet research was carried out about ergonomic structures used in medical devices. Websites of companies working in the medical device areas like Philips or Siemens were extensively visited to get initial inspiration from their designs and ergonomics of mammography devices, X-ray or Ultrasound devices and MRI devices. Particular attention was paid to MRI devices because their structure was similar compared to the DIET device, as the patient lies horizontally on the top surface, unlike a mammogram that is performed while standing or in sitting position. A visit to the Radiology Centre in Christchurch was made to observe the imaging procedure in a breast MRI device. The radiologist was interviewed and it was noted that most of patients felt satisfied about the comfort level during MRI imaging (MAILLARD Laura, 2010). However, a slight discomfort in the sternum area was reported by few of the subjects. Figure 6.2 shows pictures of Signa HDxt 3.0T MRI scanner by General Electric (GE) as it would be used for breast imaging at Christchurch Radiology, Hagley.



Figure 6.2: Ergonomic design of Signa HDxt 3.0T (GE) used for MRI imaging at Hagley Radiology which was the source of inspiration of design considerations for DIET clinical prototype

Ergonomic design of two more machines, the Achieva 3.0T Breast Coils, Philips and Magnetom Espree 1.5T, Siemens was also studied in detail to figure out the comfort angles for different parts of human body. Salient points from the initial design research include:

- a. Slightly elevated and curved top surface to hold the patient during exam ensures comfort
- b. Design has to be modular and adjustable to accommodate various size dimensions of arms, legs, torso and breasts
- c. Each solution included a support for head either in shape of pillow or a headrest
- d. There are two possibilities for resting the arms; introduce a proper arm rest or make use of the possibility of placing the arms beside the body
- e. Torso near the chest was straight while arms and legs were inwardly bent
- f. Each solution included two holes, one for each breast
- g. From this initial research on the MRI machines two comfort angles i.e. angle between legs and torso ($\alpha= 170^\circ$) and angle between arms and shoulders ($\beta= 145^\circ$) were been defined for the most comfortable position as shown in Figure 6.3.

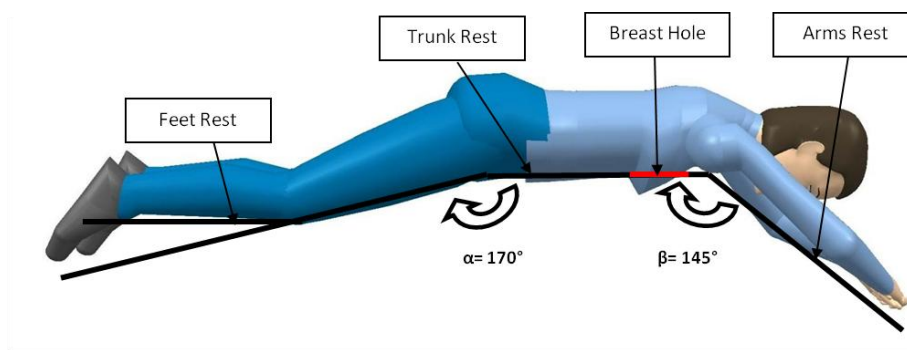


Figure 6.3: Comfort angles between legs and torso and between arms and shoulders defined as results of initial research on MRI machines

6.4 DIET design specifications

To identify the specifications for the overall design of the main frame of DIET clinical prototype, the requirement vector was divided into three main categories.

6.4.1 Ergonomic specifications

NASA's documents on anthropometric dimensional data (NASA) were studied and 50th percentile of 40 years old American woman was chosen to accommodate an average female. Based on those values a list of specifications for the ergonomics design of DIET clinical prototype was

formulated. Ergonomics specifications identified during the initial research required the system to be able to accommodate following:

- Range of breast diameters \approx 110mm, 130mm, 150mm
- Range of breast heights \approx 30 – 150 mm
- Distance from middle of the breast to top of hands \approx 600-670 mm
- Distance from middle of the breast to head segment \approx 400-470 mm
- Distance from middle of the breast to shoulders \approx 100-125 mm
- Distance from middle of the breast to hips \approx 180-220 mm
- Distance from middle of the breast to feet \approx 800-955 mm
- Arm's angle $< 35^\circ$
- Max angle of neck inclination for headrest design $\approx 84^\circ$
- Max shoulder width \approx 420 mm
- Bizgomatic width for headrest design \approx 145 mm
- Top surface to have two holes, one for each breast

6.4.2 General specifications

- Max weight \approx 45 kg
- Max width \approx 800 mm
- Max height \approx 400 mm
- Frame material : Aluminium
- Strong enough to support human weight
- Top surface to ensure comfort to the patient
- Be transportable by a single person in a normal car

6.4.3 Technical specifications

- Have an internal compartment of 600 (L) x 600 (W) x 280 (H) mm³ to be able to incorporate electronics and hardware
- Able to install 5 cameras at an angle of 72° between each
- Allows a working distance (distance between camera lens and breast) of 200-250 mm
- Modular design to accommodate future modifications
- Allows the technical person easy access to the inside of the device for maintenance
- To be installed by a single person in less than 10 minutes

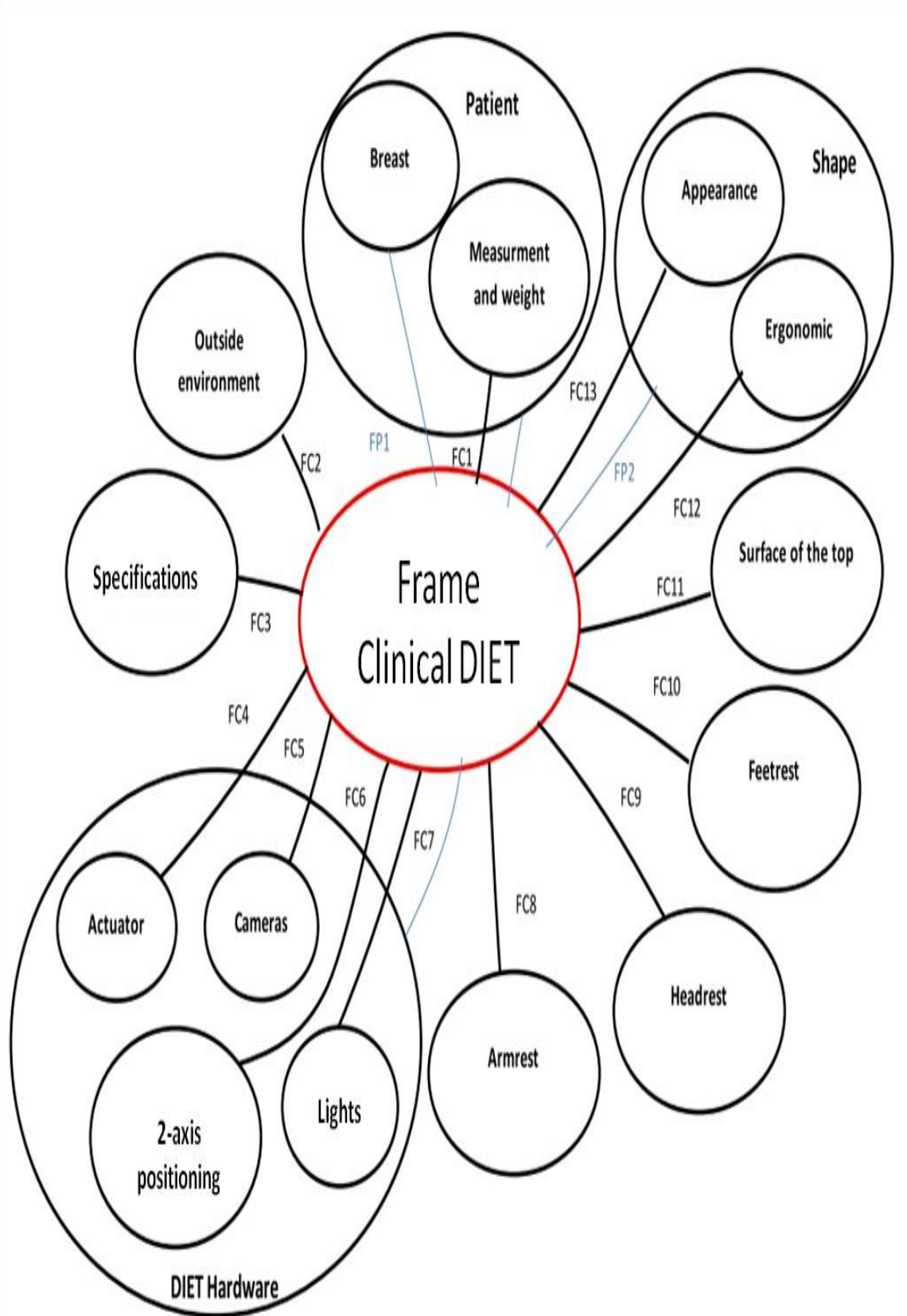


Figure 6.4: Octopus diagram for functional analysis of main frame of DIET clinical prototype

6.5 Functional analysis of design

Before starting the final design of the main frame for DIET clinical prototype, a functional analysis was done with the help of an Octopus Diagram to define the relationship of object to primary and constraint functions. Relationship of the object to different primary and constraint functions is shown in Figure 6.4. Details of the identified primary and constraint functions in Figure 6.4 are given below:

6.5.1 Primary functions

- FP1: Allows DIET hardware to detect breast cancer
- FP2: Allows a comfortable test for the patient

6.5.2 Constraint functions

- FC1: Supports the measurements and weight of the patient
- FC2: Be adaptable to outside environment
- FC3: Respects specifications defined by R vector
- FC4: Accommodates actuator
- FC5: Accommodates cameras
- FC6: Accommodates 2-axis positioning system
- FC7: Accommodates strobe lights
- FC8: Be adaptable to armrest
- FC9: Be adaptable to headrest
- FC10: Be adaptable to feet rest
- FC11: Be adaptable to top surface
- FC12: Respects the ergonomics shape
- FC13: To have acceptable appearance of a medical device

6.6 Initial design concept

The initial design concept of the DIET clinical prototype was inspired by the Signa HDxt 3.0T (GE) [Fig. 6.2] with minor modifications. The measurements of machine taken during the visit of Christchurch Radiology, Hagley generally met the criteria set by specifications defined for DIET

clinical prototype. It was decided to design a mock-up shape on similar lines to assess the compatibility for DIET application. The whole system was to be designed in such a way that it could be placed on an existing examination table. Two flaps were included for subject's arms and legs. The leg flap was to be used with a triangular shaped foam pillow. This concept involved just one hole for the breast. The subject had to shift sideways for examining the second breast. Because of this shift, an inward curved surface could not be designed and a flat surface was required. Two modest grooves were to be made in the top foam for making the position of the idle breast more comfortable. A wooden headrest (with foam) having a sliding rail system was proposed for making the adjustments as per the size of the neck. The enough space was kept on the top surface to accommodate arms, if the subject desired to place arms alongside torso. Figure 6.5 shows CAD drawings of concept-1 for the ergonomics design of this DIET clinical prototype.

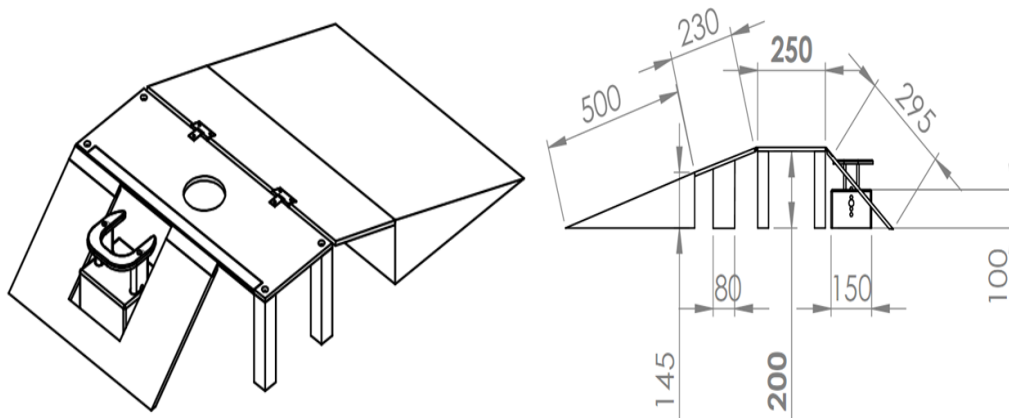


Figure 6.5: CAD representation - Concept-1 of ergonomics design of DIET clinical prototype

6.7 Evaluation - initial design

A wooden (18 mm thick) mock up device was constructed to assess the proposed ergonomics, space requirements and functionality, as shown in Figure 6.6. Views were obtained from five volunteer office mates on the layout and degree of comfort.



Figure 6.6: Wooden mock up device constructed to evaluate general space requirements and functionality

The following observations were recorded:

- a. The shape of the device was generally suitable for a breast examination.
- b. The most comfortable position for arms is in leaning position. When the arms were rested alongside body it applied high pressure on the head area.
- c. One-hole arrangement caused discomfort for the second breast, necessitating the requirement of one hole for each breast.
- d. It was also observed that when the breast was placed in the hole for examination, the armrest was slightly too far on the right side. So, it was determined that either the arm rest should be moved closer to the centre of the device or increase the width of the armrest and keep it equivalent to the overall width of the device.
- e. Headrest should be flexible enough to allow adjustment in height, length and inclination.
- f. To create this wooden mock up device, size dimensions of Signa HDxt 3.0T (GE) were generally followed. It allowed a space underneath of $800 \times 250 \times 300 \text{ mm}^3$ which was largely insufficient to allow installation of electronics and hardware required for DIET technology.

6.8 Final design concept

The final design involved building the device in two tiers:

- (1) The frame to provide ergonomic stature to DIET clinical prototype encompassing all the hardware required to perform DIET imaging
- (2) The top surface to provide overall housing and encompassing breast holes, armrests and space torso and legs.

It was decided to construct the top surface such that it could be folded (collapsed) during transportation and extended during layout for the operation. This concept is presented as a CAD representation in Figure 6.7. An adaptable massage table headrest with adjustable height, length and inclination was also chosen as it offered the flexibility of choosing between the crescent shaped cushion and a flat pillow. It was decided to provide wheels on one side for easy portability and four feet on the other better positioning and layout during examination.

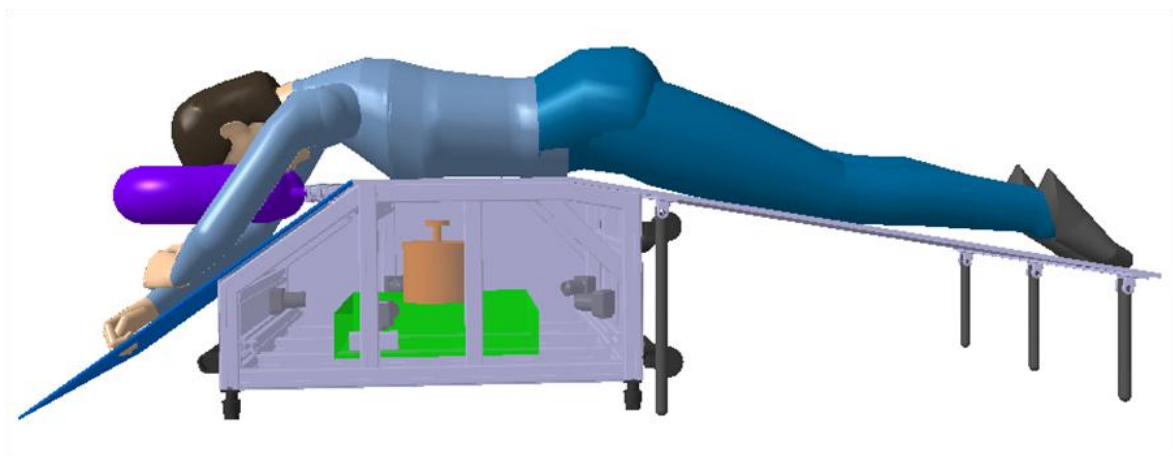


Figure 6.7: CAD representation of final design concept for DIET clinical prototype

6.8.1 Construction of ergonomic frame

Flexible construction of the main frame was required to enable subsequent installation of the actuator, cameras, strobe lights, 2-axis position rail, real-time controller cRIO, motors, motor drives, junction box and power supplies. MayTec Aluminium (GmbH, Germany) (MayTec) provides comprehensive and harmonised profile systems for flexible and modular construction. The profile bar (30 x 30, 4F, plain) was chosen to construct the overall structure of the main frame due to its modularity, robustness, and range of connecting parts required for assembly. This aluminium profile bar comes with 8.2mm, 4-sided slot to accommodate fixtures. Fixation in the slot can be done through an inclined nut and bolt system that can be slipped into the slots at any time even after assembly. The profile systems can be tailored to any application. The bar

profile was downloaded from the manufacturer's CAD library and used in drawings. The drawings of the ergonomic frame meeting the criteria defined during initial research and functional analysis were prepared using Solidworks (B. Pierrick, 2011).

These drawings along with dimensions and quantity of each individual part required to assemble the main frame of clinical DIET were sent to the local suppliers (AutoLine (Automation)) for sizing and cutting. The drawing of main frame design with dimensions and quantity of each subcomponent is shown in Figure 6.8 and the ergonomic angles of different pieces are shown in Figure 6.9.

A stronger profile (30 x 60, 4F, plain) was chosen for installing the headrest so that it could sustain the weight of the head. The sized pieces were assembled using the fastening elements provided by the manufacturer. Slider elements were used to ensure translation of headrest fixation, two holes were drilled and bronze bushings were inserted to allow smooth sliding and the headrest was fixed, as shown in Figure 6.10.

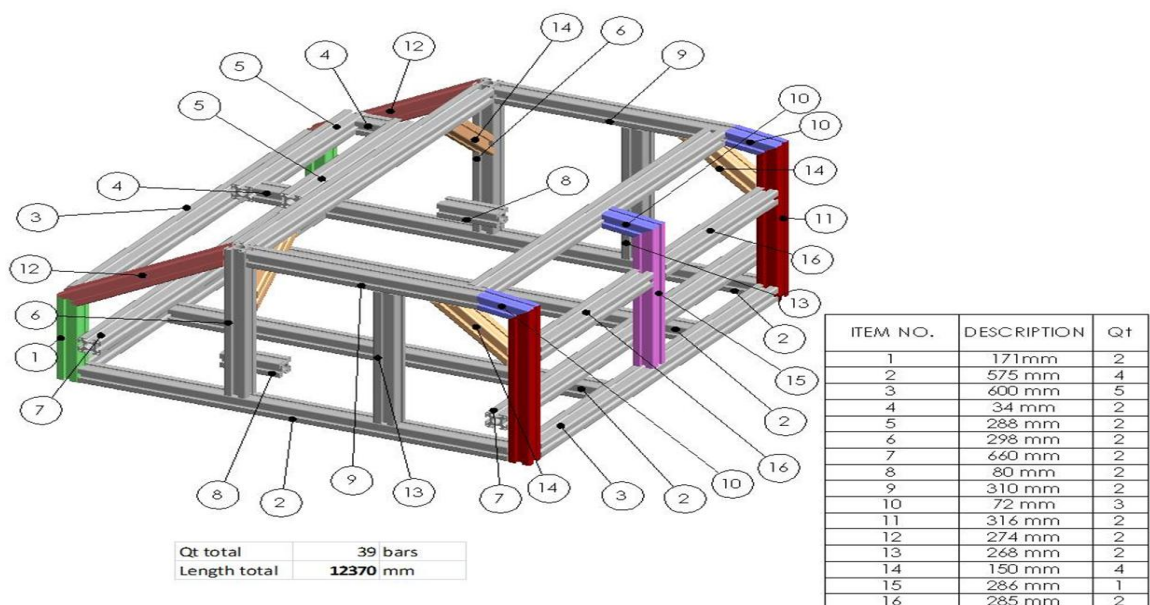


Figure 6.8: CAD drawings of main frame along with quantity and measurements as sent to AutoLine (MayTec's local suppliers) for profile sizing. The lengths shown in colour have different angles required to meet the criteria of ergonomics defined in the functional analysis [FP2, FC3]

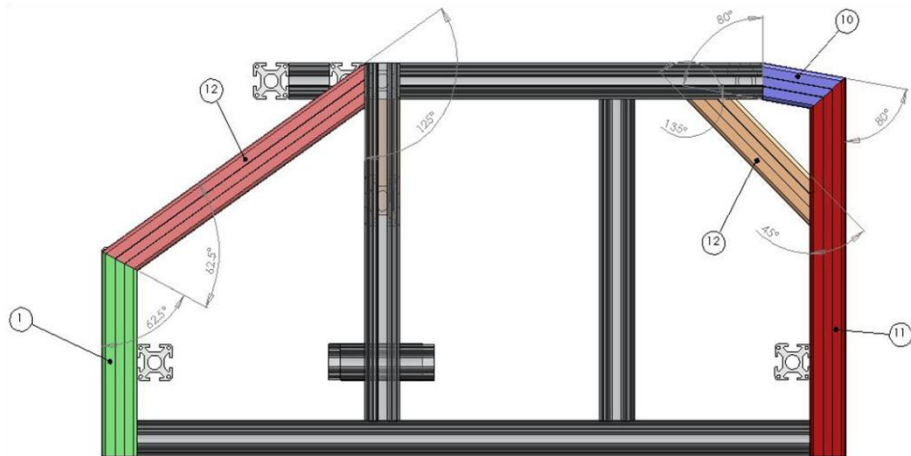


Figure 6.9: CAD drawings showing different ergonomic angles of various parts. Part 15 shown in Figure 6.8 had the same angle as part 11

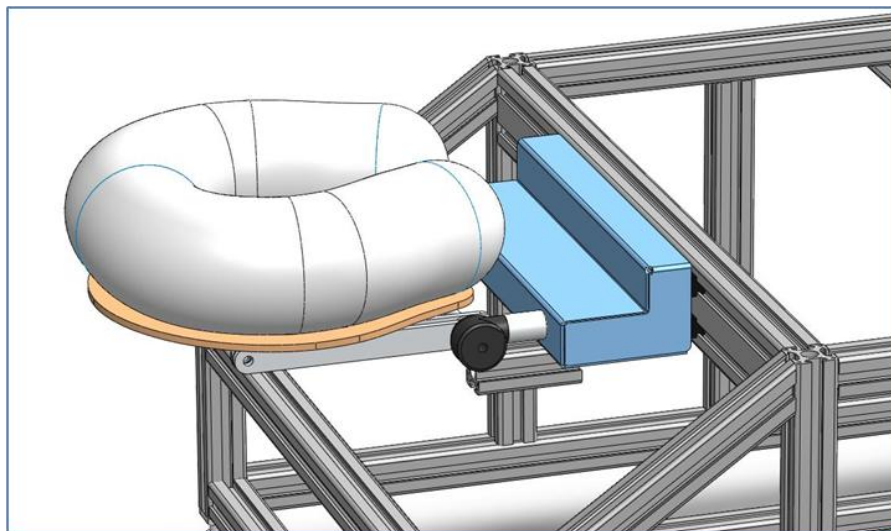


Figure 6.10: Installation of headrest on the main frame

Before the installation of the hardware of imaging technology could take place, an ergonomic trial of the main frame was conducted on 23 female subjects to obtain their views on degree of ease to undergo breast examination. Based on the observations of the ergonomic trials some modifications in the overall design were subsequently made. Ethics approval for this study was obtained from the University of Canterbury Human Ethics Committee under a Low-Risk application.

6.8.2 Ergonomic trial

The aim of the ergonomic trial was to test the level of comfort of the clinical DIET prototype with maximum women of different physical dimensions and ethnic backgrounds with a view to improve the overall ergonomics of the system. Tests were conducted to assess general level of comfort and degree of ease with which a female subject can undergo clinical trial on the new ergonomics design. Ethical approval of low risk research involving human participants for “Ergonomics of a clinical prototype Digital Imaging Elasto Tomography (DIET) breast cancer screening system” was obtained from the University of Canterbury Human Ethics Committee (HEC).



Figure 6.11: The setup used for ergonomic trials

The aim of the study was to identify improvements and carry out modifications in the ergonomic design. Thus, it was performed before finalizing the material for the top surface. The tests were conducted with gym foam on a wooden top and a triangular foam pillow was used for the leg extensions. A rectangular cut was made in the wooden top surface to provide space for the comfort of both breasts but only a single hole was made in foam, for the breast under examination. This trial setup is shown in Figure 6.11.

A total of 23 female subjects from different ethnic backgrounds were tested fully clothed. Their opinions were recorded with specific focus on level of comfort level and degree of ease to undergo a medical examination for a period of 15-20 minutes. Based on the views obtained and observations made, certain improvements in the overall design of the frame were made to make the system more user-friendly.

6.8.2.1 Ergonomic trial protocol

The study was conducted in a separate room to ensure privacy to the subjects and a female observer was present at all times. An information sheet was served and informed consent from each subject was obtained before start of the trial. During the trial, the subject had to lie down on the device (full clothes on) with one breast hanging pendant through the hole. Participation of each subject took approximately 10 minutes.

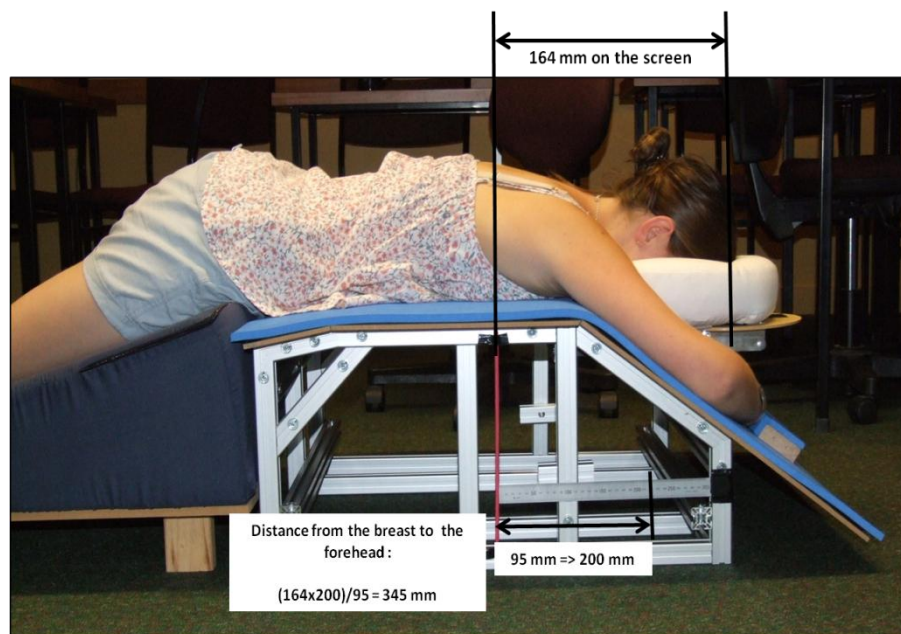


Figure 6.12: Ergonomic trial setup explaining how various anthropometric dimensions were recorded

Two pictures of each subject were taken to ascertain distance from the breast to forehead and distance from the breast to hip. A rod (red) was placed on the device to determine the position

of the breast and a ruler was placed to measure the dimensions of each subject as explained in Figure 6.12.

Views were obtained from the subjects just after lying on the device, after an interval of 3 minutes, and at the end of the trial. Subject height and ethnicity information were obtained. Code names were allotted to identify the subjects and the information obtained was only shared amongst the investigators. Any pictures to be used in research publication had the face of the subject blacked out. Two different headrests (one crescent shaped and one flat) were also tested. The following procedure was repeated for every subject:

- a. The subject lay down on the device with one breast approximately centred on the breast hole.
- b. Setting of the headrest was adjusted to match subject size
- c. Distance of breast-to-forehead and breast-to-hip were recorded
- d. A picture was taken from side, such that face of the subject was not visible
- e. Questions about level of comfort were asked
- f. After three minutes of lying still on the device, same questions were again asked
- g. The headrest was changed from crescent to flat and same questions were repeated.

The following questions about level of comfort were asked:

- a. What is the general level of comfort?
- b. What is the level of comfort in the neck area
- c. What is the level of comfort in back?
- d. What is the level of comfort in arms/shoulders?
- e. Which headrest was a better option?
- f. Any comments/suggestions.

6.8.2.2 Ergonomic trial results

23 female subjects from seven different ethnic backgrounds participated in the ergonomic trials for the DIET clinical prototype. A 66% level of comfort was reported by the participants soon after lying on the device, after 3 minutes remaining in position the comfort level was reported to be 64% and after 10 minutes remaining in position a 62.55% level of comfort was reported by

the cohort on average. In 57% of the cases the headrest needed to be adjusted. Overall, 61% of the participants felt more comfortable on the crescent headrest, while 39% felt more comfortable with flat pillow. Some discomfort in the neck area was reported by women with shorter heights.

Initial ergonomics research had shown that the distance between the breast and the top of the head for the 50th percentile was close to 46 cm. The cohort participating in the DIET ergonomics trial was from different ethnic backgrounds and the results showed the average distance between forehead and the breast was 32.6 cm, which lead us to believe that the distance of the headrest needed to be reduced. Figure 6.13 shows percentage of ethnic representation of DIET ergonomic cohort.

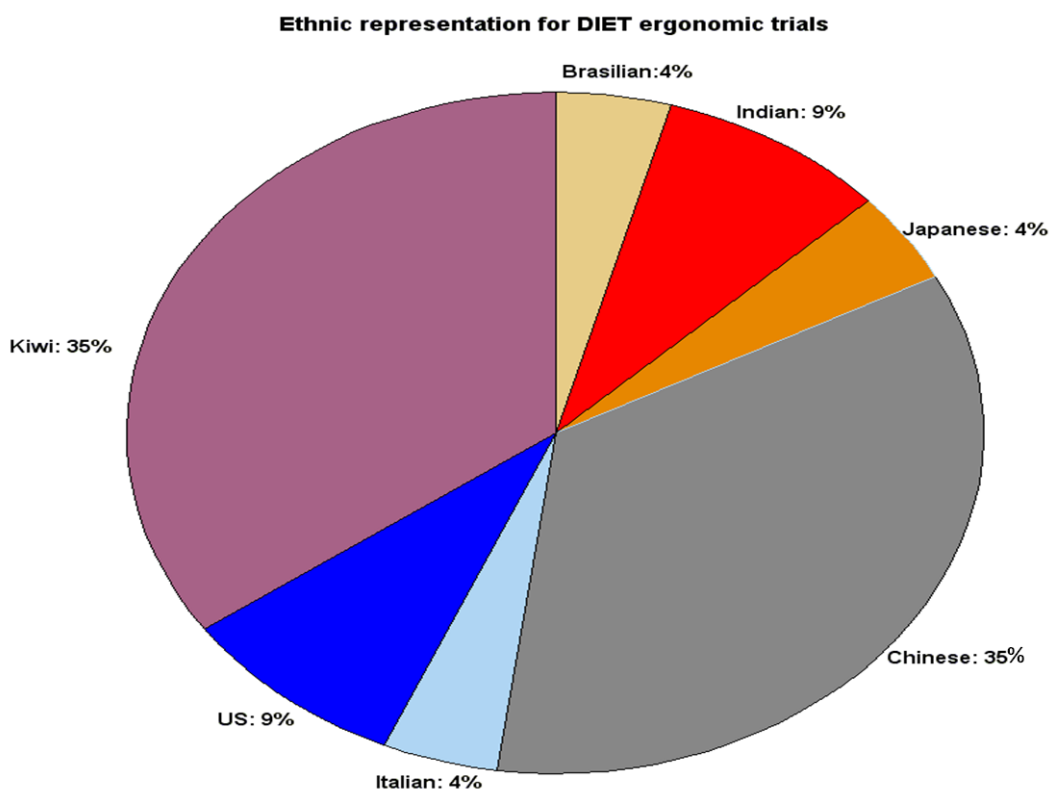


Figure 6.13: Ethnic representation of ergonomic trials for DIET clinical prototype

The average height of the subjects participating in DIET ergonomic trials was 162.2 cm and average measured breast-to-forehead distance was 32.6 cm. This dimension was kept close to

46 cm in initial DIET design conception and the headrest was positioned accordingly. It proved to be far less (32.2 cm) when a trial was conducted on a cohort of women with different ethnic backgrounds and due to this reason, headrest repositioning had to be done in a majority of cases. Equally, same small discomfort in the neck area was also reported by most of the participants, especially those with shorter heights. Figure 6.14 shows the mean, μ , and standard deviation, δ , values of different anthropometric dimensions measured during the trials from DIET application point of view.

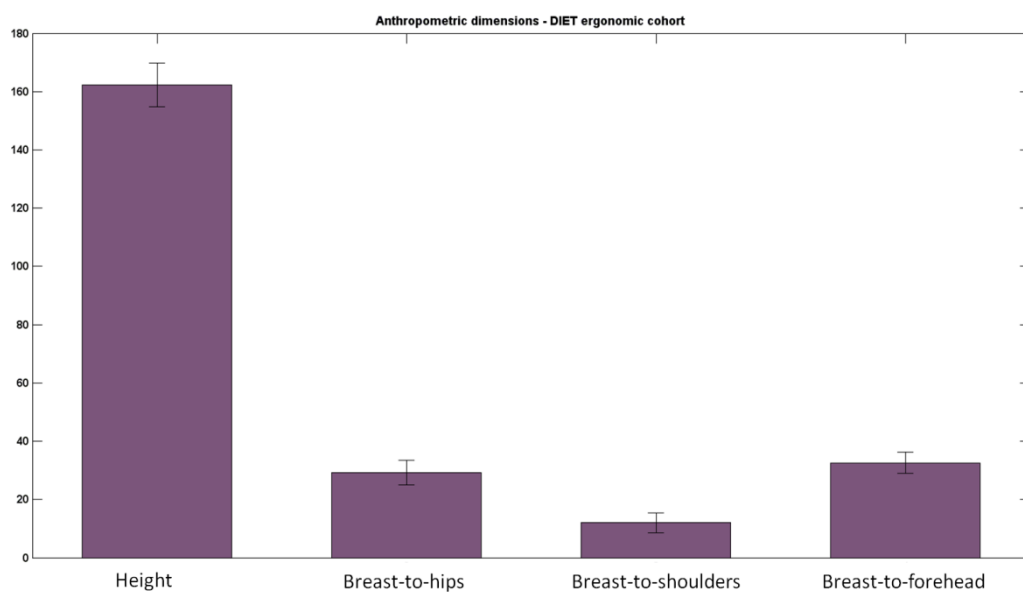


Figure 6.14: Mean, μ , and standard deviation, δ , values of different anthropometric dimensions of DIET ergonomic trial cohort

To ensure uniformity in reporting, the grading of comfort level was characterised into four different levels (1-4), depending upon the degree of ease to undergo the trials. Definitions for each level of comfort were defined:

- Level-1: Very comfortable
- Level-2: Comfortable
- Level-3: Not so comfortable
- Level-4: Painful

The mean values, μ , of level of comfort reported by the participants at three different stages of trial are presented in Table 6.1.

Table 6.1: Grading chart of reported comfort levels in various areas of body

	Soon after lying	After 3 minutes	End of the trial
General level of comfort	1.9	2.1	2.2
Level of comfort in the neck area	1.7	1.7	2.4
Level of comfort in the back	1.7	1.7	1.8
Level of comfort in shoulders/arms	1.6	1.7	1.8

The average overall level of comfort reported at the end of the trials was 62.5%. The general level of comfort reported was 2.2. This outcome was mainly due to the reason that the foam used for the top surface cushioning was not comfortable and most of the participants opined to replace it with better quality foam. The reported level of comfort in the neck area was 2.4, in between comfortable and not so comfortable, and in 57% of the cases the headrest had to be repositioned during the trial. This outcome was mainly due to the over extension of the headrest segment in the initial design and led to a subsequent reduction in final design.

6.9 Reduction of headrest segment

A stiffer profile (30 x 60, 4F, plain) was chosen for installing the headrest so that it could sustain the weight of the head. The sized pieces were assembled using the fastening elements provided by the manufacturer. Slider elements were used to ensure translation of headrest fixation, two holes were drilled and bronze bushings were inserted to allow smooth sliding and the headrest was fixed as shown in Figure 6.10.

During the ergonomic trials it was observed that the headrest segment was a bit too far away from the axis of breast (bust-point) and required a required a reduction of approximately 20 cm. The headrest segment was therefore replaced by a standard profile (30 x 30, 4F, plain) and a

reinforcement bar was added to the base of the headrest to ensure robustness, as shown in Figure 6.15.

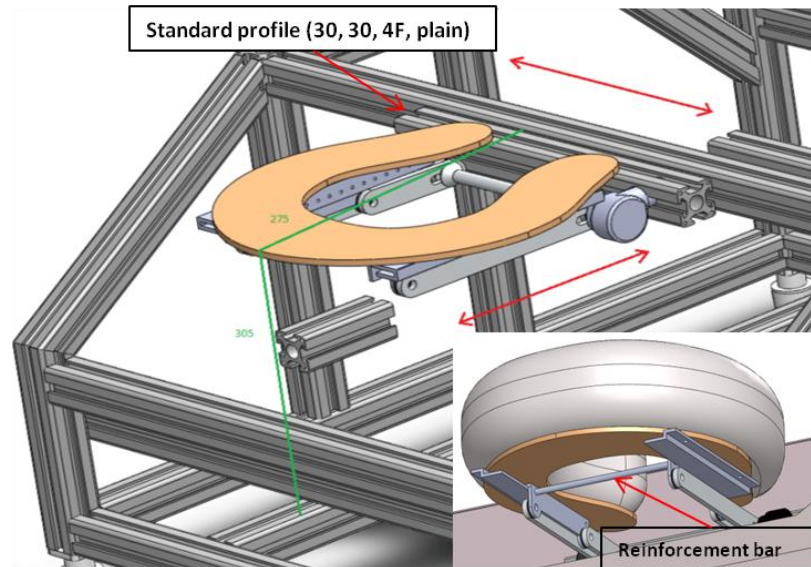


Figure 6.15: Modification to reduce the overall length of headrest segment carried out as a result of ergonomics trials

6.10 Hardware installation and integration

The frame dimensions provided an internal compartment of 700 (L) x 650 (W) x 300 (D) mm³ for hardware installation. Hardware details with mounting dimensions are given in Table 6.2. There was a diverse range of technical systems and programming languages that needed to be connected. The actuator, strobe lights, 2-axis positioning and z-axis positioning systems run through a standalone real-time controller from National Instruments NI cRIO 9012. There were three different C-series modules NI 9215 (Analogue Input (AI) module), NI 9263 (Analogue Output (AO) module) and NI 9403 (Digital Input/output (DIO) module) used for real-time control. Apart from these, other integral subsystems were required to be installed for DIET imaging.

The DIET frame internal compartment provided sufficient space to install the required equipment. However, polystyrene cut out models were prepared and different layouts were tested for space optimisation. Wiring rails were installed on four sides of outer periphery for

efficient provision of electrical connections to devices where required. Cameras and the strobe system were installed on the frame profile bar at 72° from one another, and a USB hub was placed centrally for easy access to all cameras.

Table 6.2: Mounting dimensions of DIET imaging hardware

Equipment	Quantity	Allied Accessories	Approx Mounting Dimensions (L x W x D) mm ³
Power Supplies (24 VDC, 15 Amp)	2	Wires	198 x 81 x 42
2-axis positioning system	1	2 Stepper Motors	400 x 400 x 70
Direction Control PCB	1	Wires	40 x 30 x 30
Actuator	1	Damping feet, Z-axis positioning system	200 x 200 x 200
NI cRIO 9012	1	NI 9215, NI 9263, NI 9403	170 x 90 x 130
Cameras + Strobe Lights	5	USB/Power cables	150 x 100 x 130
USB 2.0 Hub	1	USB/Power cables	130 x 40 x 70
Step Down PCBs	5	Wires	70 x 40 x 40
Analogue Servo Drive AMC 25A8	1	Wires & Cables	125 x 75 x 25
Chopper Drive Haydon DCS 4020	1	Wires & Cables	115 x 75 x 33
Wiring Rails	4	Wires & Cables	550 x 30 x 50
Connection Box	1	Wires	350 x 50 x 50

A 2-axis positioning system with two stepper motors MDrive 23 was screw tightened in the middle. The damping feet of the actuator were fixed on the inner frame of the 2-axis positioning system and the step-down PCBs were installed on the outer frame. A NI cRIO 9012 was placed towards lower right corner (feet side) and a junction box with terminal connections of equipment to NI sub-modules was provided next to cRIO. Finally, 2 motor drives were positioned in the top right corner and 2 power supplies were installed in the top left corner. Figure 6.16 shows the inside views of the DIET clinical prototype, explaining positioning of the various hardware components described in Table 6.2.

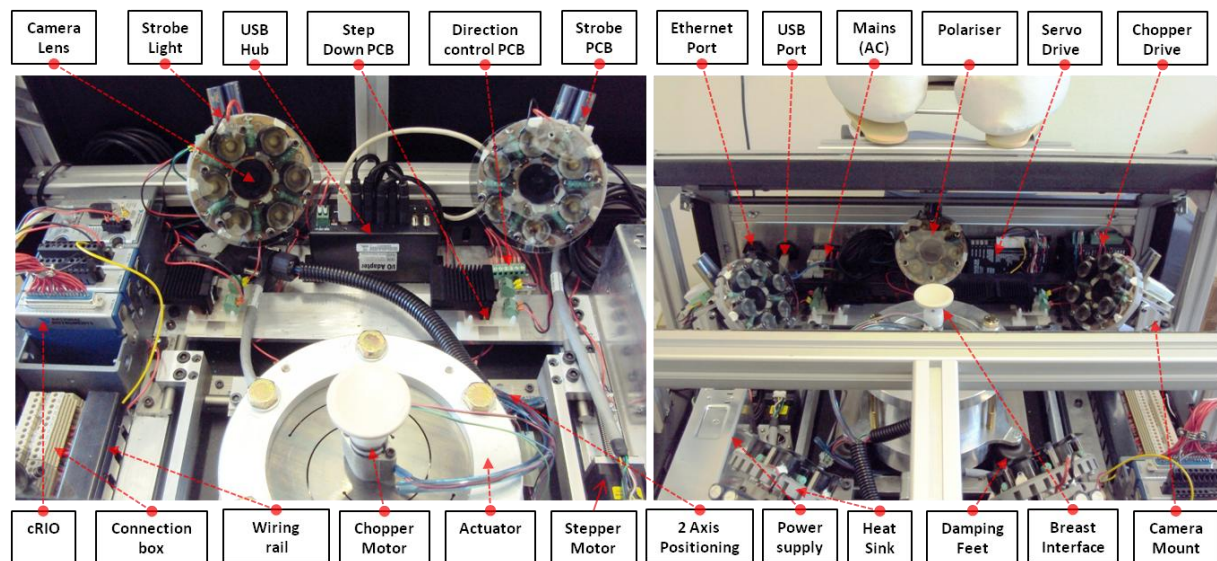


Figure 6.16: Internal view of DIET clinical prototype showing positioning of various hardware components required for optical imaging; Feet side (left), Head side (right)

6.11 Connections and cabling

For wiring, a rail mounted terminal block system was used and installed in the device (Glasbrenner, 2012). The main advantage of this wiring solution is its flexibility and modularity. This system makes it easy for subsequent changes and additions and makes it easy to connect two or more terminals with each other, since these connectors are provided with jumper channels. A total of 61 total terminals were required for entire wiring. The current draw requirement of each electronic component is given in Table 6.3.

Two power supplies were set at an input of 230 VAC, which can be changed to 115 VAC if required (Traco Power 24VDC, 15 A). One power supply was dedicated to provide power to 5 strobe lights, each requiring 2.5 A, and the other was specified for the rest of the electronic hardware. The connection between the actuator and terminal block system was implemented with a 15-pole D-Sub (D-Subminiature) plug connection, in view of eventual maintenance work.

Table 6.3: Peak current requirements of various hardware components used for DIET imaging

Hardware	Max Peak Current (A)
5 strobe lights (6 power LED board)	12.5
NI cR012 9012	0.5
Actuator (voice coils + LVDT position sensor)	3.5
USB 2.0 hub	2.5
2-axis positioning system (2 stepper motors)	1.2
Analogue Servo Drive AMC 25A8	0.3
Chopper Drive Haydon DCS 4020	1

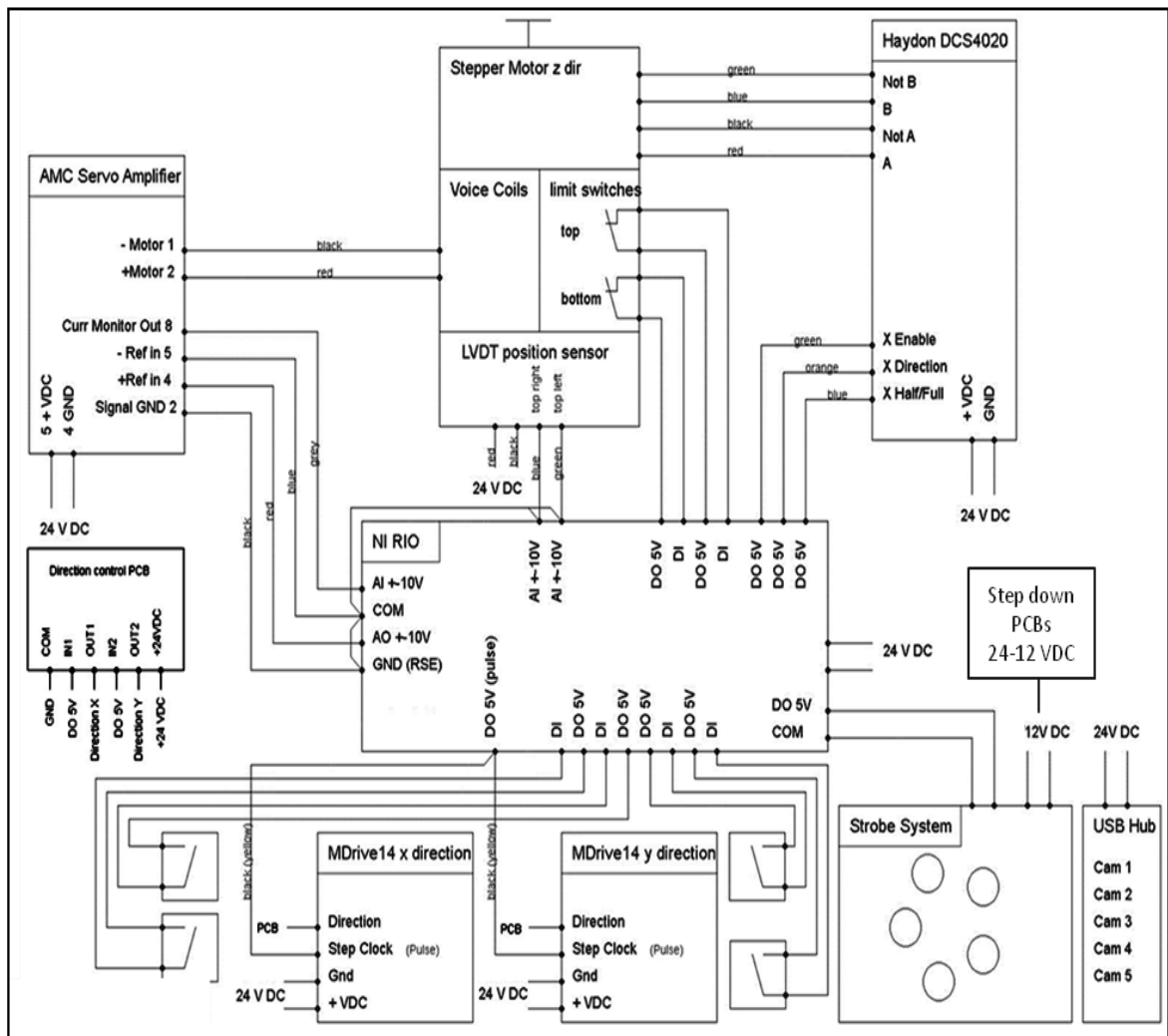


Figure 6.17: Principal wiring schematic of clinical DIET prototype

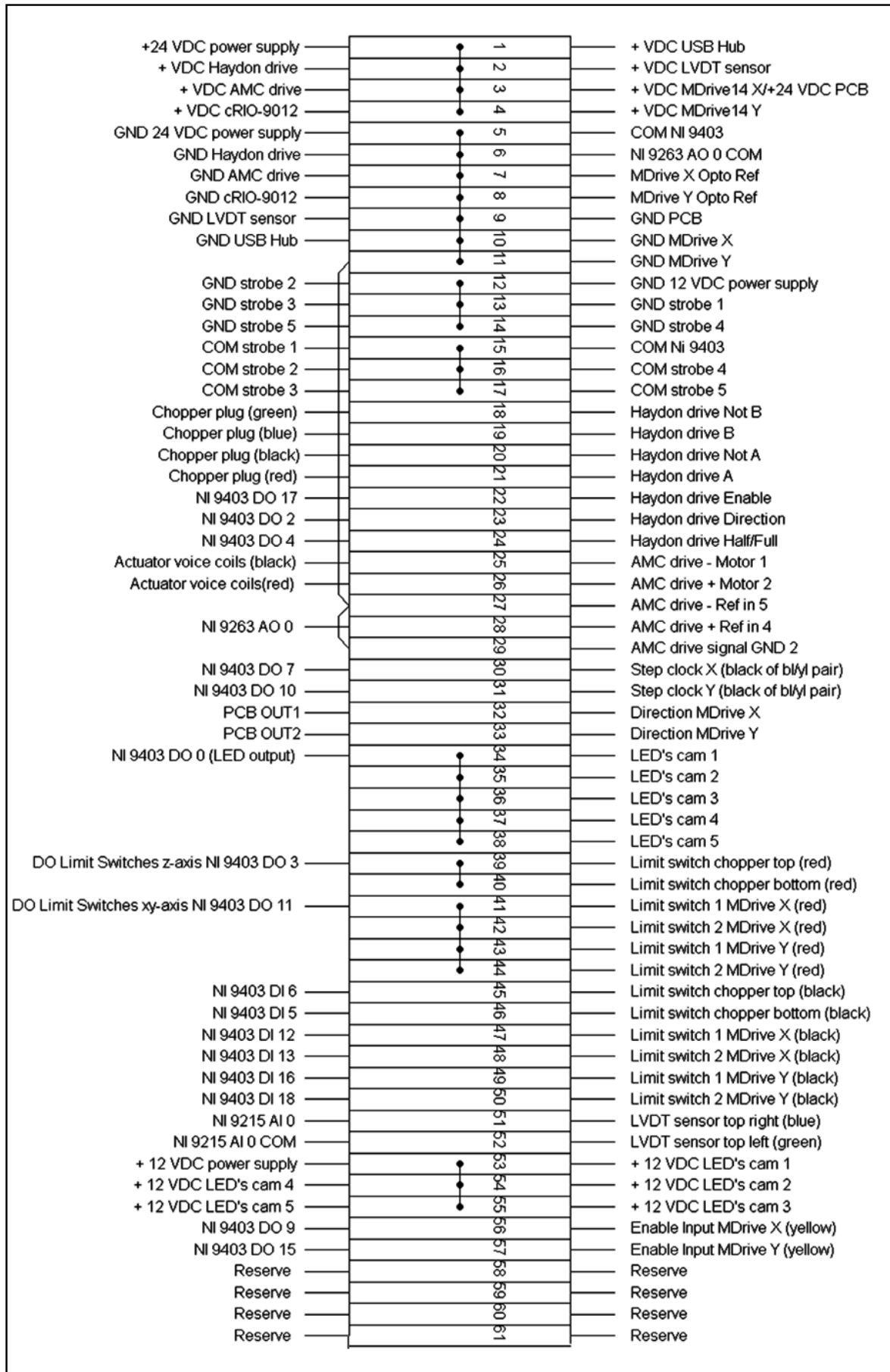


Figure 6.18: Terminal connection diagram of clinical DIET prototype

This way the actuator can be removed from the system without the necessity to disconnect each cable individually. Flexible 0.5 mm² hook up cables were used for whole wiring, except for supply voltage and output of power supplies, which was 2.5 mm² flexible. An overview of how the hardware parts were connected mutually and to the power supplies is given in Figure 6.17.

Figure 6.18 shows connection diagram of all the power provided to various components of the sub systems through a 61 pin connection box. Overall, 57 pins are connected and 4 pins are kept as reserve for future modifications.

6.12 External design

The objectives of the external skin was (1) to provide comfortable surface for the patient (2) allow sliding of headrest (3) obstruct light from outside to achieve a dark room environment. Acrylic was chosen for external skin due to its robustness and ease of bending and cutting. The first idea was to bend acrylic sheet to follow the contour of aluminium frame leaving a small slot for sliding of the headrest. However, measures had to be taken to block outside light, making the design more complicated. The final solution consisted of two sheets, one to cover the top surface and the other to cover the side surface and armrests. The top surface was provided with three holes, one for the breast under examination (breast hole) and two other holes for resting the inactive breast on the left and right side, spaced 200 mm apart from the breast hole. This distance between the two breasts was calculated by taking the average of the different percentiles of female anthropometric dimensions (NASA).

This design concept allowed easy sliding of the headrest and covered most areas from outside light. However, there were still two triangular slots that had to be covered by cutting the acrylic sheet. CAD drawings of the top surface, floor, armrest, leg-rest, front panel, rear panel, and two sides were made (LESUEUR Thibaut) and sent to a local plastic moulding firm 'BNT Plastics' for

precise cutting and moulding. Figure 6.19 shows the drawings of top surface, side surface and triangular shape plates meant to obstruct the outside light.

To cater for different breast sizes, three aluminium adapters having an internal diameter of 110mm, 130mm, and 150mm respectively were made to be fixed in the breast hole. For comfort of the inactive breast, two cavity inserts were made, as shown in Figure 6.20.

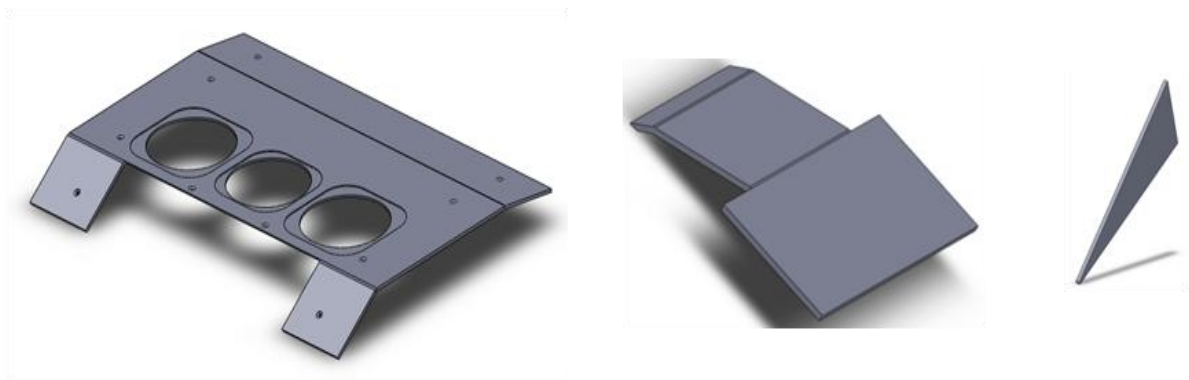


Figure 6.19: Top plate (left), armrest (centre) and triangular shape for light obstruction (right)

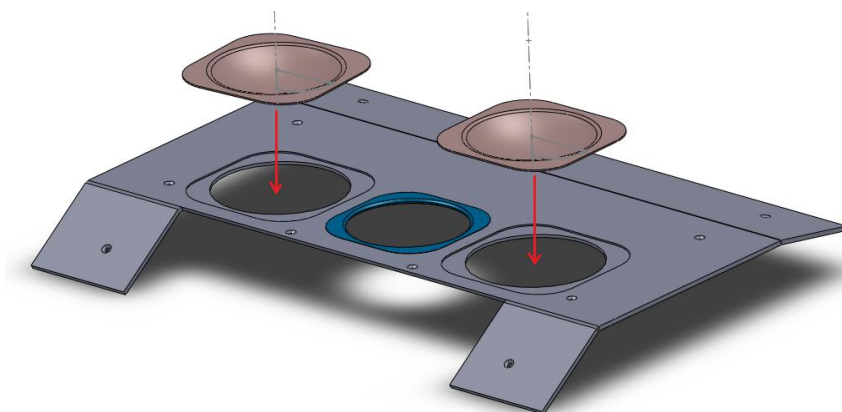


Figure 6.20: Showing breast adapter (in blue) and two cavity inserts applied for comfort of inactive breast

The arm-supports consist of two panels joined together with the help of two hinges that can be folded during transportation. An adjustable lid was applied to adjust the arm-support angle, which can vary depending upon the requirement. Similarly, two acrylic panels for the leg-

support were linked together through hinges and adjustable lids were applied to ensure folding and extension at the desired angle. This way, a pillow of any shape (triangular or square) can be used for resting the legs as shown in Figure 6.21.

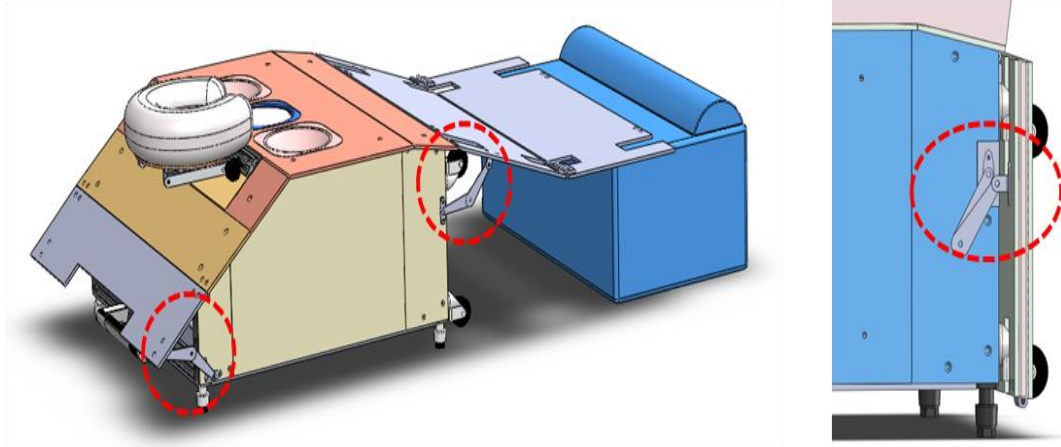


Figure 6.21: Showing positioning of arm and leg supports. These sheets can be extended at any desired angle during operation (left) and folded for transportation (right) through lockable hinges.

To ensure comfort for the patient, sheets of memory foam were cut to size and applied on the top surface, leg support panel and arm support panel. The damping feet of the actuator that provide vibration isolation to the cameras are made of silicone and cannot sustain actuator load during transportation. To avoid damage to these damping feet during transportation a 650 mm horizontal bar made from MayTec profile (30 x 30, 4F, plain) was built (Stalder, 2011).

This bar can be fixed to the actuator and side walls of the frame through 40mm M6 screws, as shown in Figure 6.22. The actuator has to be in “Home” position before fixing this transportation bar. Housing panels are then fixed to the side using the plug in screws and the system is ready for transportation. Figure 6.23 shows pictures of DIET clinical prototype in transportation mode (A), extended mode (B) and operational mode (C).

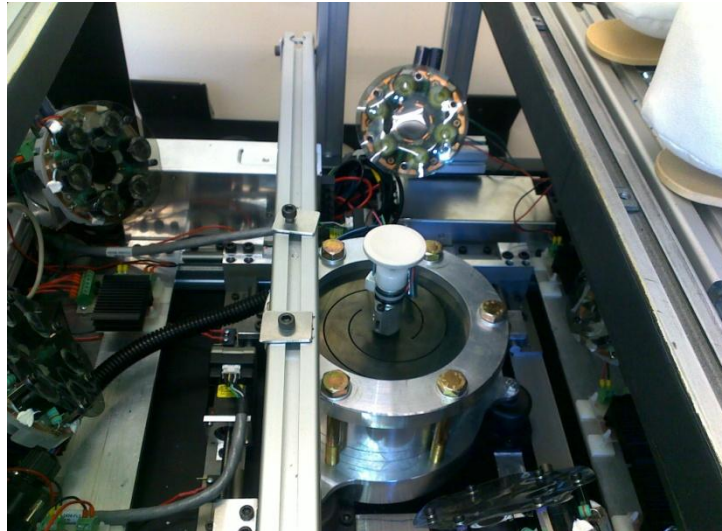


Figure 6.22: Transportation bar fixed to the actuator and sides of the frame to avoid damage to actuator's damping feet. The actuator has to be in "Home" position before fixing this bar

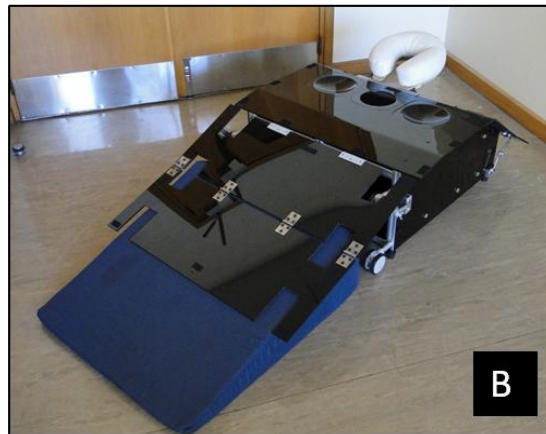
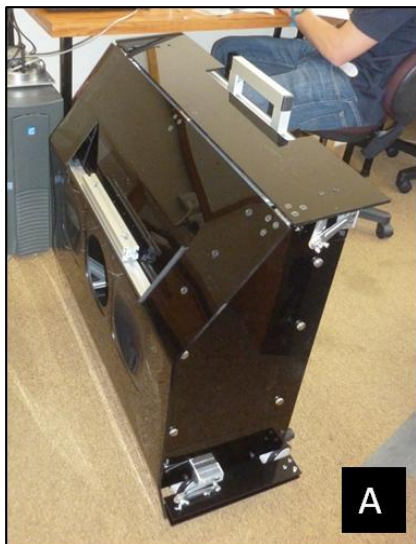


Figure 6.23: DIET clinical prototype (A) transportation mode, (B) extended mode and (C) operational mode

6.13 Summary

The clinical DIET prototype was ergonomically designed to provide comfort for patients during imaging and to ensure better mobility for multi-site trials. The physical dimensions of the prototype are (700 L x 650 W x 300 H) mm³ in transportation mode and the device weighs 45Kgs. A comparatively heavier MAYTEC frame was chosen for the prototype with a view to achieve the flexibility in positioning of various DIET subsystems. The frame material is flexible and promises flexibility for future add-ons and modifications. Now, once the size specifications and the installations/positioning of various subsystems have been finalized a further reduction in the overall weight can be achieved by choosing a lighter material for the frame.

Before finalizing the design, a low risk ethical approval was obtained and the ergonomic trial was conducted on 23 female subjects. Based on their observations certain changes were implemented. Installation/integration of the hardware required for DIET imaging was successfully carried out in the specified space and the system is operational. The system is covered by acrylic housing panels from all sides to protect the imaging environment from outside light.

DIET clinical prototype ensures comfort to the subject under examination. In addition to the main breast hole, it carries two cavities to hold the inactive breast in a comfortable position. It contains a head-rest, arm-support and leg-support to ensure ease to the patient during examination. The top surface was ergonomically designed keeping the anthropomorphic dimensions of women of 50th percentile in view. The memory foam was applied on the top surface to ensure comfort to sternum area. The system is wheeled to ensure easy portability and has height adjustable feet to ensure levelled positioning during examination.

Chapter 7

7 IMAGING SOFTWARE AND GUI

7.1 Background

A DIET imaging session is executed at a sweep of different frequencies (10-100Hz) depending on the fundamental frequencies of the breast and the post-processing software algorithms used for diagnostics. At each frequency, ten optical images are captured by each camera. Before the examination can start, the cameras system needs to be initialized and calibrated. A calibration cube is placed above the center of the actuator. This step is necessary to reconstruct the motion in 3D (Brown, 2008a). The imaging Process consists of the following basic steps:

- a. *Initializing the cameras:* Before the adjustments and the actual imaging can start the cameras need to be initialized.
- b. *Placing the calibration cube:* This is necessary to ensure the right focus of each camera and to identify their position. By comparing the images with the known patterns and size of the cube it is possible to reconstruct a 3D-model of the breast.
- c. *Capturing and saving Calibration Images:* Each camera captures one image of the calibration cube. The calibration images are saved in BMP format on the external computer in a particular folder including information about patient's name, date and time.
- d. *Actuator positioning:* After the calibration, the woman lies on the device with one breast hanging through the hole and the actuator is positioned according to the breast's size dimensions. The actuator interface needs to be adjusted in such a way, that it presses against the bust-point. This happens by moving the whole actuator on 2-axis positioning

system, on which it is mounted. A small stepper motor is used to move the breast interface in upward direction.

- e. Capturing and saving motion images (for 10 phases): Once the adjustments are done the actuator begins to oscillate vertically at chosen values for frequency and amplitude, and the strobe lights start flashing with the same frequency at the same point of motion during one exposure. This procedure continues until every camera has captured ten images at that particular frequency.

Once the imaging of a particular subject is complete, the folders containing calibration and motion image files are fed to the surface-motion reconstruction software. A 3D surface is reconstructed by measuring the motion using optical flow implementation. The output of this software is in the form of *MatLab (.m)* files which are further fed to the diagnostic software, for detection of tumour within the healthy breast tissue. The presence, location and approximate size of the tumour is identified using two different diagnostic software. Specifically, a 'Surface Based Detection' and 'Separate Modal Analysis' method.

7.2 Previous work and scope of current research

Previously, imaging software 'dSweep' to control cameras, actuator and strobe lights had been written in C++, using a Linux platform. The imaging parameters including amplitude, number of frequencies, and phases to be captured were fed to the software through a configuration file. This software was written to control previous versions of cameras (Canon G9), previous versions of strobe lights (comprising 127 low power LEDs), and a previous actuator that had no positioning control (Feng, 2010a). The user interaction was done through MS-DOS command line and was difficult to comprehend by a non-skilled operator. With new cameras (IDS UI 225x SE-C), newly developed strobe lights (comprising 6 power LED), and a 3-voice coil actuator with 3-axis positioning system, a new imaging/control software system had to be developed. The cameras

were initially programmed in C++ using MS Visual Studio-2010. The strobe lights, actuator and 3-axis positioning systems were to be controlled by a real-time controller, FPGA (cRIO NI 9012). Software for controlling this hardware was written using LAbVIEW-8.6 Virtual Instrument (VI).

Moreover, one of the main objectives of DIET breast screening technology is that a person with no clinical imaging skills should be able to run the system. Due to the complicated user interface and skills required for the previous imaging software, an engineer had to be present all times to run the imaging software. During the limited in vivo trials, it was felt that a Windows based Graphical User Interface (GUI) was required to make the system more user friendly.

Windows based GUI was ultimately developed in C# using MS Visual studio-2010. Accordingly, cameras were reprogrammed in C#. A real time video from two cameras installed at 72° , was made available to the operator to facilitate actuator's positioning according to various breast sizes, without manual intervention.

7.3 Integrated imaging control software

One of the most important objectives in the development of the clinical DIET prototype, in addition to its better performance in terms of hardware and portability, was an improvement in imaging code in terms of imaging time and its user friendly interface. The main steps involved in the imaging procedure are the initialization and calibration of cameras, positioning of the actuator, and capturing and saving of images at 10 phases by each camera at each actuation frequency. Figure 7.1 shows a flow diagram of the steps involved during DIET imaging procedure.

The main components of this integrated imaging software are the image capture code, hardware and software interaction, real-time video during imaging, and Graphical User Interface (GUI). An integrated client-server environment was created to control an array of 5 industrial cameras,

high power strobe flash system, 3-voice coil actuation unit with LVDT position sensor, and actuator positioning system in 3-axis (Glasbrenner, 2012).

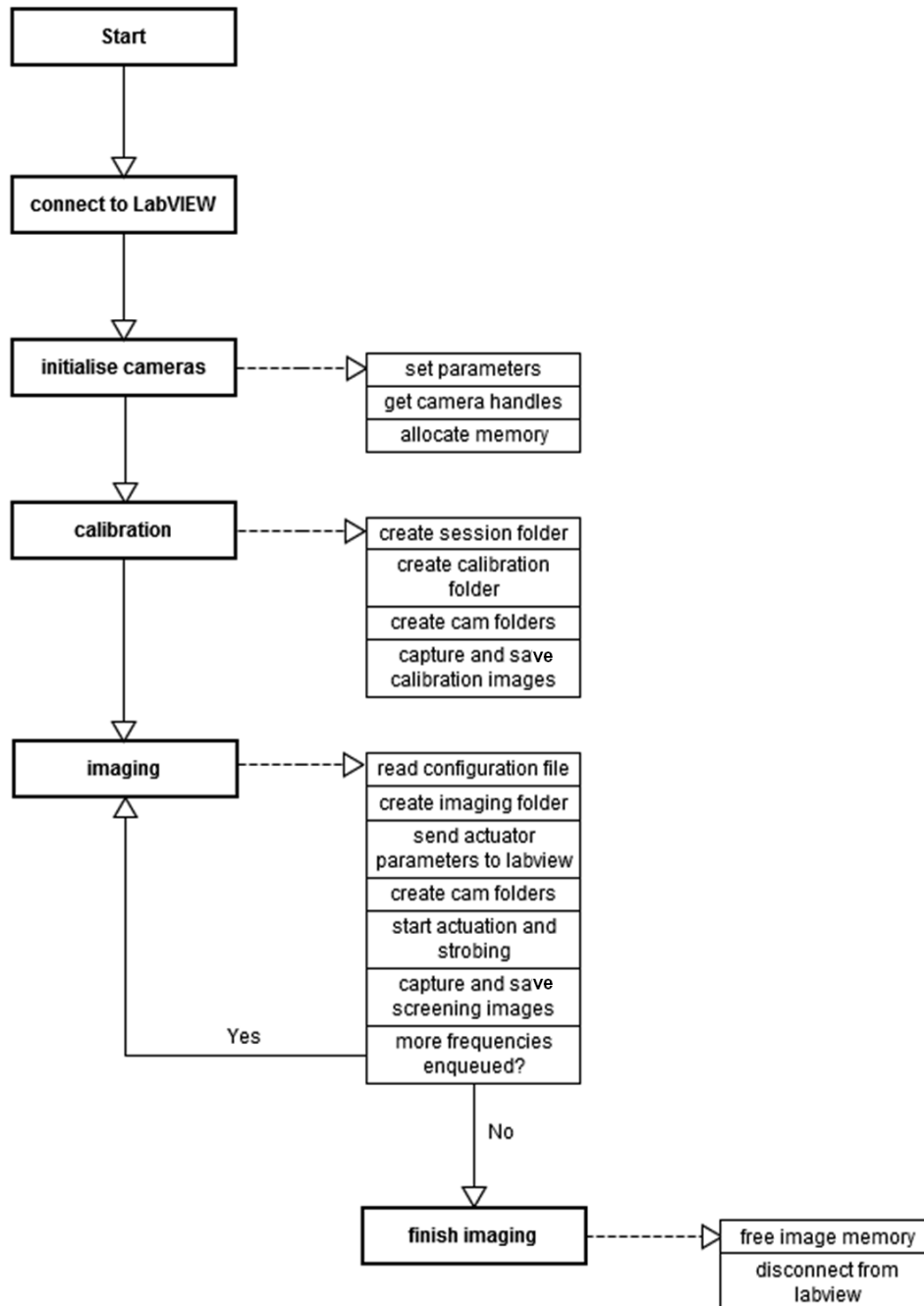


Figure 7.1: Flow diagram of DIET imaging procedure

7.3.1 Image capturing code

The IDS Imaging software was initially written in C++ using MS Visual Studio-2010 and subsequently converted to C# for better adaptation to a Graphical User Interface (GUI). The image capture software is capable of taking run-time input parameters for initialising an array of 5 industrial cameras (UI 225x SE-C) and synchronises the image capture with flashes from strobe lights to freeze motion.

Initially, image capture and saving was done sequentially, which was not an efficient solution in terms of timing. Thus, a thread safe *uEYE* API was implemented to introduce multi-threading. Image capture and saving is now done by a dedicated thread, thus reducing the overall image capture time for one frequency from 252 s (stage-1 prototype) to 28.4 s (DIET clinical prototype). This time includes camera initialisation, image capture and saving of calibration images and 10 motion images by each camera at one particular frequency.

7.3.2 Hardware and software interaction

The LabVIEW code controls the actuator, the strobe lights and the xyz-positioning system and runs as a standalone controller on the National Instruments cRIO NI-9012. This configuration allows it to run the device with any machine without the requirement of having LabVIEW installed. Figure 7.2 shows key software components of the DIET system.

The imaging code runs on this external machine and communicates with the LabVIEW controller via TCP/IP. The imaging code consists of the imaging server, which controls the IDS cameras, and the imaging client. The latter handles the settings, such as the actuation frequency, phase, the amplitude duty cycle for the strobe lights, and user defined camera parameters. There are three different C-Series modules by National Instruments to control these settings: (1) NI-9215 analogue input (AI) module, (2) NI-9263 analogue output module (AO) and (3) NI-9403 digital

input and output (DIO) module. The details of the analogue and digital I/O signals required to control various hardware components are defined in the following sections.

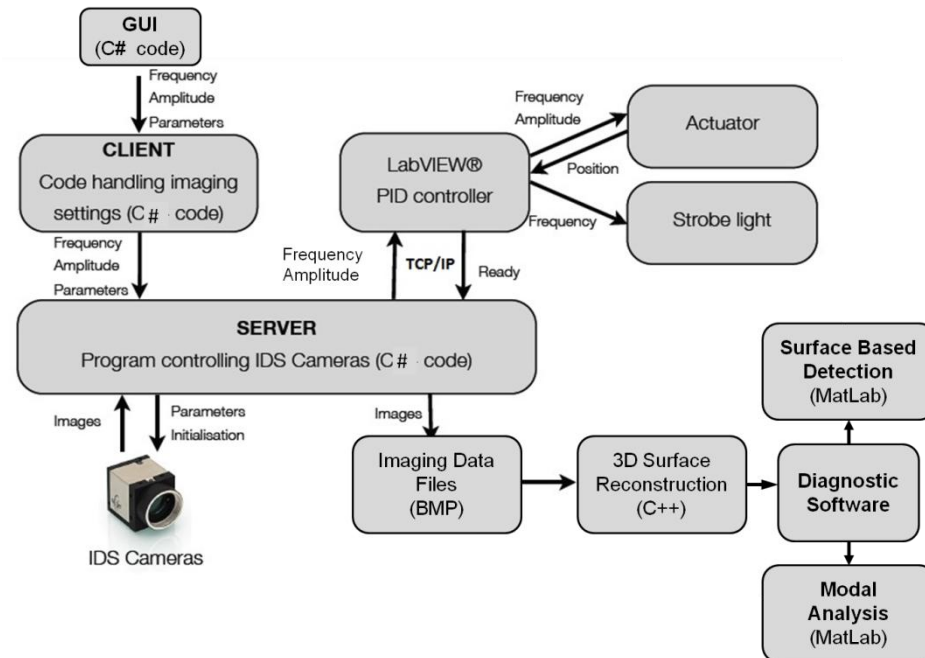


Figure 7.2: Block diagram of key hardware and software components of clinical DIET system

7.3.2.1 Analogue Signals

Vertical position (upwards direction) control of the actuator is enabled using a Linear Variable Differential Transformer (LVDT) position sensor, which is built into the actuator. It consists of three coils, one primary coil, two secondary coils and one magnetic core in between. The secondary coils are connected in series in opposite phase so that the tensions cancel each other. The resulting voltage is zero when the two coils are symmetrical, which occurs when the core is in the centre. As the core moves away from the centre this symmetry is disturbed, and, as a result, an analogue output voltage is generated. The phase of this analogue voltage signal, with respect to the excitation, specifies the direction and the value specifies the size of the asymmetry. This output voltage signal is measured by the NI-9215 analogue input (AI) module.

The actual amplitude of the actuator is displayed together with the set point variable on the GUI of the LabVIEW VI (virtual instrument) [Fig. 7.3]. The amplitude value from the binary signal of the NI-9215 is calculated and converted into this amplitude value in mm. This value is required for the proportional–integral–derivative (PID) feedback controller for the actuator, which is implemented in a separate VI.

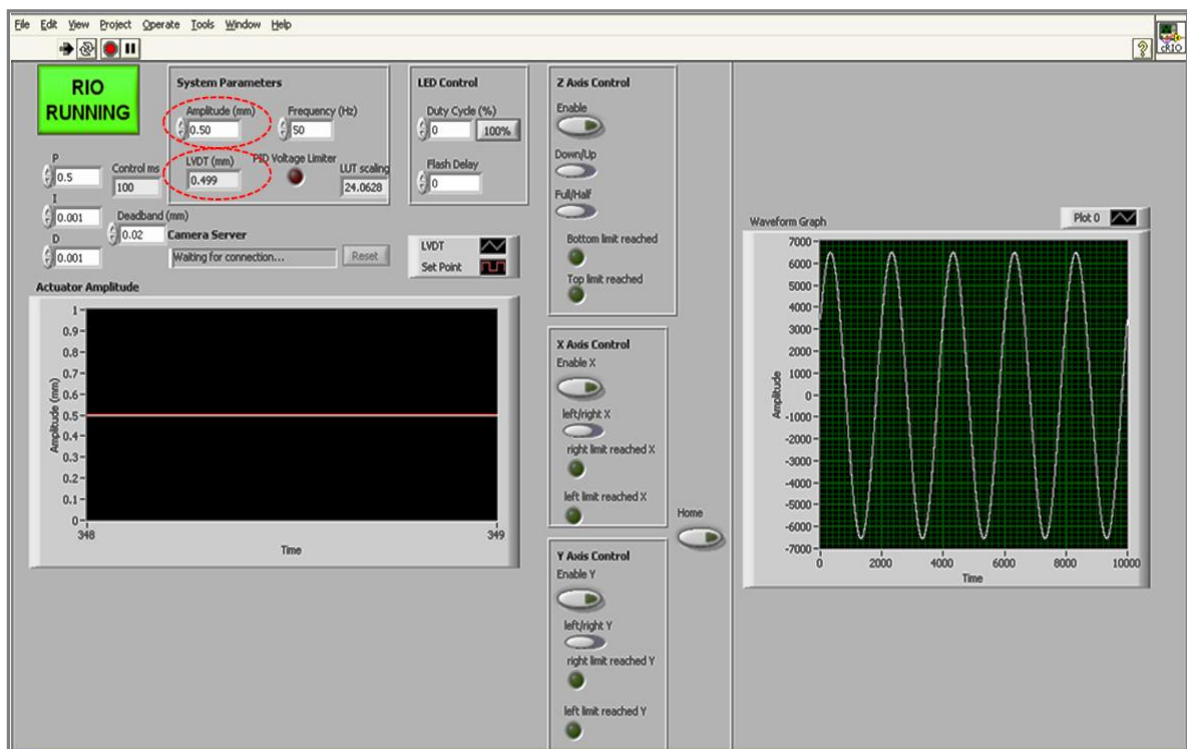


Figure 7.3: Control panel of the LabVIEW VI showing desired value of actuation amplitude (set point =0.5mm) and the measured value from LVDT (process variable =0.499mm)

This PID controller calculates an error value as the difference between the measured value and the desired set point to minimise any deviation of the actuator from the reference input, as shown in Figure 7.4.

The second analogue signal is an output signal from the NI-9263 (AO) module to supply the differential reference input for the analogue AMC servo drive, which powers the 3-voice coils of actuator and drives them at the set particular frequency.

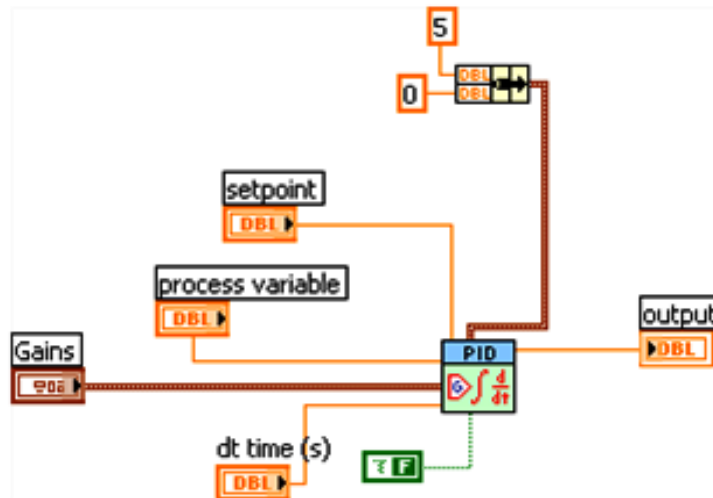


Figure 7.4: Block diagram of the PID controller LabVIEW VI

7.3.2.2 Digital Signals

The main advantage of using digital control signals is comparatively lesser interference and noise than analogue signals. Moreover, they are easy to manipulate and the programming is simple. All digital signals used in the clinical DIET system are digital 5V Transistor-Transistor Logic (TTL). These signals are handled by the NI-9403, which is a 32-Channel digital input-output module (DIO). Altogether, there are 18 digital signals, split into 6 input and 12 output signals.

Three main hardware parts are controlled by these digital signals:

- Haydon chopper drive (Z-axis control including limit switches)
- Strobe light system
- 2 MDrive-23 micro-stepper motors (XY-axis control including limit switches)

32-Channel digital input-output module (DIO) NI-9403 is defined as Module 3 (mod3) in the DIET Control LabVIEW project (*diet_control.lvproj*). The details of the input and outout digital signals are shown in Table 7.1. For the wiring diagram and connections refer to Figures 6.17 and 6.18.

Table 7.1: List of digital control signals vis-a-vis pin assignment on DIO module NI-9304 (mod3)

Signal Specifications	NI-9304 Pin Number
<u>Digital Input Signals (5 V TTL)</u>	
Limit switch (LS) Input signal for Z-axis position control (Bottom)	DIO5
Limit switch (LS) Input signal for Z-axis position control (Top)	DIO6
Limit switch (LS) Input signal for X-axis position control (Left)	DIO12
Limit switch (LS) Input signal for X-axis position control (Right)	DIO13
Limit switch (LS) Input signal for Y-axis position control (Left)	DIO16
Limit switch (LS) Input signal for Y-axis position control (Right)	DIO18
<u>Digital Output Signals (5 V TTL)</u>	
LED Output control signal	DIO0
Direction control Z-axis motion	DIO2
Pulse signal for Z-axis positioning (Enable)	DIO17
Limit switch (LS) Output control Z-axis positioning	DIO3
Speed control Z-axis (Full/Half)	DIO4
Pulse signal for X-axis position control	DIO7
Direction X-axis position control	DIO8
Disable MDrive-X (X-axis motion)	DIO9
Limit switch (LS) Output control XY-positioning	DIO11
Pulse signal for Y-axis position control	DIO10
Direction Y-axis position control	DIO14
Disable MDrive-Y (Y-axis motion)	DIO15

7.3.3 Socket communication for FPGA control through TCP/IP

The control of the cRIO NI-9012 FPGA controller was implemented through a graphical user interface (GUI) by sending particular messages for various control commands (string, numerical sequence or both) each assigned to a particular case-structure in LabVIEW. The cRIO waits for the socket client to connect, once the connection is established it keeps waiting for messages. TCP/IP control runs in a while loop, which executes sub-case-structures, until the conditional terminal receives a false Boolean value. Figure 7.5, shows the block diagram of this TCP/IP communications loop, in which the message “Amp” is displayed in the sub-case-structure.

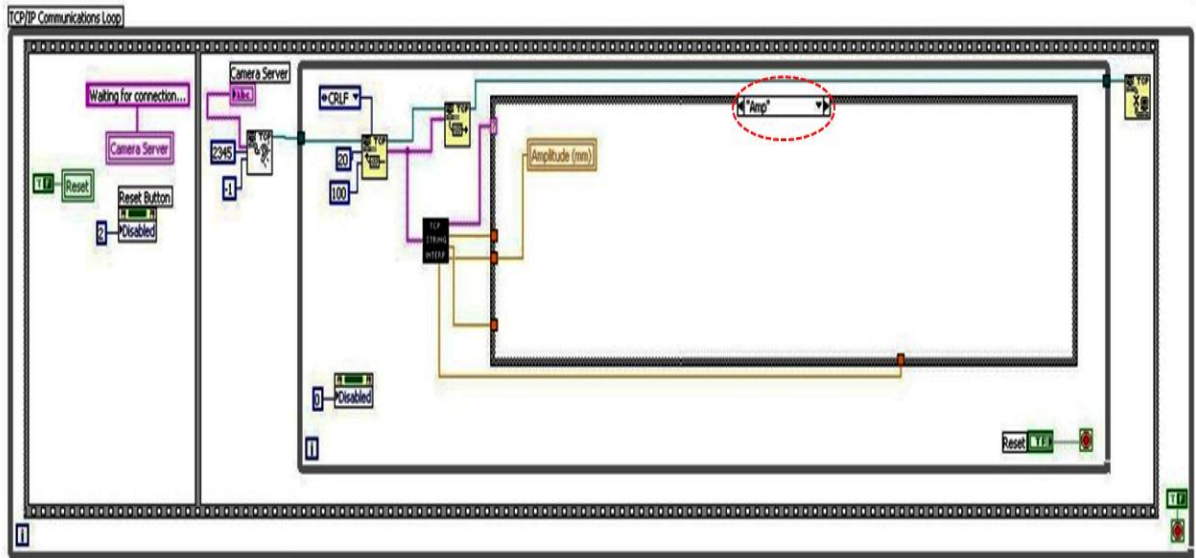


Figure 7.5: Block diagram of TCP/IP communication loop showing flat sequence structure and messaging loop. Red dotted circle shows the sub-case-structure for amplitude settings.

In the clinical DIET system control, the server IP address is '10.0.0.2' and the server port is configured at '2345'. Within the while loop shown in Figure 7.5, a flat sequence structure with two frames was implemented. These frames are executed from left to right. The socket server waits for the client to connect and displays the IP address on the front panel of the VI. The remote address is the IP address of the external machine associated with the TCP-connection. It is possible to disconnect the client from the server by pressing the reset button. The property note of this control (reset button) indicates if the control can be operated (0-enabled, 1-disabled and 2-disabled and greyed out). The TCP Listen VI shown in Figure 7.6 creates a listener and waits for an accepted connection at a specified port (2345).

This VI returns a connection ID (10.0.0.2) that goes to the port (2345). After that 'TCP wait-to-listen' function is again called to wait for a new connection. Setting the value of the timeout input to -1, ensures that the TCP Listen VI waits forever until a network connection is established, instead of waiting for a defined period of time.

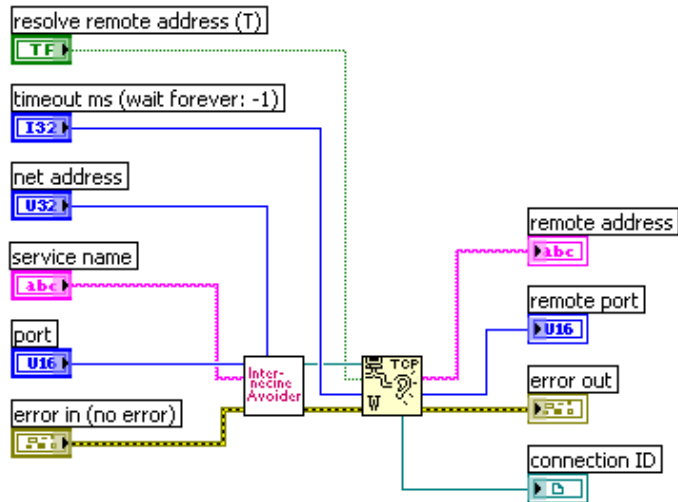


Figure 7.6: Block diagram of the TCP listen VI

Within the 'TCP Listen VI', a while loop is executed that interprets messages. Once the TCP connection is established, the TCP Read function reads messages from the network in the form of number of bytes (long [32-bit integer] from the client. The TCP write function sends 'received message' back to the client for feedback. The feedback is normally required when one of the limit switches is triggered.

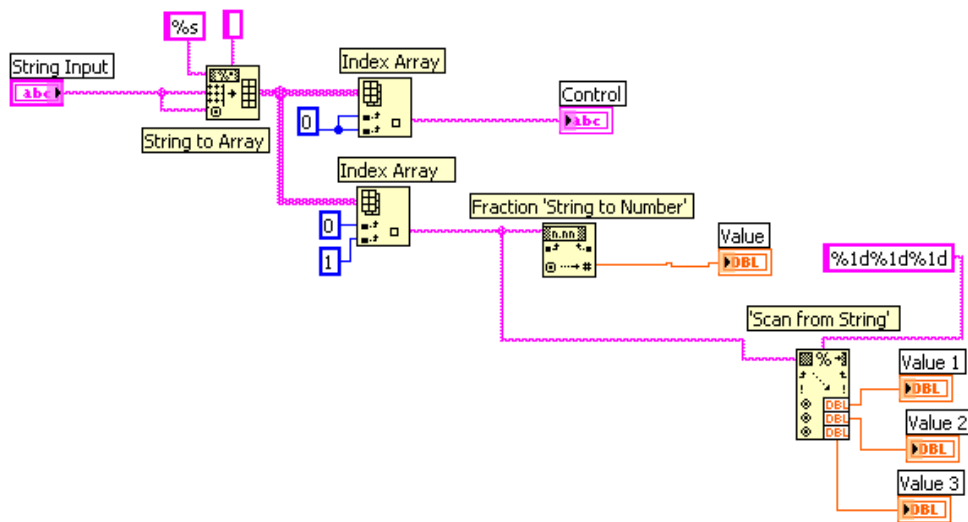


Figure 7.7: Block diagram of 'TCP String Interpretation' sub-VI. This VI splits up the messages into characters and numbers

The actual interpretation of the messages happens in the sub-VI called 'TCP String Interpretations'. It has one string input for the messages and five output values (one character and four numeric outputs) to control the corresponding code segments as shown in Figure 7.7. The input string contains either only 'character string' or 'character string followed by a single space' and after that there is a numerical value. Each message is assigned a particular case in the case-structures.

7.3.4 Message interpretation

The TCP String Interpretation sub-VI splits up the input string into an 'identifier string' and a 'number' by converting the input string into an array. With two 'Index Array' functions shown in Figure 7.7, the numbers are separated from the string. The first function returns the characters (main command) and second function returns the string of numbers. The latter is connected to a 'String to Number' function, which interprets the characters 0 through 9 and the decimal point in the string input as a 'double' and returns it.

Table 7.2: TCP/IP messages and their interpretation

Messages	Interpretation
'Amp 0.5' (range: 0.1-0.9 with an increment of 0.1)	Set actuation amplitude to 0.5 mm
'Freq 45' (range: 10-100 with an increment of 1)	Set actuation frequency to 45 Hz
'Light 1.5 (range 0.5-100 with an increment of 0.5)	Set strobe light duty cycle to 1.5%
'LightFull'	Set strobe light duty cycle to 100%
'Phase 0.2' (range 0.1-0.9 with an increment of 0.1)	Set the flash delay to 0.2
'Pos'	Reposition actuator in XYX-direction
'Home'	Move the actuator to a predefined position (required for transportation mode)
'Reset'	Set the reset process true i.e. disconnect the client from server

For example, when 'Amp 0.5' message is received from the GUI, meaning to set the actuator amplitude to 0.5 mm, the message is split into the identifier string 'Amp' and the numerical order "0.5". The identifier string is directly returned from the 'TCP String Interpretation sub-VI' to the identically named case for execution. Also connected to this case is the numeric output value from the sub-VI, which sets set point amplitude to 0.5. Table 7.2 shows list of TCP/IP messages and their interpretation.

7.3.4.1 Actuator positioning messages

The XYZ-positioning messages consist of identifier string 'Pos' followed by a single space and three numbers. To handle these messages the second 'Index Array' function returns the string including the numbers to a 'Scan from String' function. This function scans the input string and converts it into individual numbers. Each number is returned as an integer on one output of the sub-VI, namely Value-1, Value-2 and Value-3, as shown in Figure 7.7.

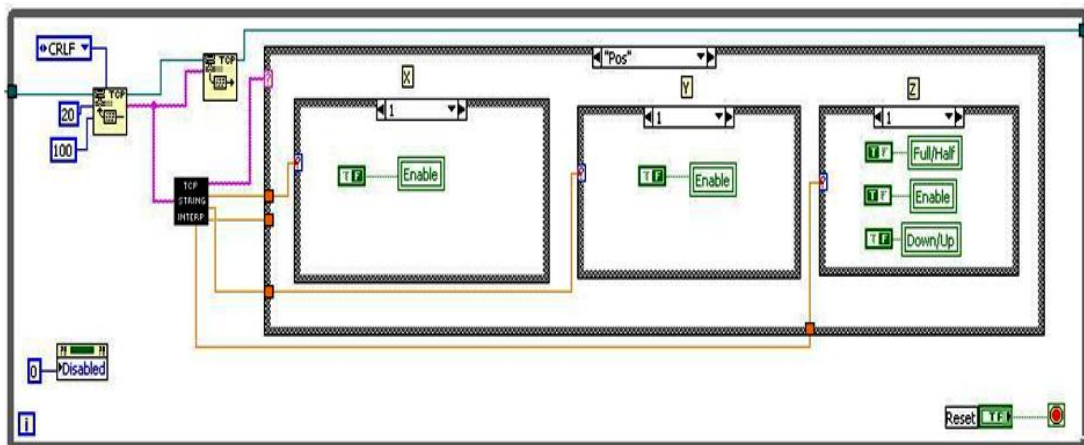


Figure 7.8: Block Diagram of the case-structure 'Pos' and three corresponding sub-case-structures for each X, Y and Z direction

As shown in Figure 7.8, the case-structure "Pos" consists of three sub-case-structures, one each for X-axis, Y-axis and Z-axis. Each value output belongs to one direction, such that value-1 is

assigned to X-axis positioning, value-2 is assigned to Y-axis positioning and value-3 is assigned to Z-axis positioning.

Table 7.3: Number of cases for each sub-case structure for XYZ-axis positioning

Case Structures	Cases
X-axis sub-case structure	0,1,2
Y-axis sub-case structure	0,1,2
Z-axis sub-case structure	0,1,2,3,4

Table 7.3 shows cases contained in each of these three sub-case-structures while Table 7.4 contains meanings of different commands specified for each axis.

Table 7.4: Depiction of each integer value for respective positioning system

Case	0	1	2	3	4
X-axis	Move left	Disabled	Move right	-	-
Y-axis	Move left	Disabled	Move right	-	-
Z-axis	Move down with full speed	Move down with half speed	Disabled	Move up with full speed	Move up with half speed

For example a message ‘Pos 113’ would mean X-axis and Y-axis positioning to be disabled and a control signal to chopper motor drive will be sent to move the Z-axis positioning system upwards at the full speed. It is unlikely that an operator will be positioning actuator in more than one axis at one time, as they will be doing it through sliders and press buttons. However, it is possible to move the actuator to a predefined position, as each of the three numbers within the ‘Pos’ message is interpreted individually. ‘Pos 021’ would move the actuator towards left in X-axis, towards right in Y-axis and downwards at half speed in Z-axis. ‘Home’ is the command to move the actuator (in all 3-axes) to a predefined position specified for the transportation mode. This option is kept to facilitate fixation of the transport-bar, for locking the actuator motion to provide protection to the damping feet of actuator (Stalder, 2011).

7.3.4.2 Limit switch (LS) control messages

To ensure safety and protection the patient and system itself, six limit switches were installed to control the motion of positioning system beyond certain limits in all 3-axis. For LS message handling, a specific TCP/IP communications loop was included in the LabVIEW code as shown in Figure 7.9 (Glasbrenner, 2012).

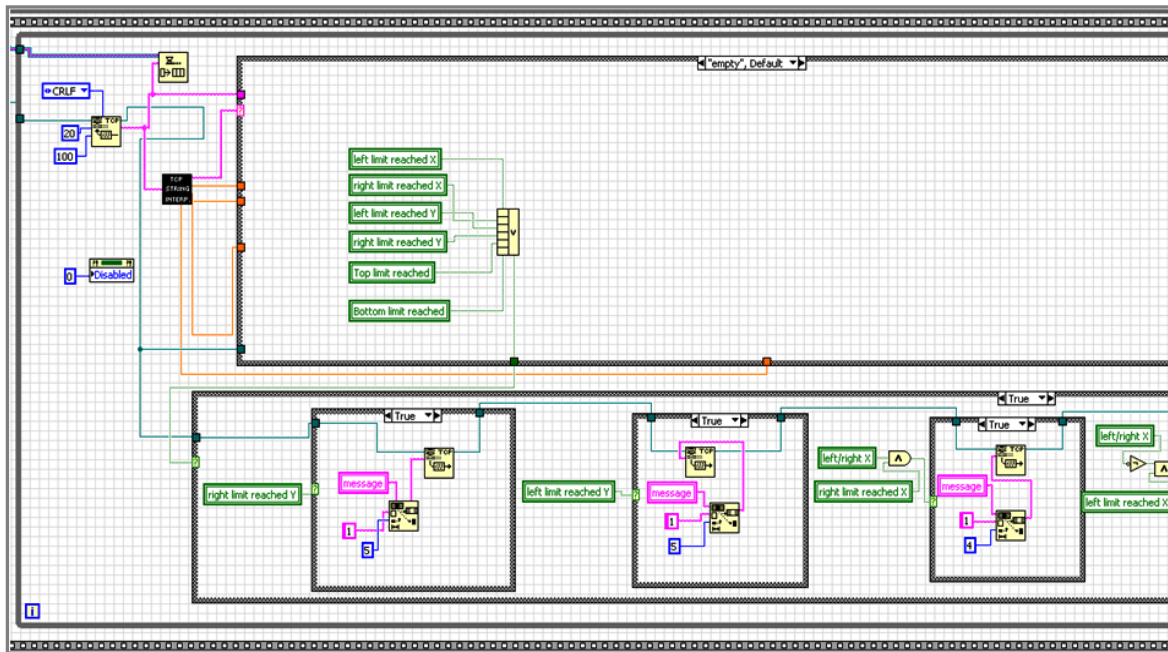


Figure 7.9: Block diagram of case structure handling LS control messages incoming (upper) and outgoing (lower). Incoming messages (limit reached) stops the motors to move actuator further while outgoing messages to prompt the operator.

The lower case-structure consists of two cases: 'True' and 'False'. If one of the limit switches is triggered this will cause the case 'True' to execute. If no limit switch is triggered all cases of the lower case structure remain false and the received message, to reposition the actuator in a particular direction, is passed to the FPGA controller to execute the command. Once one limit switch is triggered, corresponding case becomes true and a message is sent to the socket client, depending on the earlier command message. This action causes the corresponding control on the GUI to be greyed out disabling further movement and shows the operator that the actuator has reached a limit.

7.4 DIET IDS LiveVIEW

One of objectives of the DIET clinical prototype was that the operator should be able to operate the system with minimal technical skills and the positioning of the breast actuator should be done remotely. To achieve this goal, it was necessary present the operator with a video of the inside of the system, as well as control on lights and actuator positioning. The IDS manual suggests programming visualization applications in C#, using the *uEye.cs* header files. Software was developed in C# to provide LiveVIEW from all 5 IDS cameras in real time. The messages for XYZ-positioning of the actuator were also implemented in the programme providing control of the 3-axis position system to the operator.

7.4.1 Initial design concept

The initial software design concept was based on a one-window operation. The user interface would include a single window providing all the controls required for DIET imaging procedure and transmitting real-time videos from all 5 cameras during the whole session. Figure 7.10, shows a graphical user interface (GUI) of the initially developed DIET IDS LiveVIEW software. The GUI included all prerequisites required for a standard DIET imaging session like connecting to the camera server, initialising and releasing cameras, capturing and saving the calibration images, controls for repositioning the actuator and capturing and saving surface motion. The GUI presents live video from all 5 cameras during the whole process. Sliders were provided to control positioning using these images.

It should be noted that USB2.0 bandwidth limits the smooth transaction of video frames from all 5 cameras at one time, resulting into a jerky video. Buttons were provided to start or stop LiveVIEW from any particular camera thus allowing the operator to get real-time videos from only the required cameras.

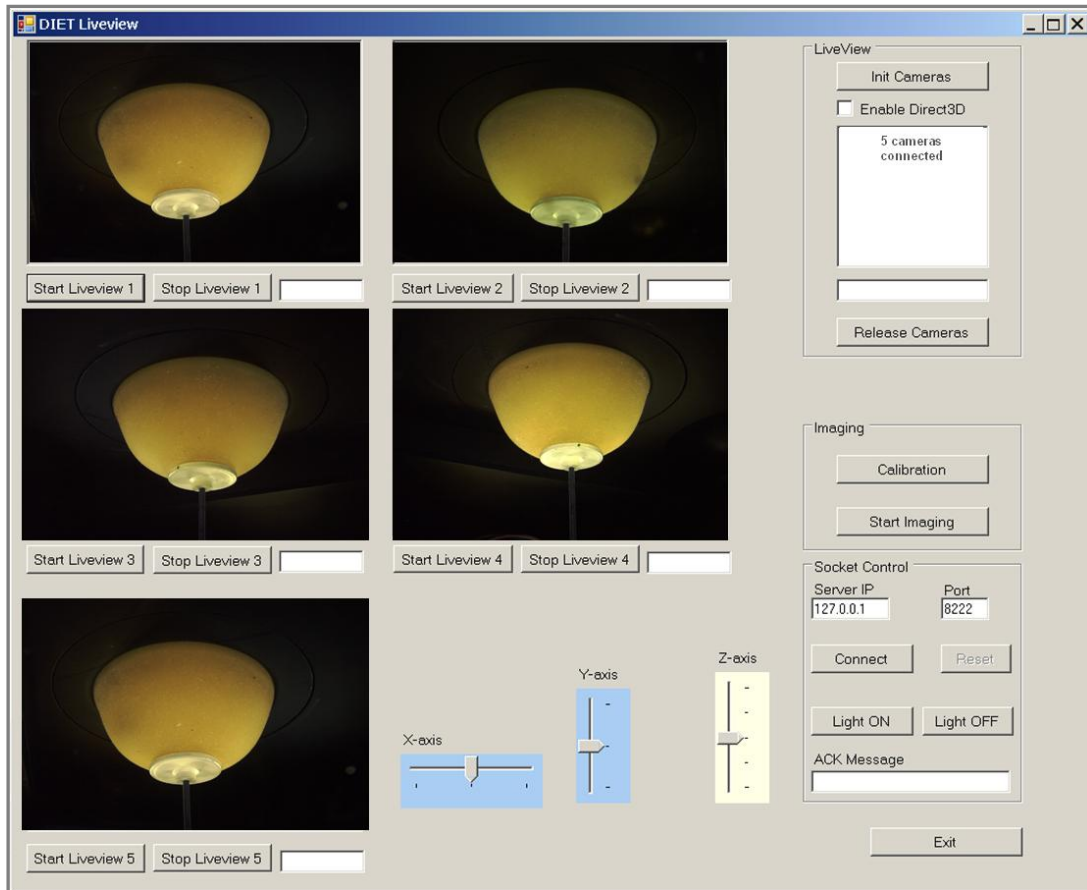


Figure 7.10: Graphical user interface of initially developed DIET IDS LiveVIEW software, displaying real time video from all 5 cameras

7.4.2 Final software design

LiveVIEW from two cameras placed on opposite axis was deemed sufficient to provide the inside view of the system required to reposition the actuator. The motion of the breast interface in the upwards direction could be seen even with a single camera. It was therefore decided to implement a multiple-window based user-friendly GUI and restrict LiveVIEW to only two cameras to improve image quality. Figure 7.11, shows the final design concept of the LiveVIEW widow based on displaying real-time video from two cameras installed at opposing axes. The operator is provided with control on lights and can position the actuator in all three dimensions with the direction control buttons. To ensure the quality of motion capture, the operator is also provided with an option to take unsaved 'Test Images' before proceeding with the actual imaging session.

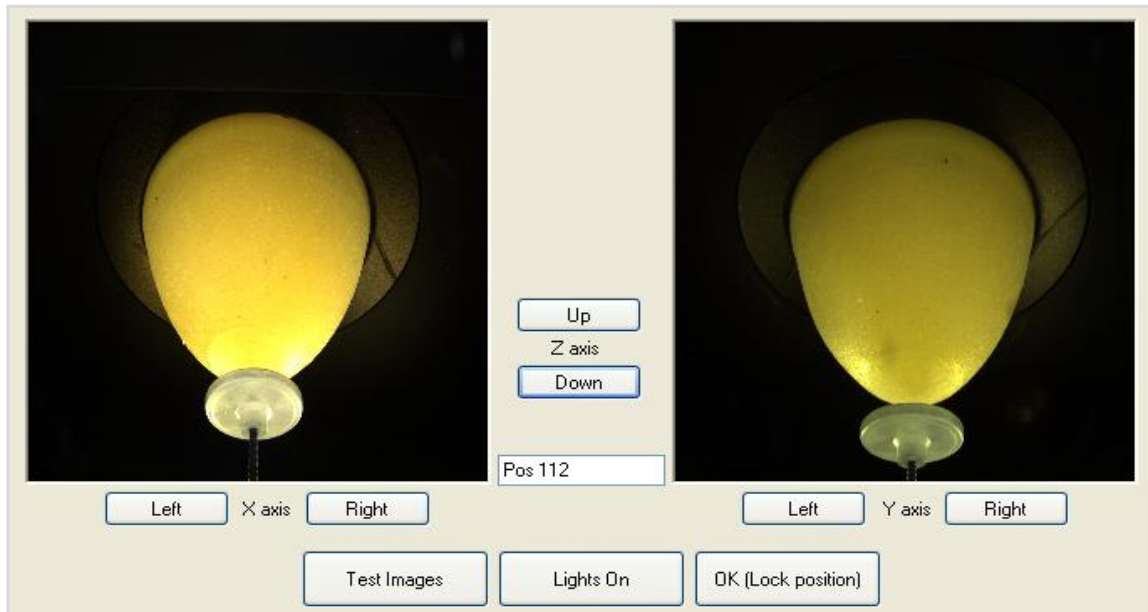


Figure 7.11: LiveVIEW window of GUI displaying real-time video from two cameras to present the operator with an internal view of the system during imaging. LiveVIEW enables the operator to reposition the actuator remotely in 3-axis depending upon the size dimensions of the breast under screening

7.5 Graphical user interface (GUI) and user manual

A well designed GUI was important to conduct large scale trials. Thus, all the imaging and control software were integrated and a window-based GUI was developed in C#. The GUI runs on an external machine (Host-PC) that has a TCP/IP socket connection to DIET clinical prototype. Currently, a Dell Laptop XPS M1210 is being used as the Host-PC. This machine has a 2 GHz processor with 2GB RAM and runs Windows XP Professional 2002.

With the development of this user interface, the operator does not have to be present all the time during the examination. After inputting the subject's details and other parameters, the operator can leave the examination room once the subject takes position and can come back once the imaging is finished. To run an imaging session using the DIET clinical prototype, the camera cable (USB 2.0) cable and the Ethernet cable from FPGA (cRIO NI 9012) controller need to be connected to Host-PC.

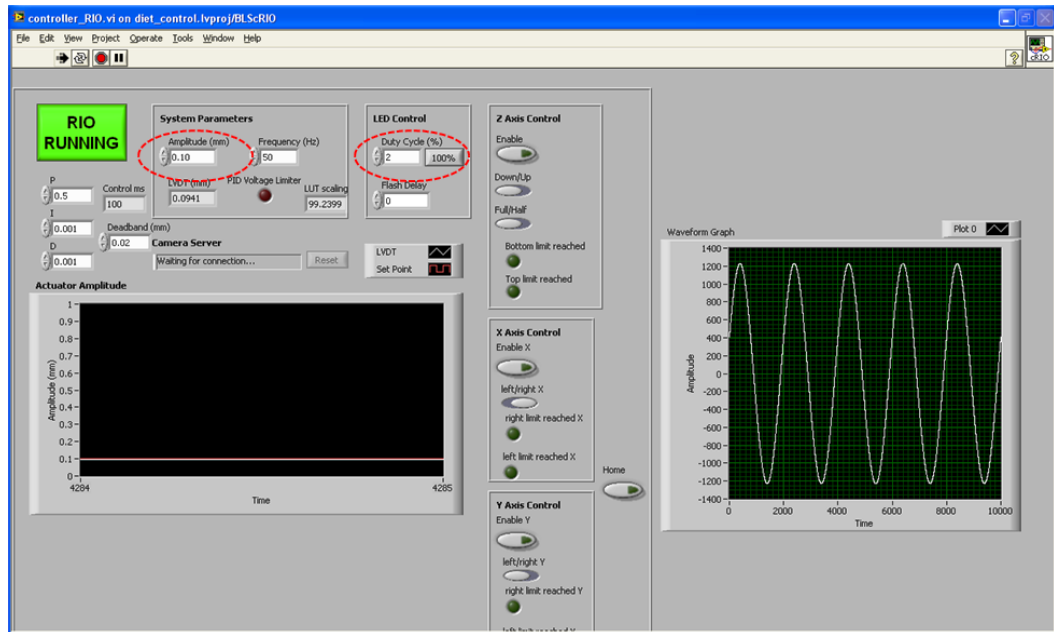


Figure 7.12: LabVIEW controller VI required to be running in the background during calibration process

Once, the LAN connection is established between FPGA and Host-PC, the following procedure needs to be run:

- a. Open DIET Control folder and launch LabVIEW project '*diet_control_lvproj*'
- b. Run '*controller_RIO.vi*' and set amplitude to 0.1 and duty cycle to 2% as shown in Figure 7.12. These settings are temporary and required for cameras calibration only. The settings for the Imaging Session will be sent by the imaging software, automatically. With the robust camera mounts and latest developments in the image reconstruction software, the camera calibration is required only once after it is being transported from one place to another. Once the system is established for screening, there is no requirement of calibrating the cameras each time.
- c. Launch '*DIET_System_Control.exe*' included in '*diet_control_lvproj*' by double clicking and a window will pop up as shown in Figure 7.13, displaying a main button 'Subject Imaging' for the operator to start the imaging session. This window also contains 'Test Mode' for the maintenance engineer providing direct access to LiveVIEW and Manual

Actuator Control and other system setting for maintenance purposes. Test Mode will be discussed later, under a separate heading in Section 7.6.

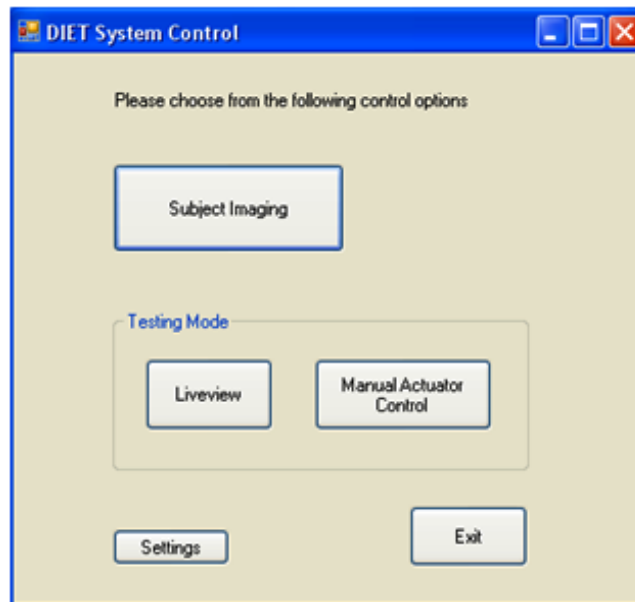


Figure 7.13: The first window of GUI displaying various control options. The operator needs to press ‘Subject Imaging’ button. The test mode and control settings have been provided to be handled by the service engineer for maintenance purposes

- d. On pressing ‘Subject Imaging’ a window will appear showing system’s current date and time, and asking the operator to enter details for the particular imaging session to include subject’s code (name), which breast to image (left or right) and actuation parameters (frequency range and amplitude), as shown in Figure 7.14. This window also contains a check box asking the operator whether the camera calibration is required or not? With robustly installed cameras and the new developments in the optical flow surface reconstruction software the calibration has now become a single time process. However, it is recommended to do the calibration once the system is being set at new location. On pressing the ‘OK’ button a folder with subject name will be generated on the hard disk of the Host-PC having a subfolder, the name of which contains date and time of the test and a letter ‘L’ or ‘R’ indicating which breast was imaged (left or right).

Figure 7.14: Patient's details and actuation parameters are fed into this form

- e. If camera calibration was required and operator had checked in the calibration 'check box' in the previous window, the 'Calibration' window will appear, as shown in Figure 7.15. The operator will place the calibration cube (Brown, 2008a) in the breast hole and press the 'Calibrate' button. On pressing the 'Calibrate' button, the connected cameras are initialized, camera parameters are loaded from the *'ini.file'* and the calibration images appear in respective picture boxes. A calibration folder is created in subject's existing subfolder. The software also measures time taken during initialization and calibration processes and displays it for the consumption of operator. The number of connected cameras is also displayed to ensure safety. This option was kept to prompt the operator, just in case the cable of any camera was removed from the USB hub during transportation. On pressing 'OK' on the calibration window, the calibration images are saved in the calibration folder for post-processing and 'Actuator Positioning' window pops up, as shown in Figure 7.16. The operator removes the calibration cube and the subject takes position on the device, with the breast to be examined hanging pendant through the 'breast hole'. The 'Calibration' interface also displays the time taken (in

seconds) for cameras initialization and capturing/saving of calibration images from all 5 cameras.

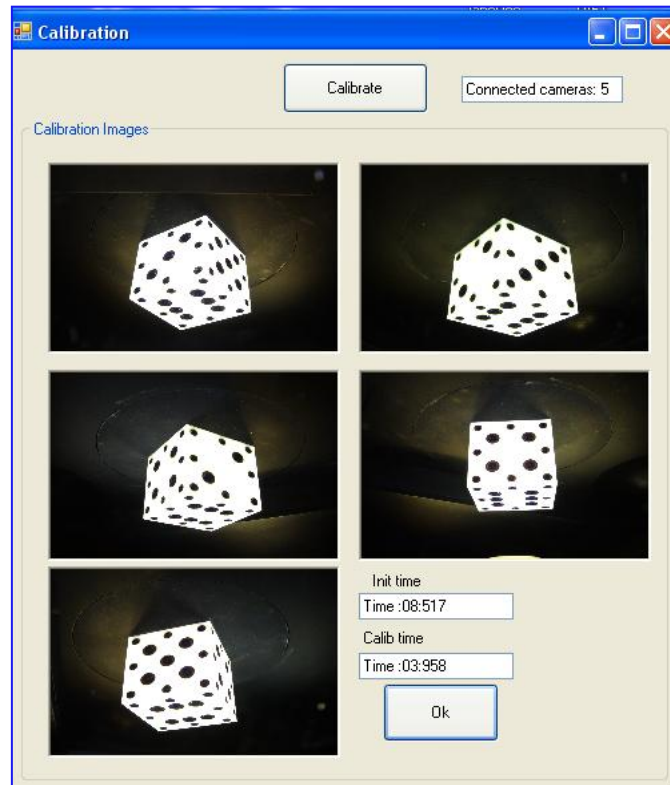


Figure 7.15: Calibration window displaying images of the calibration cube

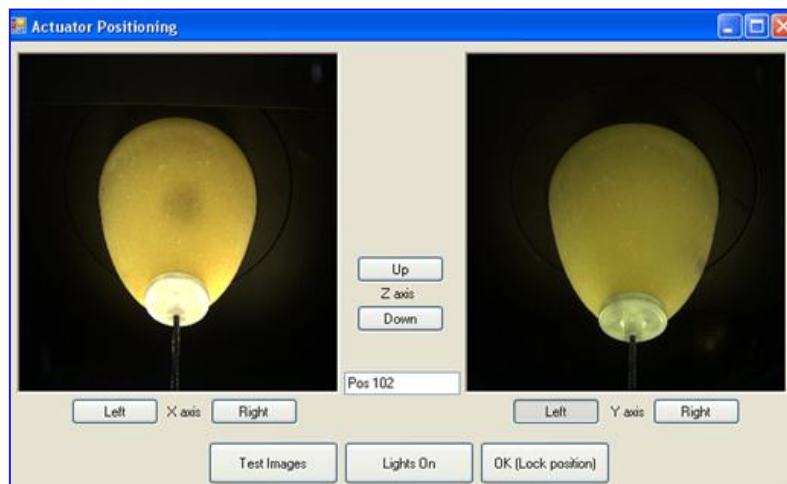


Figure 7.16: Actuator positioning window presenting real-time video (LiveVIEW) from 2 cameras installed 72° apart. The operator can reposition the actuator according to the size dimensions of the breast using this interface.

- f. If the calibration check box was not ticked, the Actuator Positioning interface will pop up straight away and the subject will take position. The 'Actuator Positioning' window has been designed to present the operator with a real-time video from inside of the system, so that they can reposition the actuator using the 3-axis positioning system. The actuator needs to be repositioned such that the breast interface exactly presses against the bust-point of the breast. If an 'Imaging Session' is part of an on-going screening programme, then the operator does not need not to take the 'Test Images'. In that case they will press 'OK (Lock position)' button and it will directly take them to the 'Start Imaging' interface.
- g. Once the operator presses the 'OK(Lock position)' button on 'Actuator Positioning' window 'Form_Imaging' will appear on the screen, as shown in Figure 7.18. This interface contains the subject's name, path to the folder where the images are going to be saved, range of required input frequencies with step size and the breast side (left or right) to be imaged. The operator now needs to press 'Start Imaging' and the actual imaging will start. A separate folder for motion capture at each frequency is created on pressing the 'Start Imaging' button; the name of the folder displays date, time, amplitude and frequency at which the imaging was done. At this stage, client-server hand shaking takes place and required commands for setting the desired actuation (frequency and amplitude) and lighting parameters are sent to the server. The chosen parameters are set by the cRIO controller and the breast starts vibrating at the desired frequency and amplitude. The cameras are reinitialized, camera parameters are loaded from the '*ini.file*' and cameras start freezing breast motion at the set phase delays with the help of strobing lights (Hann, 2009, Peters, 2007). Five subfolders (Cam1, Cam2, Cam3, Cam4 and Cam5) are created in the main folder for onward saving of motion images from each respective camera. Each camera captures 10 images at a particular frequency and these images are saved in the respective folders. The same process is

repeated for all the defined range of vibration frequencies. Once 'Start Imaging' button is pressed it is disabled and the 'Stop Imaging' button is enabled. Once imaging at all the desired frequencies is finished, the total imaging time is displayed in the message box and 'Start Imaging' button is reactivated.

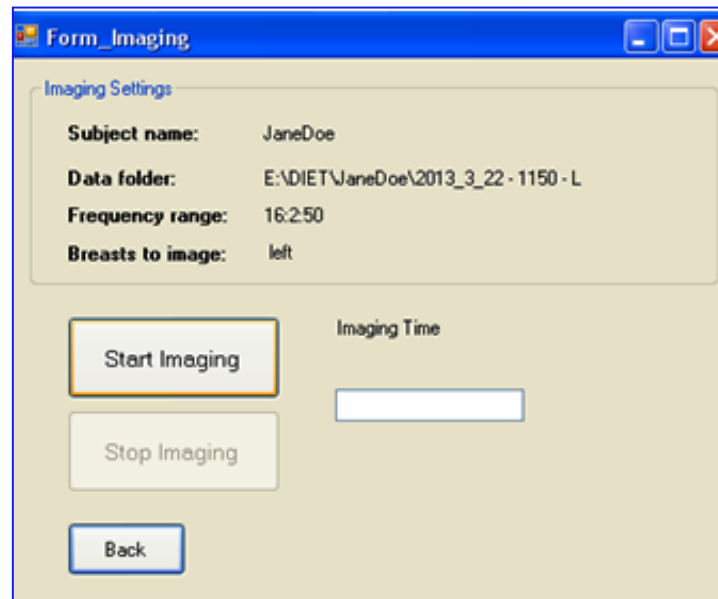


Figure 7.17: 'Form_Imaging' interface which enables the operator to start actual imaging session

7.6 Test mode

For maintenance purposes a 'Test Mode' option has been provided in the first interface of GUI that provides access to specific controls of the DIET system. This option is meant for service engineers and provides manual control of actuator for testing, as shown in Figure 7.18. With the help of this 'Manual Actuator Control' the maintenance staff can connect to various numbers of DIET devices at desired IP address and socket. This option was incorporated so that a single software system could be used for every DIET device in the view of future of commercialisation of the DIET technology.

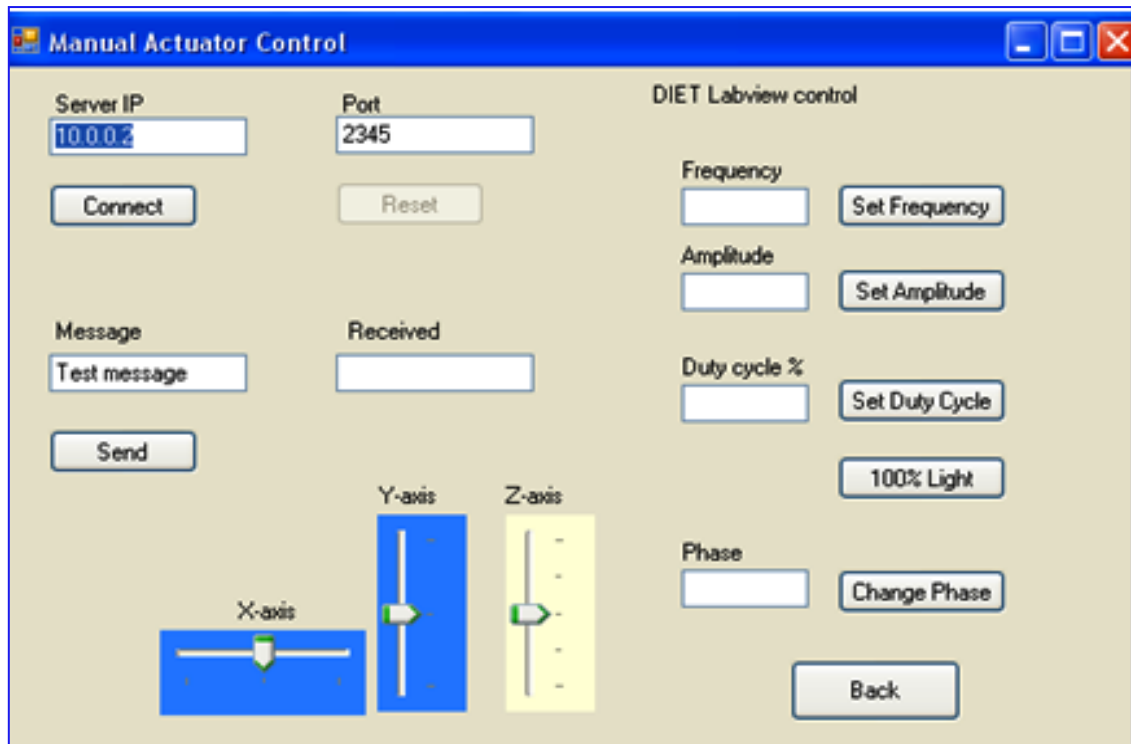


Figure 7.18: Manual actuator control interface provided to facilitate the service staff to monitor performance of different DIET breast cancer screening systems.

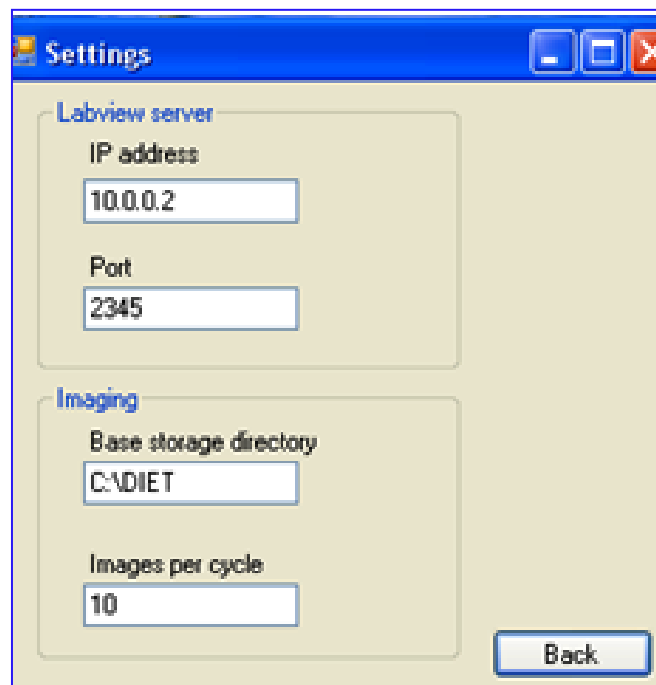


Figure 7.19: User interface to make quick changes in the software in order to change the path to base directory and number to be captured on each motion frequency

'Test Mode' also provides a shortcut interface to change the path to 'Base storage directory' (location of images to be saved) and 'Images per cycle' (number of images to be captured at one particular frequency) without making any changes to the source code [Figure 7.19].

7.7 Summary

Imaging technology in the previous DIET prototype was programmed using a console application and it was not possible to run the system with a non-skilled operator. The new IDS cameras, strobe lights, the motion actuation unit and 3-axis positioning system were programmed in C# using visual studio. The FPGA (cRIO NI 9012) was programmed in LabVIEW and various motion input subsystems were controlled using a client-server environment. The TCP/IP connection was established to provide client-server environment which communicated through sockets. A real-time video from two different cameras (installed at 72° apart) was incorporated to facilitate positioning of the breast interface according size dimensions of breast, under screening. A windows based graphical user interface (GUI) was designed enabling an operator to run the system, without significant operational training. Finally, a testing mode was provided to monitor performance of different DIET systems employed in large scale screening programmes.

Chapter 8

8 SILICONE BREAST PHANTOMS FOR ELASTOGRAPHIC IMAGING EVALUATION

8.1 Background

Pathological changes, such as the development of different types of carcinomas alter the elastic properties of human tissues resulting in stiffness contrasts of 5:1 between cancerous and healthy tissues (Krouskop, 1998, Samani, 2007, Samani A, 2003, Sarvazyan, 1995). This contrast has given rise to research in the field of elastic parameter estimation of human tissues (Weaver et al., 2001, McKnight et al., 2002, Ernest et al., 2005, Krouskop, 1998, Samani, 2007, Egorov, 2008, Chu and Rutt, 1997, Hall et al., 2003, Madsen, 2006, Muthupillai et al., 1995, Muthupillai et al., 1996, Plewes et al., 1995, Siegmann et al., 2010, Sinkus et al., 2005, Zhu and Hall, 2002, Parker et al., 2011), resulting in the development of several elastographic imaging techniques. For breast cancer detection, palpation or clinical breast examination (CBE) remains the most common procedure to date, despite inherent limitations of subjectivity and low sensitivity (Kopans, 2007, McDonald, 2004). Other detection modalities include mammography, ultrasound, CT and MRI. Mammography is the only modality currently approved for screening applications, due to its low cost and relatively short test duration, in spite of the invasiveness from the induced radiation.

To overcome these limitations, a range of elastographic imaging techniques has been introduced. Mechanical properties of the breast can be estimated in vivo with Ultrasound Elastography (USE) (Evans, 2010, Sharma et al., 2004, Ophir et al., 1996, Khaled et al., 2006) and

Magnetic Resonance Elastography (MRE) (Doyley and Weaver, 2005, Manduca, 2001). However, the associated cost for MRE is relatively high, rendering it less suitable for large scale screening programs. Equally, the resolution and cost of current USE methods are not yet acceptable.

Despite extensive characterization of the elastic properties of structural materials, mechanical properties of many biological materials remain unknown or uncertain. This outcome is due in part to the technical difficulty of measuring visco-elastic tissues (Fung Y.C., 1993, Devi et al., 2007, Nightingale et al., 2000, Ophir et al., 1996) (particularly in-vivo). Inter-subject variation for a given tissue type plays a further role. The stiffness of healthy and cancerous breast tissues have been investigated and stiffness contrasts in the range of 5:1 have been reported for carcinomas (Krouskop, 1998, Samani, 2007, Egorov and Sarvazyan, 2008, Xing Liang, Sinkus, 2005, Plewes, 2007, Srivastava, 2011). Hence, for developing novel elastographic methods, what is needed is a simple replicable test phantom that provides a realistic platform for development.

8.1.1 Breast phantom materials

Based on the measured elastic properties of human breast tissues, researchers have developed phantoms for validation of elastographic imaging systems. Various materials have been used to mimic human breast tissues and the elastic properties of these materials cover a wide range.

Table 8.1: Materials used for mimicking breast tissues and the measured values of Young's modulus by previous investigators

	Material used	Young's Modulus (kPa)	
		Background	Inclusion
Samani & Plewes (Plewes, 2007)	Gelatin (Sigma-Aldrich)	11.74	31.30
Xing Liang et al (Xing Liang)	Silicone RTV -615 A	8.55	359.18
Madsen et al (Madsen, 2006)	Gelatin & Safflower oil	16-19	59-72
Egorov et al (Egorov and Sarvazyan, 2008)	Silicone Gel SEMICOSIL	6	75
Peters et al*	Silicone Gel A-341C & LSR-05	26-33	98-135

*Peters et al (Peters, 2008b), measured only the in-phase component of Young's modulus, storage modulus (E')

Table 8.1 contains data pertaining to previously reported elastic properties of breast phantoms. It is worth noting that the stiffness parameters are highly dependent on the material used and that the results differ significantly in static and dynamic testing.

8.1.2 Design of anthropomorphic breast phantom

Breast shaped phantoms of varying tissue properties and tumour location and size can be used to test elastographic imaging modalities such as MRE,(John, 2001) USE and DIET. Furthermore, it is desirable to obtain phantoms that are stable over time, easy to fabricate, and have elastic properties matching those of human breast tissues (Abbas and Donald, 2004, Madsen, 2006, Sinkus, 2005, Egorov and Sarvazyan, 2008, Plewes, 2007, Peters, 2008b).

In this work, a method of creating anthropomorphic breast phantoms of varying elastic and damping properties is presented. Mechanical testing of various silicone compositions was undertaken to compare their elastic properties. Validation was performed on geometrically different example phantoms used in the DIET system and in MRE research.

8.2 Materials and Methods

8.2.1 Phantom specifications and tissues to model

During DIET imaging, the patient lies horizontally face down, while the breast is hanging pendant through a hole. The breast is actuated at a range of frequencies (10-50 Hz) and the breast surface motion is optically imaged through an array of digital cameras. Motion is reconstructed in 3D to obtain Bode plots and analyze effects of stiffer inclusions on the amplitude of motion, phase disruption and variation in natural frequencies (Lotz, 2011b, Chase, 2009, Lotz, 2010, Lotz, 2011a, Lotz, 2012, Peters, 2008b, Brown et al., 2012). The phantoms required for in vitro DIET trials, need to mimic an average female breast, both geometrically as well as from a stiffness

point of view. The size specifications used were as follows (Hamas, 2000, Nipshagen et al., 2007, Hamas, 1999):

- Approx 110 mm in diameter at the base (chest wall)
- 65 mm long in P-A (posterior – anterior) direction
- Taper as illustrated in Figure 8.1(A).

Based on the anatomy of the breast following tissues were required to be modelled:

- Skin: To include a compressive or constraining traction
- Adipose
- Tumour
- Pectoral muscle

8.2.2 Elastomers used:

Conventional, two component (base plus curative) silicones, room temperature vulcanizing (RTV) silicones (curable at room temperature) were chosen based on their resulting elastic parameters, long term stability, ease of handling, and ability to be moulded. They can be stored long term to enable significant re-use without degradation (Colas, 2005, Homma et al., 2000).

These materials include:

- SoftGel A-341C (Factor II Incorporated, AZ, USA): This material is a translucent, low viscosity RTV silicone gel that develops much of the same dimensional stability and non-flowing characteristics of a solid silicone elastomer. The gel is used to produce healthy and cancerous tissues. Curing time is approx 1 hour at room temperature (20-25° C)(Factor II).
- DC 200 Silicone Fluid 50 cs (Dow Corning Corp. MI, USA): This material is used as thinning agent to be mixed with silicone gel to produce softer elastic properties of the cured material. This material is now available under a new product name i.e. Xiameter PMX 200 (Silicones).
- LSR-05 Silicone Elastomer (Factor II Incorporated, AZ, USA): This material is a 1:1 platinum cured translucent low viscosity RTV that cures in approximately 3 hours at room temperature. When cured, it yields hard elastic properties and can be used for fabrication of tumours and skin in appropriate proportions (Inc.).
- Elastosil P7600 RTV-2 A/B (Wacker Inc., AG, Germany): The cured silicone exhibits a similar elasticity as A-341C, but with much higher internal damping. With Dow Corning Fluid 50 cs in 1:1 ratio, it exhibits very desirable elastic properties and can be used for phantoms with lower Young's modulus values. Vulcanization is approx 6-8 hours at room temperature or 1 hour at 100° C (Chemie).

8.2.3 Selected compositions for dynamic mechanical analysis

Eight compositions were chosen to deliver a range of mechanical properties to best match reported tissue characteristics (Krouskop, 1998, Samani, 2007, Samani A, 2003, Sarvazyan, 1995, Egorov and Sarvazyan, 2008, Xing Liang, Sinkus, 2005, Srivastava, 2011). From these compositions phantoms for MRE and DIET imaging were developed. Five cylindrical samples (8 mm thick, 28 mm diameter) from each composition using the same batch of silicone were cast for mechanical testing. The compositions of silicone materials chosen for DMA testing were as follows:

- A: 100% SoftGel A-341C
- B: 70% SoftGel A-341C + 30 % DC 200 Silicone Fluid 50 cs
- C: 50% SoftGel A-341C + 50 % DC 200 Silicone Fluid 50 cs
- D: 30% SoftGel A-341C + 70 % DC 200 Silicone Fluid 50 cs
- E: 100% LSR-05 Silicone Elastomer
- F: 80% SoftGel 341C + 20 % LSR-05 Silicone Elastomer
- G: 100% Elastosil P7600 RTV-2
- H: 50% Elastosil P7600 RTV-2 + 50% DC 200 Silicone Fluid 50 cs

8.2.4 Dynamic mechanical analysis

The samples were tested in compression at room temperature. A Q-8000 dynamic mechanical analyzer (DMA) (TA instruments, New Castle, DE, USA) was used to dynamically test samples over a range of 4 – 50 Hz (isothermally) at room temperature. Storage modulus (E'), loss modulus (E'') and damping ratios ($\zeta = \frac{E''}{E'}$) were obtained using a viscoelastic bar model defined:

$$\bar{F} = \frac{AE^*}{t} \bar{X} \quad (8.1)$$

where \bar{F} is the measured force amplitude, \bar{X} is the corresponding displacement amplitude, A is sample cross-section area, t is sample thickness and E^* represents the complex valued viscoelastic Young's modulus ($E^* = E' + iE''$).

The model equation assumes that transverse strains are negligible. In fact, because of constraints applied by the platens of the DMA, transverse strains in the sample are significant, so stiffness computed using Equation (8.1) will be higher than the actual sample stiffness. To account for this offset, the DMA stiffness estimates apply an empirical correction factor based on sample geometry (Almagableh et al., 2009, Instruments, 2004), so that:

$$E^* = \frac{\bar{F}F_e t}{\bar{X}A} \quad (8.2)$$

where F_e is the clamping correction factor, determined by the DMA using finite element analysis of the sample deformation. For a solid circular sample of thickness, $t = 8\text{mm}$, diameter, $D = 28\text{mm}$, and Poisson's ratio, $\nu = 0.45$ (assumed), $F_e = 0.5487$ was calculated using (Almagableh et al., 2009, Instruments, 2004):

$$F_e = \frac{1 - 1.999 * \nu + 0.03745 * \left(\frac{t}{D}\right) + 2.457 * \left(\frac{t}{D}\right)^2 - 1.244 * \left(\frac{t}{D}\right)^3}{1.009 - 1.814 * \nu + 0.8257 * \nu^2 - 0.1303 * \left(\frac{t}{D}\right) + 2.776 * \left(\frac{t}{D}\right)^2 - 1.461 * \left(\frac{t}{D}\right)^3} \quad (8.3)$$

8.2.5 DMA testing procedure

The required preload was calculated to produce a 1% pre-strain based on the estimated modulus of the first sample of each composition. The main points of the adopted methodology for DMA testing include:

- a. The dynamic strain was set to 2%, half of the peak-to-peak difference (i.e. strain = $\pm 2\%$).

- b. The 'Force Track' was set to 125%, which means the DMA applies 125% of 2% extra preload to make sure the top plate does not lose contact with the top surface of the sample. In other words, approximately 3.5% pre-strain was applied, and then oscillated at $\pm 2\%$.
- c. The Young's modulus E^* calculated according to Equation 8.1 also accounts for clamping effects of the material surfaces as DMA applies an empirical correction factor to account for this. The modulus is calculated in terms of its real and imaginary components i.e. storage modulus (E') loss modulus (E'') and damping ratio ($\zeta = E''/E'$).
- d. The correction factor, Fe , for the boundary conditions assumed a Poisson's ratio of 0.45 for these samples and $Fe \approx 0.55$.
- e. One DMA measurement was recorded for each of the five samples and variation was gauged by using multiple samples rather than multiple measurements on the same sample. The coefficient of variation was calculated on the basis of accumulative mean, μ , and standard deviation, σ , of all the five samples.

8.2.6 Phantom moulding

8.2.6.1 Design of mould

A custom mould matching the general shape of a human breast was constructed. The mould consisted of two assemblies. First, there was a cavity [Fig. 8.1 (A)] and a core [Fig. 8.1 (B)], such that there was a 1 mm gap between the two, when the second assembly, the core, seated in the cavity [Figure 8.1 (C)].

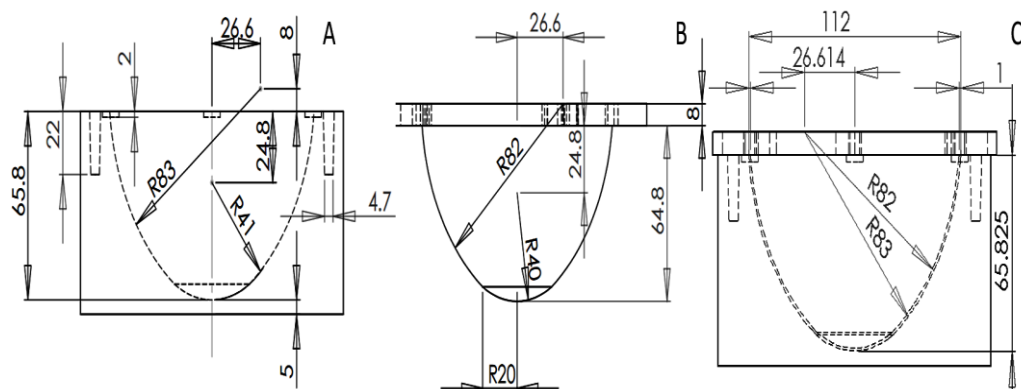


Figure 8.1: Drawings of phantom mould (A) cavity, (B) core and (C) complete assembly showing 1mm gap between cavity and core

The core was used to mould a skin that can have a significant effect on the overall mechanical response of the phantom due to the compressive constraining traction it supplies, thus affecting the surface motion reconstruction in DIET. The mould was designed as a 3D CAD model and CNC milled out of aluminium.

8.2.6.2 Moulding procedure

A set of 13 anthropomorphic phantoms was developed, including one homogenous healthy (with no inclusion) and 12 heterogeneous phantoms each with a stiffer inclusion (tumours) of various sizes (5mm, 10mm, and 20mm) embedded at different depth wise locations (A, B, C and D), as shown in Figure 8.2 (A, B and C). B10 for example, shows a 10mm tumour at location B. A detailed description of these locations is given in Table 8.2.

Each of these inclusions were positioned at 6-o'clock (feet side) when viewed from the front [Figure 8.2 (D)]. To assess the range of possibilities to detect presence of more than one tumour within the same phantom, the MRE phantom was made rectangular block shaped (dimensions: $60 \times 40 \times 40 \text{ mm}^3$) with two square inclusions (dimensions: $20 \times 20 \times 20 \text{ mm}^3$) with different elastic parameters.

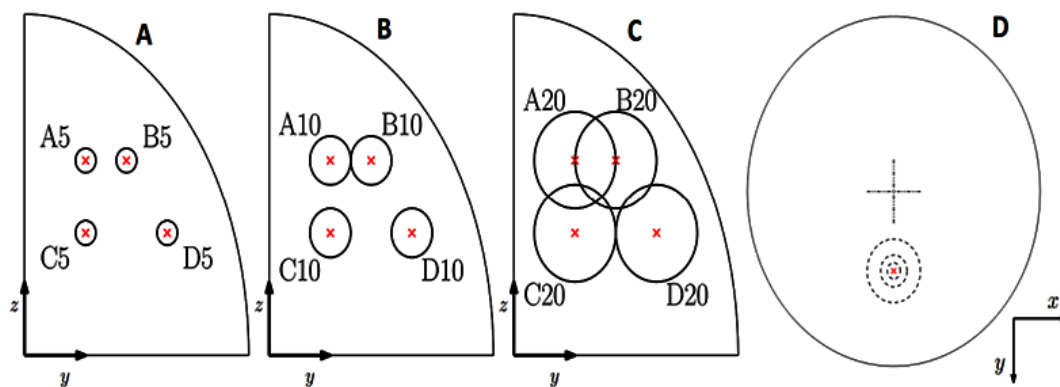


Figure 8.2: Depth locations of inclusions (A) 5mm, (B) 10mm and (C) 20mm, and (D) 6-o'clock position when the breast is viewed from front.

Table 8.2: Description of tumour location (depth) in heterogeneous breast phantoms

Location	Distance from chest muscle (mm)	Distance from centre of the breast (mm)
A	40	15
B	40	25
C	25	15
D	25	35

Before starting to mould the DIET phantom, a release agent Silicone Star (Sta-Lube, Auckland, NZ), was thinly sprayed on the core so that it leaves the skin attached to the inner surface of the cavity during extraction. The detailed procedure to create an anthropomorphic silicone breast phantom is described:

a. Skin: 50 g of silicone material were required to fabricate 1 mm of skin. The material was mixed per the composition chosen and few drops of coloration Suntan FI-227 and White FI-200 (Factor II - Factor II Incorporated, AZ, USA) was mixed to get the skin tone. The mix was stirred in a plastic container, and de-aired in a vacuum chamber for 15 minutes. The material was then poured into the mould, the core was placed into the cavity and the material was left for curing for 2 hours at room temperature. For extraction the core was lifted gradually by tightening the jacking screws one by one, as shown in Figure 8.3(A). The skin was left attached to the inner surface of the cavity for subsequent moulding of the other tissues.

b. Tumour: The silicone composition chosen for tumour was mixed in a disposable paper glass, stirred, de-aired and left for curing for one hour. After curing, the silicone was released and cut into spherical tumours of 5mm, 10mm, and 20mm diameter. The tumour was suspended in the mould using a thin wire at the desired location and the material for the adipose tissue was poured into the mould as shown in Figure 8.3(B).

c. Adipose tissue: 300 g of material chosen for adipose was mixed in the recommended ratios, and de-aired for 15 minutes. The material was slowly poured into

the cavity withholding the prefabricated skin, to avoid formation of air bubbles. This material was enough to fill the mould cavity, leaving a 10 mm gap at the top for subsequent moulding of the chest muscle as shown in Figure 8.3(C). At room temperature, this material took almost 3 hours to cure.

d. Pectoral Muscle: After the material in the mould was properly cured, the wire holding the tumour was slowly pulled and a circular acrylic disc with three attached bolts [Figure 3(D)], was placed on top of the material. This disc was meant to mimic the effect of the rib cage, presenting a stiff backing and the bolts helped in mounting the phantoms during DIET imaging. 88 g of a final silicone compound was poured around the disc as shown in Figure 8.3(E) and left at room temperature to cure for one hour.

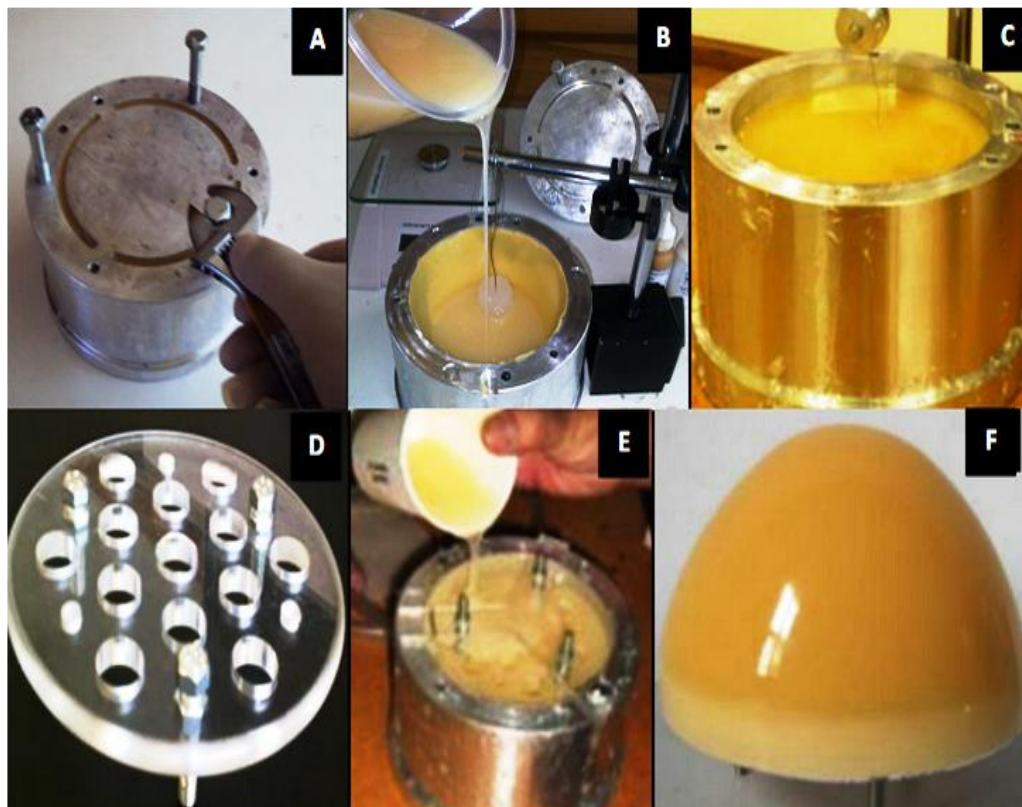


Figure 8.3: Moulding procedure of silicone breast phantoms: (A) process of core extraction (B) procedure of placing a stiff tumour into the healthy tissue, (C) cured healthy tissue, (D) circular disc with bolts, (E) method of applying a circular disc during moulding of pectoral muscle, (F) the moulded breast phantom.

Extreme care has to be exercised while extracting the phantom to avoid damage to the skin. Individual silicone components were well bound to each other and allowed robust handling of the phantom as a single unit [Figure 8.3(F)].

8.2.7 Phantom imaging

8.2.7.1 DIET imaging

Red, green and blue papers were cut approx (1mm x 1mm) to form fiducial markers and 1200-1500 of these markers were applied on each phantom to cover the surface. Silicone provided natural adhesion. The markers purpose of applying these markers was to ensure robust motion tracking when optically imaged with the DIET system (Brown, 2008a, Chase, 2009, Lotz, 2010, Lotz, 2011a, Lotz, 2012, Brown, 2010, Brown, 2008b, Brown, 2007).

During the imaging procedure each one of these 13 phantoms, was individually mounted on a metallic plate (200 mm x 150 mm) and hung pendant through a hole in the DIET clinical prototype. The phantom was vibrated using harmonic sinusoidal actuation of 0.5 mm amplitude, over a range of 10-50 Hz with a step size of 1 Hz. The motion was frozen at every 36 degrees and 10 optical images at each frequency were obtained using an array of 5 digital cameras in the device. The motion was reconstructed in 3D (Brown, 2007, Brown, 2008b, Brown, 2008a, Brown, 2010) and a spherical coordinate system was defined to describe the location of the applied fiducial markers.

The whole breast phantom was discretized into 126 segments to account for uneven marker coverage (Lotz, 2012) and Bode diagrams of the frequency response (with respect to the actuation) were obtained covering the first and second resonant frequencies for each segment. The resonant frequencies obtained were compared across the surface to observe differences in behaviour. To assess statistical significance of the differences observed, a two-sample t-test was

used to reject the hypothesis that two areas were similar in resonance behaviour. A significance threshold of $\alpha = 0.01$ was chosen, indicating a 99% confidence interval. The hypothesis tested was whether the area of interest with the phantom tumour inclusion has the same or different second resonance compared to the rest of the surface (Lotz, 2011b, Lotz, 2012).

8.2.7.2 MR imaging

MRE was performed on the MRE phantom using a Philips Achieva 3T MRI system. A piezoelectric actuator driven at 100Hz was used to generate harmonic motion, which was measured in all three coordinate directions using an echo planar imaging sequence with added motion sensitizing gradients. Full volume measurements in all three motion directions were taken using 2mm isotropic voxels. A subzone based algorithm was then used to estimate the viscoelastic mechanical property distribution by iteratively updating an estimate of the properties to minimize the difference between the displacements predicted by a computational model and the measurements (Van Houten, 2001).

8.3 Results

8.3.1 Elastic properties of tested materials

Accumulative mean, μ , of storage modulus, E' , and damping ratios, ζ , were obtained for all five samples from each composition using the DMA measurements. E' ranged from 2 kPa (composition D) to 570 kPa (composition E), and ζ ranged from 0.03 (composition B) to 0.56 (composition H). Samples from Composition D were the softest and showed abrupt anomalous behaviour at high frequencies, mainly due to its very low stiffness and machine resonance.

To show the extent of variability, standard deviations, σ , were obtained from the DMA measurements and coefficients of variation, C_v , were calculated for all compositions and plotted

along with mean, μ , values. Coefficients of variation in most cases were reasonably low, except for composition D, which may be attributed to experimental errors in testing that material.

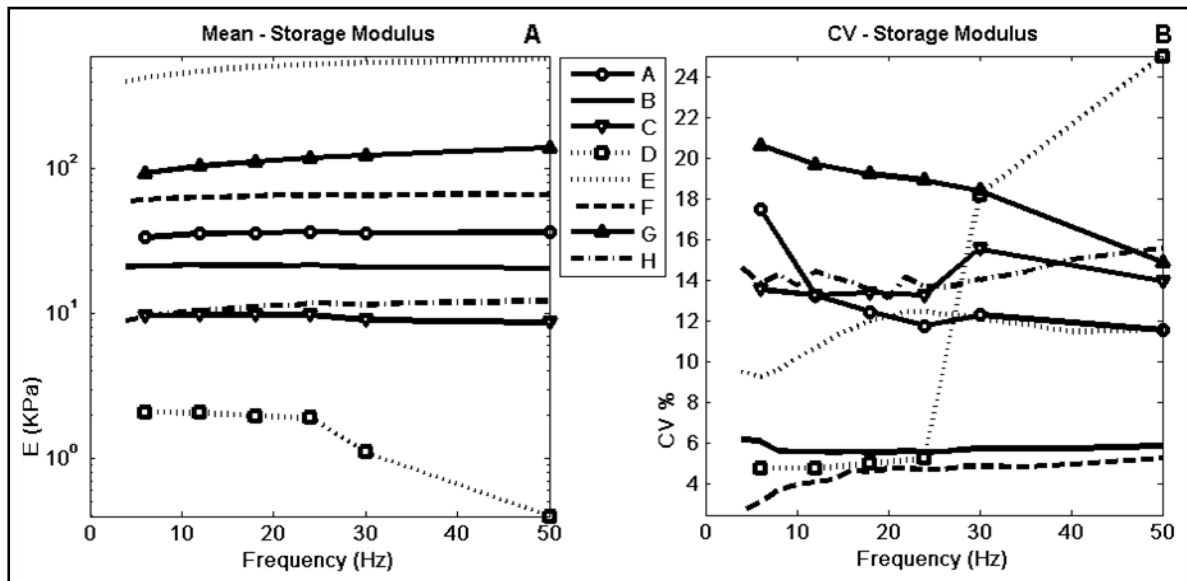


Figure 8.4: (A) Mean values, μ , and (B) Coefficient of variation ($C_v = \sigma/\mu$) for the storage Modulus E' , of the measured compositions

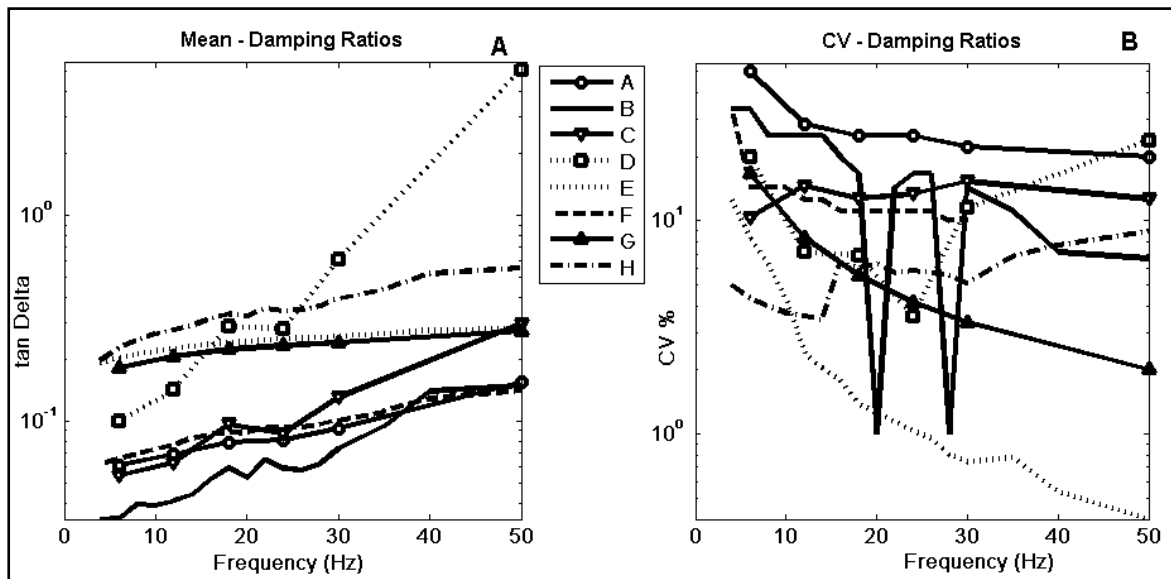


Figure 8.5: (A) Mean values, μ , and (B) coefficient of variation ($C_v = \sigma/\mu$) for the damping ratios, ζ , of the measured compositions

Figure 8.4 and Figure 8.5 show the obtained mean value, μ , and coefficient of variation, C_v , for the storage modulus, E' , and damping ratios, ζ , as the result of DMA measurements. These DMA results are tabulated in Table 8.5 and Table 8.6 (Appendix C & D).

8.3.2 Phantom application

8.3.2.1 DIET results

Based on the DMA results, the compositions chosen for different tissues in DIET phantom and their elastic parameters are tabulated in Table 8.3. The breast phantoms were imaged using the DIET clinical prototype (Chase, 2009, Lotz, 2011a) and the surface motion was reconstructed in 3D. The whole surface was discretized into 126 segments and the frequency response was studied in each segment to analyse variations in first and second natural frequencies.

Table 8.3: Materials used for mimicking different tissues in DIET anthropomorphic breast phantoms

Tissue	Composition	Material	Storage Modulus, E'	Damping ratios, ζ
Skin	F	80% SoftGel A-341C + 20 % LSR-05 Silicone Elastomer	60	0.09
Tumour	A	100% SoftGel A-341C	36	0.08
Adipose	C	50% SoftGel A-341C + 50 % DC 200 Silicone Fluid 50 cs	9.5	0.06
Pectoral Muscle	A	100% SoftGel A-341C embedded into a circular acrylic disc with holes	36	0.08

As can be seen in Figure 8.6, the locations of the first and second natural frequencies were noticeably different around the phantom tumour location, when compared to homogenous, healthy areas. The first natural frequency in the healthy case was 16 Hz, whereas at the tumour area it shifted to about 18 Hz, also the damping of the healthy case was clearly lower compared to the tumour case (Lotz, 2011b). Interestingly, it was observed that the second natural frequency shifted towards the lower range (Lotz, 2012).

The two-sample t-test was used and p -values were obtained to give indication of the difference in the observed metric in one segment, compared to the remaining breast surface. To analyse these differences across the breast, the results of t-test were used for all 13 phantoms.

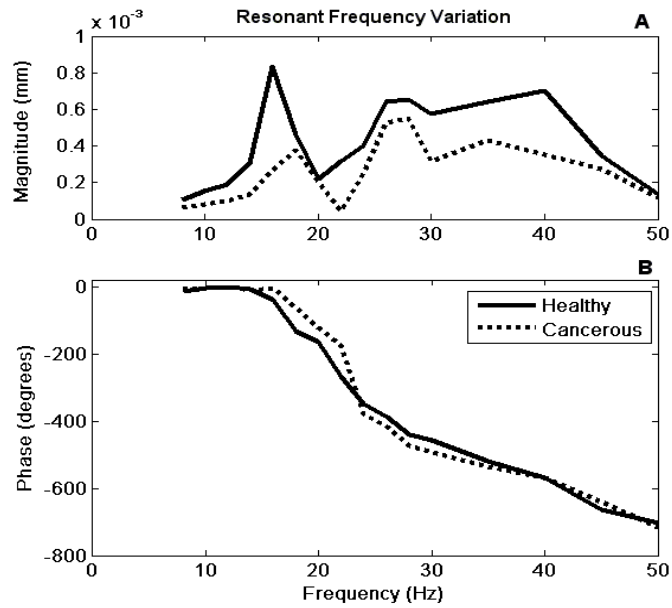


Figure 8.6: Bode plot of healthy and tumour inclusion phantom data set showing shift in the first natural frequency

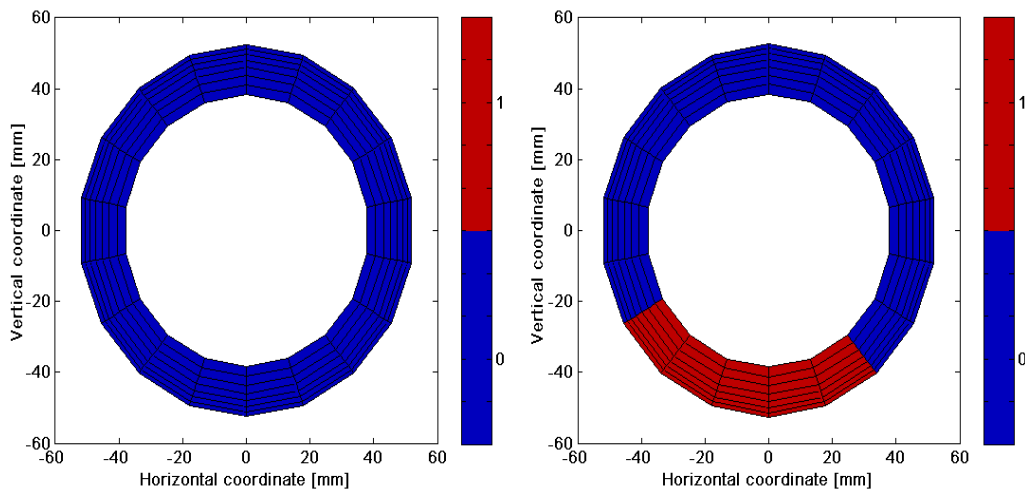


Figure 8.7: Result of t -test for phantoms (A) healthy and (B) having a 20mm tumour at 6 o'clock. The thresholded outcome $1-p$ [hypothesis rejected (red) or accepted (blue)] is shown in each case, indicating a (lower) second natural frequency and thus a stiffer inclusion at the red area.

Figure 8.6 (A & B) shows the t-test results for a healthy phantom, with no inclusion, and for a phantom with a 20mm tumour at location B (Table 8.2) in the 6 o'clock position. The red area (value 1) shows segments where the null hypothesis was rejected, indicating an abrupt change in the second natural frequency with a 99% of confidence level (Lotz, 2012). The healthy phantom, as a form of validation was consistently P-0, as expected.

8.3.2.2 MRE results

To show the range of possibilities in mechanical motion properties test, the MRE phantom was made in a rectangular shape. Two square shaped inclusions, one with lower and one with higher stiffness than the background were embedded in this phantom to assess the possibility of detecting a softer inclusion in the harder background.

The detailed compositions used for mimicking background and tumours for the MRE phantom are given in Table 8.4. MRE reconstructions of this phantom using an established software program (Van Houten, 2001, Van Houten et al., 2003) also distinguished inclusions from the background and clearly indicated the presence of both inclusions in the phantom, in the observed metrics, as shown in Figure 8.8 (A-D).

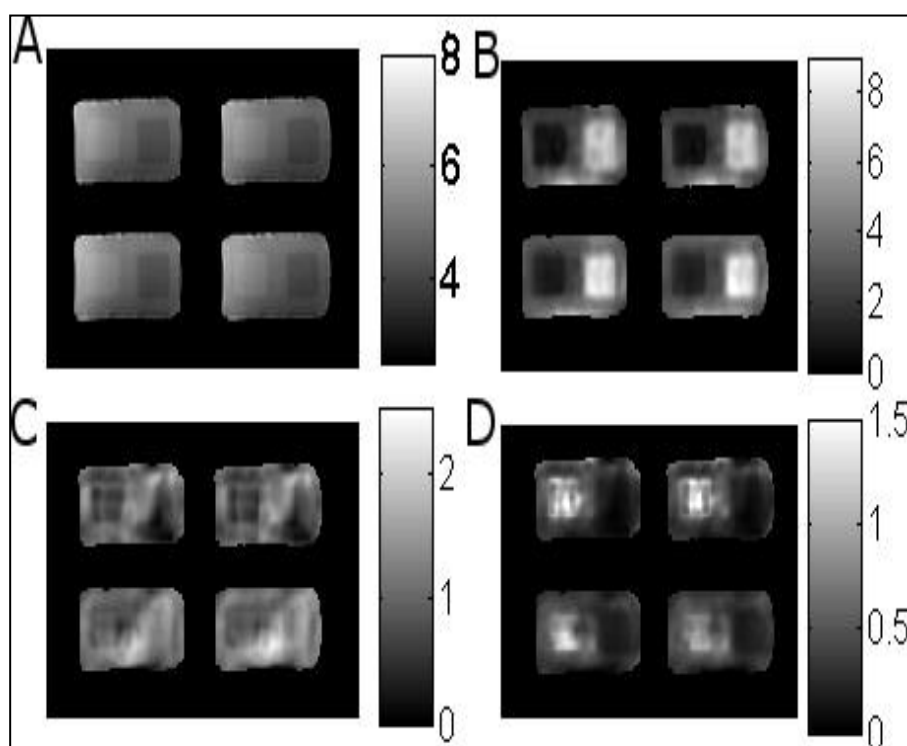


Figure 8.8: MRE Reconstruction of a phantom with composition A background and two inclusions: composition C on the left and composition A on the right. A subset of slices from the full volume data read shown: (A) is a T2* weighted image, (B) is the storage modulus (kPa), (C) is the loss modulus (kPa) and (D) is the damping ratio.

Table 8.4: Materials used for mimicking background and inclusions in the MRE phantom

Tissue	Composition	Material	Storage Modulus, E' (kPa)	Damping ratios, ζ
Background	B	70% SoftGel A-341C + 30 % DC 200 Silicone Fluid 50 cs	21	0.05
Tumour1	A	100% SoftGel A-341C	36	0.08
Tumour2	C	50% SoftGel A-341C + 50 % DC 200 Silicone Fluid 50 cs	9.5	0.06

8.4 Discussion

This study was conducted to estimate elastic properties of various silicone materials to ascertain how well various components of human breast tissue could be mimicked to create anthropomorphic breast phantoms for testing elastographic imaging modalities. In particular, it is important that such a phantom has comparable elastic properties to give a relevant evaluation of an imaging system. Hence, this work tests that main principle.

The dynamic mechanical testing was critical in assessing the stiffness parameters of various silicone elastomers and providing benchmarks for development of a realistic breast phantom. The DMA results are consistent and provide a good match to reported human breast tissue elasticity and breast phantoms previously used for research. There were some abrupt anomalies observed over higher frequencies with the very soft samples of composition D (30% SoftGel A-341C + 70% DC-200, $E' = 0.4 - 2.1$ kPa), which may be attributed to experimental errors. The machine resonance at higher frequencies might have dominated the elastic forces of this softest material due to inertial forces, leading to significant errors in the stiffness estimates of composition D.

These results provide a basis for a wide selection of materials to mimic skin, healthy and cancerous tissues in the breast. Composition C (50% SoftGel A-341C + 50% DC-200, $E' = 9$ kPa, $\zeta = 0.06$) was chosen to replicate the combined effect of the fatty and fibro-glandular tissues

present in the female human breast, as a 3 composite silicone phantom that captures both tissues separately is not entirely feasible. Composition A (100% SoftGel A-341C, $E' = 35$ kPa, $\zeta = 0.08$) was used to mimic cancerous tumors in the DIET anthropomorphic breast phantom, yielding a stiffness contrast of almost 4x.

DMA results for storage modulus, E' , for all the eight compositions ranged from 2 to 570 kPa, covering almost the whole range of elastic properties of various healthy and diseased human breast tissues reported by the previous studies. The minimum value of Young's modulus ($E^* = E' + iE''$) for adipose tissue, has been reported by Liang et al. (Liang et al., 2008) as 0.42 kPa and the maximum value for carcinoma 460 ± 178 kPa at 20% compression has been reported by Krouskop et al. (Krouskop, 1998). However, Saravazyan et al. (Saravazyan, 1995) reported 100-5000 kPa for a palpable nodule, which is exceptionally high compared to other studies. These differences can be attributed to different measurement techniques adopted by these researchers.

This study establishes a broad range of values that can be obtained using commonly available silicone elastomers. More experiments by varying the ratios of the mixtures can further increase the selections that are able to mimic a range of tissues. Other compositions with higher damping can also be chosen, depending upon the required application and elastographic modality being used, which would also allow some matching of energy dissipation properties, as well. DMA results may prove to be useful for developing phantoms of other human organs depending upon the elasticity requirements. Two different types of phantoms were constructed and tested using DIET and MRE modalities, and results show a meaningful tissue contrast matching clinical observations that is required to distinguish between healthy and cancerous tissues. Hence, it is able to create clinically valid elastic phantoms.

It was noted that the damping ratios of the chosen materials were relatively low compared to human breast tissue, and it would be interesting to see the results of phantoms developed with a higher damping material as a future study. Composition H (50% Elastosil P7600 RTV-2 + 50%

DC 200 Silicone Fluid 50 cs with $E' = 8.9 - 10.2$ kPa and $\zeta = 0.20 - 0.56$) bears strong candidature for a future study. The hyperelastic behaviour of breast tissue has not been given due emphasis in this research and a future study with a main focus on matching the nonlinear elasticity properties of the breast bears a great potential.

Moreover, as the main focus of this research was to develop breast phantoms with matching elastic properties for optical imaging and elastographic methods, consideration was not given to matching the magnetic properties of the tissue. Thus, while the main goal of matching fundamental stiffness moduli is met, there are avenues for improvement.

Finally, the anthropomorphic breast phantoms developed for evaluation of DIET breast cancer screening system, proved to be easy to handle. Phantoms constructed two years ago are still in good condition and remain in use for DIET in vitro trials. Hence, they provide a means of providing ground truth measurements in developing new modalities.

8.5 Summary

Eight compositions were mechanically testing using DMA, revealing a range of material properties spanning over $E' = 2 - 570$ kPa. Anthropomorphic breast phantoms comprising skin, adipose tissue, cancerous tumour and pectoral muscles were constructed, and tested using a DIET system. During the modal analysis of these phantoms, a significant shift in first and second resonance frequencies was observed in the inclusion areas, proving them useful for in vitro evaluation of elastographic imaging modalities.

To assess the range of possibilities a silicone phantom with two inclusions having different elastic parameters was put to trial using an MRE system. This phantom showed intrinsic contrast in the $T2^*$ weighted images, and the mechanical property images also clearly showed stiffness contrast between the materials of background and the two tumours.

The anthropomorphic breast phantoms provided stable response in handling and use. The breast phantoms developed for DIET evaluation are still in use after two years. Varying stiffness properties can be achieved by altering the ratios of the investigated materials, and, it is hoped, that this study proves to be a basis for mimicking soft tissues of other human organs.

Chapter 9

9 DIAGNOSTIC EVALUATION THROUGH SURFACE MOTION RECONSTRUCTION

9.1 Background

The first version of the DIET system measured skin surface motion by tracking hundreds of fiducial markers applied to the breast. Detected marker positions were matched between consecutive images, and between the neighbouring cameras, enabling reconstruction of motion of each marker, in 3D (Brown, 2007, Brown, 2008b, Brown, 2008a, Brown, 2010). To reconstruct the breast surface motion, all possible correspondences between pairs of markers were computed, and the breast surface, with a subset of correctly reconstructed positions lying close to the surface, was estimated using a local Random Sample Consensus (RANSAC) approach (Brown et al., 2012). These fiducial markers had to be applied over the entire breast before the start of each imaging session, costing time and inconvenience to the patient. To cut on the time cost and make the DIET breast screening easier to use, it was desirable to eliminate the requirement of the fiducial markers.

9.2 Elimination of fiducial markers

In parallel research, a new approach based on a combination of algorithms was developed to compute the 3D motion of the breast surface. A computer vision system for accurately measuring the three-dimensional (3D) surface motion of breast was developed. Model-based segmentation was used to identify the profile of the breast, and the 3D surface was reconstructed by fitting a model to the profiles. The surface motion was measured using a

customised optical flow (OF) implementation and motion of points on the surface were reconstructed by fusing the OF with reconstructed surfaces. This approach eliminated the requirement of applying fiducial markers on the skin, for robust tracking, thus making the system more user friendly. This process of 3D surface motion reconstruction consists of four main stages.

9.2.1 Model based segmentation

The DIET clinical prototype is designed to a range of different shapes and sizes of breast. Thus, the position of the breast and actuator can vary substantially between subjects. To compute the boundaries of the actuator and the breast, simple colour segmentation based on a model of the intensity and saturation is used to assign a likelihood of each pixel being background, breast or actuator.

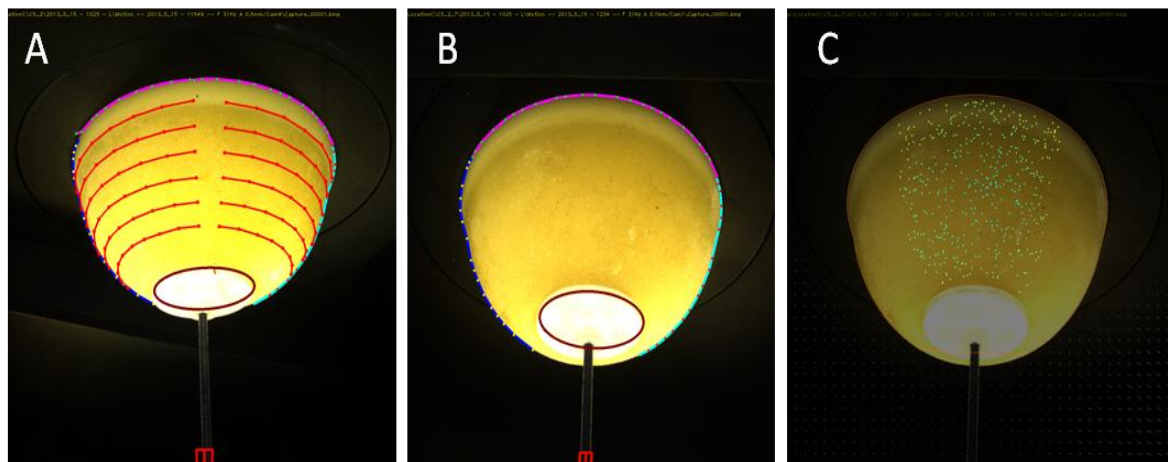


Figure 9.1: (A) Stage-1 of motion reconstruction, where the breast is segmented and the actuator interface position is identified, (B) Stage-2, showing 3D surface profiling of the breast, and (C) Stage-3, output of the dense optical flow (OF) computation

Next, a histogram equalisation is applied to reduce the effects of frame-to-frame illumination and colour variation between datasets. This process produces an actuator image, where the actuator components are clearly visible, and a skin image, from which breast location and profile

can be extracted. The actuator interface consists of two components, a metallic disc and a thin rod. It is modelled as a thin line connected to an ellipse. To locate the breast in the skin image, an active contour model, 'snake', is used (Kass et al., 1988). Figure 9.1 (A) shows a segmented breast image after identifying the actuator interface and the lead screw.

9.2.2 3D surface reconstruction

In the second stage, the breast surface is represented by a set of points, in spherical polar coordinates (r, ϑ, α) . The origin is fixed at the centre of the breast hole, and for each point, ϑ and α , are also fixed. The radial distance, r , is estimated using a Levenberg-Marquardt optimisation to minimise the distance between points on the breast contours and the projected model points. Surface smoothness is modelled by minimising the differences between neighbouring values of r . The 3D surface model projected on the 2D surface profiles is estimated by interpolation, as shown in Figure 9.1 (B).

9.2.3 Optical flow (OF) computation

In the third stage, a modern dense OF algorithm (Galvin et al., 1998, Mémin and Pérez, 1998, Alvarez et al., 2000) is applied to pairs of successive frames of images to recover the motion by tracking the skin texture. When the images are displayed successively, a sufficient variation in the skin is observed, enabling the detection of surface motion. A limitation of the dense OF technique is its inherent sensitivity to light variation (Deqing et al., 2010, Crum et al., 2004). Despite choosing the optimum settings for uniform illumination, some variation of light was still observed across the images and frame-to-frame.

This variation in lighting can be due to two reasons: 1) changing angle of the breast surface with respect to lights, and 2) spatial variation in light intensity (Botterill et al., 2012). This lighting variation is corrected by estimating the average illumination across the breast, by convolving the

greyscale image with a large Gaussian kernel. The colours are then updated to get the uniform lighting across the breast (Deqing et al., 2010, Rudin et al., 1992). Figure 9.1 (C) shows output of the dense optical flow (OF) computation.

9.2.4 Surface motion reconstruction in 3D

To detect disruption in surface motion behaviour, surface based technique for DIET diagnostics, uses measurements of the motion in 3D. Once the 3D surface of the breast and OF has been computed, the motion of any 3D point on the breast can be reconstructed using any non-linear optimisation method. Each 3D point with coordinates $X = [X_1, \dots, X_N]$ over N time-steps, lies on the corresponding surface, S. The estimation of corresponding surface, S, has errors and assumed to be independent, and normally distributed with standard deviation, σ . The X minimization can be defined:

$$c_{surface}^2 = \sum_{i=1}^N \left[\frac{d(X_i, S)}{\sigma} \right]^2 \quad (9.1)$$

where $d(X_i, S)$ is the distance of point, X_i , from the surface, S.

The motion of each point is constrained by OF fields of the reference camera (cam-1). This camera has a projection function, π , mapping points from 3D space to pixel coordinates. For each point, the constraint is defined:

$$c_{OF}^2 = \sum_{i=1}^N \left[\frac{\{\pi(X_{i+1 \text{ mod } N}) - \pi(X_i)\} - U_i\{\pi(X_i)\}}{\sigma_{OF}} \right]^2 \quad (9.2)$$

where σ_{OF} is the error in estimating the OF.

For each point, X_1 is fixed and $[X_2, \dots, X_N]$ are optimised to minimise $c_{surface}^2 + c_{OF}^2$. The smoothness constraints on the surface and OF fields are imposed to ensure that neighbouring

points have similar motion. One motion set includes 2500 points and the motion of each point is reconstructed to provide input for the DIET diagnostic.

This system is implemented in C++ and makes extensive use of Eigen-matrix and OpenCV libraries which are easily available as a free download (Library, Libraray). Reconstructing moving points on a breast takes 90 seconds on a Windows PC with an Intel 17, 8-core processor running at 2.93 GHz. This reconstruction includes segmenting 50 images sized 1600 x 1200, reconstructing ten 3D surface profiles, computing 50 OF fields, and reconstructing 2500 moving surface points. This new marker-less motion reconstruction system is compatible with the diagnostic technique based on the previous marker-based motion reconstruction.

9.3 Data acquisition

All phantoms were imaged with the clinical DIET system at a range of frequencies between 16-70Hz, at actuation amplitude of 0.5 mm. The camera pixel clock was set at 5 MHz and the frame rate at 1 fps. The camera shutter remained open for 250 ms, exposure time, at an aperture opening of F8, and, a pulse signal of 0.5% duty cycle of the input frequency was chosen to freeze the surface motion of the vibrating breast. These settings provide the optimum uniformity of illumination, minimise the glare, and ensure smooth reconstruction of surface motion in 3D. At each input frequency, ten images from each camera were captured and saved on the Host-PC in BMP format.

9.4 Tumour detection methodology

The motion of each surface point in 3D resembles an elliptical path representing steady state damped harmonic oscillation. A sine curve is fit to every ellipsoid to determine amplitude, A , and phase, φ , relative to the actuator vibration for every marker displacement $u(t)$:

$$u(t) = A \sin (\omega t + \varphi) \quad (9.3)$$

Best tumour detection performance can be achieved if imaging is performed close to the resonant frequencies, due to the strength of the captured signal and the magnitude contrast between softer and stiffer tissues. The motion on the surface of the breast is affected by the elastic properties of the underlying tissues. The phase of the oscillation relative to the actuation vibration, φ , is affected, showing less delay around stiffer areas that are potential tumours, compared to the healthy areas.

In particular, the phase, φ_z , that is in line with the direction of actuation, z-direction, is very well suited for tumour detection and the surface motion disruption signatures are more pronounced around the resonant frequencies (Lotz, 2012, Lotz, 2011b). A stiffer inclusion affects the vibration response and disturbs the surface motion pattern, which is not seen in phantoms with no inclusions (Lotz, 2010).

9.5 Diagnostic outcome

By focusing on the phase delay on the surface, the presence of an area of higher stiffness can be identified, thus, diagnosing the mass location (Lotz, 2010). Results obtained on 12 cancerous phantoms, with 20 mm, 10 mm and 5 mm inclusions, and a healthy phantom, with no inclusion, are shown in Figure 9.2. The phantoms are characterised according to the size and location of inclusions, as described in Section 8.2.6.2 and Figure 8.2 (Amer et al., 2013).

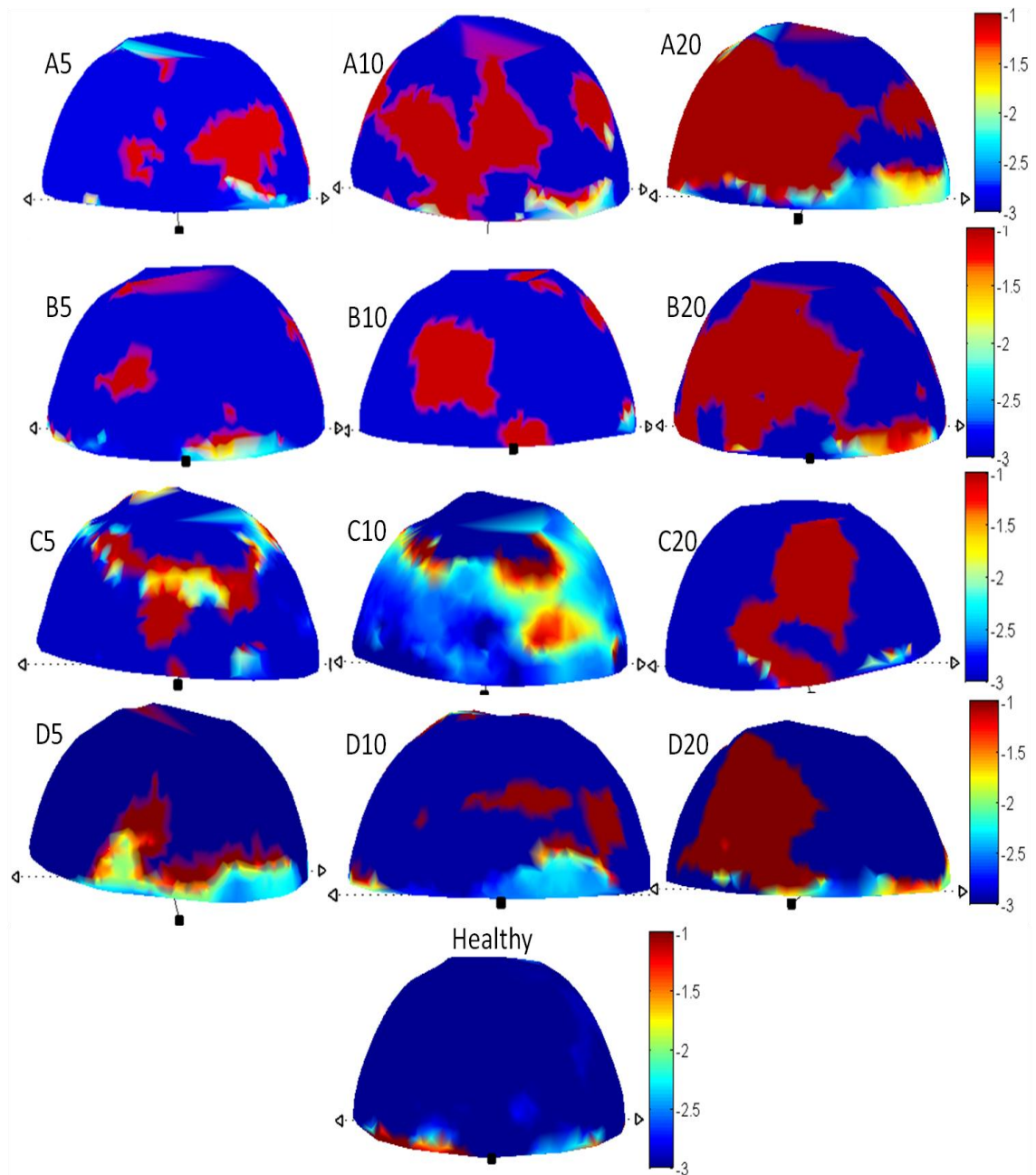


Figure 9.2: Surface motion disruption measured in terms of phase delay in the direction of actuation in the inclusion areas, identifying the presence and location of tumour. Left panel shows results of phantoms with 5mm tumour, the middle panel shows results of phantoms with 10 mm tumours and the right panel shows results from the phantoms with 20 mm tumours. The result of a healthy phantom (with no inclusion) is displayed at the bottom. These results were processed for input frequencies between 31-33 Hz.

9.6 Discussion

Due to the visco-elastic behaviour of the silicone used in breast phantoms, a phase delay of surface oscillations was observed (φ_2). A stiffer inclusion affects the vibration response and

disturbs the surface motion pattern, which is not seen in case phantoms with no inclusions. By characterising the phase delay on the surface, the presence of an area of higher stiffness can be identified, diagnosing the mass location. The frequency with the strongest diagnostic signal varies with every breast and needs to be identified individually (Feng et al., 2010), but is a process that can be automated in an initial frequency sweep.

However, in the silicone phantoms the most pronounced response was observed around the second natural frequency. The imaged frequencies of all results presented in Figure 9.2 are in the range of 31-33 Hz (Lotz, 2012, Lotz, 2011b, Lotz, 2010). It was noted that the phase pattern in the phantoms with inclusions differed significantly from the healthy phantom around the location of the inclusion. The angular locations of all almost all 20 mm, 10 mm, and 5mm inclusions were identified at the 5-7 o' clock position for tumours at 6 o' clock. This disruption in motion response was more clearly observed at Location A, B, and D.

At Location C, where the inclusions were deepest, 25 mm from the chest muscle and 15 mm away from the centre of the breast, the 20 mm tumour was clearly identifiable but the 5 mm and 10 mm tumours left only slight signatures. Location D, where the vertical distance of the inclusion from the chest wall was the same as Location C but the horizontal distance from the surface was less, provided better results compared to Location C. The angular location of inclusions was at the 6 o' clock position, and was clearly identified in almost all the phantoms. Results also corresponded well with the size of the inclusion. All 20 mm inclusions had an obvious presence, and left significantly pronounced signatures compared to the 10 mm and 5 mm inclusions. The signatures of tumours varied directly with the locations, 'depth' where the inclusions were embedded. The tumours were identified more clearly around the second resonance, which was in the range of 31-33 Hz, for silicone phantoms.

At frequencies outside this range, involvement of noise distorted the results. Within range of second resonance, it was also noted that the tumour signatures directly varied with respect to

the frequency. As can be seen in Figure 9.3, the 5mm tumour was not visible at 31 Hz and 32 Hz, whereas it showed clearly at 33 Hz. In the case of the 10 mm tumour, there was a slight indication at 32 Hz that became much more obvious at 33 Hz.

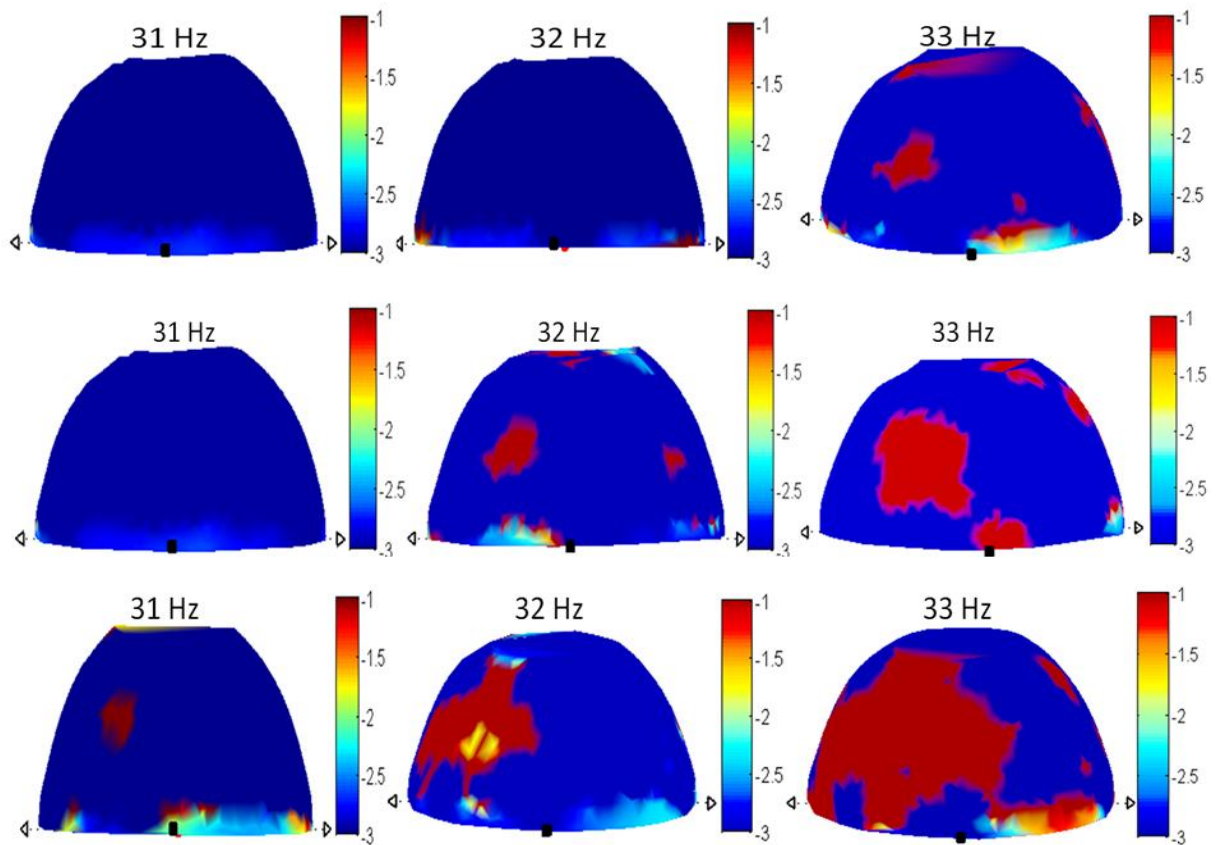


Figure 9.3: Tumour signatures as a function of input frequencies, in the range of second resonance, 31-33 Hz. (top) A phantom with 5 mm inclusion at location B, (centre) A phantom with 10 mm inclusion at location B, and (bottom) A phantom with 20 mm inclusion at location B

Of particular importance is the fact that 5mm tumours were identified at three different depth locations. This performance is comparable to, or exceeds, mammography or ultrasound, where detection of such small lesions can be highly operator dependent (Berg et al., 2006, Kopans, 1998). The average (all depths) lesion detected by mammography is typically reported as 10 mm (Pisano et al., 2008). With improved methods of detection and further advancement in technology, it is hoped that detection of 5 mm tumours will be possible, based on the preliminary results, using the DIET system.

The sensitivity of the imaged motion data to detect the presence of stiff inclusions indicated in Figure 9.2, where almost all cases could be clearly identified by visual inspection should be exploited to form the basis of an automated and robust tumour detection method, where motions detected by the DIET camera system are processed automatically to evaluate the most likely location of a stiffer inclusion (Lotz, 2011b, Peters, 2008a, Lotz, 2012). In a screening application, knowledge of the exact location or size of an inclusion is not as important as a high specificity of its existence to eliminate false positives. However, additional statistical methods and related model-based techniques, in combination with excellent *a priori* knowledge available from direct analysis of the surface motion patterns, will further enable the ability of this approach to generate a sensitive, specific and consistent process for pre-screening.

9.7 Summary

The 3D surface motion reconstruction of the Stage-1 DIET prototype was dependent on the application of fiducial markers on the breast skin for robust tracking, costing time and adding discomfort for the patient and nursing staff. A computer vision system for accurately measuring the 3D surface motion, without the use of these markers has been developed. Model-based segmentation is used to identify the profile of the breast, and the 3D surface is reconstructed by fitting a model to these profiles. Finally, the surface motion is measured using a modern optical flow (OF) implementation, which is customised to this application.

Phase delay in the induced sinusoidal vibration was chosen as potential tumour detection metric, and surface motion of 13 anthropomorphic silicone breast phantoms was manually analysed to assess this OF method. Inclusions of up to 5 mm were identified in the healthy breast tissues, surpassing the performance of manual palpation, and that of the prior prototype and surface motion tracking approach.

Chapter 10

10 DIAGNOSTIC EVALUATION THROUGH SEPERATE MODAL ANALYSIS

10.1 Background

In DIET, sinusoidal mechanical vibrations are applied to the breast and the resulting 3D surface oscillations are captured in 3D by an array of cameras surrounding the breast. The surface vibration response is analysed to detect disturbances in the observed vibration patterns, indicating a higher stiffness area within the healthy soft tissues (Peters, 2009, Brown, 2010, Brown, 2007). These high stiffness areas or inclusions may be considered potentially diagnostic.

Finite element (Peters, 2009) (FEM) or surface based methods (Lotz, 2010) can be used to detect the presence, estimated size and location of tumour. FEM provides a full 3D electrographic map of the breast, but is computationally expensive due to the need for complex, ill-conditioned inverse problem solutions (Peters, 2008a). Surface based methods (Lotz, 2010) show promising results, but rely on a visual inspection of the surface response at different imaging frequencies. Both methods thus involve an added time and cost and require an expert operator to analyse the results of 3D motion reconstruction. The minimal modelling method presented in (Lotz, 2011b) uses a broader range of imaging frequencies and fits a simple mechanical model to the frequency response of the breast surface, thus providing a software based diagnosis that is fully automated. This concept has been proven to be reliable for shallow tumour of 20 mm in diameter, but the analysis remains inconclusive for smaller inclusions.

This research presents a concept to detect the smaller inclusions, using principles of modal analysis theory (Lotz, 2012), where the frequency response of a system with multiple degrees of freedom (MDOF) is considered to be the summation of the frequency responses corresponding to each of its modes (He and Fu, 2001, Schmitz and Smith, 2008). Hypothesis testing was used to detect significant changes in the second natural frequency as being indicative of the presence of tumour. The objective was set to detect a tumour size of at least 10 mm, as this value is clinically significant in current screening applications (Michaelson, 2002).

10.2 Data acquisition

A set of 13 anthropomorphic silicone breast phantoms were developed [Chapter 8], including one homogenous healthy (with no inclusion) and 12 heterogeneous phantoms each with a stiffer inclusion (tumours) of various sizes (5mm, 10mm, and 20mm) embedded at different depth locations, as shown in Figure 8.2 and Table 8.2 (Amer et al., 2013). Each of these inclusions was positioned at 6-o'clock when viewed from the top or peak looking downward. To ensure robust tracking of the surface motion, fiducial markers were applied on the surface randomly (Brown, 2007) and the phantoms were vibrated using harmonic sinusoidal actuation of 0.5 mm amplitude, over a range of 10-50 Hz with a step size of 1 Hz.



Figure 10.1: Silicone breast phantom with examples of stiffer inclusions embedded inside

Figure 10.1 shows picture of a breast phantom with different sizes of embedded tumours. These inclusions have a stiffness contrast of approximately 4:1 compared to the phantom, as described in Chapter 8 (Amer et al., 2013).

Imaging of these phantoms was performed using the DIET clinical prototype (Lotz, 2011a). The motion was reconstructed in 3D (Brown, 2007, Brown, 2008b, Brown, 2008a, Brown, 2010) and a spherical coordinate system was defined to describe the location of the applied fiducial markers, as shown in Figure 10.2. Angle α is the elevation angle, with 0° being at the chest wall and 90° at the bust-point. Angle ϑ is the rotational angle, starting with 0° at the 12-o' clock position when viewed from front. The whole breast phantom was discretised into 126 segments in terms of α and ϑ , to account for uneven marker coverage (Lotz, 2012) and Bode diagrams of the frequency response with respect to the sinusoidal actuation were obtained covering the second resonant frequencies for each segment. The tracked motion path for each marker resembles an elliptical path in 3D-space.

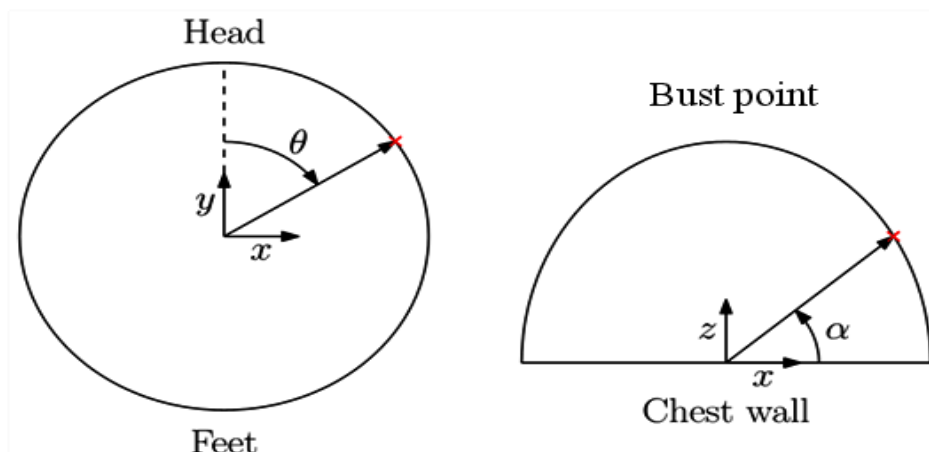


Figure 10.2: Defining angle α and ϑ . Angle α is the elevation angle with 0° at the chest wall and 90° at the bust-point, and ϑ is the rotational angle, starting with 0° at 12-o' clock position when viewed from the front, rotating clockwise.

A sine curve was fit to these ellipsoids to determine the amplitude, A , and phase, φ , in 3D for every marker displacement. The resonant frequencies obtained were compared across the surface to observe differences in behaviour between the (126) segments. Displacement data only in the vertical direction of actuation, characterised by A_z and φ_z were used. Bode diagrams of the frequency response with respect to the actuation were generated using first and second natural frequencies. Figure 10.3 shows a typical Bode diagram for one of the segments of the breast surface.

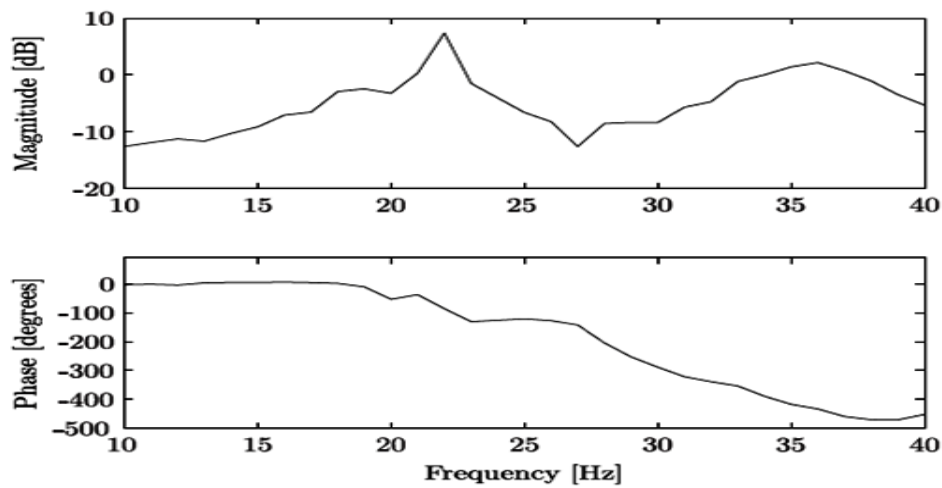


Figure 10.3: A typical Bode diagram for one of the segments of an imaged breast showing the first two natural frequencies

10.3 Modal parameter estimation

The equation of motion for a linear system with n degrees of freedom (DOF) can be defined:

$$M\ddot{q}(t) + B\dot{q}(t) + Kq(t) = f(t) \quad (10.1)$$

where $q(t)$ is the displacement vector of length n , $f(t)$ the load vector of length n , and M , B , and K are $n \times n$ mass, damping and stiffness matrices. Under the assumption of proportional damping, the condition $KM^{-1}B = B M^{-1}K$ holds. Equation 10.1 can be decoupled using the

matrix of eigenmodes U_o . By substituting the coordinate transformation $q(t) = U_o p(t)$ in Equation 10.1, followed by a pre-multiplication factor, U_o^T , the decoupled equation of motion can be defined:

$$U_o^T M U_o \ddot{p}(t) + U_o^T B U_o \dot{p}(t) + U_o^T K U_o p(t) = U_o^T f(t) \quad (10.2)$$

When the matrix of eigenmodes U_o is mass normalised ($U_o^T M U_o = I$), Equation 10.2 transforms:

$$I \ddot{p}(t) + 2\mathcal{E}\Omega_0 \dot{p}(t) + \Omega_0^2 p(t) = U_o^T f(t) \quad (10.3)$$

where \mathcal{E} is a diagonal matrix with dimensionless modal damping factors ζ_k , and Ω_0 is a diagonal matrix with un-damped natural frequency ω_{ok} noting that it is Ω_0^2 . Under the assumption of harmonic excitation and response, and using the back-substitution of the coordinate transformation $q(t) = U_o p(t)$, the frequency response matrix is obtained:

$$\begin{aligned} \hat{q}(\omega) &= U_o (-\omega^2 I + 2j\omega\mathcal{E}\Omega_0 + \Omega_0^2)^{-1} U_o^T \hat{f}(\omega) \\ &= \sum_{k=1}^n \frac{u_{ok} u_{ok}^T}{-\omega^2 + 2j\zeta_k \omega_{ok} \omega + \omega_{ok}^2} \hat{f}(\omega) \end{aligned} \quad (10.4)$$

In the case of single-input-single-output (SISO), multiple degrees of freedom (MDOF) system, Equation 10.4 reduces to a summation of a single mass-spring-damper system multiplied with a constant, which is determined by the modes of the system. As this tumour detection concept only takes the first two natural frequencies into account, Equation 10.4 can be written:

$$\hat{q}(\omega) = \frac{A1}{-\omega^2 + 2\zeta_1\omega_{O1}\omega j + \omega_{O1}^2} \hat{f}(\omega) + \frac{A2}{-\omega^2 + 2\zeta_2\omega_{O2}\omega j + \omega_{O2}^2} \hat{f}(\omega) \quad (10.5)$$

where $A1$ and $A2$ are constant multiplication factors determined by the eigenmodes of the system.

In this way, the problem of fitting the data in the Bode diagram in Figure 10.3 can be reduced and the data can be split in two to fit each natural frequency independently.

Fitting the two peaks at once proved difficult using a nonlinear least square method. The model structure is capable of capturing the response shown in Figure 10.3, as verified by manual parameter estimation. However, these nonlinear least squares methods found local minima or identified 'false' peaks due to noise in the data. To overcome this problem, the data was split into two parts and fit independently.

First, the end of the first peak was determined, under the assumption that the end of this peak was characterised by a local minimum in the magnitude and a phase of 180° . Robustness margins were incorporated to ensure reliable results with noisy data. The fitting procedure described in (Lotz, 2011b) was used to determine the first natural frequency, ω_{O1} , and the corresponding damping factor, ζ_1 , using data up to the end of the first peak. This method proved to be very robust and reliable.

The second natural frequency was identified using the data for frequencies larger than the first natural frequency, ω_{O1} , and the entire model structure, as defined in Equation 10.5, was used to assure a good match in phase. This approach produced reliable results for the second natural frequency, ω_{O2} , and corresponding damping factor, ζ_2 . By combining the results from the two identification procedures, reliable fits were obtained. These fits allowed further analysis on the modal parameters, especially the second natural frequency, ω_{O2} , for diagnostic purposes.

10.4 Statistical diagnostic analysis

To account for the uneven coverage of the fiducial markers on the surface, the breast was divided into 126 small segments in terms angles, ϑ and α . The analysis was performed with 18 segments in the ϑ -direction, and 7 segments in α -direction, moving from 15° to 45° to avoid areas just around the actuator and around the chest wall in poor or no response. More specifically, the actuator and the chest wall disturb the surface motion by their dominant boundary conditions, yielding less useful response. Increasing the number of segments could result in a higher resolution, but also increases the chance of gaps in the data due to gaps in fiducial marker coverage. Figure 10.4 shows an example of the segments used overlaid upon a triangulation of the tracked fiducial markers.

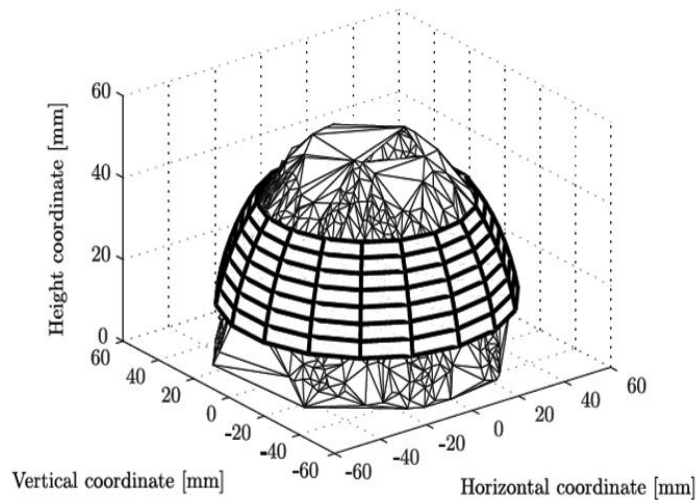


Figure 10.4: An example of the used segments, overlaid upon a triangulation of the tracked fiducial markers

The two resonant frequencies identified from data within each segment were compared across the surface of the breast. It was observed that the area of the tumour location shows a lower second natural resonance compared to the healthy areas. To assess statistical significance of the differences observed, a two-sample t-test was used to reject the hypothesis that two areas were similar in resonance behaviour. A significance threshold of $\alpha = 0.01$ was chosen, indicating a 99%

confidence interval. The hypothesis tested was that the area of interest has the same or different (lower) second resonance compared to the rest of the surface (Lotz, 2011b, Lotz, 2012).

To analyse significant changes in this metric within the breast, the segments were regrouped in two further sub-groups in the ϑ -direction. The first group included all segments within a 60° range in ϑ -direction. The second group consisted of all other segments. This process was repeated for all 18 ϑ -direction segments, thus, ensuring a large enough dataset to generate a meaningful distribution.

The p -values obtained provided a statistical measure of the difference in the observed metric in one area of the breast, compared to the remaining surface. A segment with a low p -value, specifically a p -value below the α -level 0.01, indicated a significantly lower second natural frequency in that section, which is an effect consistently observed around the areas of stiffer inclusion.

10.5 Outcome of the separate modal analysis

The method discussed in Section 10.4 was applied to all 13 silicone phantoms (Amer et al., 2013). A typical example of the fitting procedure is shown in Figure 10.5. Separate fits for the first and second natural frequency are shown, the sum of these fits produces a close match to the original measurement.

In Figure 10.6, a healthy segmented phantom viewed from the front, overlaid with a colour-map of the second natural frequency, ω_{02} , is shown. Figure 10.7 shows the colour-maps of all 12 breast phantoms with inclusions of different sizes at different locations. B10 for example, shows a 10mm tumour at location B, description of tumour locations can be found in Table 8.2. At the tumour location (6-o' clock position) statistically significant differences in natural frequency

were seen. In the 20 mm and 10 mm cases, decreases in natural frequency of about 10% were evident by a visual inspection. The 5 mm tumour and the healthy cases remained inconclusive.

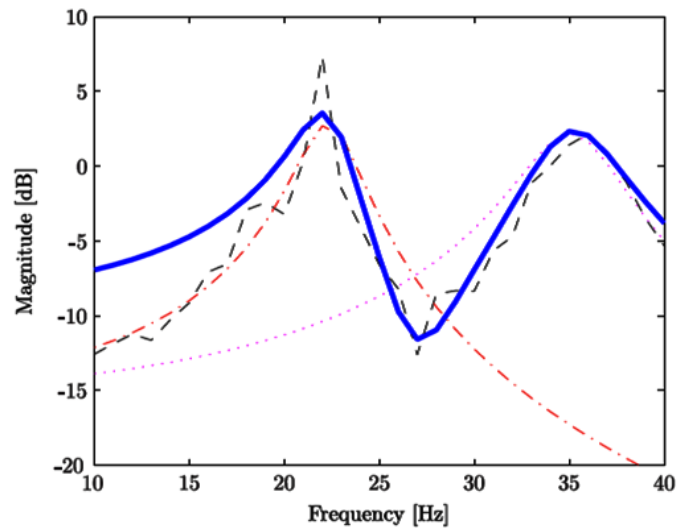


Figure 10.5: A typical example of the fitting results. Measurement data is shown in dashed black, fit of the first natural frequency in dash-dotted red, fit of the second natural frequency in dotted magenta and the combined fit is shown in solid blue.

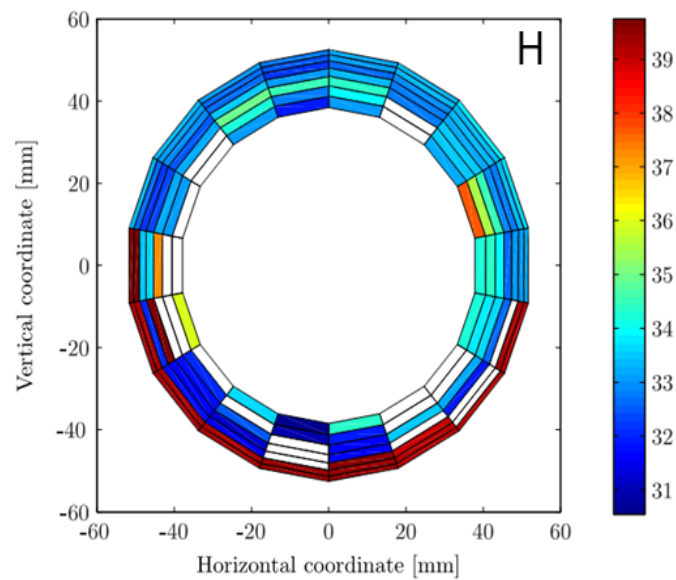


Figure 10.6: Segmented healthy breast phantom viewed from the front with a colour-map of second natural frequency, ω_{02} , in Hz

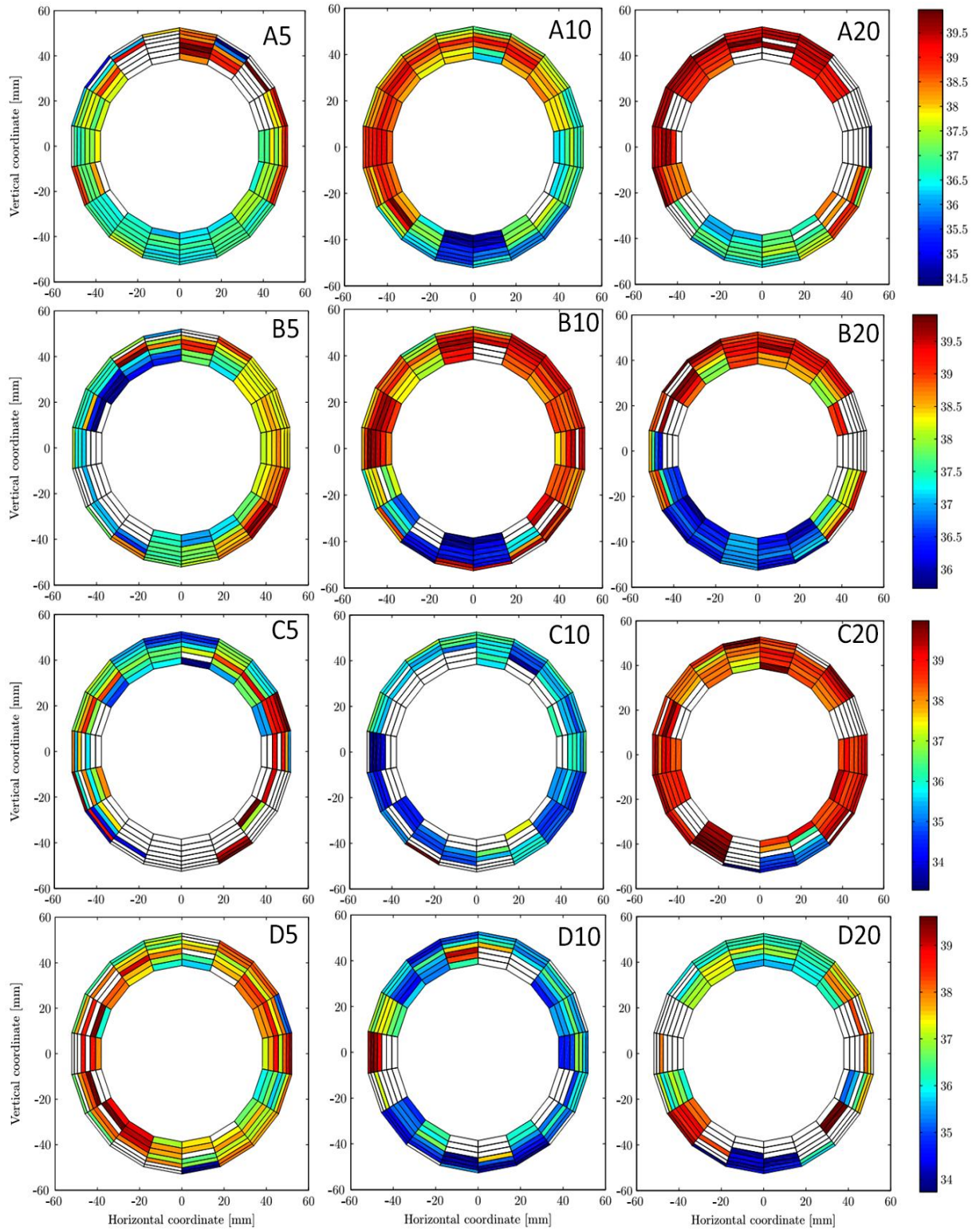


Figure 10.7: Segmented breast phantoms with inclusions viewed from the front with a colour-map of second natural frequency, ω_{02} , in Hz. Left column shows results of phantoms with 5 mm tumour, middle column shows results of phantoms with 10 mm tumours, and the right column shows results of phantoms with 20 mm tumours, at locations A-D. Blank (white) segments indicate bad model fits due to noise and gaps in the data.

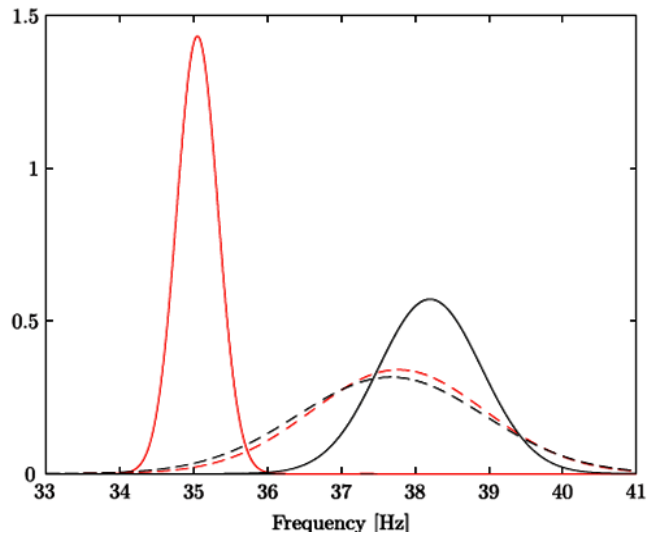


Figure 10.8: Probability density functions for the normal distributions in two different segments of the breast phantom with a 10 mm tumour. The solid red line represents the data in the segment $160^\circ < \vartheta < 220^\circ$ and the dashed red line corresponds to data outside this segment. Similarly, the solid black line show data in the segment $300^\circ < \vartheta < 360^\circ$ and the dashed black line considers the data outside this range.

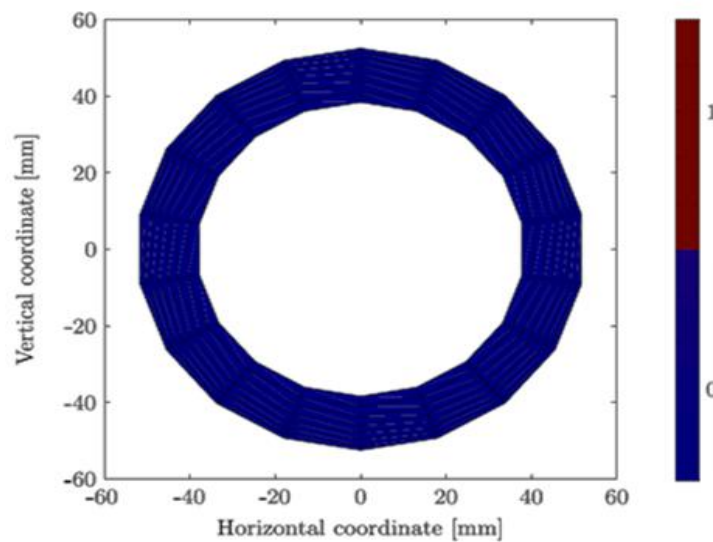


Figure 10.9: Result of the t -test for a healthy phantom (no inclusion), showing that the hypothesis was accepted in all 126 segments across the surface and no difference in second natural frequency was observed

The probability density functions for the normal distributions in two different segments of breast phantom with 10 mm tumour are shown in Figure 10.8. The black lines represent the distributions for the range $300^\circ < \vartheta < 360^\circ$ (top of the breast) and the red lines represent the distribution for the range $160^\circ < \vartheta < 220^\circ$ around the location of the tumour. The solid lines represent the data in the given ranges, the dashed lines correspond to all the data outside this

range. Clearly, the data with $160^\circ < \vartheta < 220^\circ$ (solid red) has a different mean than the data outside this region (dashed red).

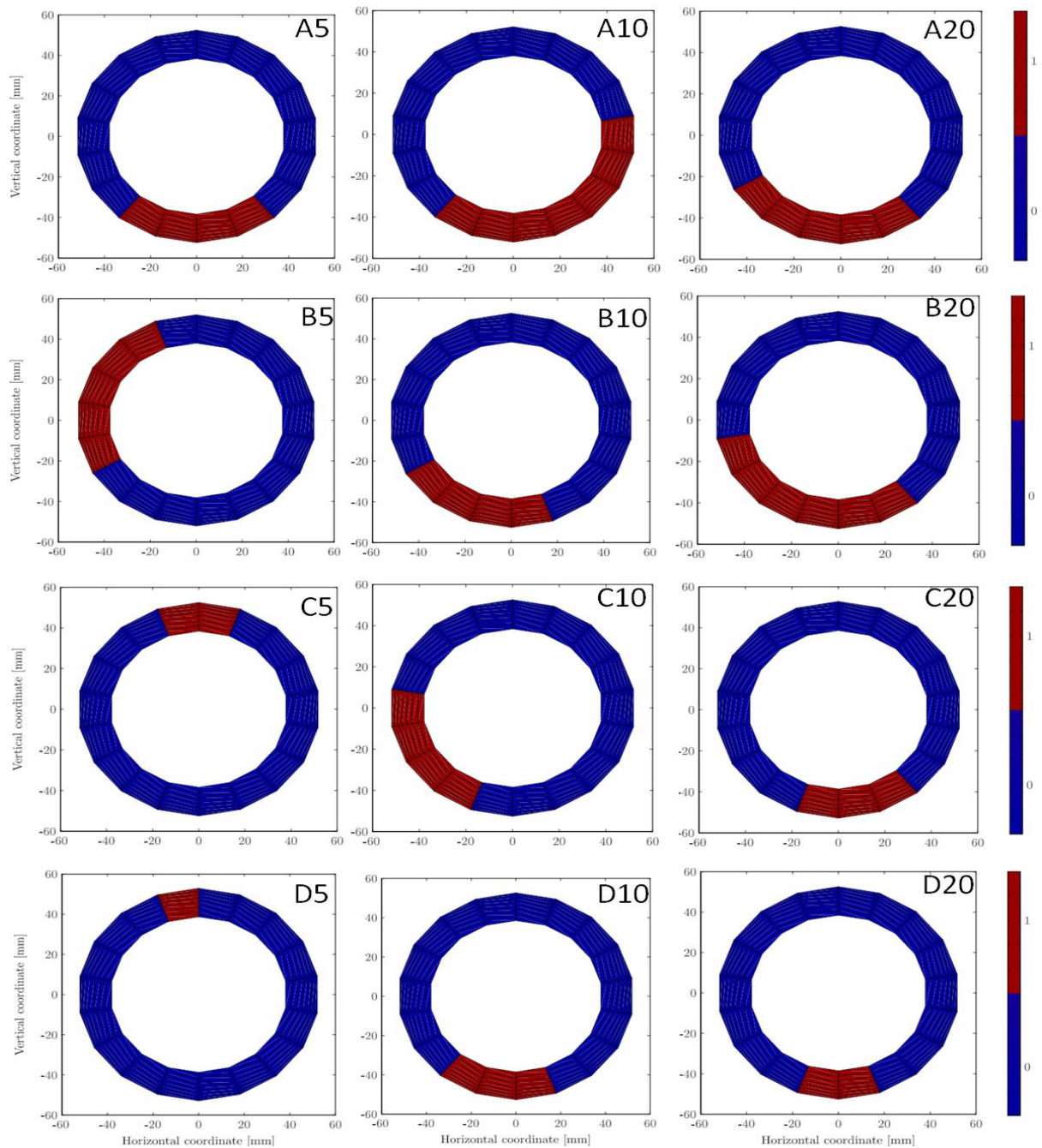


Figure 10.10: Results of the t -test for phantoms with different tumour sizes: 5 mm [A-D] (left), 10 mm [A-D] (centre), and 20 mm [A-D] (right). The threshold outcome $1-p$ (hypothesis rejected (red) or accepted (blue)) is shown in each case, indicating a lower second natural frequency and thus a stiffer inclusion at the red areas.

In the second case, the two distributions corresponding to the data within $300^\circ < \vartheta < 360^\circ$ range (solid black) and the data outside this range (dashed black), show a great amount of overlap.

Figure 10.10 shows results of the t -test for all 12 breast phantoms with tumours. The red areas (value-1) show segments where the hypothesis was rejected, indicating a lower second natural frequency, ω_{02} , with a 99% confidence interval.

To analyse the differences in the resonance behaviour across the breast, the t -test results were used for all 13 phantoms. The hypothesis used was that no difference was observed in the second natural frequency, ω_{02} , across all the 126 segments of the breast surface. Figure 10.9 shows the result of t -test for a healthy phantom, and that the hypothesis was accepted (blue) in all 126 segments across the surface of the breast phantom.

10.6 Separate modal analysis as a diagnostic tool

The modal analysis of the breast has potential to identify areas of higher stiffness as previously shown for a phantom with a 20 mm tumour (Lotz, 2011b). This extended study verified a concept to expand the modal analysis to a second resonant frequency. With higher frequencies, a higher resolution in detection performance is likely. The proposed method using the model in Equation 10.5 produced good model fits. The model was able to capture the frequency response data from the surface of the oscillating breast phantoms.

By splitting the problem into two parts, the method discussed in (Lotz, 2011b) was used to first identify the first resonance, and proved to be robust and reliable. The fitting of the second peak gave problems for segments close to the chest wall and to the actuator. However, in other segments, the fits were reasonably good. Due to the relatively high damping, resonances higher than first order were more affected by noise and less observable. However, the second natural frequency identified over the surface of the breast showed a marked decrease around the tumour location. For the phantoms with 10 mm and 20 mm tumours, this distinctive behaviour showed clearly. However, but was not observed in the healthy phantom without an inclusion.

The 5 mm inclusions did not show a clear and distinctive behaviour in the second resonance. The reason of this noncompliance could be the dominant damping effects or problems in the model fitting, as evident in the blank (white) segments seen in Figure 10.7. Imaging the breast at higher frequencies and analysing the 3rd natural frequency might prove to be more conclusive for smaller inclusions. In this analysis, the shift in resonance behaviour was verified statistically, with a 99% confidence level. The fact that the results were consistent for 10 mm and 20 mm inclusions further indicated that the results were not coincidental.

For some phantoms, the identified inclusion area deviated from the expected tumour location. One reason for this result could be off-centred induction of vibrations during DIET imaging. A second, is that placing these inclusions and orienting the phantom exactly for testing is not precise. Finite Element (FE) simulations of exactly the same situation also show a similar deviation in the disturbance of the motion data and deviations up to 45° are considered to be acceptable (Lotz, 2012), mainly for the reasons outlined.

10.7 Summary

This research presented a concept to detect stiffer inclusions in the healthy breast tissues by using principles of modal analysis theory. Hypothesis testing was used to detect significant changes in the second natural frequencies, indicating presence of tumour. The objective was to detect at least a 10 mm tumour, which is a clinically significant size, in screening applications. This goal was successfully achieved. The approach presented is capable of detecting tumours of 10 mm in diameter or larger in silicone phantoms in an objective way, by only analysing surface motion of the oscillating breast. The approach is computationally inexpensive and well-conditioned, especially when compared to inverse finite element analysis. If in-vivo validation yields similar results, the method presented could be used to detect the existence and approximate location of a stiffer inclusion in clinical real time within moments of testing. This

method provides software based diagnosis based fundamental mechanics and statistical analysis, and does not require any human intervention. Combined with the DIET system, this approach could provide a reliable screening modality, complementary to mammography and other screening techniques currently in use.

Chapter 11

11 CONCLUSIONS

The research presented in this thesis has developed and validated a fully functional clinical prototype of the DIET breast cancer screening system ready and suitable for use in large-scale clinical trials. The major objective of the research was system development of the imaging technology for the DIET system with a particular focus on image quality, imaging speed, robust vibration actuation, ergonomic design and a new imaging procedure.

These objectives have been achieved. The image capture system is capable of capturing 50 motion images, from an array of five industrial cameras, in 17.4 seconds, at one frequency, a 93% reduction in imaging time compared to the previous system. A clinical prototype on the standards of modern elastographic imaging medical devices has been ergonomically designed. A specific focus has been given to the modularity of all the subsystems to allow any future hardware and software modifications, enabling much of DIET's advantages regarding portability of the method.

The main components of the DIET system developed during this research are: 1) the imaging array of five industrial cameras for robust capturing of quality images in the least possible time; 2) the development and synchronisation of strobe flash system to eliminating the requirement of high speed, expensive cameras; 3) the design, development and implementation of an application-specific steady state sinusoidal harmonic vibration motion actuator with automated positioning control in 3-Axis and superior performance to prior solutions; 4) the overall ergonomic design of the device and integration of the imaging technology to ensure patient comfort, ease of operation, speedy trials and portability of the medical device; and 5) the

automated imaging software and Windows-based graphical user interface (GUI), ensuring automated image capture with minimal operator skills.

Moreover, a new approach for 3D motion reconstruction based on modern OF techniques has successfully been implemented, which eliminates the requirement of fiducial markers for robust tracking. A new software-based, fully automated, diagnostic approach using a separate modal analysis of the breast has also been developed. Finally, 13 anthropomorphic silicone breast phantoms with matching stiffness parameters were constructed to assess the performance of the developed system and the clinical DIET system has been diagnostically evaluated and tumours of to the size 5 mm have been successfully identified using two different tumour detection techniques.

More specifically, the time for acquisition of motion images at a single frequency with Stage-1 DIET prototype, was over 4:12 minutes, thus, a sweep of 20 frequencies, required approximately 1:20 Hours. This imaging time was not suitable for a breast cancer screening application. In clinical DIET system, an array of software controlled industrial cameras has been developed and the image capture time has been reduced to 17.4s at one frequency, this would enable a screening of 10-20 frequencies in 3-6 minutes per breast.

The previous system provided 10 kcD illuminations for DIET imaging, which entailed longer exposure times and a higher duty cycle (2%) for pulse generation. The longer exposure increased overall imaging time and also caused blurriness in the resulting images. There was also no mechanism for reduction of glare, which caused loss of information in the motion data. A new strobe flash system with high power LEDs was designed increasing the overall illumination by a factor of $\sim 10x$. A circular polarizer has been applied which attenuate the glare twice, once while leaving the light source and again while entering the camera aperture. The pulse generation duty cycle has been reduced from 2% to 0.5% and exposure time from 2s to 250ms. The design and implementation of this new strobe illumination system has eliminated blurriness from

motion images, provided a ~100% reduction of glare, and increased the image capture speed by a factor of ~15x. Moreover, with the synchronisation of this strobe system with actuation, the need for high frame rate, expensive, CCD cameras has been eliminated.

The vibration actuation in the stage-1 DIET system showed limitations, particularly in terms of size and positioning. The mechanical response of the breast was modelled, and the actuation stroke and force requirements were estimated to integrate 3-voice coils in the actuation system. For accurate synchronisation, a real-time controller was programmed to communicate with Host-PC through TCP/IP, using an LVDT feedback. Vibration analysis was conducted and damping feet were implemented to provide vibration isolation to the cameras. Overall, a compact and accurate actuation system capable of providing actuation of 1-2 mm peak-to-peak at frequency range of 10-90 Hz was designed and implemented, with a remote and automated 3- axis positioning control providing a much more effective and flexible solution.

All the subsystems were installed and integrated in the ergonomically designed DIET clinical prototype, to ensure patient comfort and ease of operation. A low risk ethical approval was obtained and an ergonomic trial was conducted with participation from 23 female subjects to finalise the ergonomics. The top surface was ergonomically designed in view of the anthropomorphic dimensions of women of 50th percentile. The resulting system design is wheeled to ensure easy portability and has height adjustable feet to ensure levelled positioning during examination. The physical dimensions of the system (700 L x 650 W x 300 H) mm³ and its weight (45 Kg) ensure the mobility and portability expected from this screening concept. The overall design promises flexibility for future modifications.

The imaging procedure in the previous DIET prototype was dependent on a console application and it was not possible to run the system with a non-skilled or lesser-skilled operator. The imaging procedure has been automated and a Windows-based graphical user interface (GUI) has been developed to ensure system operation without any operational training. A real-time video

from two different cameras has been incorporated to facilitate positioning of the breast interface according to breast size and a testing mode has provided to monitor performance of a number of DIET systems employed in large scale screening programmes. All of these changes help this DIET concept reduce cost and time for screening, while increasing its flexibility and compatibility as a potential screening tool.

To assess the system and diagnostic performance, 13 anthropomorphic breast phantoms comprising skin, adipose tissue, cancerous tumour and pectoral muscles were constructed. To mimic breast tissues, eight compositions were mechanically testing by DMA, revealing a range of material properties spanning over $E' = 2 - 570$ kPa. The developed phantoms were used for ex-vivo trials of the clinical prototype using two different diagnostic techniques and inclusions of up to the size of 5 mm were successfully identified. Similar phantoms were also subjected to MRE, which showed intrinsic contrast in the T2* weighted images. The mechanical property images also clearly showed stiffness contrast between the materials of background and tumours. It is hoped, that this aspect of the overall research presented will provide a basis for mimicking soft tissues and developing phantoms of other human organs, as well, providing further research outcomes.

The 3D surface motion reconstruction of the Stage-1 DIET prototype was dependent on the application of fiducial markers for robust tracking, costing time and adding discomfort for the patient and nursing staff. A computer vision system for accurately measuring the 3D surface motion, without the use of these markers has been developed. This OF based method met or exceeded prior methods.

During the diagnostic evaluation two different modalities were used. The phase delay, φ_z , in the induced sinusoidal vibration was chosen as potential tumour detection metric. Surface motion of 13 anthropomorphic silicone breast phantoms was then manually analysed to assess elastographic tissue characterisation using DIET clinical system. Inclusions of up to 5 mm were

identified in phantoms, surpassing the performance of manual palpation, and that of the prior prototype and surface motion tracking approach.

Finally, a new diagnostic technique using the principles of modal analysis theory has been developed to identify stiffer inclusions in the healthy breast tissues. Hypothesis testing was used to detect significant changes in the second natural frequencies that indicated presence, location and size of the tumours. This approach is computationally inexpensive and well-conditioned, especially when compared to inverse finite element analysis. The approach presented is capable of detecting tumours of 10 mm in diameter or larger in silicone phantoms. If in-vivo validation yields similar results, the method presented can be used to detect the existence and approximate location of a stiffer inclusion in clinical real time within moments of testing. This method provides software based diagnosis based on fundamental mechanics and statistical analysis, and does not require any human intervention. Combined with the DIET system, this approach can provide a reliable screening modality, complementary to mammography and other screening techniques currently in use.

In summary, the major requirement of this research was the system development of the clinical DIET prototype system that required several major improvements to realize full potential of the DIET concept. The main components of this research were the hardware development of the imaging technology, software implementation, automation of the imaging procedure and diagnostic evaluation of the DIET technology. All of these requirements were successfully accomplished and the clinical DIET prototype system is ready and suitable for a large scale human trial to establish the sensitivity and specificity of this novel breast cancer screening technology.

Chapter 12

12 FUTURE WORK

The following short sections offer potential avenues for future development and DIET research.

12.1 A large scale clinical trial

The next major aim for the DIET project is to conduct a large scale clinical trial. Once adequate clinical data has been acquired, it may be analysed by an isolated research group using finite element method, surface based detection, and separate modal analysis, to establish the sensitivity and specificity of this novel breast cancer screening technology, which has the potential to surpass manual palpation and can be used as screening modality, adjunct to mammography.

12.2 Optimisation of illumination

The important innovation of the OF estimation that has replaced the coloured fiducial system with features extraction directly from the breast surface is highly sensitive to light variation. During the performance evaluation, slight light variation was observed frame-to-frame. This variation could be due to the changing angle of the breast surface with respect to light or due to spatial variation in the light intensity. This issue of illumination variation has been addressed in the software during the motion reconstruction. However, a future DIET system will seek improvement in the hardware configuration of the lighting scheme.

Botterill et al. (Botterill et al., 2012) have suggested an illumination optimisation scheme to design a new lighting configuration on the principle that with multiple sources, illumination

should be provided predominately at low incidence angles. They have suggested repositioning the existing 5 light configuration such that four lights are positioned on the four outer edges of the hemisphere containing the cameras and one overhead close to the breast. This repositioning was not possible in the developed system due to space constraints. However, these recommendations should be given due priority in the construction of a second clinical system, if the technology is accepted for commercialization.

12.3 Upgradation of the Host-PC

DIET system is currently using a host machine running Windows XP at 2 GHz dual core processor with 2 GB RAM. This machine is being used for imaging only, due to the National Instrument Licence restrictions, for the use of LabVIEW. For surface motion reconstruction and diagnostic evaluation another Windows PC with an Intel i7, 8-core processor running at 2.93 GHz is being used. Before the start of a large clinical trial, it is desirable to upgrade the Host-PC to provide one window operation starting from image capture to diagnostics. It will ensure better image download speed and further reduce the processing time.

12.4 More realistic breast phantoms

The phantoms used in this research were produced to mimic human breast tissue elasticity. While the Young's modulus, E^* , matched well, the damping characteristics found to be on the lower side. A composition with a storage modulus, E' , of 9 kPa was used for mimicking adipose which is a bit higher than the reported. A more realistic breast phantom, with lower storage modulus, E' , and higher damping characteristics for the fatty tissue can be produced, in the light of DMA measurements presented in Chapter 8.

The developed phantoms have been tested for evaluation of DIET and MRE systems and it is expected that the same can be used for ultrasound elastography (USE). However, their use for USE could not be ascertained, and it would be worth testing for USE evaluation.

12.5 Further research in tumour detection through separate modal analysis

The analysis presented in Chapter 10 only uses the surface motion in the direction of actuation. However, the surface of the breast moves in 3D space. Therefore, multidimensional models might be useful to further enhance the tumour detection algorithm for the DIET system. In particular radial direction seems suitable for this analysis and should be incorporated as a further improvement.

The 5 mm tumour did not show distinctive behaviour at the second resonance in this analysis. This could be due to problems in model fitting, as evident in the white segments seen in Figure 10.7. Imaging the breast up to higher frequencies and incorporating the 3rd natural frequency might give conclusive results for smaller inclusions.

12.6 Robust reconstruction of 3D skin surface

With the innovative OF estimation for surface motion reconstruction in 3D, the requirement of applying the fiducial markers on the skin has been eliminated. During the evaluation trials of the DIET system, the results indicated that the new system is considerably more accurate than the previous marker based system. In very few cases, the motion reconstruction did not work well in the absence of markers. This can be due to inherent sensitivity of the OF estimation to the illumination variation. However, a further research would be desirable to make the motion reconstruction algorithm more robust and repeatable.

References

2002. Cancer: New Registrations and Deaths 1999. *New Zealand Health Information Service*. New Zealand Ministry of Health.
- 2004a. BreastScreen Aotearoa national Policy and Quality Standards. National Screening Unit.
- 2004b. An update on the free national screening program. National Screening Unit.
2006. Cancer Patient Survival Covering the Period 1994 to 2003. *New Zealand Health Information Service*. New Zealand Ministry of Health.
- (EO), E. O. I. *Edmund Optics Technical Support* [Online]. Available: <http://www.edmundoptics.com/technical-support/technical-library>
- ABBAS, S. & DONALD, P. 2004. A method to measure the hyperelastic parameters of ex vivo breast tissue samples. *Physics in Medicine and Biology*, 49, 4395.
- ALMAGABLEH, A., MANTENA, P. R., ALOSTAZ, A., LIU, W. & DRZAL, L. T. 2009. Effects of bromination on the viscoelastic response of vinyl ester nanocomposites. *J. EXPRESS Polymer Letters*, 3, 724-732.
- ALVAREZ, L., WEICKERT, J. & SÁNCHEZ, J. 2000. Reliable estimation of dense optical flow fields with large displacements. *International Journal of Computer Vision*, 39, 41-56.
- AMER S. KASHIF, THOMAS F. LOTZ, MATTHEW D. MCGARRY, ADAM J. PATTISON & CHASE, J. G. 2013. Silicone breast phantoms for elastographic imaging evaluation. *Medical Physics*, 40, 063503.
- ANDERSON, B. O., YIP, C.-H., SMITH, R. A., SHYYAN, R., SENER, S. F., ENIU, A., CARLSON, R. W., AZAVEDO, E. & HARFORD, J. 2008. Guideline implementation for breast healthcare in low-income and middle-income countries. *Cancer*, 113, 2221-2243.
- ASGHARI, A. & NICHOLAS, M. K. 2004. Pain during mammography: the role of coping strategies. *Pain*, 108, 170-9.
- AUTOMATION, A. Available: <http://www.autolineautomation.co.nz>
- BERG, W. A., BLUME, J. D., CORMACK, J. B., MENDELSON, E. B. & MADSEN, E. L. 2006. Lesion detection and characterization in a breast US phantom: results of the ACRIN 6666 Investigators. *Radiology*, 239, 693-702.
- BIRET PIERRICK 2011. Design improvement of the Digital Image-based Elasto-Tomography (DIET) Breast Cancer Screening. University of Canterbury.
- BOTTERILL, T., MILLS, S., GREEN, R. & LOTZ, T. Year. Optimising Light Source Positions to Minimise Illumination Variation for 3D Vision. *In: 3D Imaging, Modeling, Processing, Visualization and Transmission (3DIMPVT)*, 2012 Second International Conference on, 13-15 Oct. 2012. 222-229.

- BROWN, R. G. 2008a. *Three-dimensional motion capture for the DIET breast cancer imaging system*. PhD, Department of Mechanical Engineering, University of Canterbury.
- BROWN, R. G., CHASE, J. G. & HANN, C. E. 2012. A pointwise smooth surface stereo reconstruction algorithm without correspondences. *Image and Vision Computing*, 30, 619-629.
- BROWN, R. G., HANN, C.E., CHASE, J.G., RAY, L.E. Year. Surface Reconstruction for a DIET breast cancer screening system. *In: 17th International Federation of Automatic Control World Congress (IFAC)*, 6-11 July 2008b Seoul, Korea.
- BROWN, R. G., HANN, C.E., CHASE, J.G. 2010. Vision-based 3D Surface Motion Capture for the DIET Breast Cancer Screening System. *International Journal of Computer Applications in Technology*, 39, 72-78.
- BROWN, R. G., HANN, C.E., CHASE, J.G., RAY, L.E. 2007. Discrete Colour-based Euclidean-Invariant Signatures for Feature Tracking in a DIET Breast Cancer Screening System. *SPIE Medical Imaging*. San Diego, USA: SPIE.
- CHASE, J. G. C., NZ), PETERS, ASHTON (NORTH PERTH, AU), LOTZ, THOMAS FRIEDHELM (CHRISTCHURCH, NZ), RAY, LAWRENCE ALLEN (ROCHESTER, NY, US). 2009. *USE OF SURFACE MOTION TO IDENTIFY MECHANICAL PROPERTIES OF BIOLOGICAL TISSUE*. United States patent application 12/395,205.
- CHEMIE, W. Available: <http://www.wacker.com/cms/en/products-markets/products/product.jsp?product=12920>
- CHU, K. C. & RUTT, B. K. 1997. Polyvinyl alcohol cryogel: An ideal phantom material for MR studies of arterial flow and elasticity. *Magnetic Resonance in Medicine*, 37, 314-319.
- COLAS, A. 2005. Silicones: Preparation, Properties and Performance. Available: <http://www.dowcorning.com/content/publishedlit/01-3077.pdf>
- CONTROLS, A. M. 3805 Calle Tecate, Camarillo, CA, USA. Available: <http://www.a-m-c.com>
- CORPORATION, T. Available: <http://www.taica.co.jp/gel-english/index.html>
- COUGHLIN, S. S. & EKWUEME, D. U. 2009. Breast cancer as a global health concern. *Cancer epidemiology*, 33, 315-8.
- CREE. 2011. *LED Chips & Materials*) [Online]. Available: <http://www.cree.com>
- CRUM, W. R., HARTKENS, T. & HILL, D. L. G. 2004. Non-rigid image registration: theory and practice. *British Journal of Radiology*, 77, S140-S153.
- DEQING, S., ROTH, S. & BLACK, M. J. Year. Secrets of optical flow estimation and their principles. *In: Computer Vision and Pattern Recognition (CVPR)*, 2010 IEEE Conference on, 13-18 June 2010 2010. 2432-2439.
- DESANTIS, C., SIEGEL, R., BANDI, P. & JEMAL, A. 2011. Breast cancer statistics, 2011. *CA: A Cancer Journal for Clinicians*, 61, 408-418.

- DEVI, C. U., BHARAT CHANDRAN, R. S., VASU, R. M. & SOOD, A. K. 2007. Measurement of visco-elastic properties of breast-tissue mimicking materials using diffusing wave spectroscopy. *Journal of Biomedical Optics*, 12, 034035-034035.
- DOYLEY, M. & WEAVER, J. 2005. Magnetic Resonance Elastography: Experimental Validation and Performance Optimazation. *Alternative Breast Imaging*. Springer US.
- EGOROV, V. & SARVAZYAN, A. P. 2008. Mechanical Imaging of the Breast. *Medical Imaging, IEEE Transactions on*, 27, 1275-1287.
- EGOROV, V., TSYURYUPA, S., KANILO, S., KOGIT, M., SARVAZYAN, A. 2008. Soft tissue elastometer. *Medical engineering and physics*, 30, 206-12.
- ELTING, L. S., COOKSLEY, C. D., BEKELE, B. N., GIORDANO, S. H., SHIH, Y. C., LOVELL, K. K., AVRITSCHER, E. B. & THERIAULT, R. 2009. Mammography capacity impact on screening rates and breast cancer stage at diagnosis. *American journal of preventive medicine*, 37, 102-8.
- ERNEST, L. M., GARY, R. F., MARITZA, A. H., HAIRONG, S., JINGFENG, J., TOMY, V. & TIMOTHY, J. H. 2005. Spherical lesion phantoms for testing the performance of elastography systems. *Physics in Medicine and Biology*, 50, 5983.
- EVANS, A., WHELEHAN, PATSY, THOMSON, KIM, MCLEAN, DENIS, BRAUER, KATRIN, PURDIE, COLIN, JORDAN, LEE, BAKER, LEE, THOMPSON, ALASTAIR 2010. Quantitative shear wave ultrasound elastography: initial experience in solid breast masses. *Breast Cancer Research C7 - R104*, 12, 1-11.
- FACTOR II, I. Available: http://www.factor2.com/product_p/a-341.htm
- FENG, S. 2010a. *An Image Based Vibration Sensor for Soft Tissue Modal Analysis in a Digital Image Elasto Tomography (DIET) System*. Master of Engineering (Bioengineering) University of Canterbury.
- FENG, S., LOTZ, T., CHASE, J. G. & HANN, C. E. Year. An image based vibration sensor for soft tissue modal analysis in a Digital Image Elasto Tomography (DIET) system. *In: IEEE EMBS, 2010 Buenos Aires*. 25-8.
- FENG, S., LOTZ, T., CHASE, J.G., HANN, C.E. Year. An Image Based Vibration Sensor for Soft Tissue Modal Analysis in a Digital Image Elasto Tomography (DIET) System. *In: IEEE Engineering in Medicine and Biology Society (EMBS), 31 Aug - 4 Sept 2010b Buenos Aires, Argentina*. IEEE.
- FERLAY, J., SHIN, H.-R., BRAY, F., FORMAN, D., MATHERS, C. & PARKIN, D. M. 2010. Estimates of worldwide burden of cancer in 2008: GLOBOCAN 2008. *International Journal of Cancer*, 127, 2893-2917.
- FOUNDATION, T. N. Z. B. C. 2009/2010. Annual Report Auckland.
- FUNG Y.C. 1993. *In Biomechanics - Mechanical Properties of Living Tissues*. Springer, New York, 2nd Edition.

- GALVIN, B., MCCANE, B., NOVINS, K., MASON, D. & MILLS, S. Year. Recovering motion fields: An evaluation of eight optical flow algorithms. *In: British machine vision conference, 1998.* sn, 195-204.
- GEORGIEV, T., ZHENG, C., CURLESS, B., SALESIN, D., NAYAR, S. & INTWALA, C. Year. Spatio-angular resolution tradeoffs in integral photography. *In: Eurographics Symposium on Rendering, 2006.* 263-272.
- GLASBRENNER, J. 2012. Second Clinical Prototype of the Digital Image Elasto Tomography (DIET) Breast Cancer Screening System.
- GMBH, I. D. S. I. 2012. OBERSULM. Available: http://www.ids-imaging.de/frontend/files/uEyeManuals/Manual_eng/uEye_Manual
- HALL, T. J., ZHU, Y. & SPALDING, C. S. 2003. In vivo real-time freehand palpation imaging. *Ultrasound in medicine & biology, 29,* 427-435.
- HAMAS, R. S. 1999. The Postoperative Shape of Round and Teardrop Saline-filled Breast Implants. *Aesthetic Surgery Journal, 19,* 369-374.
- HAMAS, R. S. 2000. The Comparative Dimensions of Round and Anatomical Saline-filled Breast Implants. *Aesthetic Surgery Journal, 20,* 281-290.
- HANN, C. E., CHASE, J.G., BERG, C., BROWN, R.G., ELLIOT, R.B., CHEN, X.Q. Year. Specialised Image Capture Systems for a DIET Breast Cancer Screening System. *In: 3rd ASME/IEEE International Conference on Mechatronic and Embedded Systems and Applications, 4-7 Sept 2007 2007 Las Vegas, USA.* ASME.
- HANN, C. E., CHASE, J.G., CHEN, X.Q., BERG, C., BROWN, R.G., ELLIOT, R.B. 2009. Strobe Imaging System for Digital Image-based Elasto-Tomography Breast Cancer Screening. *IEEE Transactions on Industrial Electronics, 56,* 3195-3202.
- HAYDON MOTION SOLUTIONS. Available: <http://www.haydonkerk.com>
- HE, J. & FU, Z. F. 2001. *Modal analysis,* Butterworth-Heinemann.
- HOMMA, H., MIRLEY, C. L., RONZELLO, J. & BOGGS, S. A. 2000. Field and laboratory aging of RTV silicone insulator coatings. *Power Delivery, IEEE Transactions on, 15,* 1298-1303.
- IGUS. Available: <http://www.igus.com>
- IMAGING, I. U. 2005. *Project1: Elasticity Imaging of Breast Cancer* [Online]. Urbana: University of Illinois at Urbana-Champaign
- Available: <http://ultrasonics.bioen.illinois.edu/research.asp>
- INC., F. I. Available: http://www.factor2.com/product_p/lsr-05.htm
- INSTRUMENTS, T. 2004. *Getting Started Guide,* New Castle, Delaware.
- JASON FINCHER, A. M., CHRISTOPHER MURRAY, JAMES STEEL 2005 DIET System Actuator. Christchurch: University of Canterbury.

- JOHN, B. W., ELIJAH, E. W. VAN HOUTEN, MICHAEL, I. MIGA, FRANCIS, E. KENNEDY, KEITH, D. PAULSEN 2001. Magnetic resonance elastography using 3D gradient echo measurements of steady-state motion. *Medical Physics*, 28, 1620-1628.
- JOINSON, S. *DPreview Tutorial* [Online]. Available: <http://www.dpreview.com>
- KASHIKAR-ZUCK, S., KEEFE, F. J., KORNGUTH, P., BEAUPRE, P., HOLZBERG, A. & DELONG, D. 1997. Pain coping and the pain experience during mammography: a preliminary study. *Pain*, 73, 165-72.
- KASS, M., WITKIN, A. & TERZOPOULOS, D. 1988. Snakes: Active contour models. *International Journal of Computer Vision*, 1, 321-331.
- KHALED, W., REICHLING, S., BRUHNS, O. T. & ERMERT, H. 2006. Ultrasonic strain imaging and reconstructive elastography for biological tissue. *Ultrasonics*, 44, Supplement, e199-e202.
- KOPANS, D. B. 1998. *Breast imaging*, Philadelphia, Lippincott Williams & Wilkins.
- KOPANS, D. B. 2007. *Breast imaging*, Philadelphia, Lippincott Williams & Wilkins.
- KROUSKOP, T. A., WHEELER, T. M., KALLEL, F., GARRA, B. S., HALL, T. 1998. Elastic moduli of breast and prostate tissues under compression. *Ultrason Imaging*, 20, 260-74.
- KRUSE S, S. J., LAWRENCE A, ET AL. 2000. Tissue characterization using magnetic resonance elastography: preliminary results. *Phys Med Biol*, 45, 1579-1590.
- KUMLER, J. J. & BAUER, M. L. Year. Fish-eye lens designs and their relative performance. *In: International Symposium on Optical Science and Technology*, 2000. International Society for Optics and Photonics, 360-369.
- LENSATION. Karlsruhe, Germany. Available: <http://www.lensation.de/en/home.html>
- LESUEUR THIBAUT Design improvement of the Digital Image-based Elasto-Tomography (DIET) Breast Cancer Screening. University of Canterbury
- LIANG, X., OLDENBURG, A. L., CRECEA, V., KALYANAM, S., INSANA, M. F. & BOPPART, S. A. 2008. Modeling and measurement of tissue elastic moduli using optical coherence elastography. 685803-685803.
- LIBRARAY, E. M. Available: <http://eigen.tuxfamily.org>
- LIBRARY, T. O. S. C. V. Available: <http://opencv.org>
- LOTTIN, D. 2011. Development of a 3-axis positioning system for the DIET breast cancer screening system.
- LOTZ, T., HEEREN, AMW, KASHIF, A AND CHASE, JG 2012. Elastographic Tissue Characterisation by Separate Modal Analysis with a Digital Image Elasto Tomography (DIET) Breast Cancer Screening System. *9th IASTED Int Conf on Biomedical Engineering (BioMed 2012)*. Innsbruck, Austria.

- LOTZ, T., KASHIF, A., FENG, S., BIRET, P., DENAIS, Y., LOTTIN, D., MAILLARD, L., TIRSCHLER, T., AND CHASE, J.G. Year. A Clinical Prototype of the Digital Image Elasto Tomography Breast Cancer Screening System. *In: Proc 5th International Conference on Bioinformatics and Biomedical Engineering (iCBBE)*, 10-12 May 2011a Wuhan, China.
- LOTZ, T., SIMPSON, P.D., STOCKER, D., HANN, C.E., CHASE, J.G. 2010. In vitro evaluation of surface based non-invasive breast cancer screening with Digital Image based Elasto Tomography (DIET). *32nd Annual International Conference of the IEEE Engineering in Medicine and Biology Society (EMBS)*. Buenos Aires, Argentina.
- LOTZ, T. F., MULLER, NATALIE, HANN, CHRISTOPHER E.,CHASE, J. GEOFFREY 2011b. Minimal elastographic modeling of breast cancer for model based tumor detection in a digital image elasto tomography (DIET) system. *Medical Imaging 2011: Computer-Aided Diagnosis*, 7963 796322-6
- MADSEN, E. L., HOBSON, MARITZA A., FRANK, GARY R., SHI, HAIRONG, JIANG, JINGFENG, HALL, TIMOTHY J., VARGHESE, TOMY, DOYLEY, MARVIN M., WEAVER, JOHN B. 2006. Anthropomorphic breast phantoms for testing elastography systems. *Ultrasound in Medicine & Biology*, 32, 857-874.
- MAILLARD LAURA 2010. Design improvement of the DIET breast cancer screening system in terms of ergonomics, size and functionality. University of Canterbury
- MANDUCA, A., OLIPHANT, T. E., DRESNER, M. A., MAHOWALD, J. L., KRUSE, S. A., AMROMIN, E., FELMLEE, J. P., GREENLEAF, J. F., EHMAN, R. L. 2001. Magnetic resonance elastography: Non-invasive mapping of tissue elasticity. *Medical Image Analysis*, 5, 237-254.
- MAYTEC. Available: http://www.maytec.org/mainframe_e.htm
- MCDONALD, S., SASLOW, D. & ALCIATI, M. H. 2004. Performance and reporting of clinical breast examination: a review of the literature. *CA: a cancer journal for clinicians*, 54, 345-61.
- MCDONALD, S., SASLOW, DEBBIE, ALCIATI, MARIANNE H. 2004. Performance and Reporting of Clinical Breast Examination: A Review of the Literature. *CA: A Cancer Journal for Clinicians*, 54, 345-361.
- MCHUGH, S. *Cambridge in Colour Tutorials* [Online]. Cambridge University. Available: <http://www.cambridgeincolour.com/tutorials.htm>
- MCHUGH, S. 2011. *Understanding Camera Lenses* [Online]. Available: <http://www.cambridgeincolour.com/tutorials/camera-lenses.htm>
- MCKNIGHT, A. L., KUGEL, J. L., ROSSMAN, P. J., MANDUCA, A., HARTMANN, L. C. & EHMAN, R. L. 2002. MR Elastography of Breast Cancer: Preliminary Results. *American Journal of Roentgenology*, 178, 1411-1417.
- MÉMIN, E. & PÉREZ, P. 1998. Dense estimation and object-based segmentation of the optical flow with robust techniques. *Image Processing, IEEE Transactions on*, 7, 703-719.
- MICHAELSON, J. S., SILVERSTEIN, M., WYATT, J., WEBER, G., MOORE, R., HALPERN, E., KOPANS, D. B., HUGHES, K. 2002. Predicting the survival of patients with breast carcinoma using tumor size. *Cancer*, 95, 713-23.

- MOTICONT. Van Nuys, CA 91406, USA. Available: <http://www.moticont.com>
- MUTHUPILLAI, R., LOMAS, D. J., ROSSMAN, P. J., GREENLEAF, J. F., MANDUCA, A. & EHMAN, R. L. 1995. Magnetic resonance elastography by direct visualization of propagating acoustic strain waves. *Science (New York, N.Y.)*, 269, 1854-1857.
- MUTHUPILLAI, R., ROSSMAN, P. J., LOMAS, D. J., GREENLEAF, J. F., RIEDERER, S. J. & EHMAN, R. L. 1996. Magnetic resonance imaging of transverse acoustic strain waves. *Magnetic Resonance in Medicine*, 36, 266-274.
- NASA Anthropometry and Biomechanics. Houston, TX 77058 USA.
- NATIONAL INSTRUMENTS. Auckland, New Zealand. Available: <http://nz.ni.com>
- NATIONAL INSTRUMENTS NI 9215, 4-Channel, 16-bit, ± 10 V Analog Input Module.
- NIGHTINGALE, K. R., NIGHTINGALE, R. W., PALMERI, M. L. & TRAHEY, G. E. 2000. A Finite Element Model of Remote Palpation of Breast Lesions Using Radiation Force: Factors Affecting Tissue Displacement. *Ultrasonic Imaging*, 22, 35-54.
- NIPSHAGEN, M., BEEKMAN, W., ESMÉ, D. & BECKER, J. 2007. Anatomically Shaped Breast Prosthesis in Vivo: A Change of Dimension? *Aesthetic Plastic Surgery*, 31, 540-543.
- OPHIR, J., CESPEDES, I., GARRA, B., PONNEKANTI, H., HUANG, Y. & MAKLAD, N. 1996. Elastography: Ultrasonic imaging of tissue strain and elastic modulus in vivo. *European Journal of Ultrasound*, 3, 49-70.
- OPHIR, J., KALLEL, FAOUZI, VARGHESE, TOMY, KONOFAGOU, ELISA, ALAM, S. K. S. KAISAR, KROUSKOP, THOMAS, GARRA, BRIAN, RIGHETTI, RAFFAELLA 2001. Elastography. *Comptes Rendus de l'Académie des Sciences - Series IV - Physics*, 2, 1193-1212.
- PARKER, K. J., DOYLEY, M. M. & RUBENS, D. J. 2011. Imaging the elastic properties of tissue: the 20 year perspective. *Physics in Medicine and Biology*, 56, R1.
- PETERS, A. 2007. *Digital Image Elasto-Tomography Mechanical Properties reconstruction from Surface Measured Displacement Data*. PhD Thesis, Department of Mechanical Engineering, University of Canterbury.
- PETERS, A., BERGER, H-U., CHASE, J.G., VAN HOUTEN, E.E.W. 2006. Digital Image-based Elasto-Tomography: Nonlinear Mechanical Property Reconstruction of Homogeneous Gelatine Phantoms. *International Journal of Information & Systems Sciences*, 2, 512-521.
- PETERS, A., CHASE, J. G., VAN HOUTEN, E. E. 2008a. Digital image elasto-tomography: combinatorial and hybrid optimization algorithms for shape-based elastic property reconstruction. *IEEE transactions on bio-medical engineering*, 55, 2575-83.
- PETERS, A., CHASE, J. G., VAN HOUTEN, E. E. 2008b. Digital image elasto-tomography: mechanical property estimation of silicone phantoms. *Medical and biological engineering and computing*, 46, 205-12.
- PETERS, A., CHASE, J. G., VAN HOUTEN, E. E. 2009. Estimating elasticity in heterogeneous phantoms using Digital Image Elasto-Tomography. *Medical and biological engineering and computing*, 47, 67-76.

- PETERS, A., MILSANT, A., ROUZE, J., RAY, L.E., CHASE, J.G., VAN HOUTEN, E. E. 2004. Digital-image based elasto-tomography: Proof of concept studies for surface based mechanical property reconstruction. *JSME International Journal*, 47, 1117-1123.
- PETERS, A., WORTMANN, S., ELLIOT, R.B., STAIGER, M., CHASE, J.G., VAN HOUTEN, E. E. 2005. Digital Image-based Elasto-Tomography: First experiments in surface based mechanical property estimation of gelatine phantoms. *JSME International Journal*, 48, 562-569.
- PICKERELL, D. M. 2010. Elastography: Imaging of Tomorrow? *Journal of Diagnostic Medical Sonography*, 26, 109-113.
- PISANO, E. D., HENDRICK, R. E., YAFFE, M. J., BAUM, J. K., ACHARYYA, S., CORMACK, J. B., HANNA, L. A., CONANT, E. F., FAJARDO, L. L., BASSETT, L. W., D'ORSI, C. J., JONG, R. A., REBNER, M., TOSTESON, A. N. & GATSONIS, C. A. 2008. Diagnostic accuracy of digital versus film mammography: exploratory analysis of selected population subgroups in DMIST. *Radiology*, 246, 376-83.
- PLEWES, A. S. A. D. 2007. An inverse problem solution for measuring the elastic modulus of intact ex vivo breast tissue tumours *Physics in Medicine and Biology*, 52, 1247-1260.
- PLEWES, D. B., BETTY, I., URCHUK, S. N. & SOUTAR, I. 1995. Visualizing tissue compliance with MR imaging. *Journal of Magnetic Resonance Imaging*, 5, 733-738.
- PORTER, P. 2008. "Westernizing" Women's Risks? Breast Cancer in Lower-Income Countries. *New England Journal of Medicine*, 358, 213-216.
- RS-COMPONENTS. Available: www.rs-components.co.nz
- RUDIN, L. I., OSHER, S. & FATEMI, E. 1992. Nonlinear total variation based noise removal algorithms. *Physica D: Nonlinear Phenomena*, 60, 259-268.
- SAMANI A, B. J., LUGINBUHL C, AND PLEWES D 2003. Measuring the elastic modulus of ex vivo small tissue samples. *Phys Med Biol*, 48, 2183.
- SAMANI, A., ZUBOVITS, J., PLEWES, D. 2007. Elastic moduli of normal and pathological human breast tissues: an inversion-technique-based investigation of 169 samples. *Physics in medicine and biology*, 52, 1565-76.
- SARVAZYAN, A., EGOROV, V., SON, J. S., KAUFMAN, C. S. 2008. Cost-Effective Screening for Breast Cancer Worldwide: Current State and Future Directions. *Breast cancer*, 1, 91-99.
- SARVAZYAN A, S. A., EMELIANOV S, ET AL. 1995. Biophysical bases of elasticity imaging. *Acoust Imaging*, 21, 223-240.
- SARVAZYAN, S., SKOVORODA, A., EMELIANOV, S. 1995. Biophysical bases of elasticity imaging. *Acoust Imaging*, 21, 223-240.
- SCHMITZ, T. L. & SMITH, K. S. 2008. *Machining Dynamics: Frequency Response to Improved Productivity*, Springer.
- SCHNEINDER ELECTRIC. USA. Available: <http://motion.schneider-electric.com>

- SHARMA, A. C., SOO, M. S., TRAHEY, G. E. & NIGHTINGALE, K. R. Year. Acoustic radiation force impulse imaging of in vivo breast masses. *In: Ultrasonics Symposium, 2004 IEEE, 23-27 Aug. 2004 2004. 728-731 Vol.1.*
- SIEGMANN, K., XYDEAS, T., SINKUS, R., KRAEMER, B., VOGEL, U. & CLAUSSEN, C. 2010. Diagnostic value of MR elastography in addition to contrast-enhanced MR imaging of the breast—initial clinical results. *European Radiology, 20, 318-325.*
- SILICONES, D. C. Available:
<https://www.xiameter.com/en/Products/Pages/ProductDetail.aspx?pid=01013106&R=X70EN&C=US#characteristicsAnchor>
- SINKUS, R., TANTER, M., CATHELIN, S., LORENZEN, J., KUHL, C., SONDERMANN, E. & FINK, M. 2005. Imaging anisotropic and viscous properties of breast tissue by magnetic resonance-elastography. *Magnetic Resonance in Medicine, 53, 372-387.*
- SINKUS, R., TANTER, MICKAEL, XYDEAS, TANJA, CATHELIN, STEFAN, BERCOFF, JEREMY, FINK, MATHIAS 2005. Viscoelastic shear properties of in vivo breast lesions measured by MR elastography. *Magnetic Resonance Imaging, 23, 159-165.*
- SKOVORODA, A. R., EMELIANOV, S. Y. & O'DONNELL, M. 1995. Tissue elasticity reconstruction based on ultrasonic displacement and strain images. *Ultrasonics, Ferroelectrics and Frequency Control, IEEE Transactions on, 42, 747-765.*
- SOCIETY, A. C. Breast cancer survival by stage. Available:
<http://www.cancer.org/cancer/breastcancer/detailedguide/breast-cancer-survival-by-stage#>
- SPIEGEL, J. H. & SINGER, M. I. 2000. Practical approach to digital photography and its applications. *Otolaryngology--Head and Neck Surgery, 123, 152-156.*
- SRIVASTAVA, A., VERMA, Y., RAO, K. D., GUPTA, P. K. 2011. Determination of Elastic Properties of Resected Human Breast Tissue Samples Using Optical Coherence Tomographic Elastography. *Strain, 47, 75-87.*
- STALDER, H. 2011. Design of a 2-axes positioning system of the Digital Image-based Elastography (DIET) Breast Cancer Screening. Christchurch: University of Canterbury.
- STEIN, G. P. Year. Accurate internal camera calibration using rotation, with analysis of sources of error. *In: Computer Vision, 1995. Proceedings., Fifth International Conference on, 1995. IEEE, 230-236.*
- SYSTEMS, I. D. IDS Camera Manual. *In: IDS GMBH, G. (ed.).*
- TRANS-TEK, I. Ellington, CT 06029. Available: <http://www.transtekinc.com>
- VAN HOUTEN, E. E., DOYLEY, M. M., KENNEDY, F. E., WEAVER, J. B. & PAULSEN, K. D. 2003. Initial in vivo experience with steady-state subzone-based MR elastography of the human breast. *Journal of magnetic resonance imaging, 17, 72-85.*
- VAN HOUTEN, E. E., MIGA, M. I., WEAVER, J. B., KENNEDY, F. E., PAULSEN, K. D. 2001. Three-dimensional subzone-based reconstruction algorithm for MR elastography. *Magnetic resonance in medicine, 45, 827-37.*

WEAVER, J. B., VAN HOUTEN, E. E., MIGA, M. I., KENNEDY, F. E. & PAULSEN, K. D. 2001. Magnetic resonance elastography using 3D gradient echo measurements of steady-state motion. *Medical physics*, 28, 1620-8.

XING LIANG, A. L. O., VASILICA CRECEA, SURESHKUMAR KALYANAM, MICHAEL F. INSANA AND STEPHEN A. BOPPART, "Modeling and measurement of tissue elastic moduli using optical coherence elastography". *Proc. SPIE 6858*, 685803 (2008);
doi:10.1117/12.760779

ZHU, Y. & HALL, T. J. 2002. A Modified Block Matching Method for Real-Time Freehand Strain Imaging. *Ultrasonic Imaging*, 24, 161-176.

Appendix A

Table 1.1: Elastic properties of various healthy and diseased tissues of human breast, values show Young's modulus (KPa)

Tissue Type	Krouskop (Krouskop, 1998)				Samani (Samani, 2007)	Srivastava (Srivastava, 2011)	Liang (Xing Liang)	Sinkus* (Sinkus, 2005)	Egorov (Egorov and Sarvazyan, 2008)	Kruse {Kruse S, 2000 #293}	Sarvazyan {Sarvazyan A, 1995 #292}
	(1 Hz)		(4 Hz)							(100 Hz)	
	5 % Precomp	20% Precomp	5 % Precomp	20% Precomp							
Normal Fat	19±7	20±12	22±8	24±6	3.25±0.9	4.17±0.07	0.42	2.61±0.45	5.6-9.5	15-25	5-50
Glandular Tissue	33±11	57±19	35±14	66±17	3.24±0.6					30-45	5-50
Fibroadenoma	107±31	232±60	116±28	244±85	6.41±2.86	9.03±0.2		3.9±2.1	108		
Palpable Nodule											100-5000
Low Grade IDC					10.40±2.6		10.68	8.7±0.9			
ILC					15.62±2.6						
DCIS	25±4	301±58	26±5	307±78	16.38±1.5				68		
Intermediate Grade IDC					19.99±4	16.45±1.1					
IDC (High)					42.52±12				123	50-75	
Fibrocystic disease					17.11±7						
Infiltrating Carcinoma	93±33	409±112	112±43	460±178	18.57						
IMC					20.21						
Fat Necrosis					4.45						
Benign Fibrostatic Tissue									50		
Adenocarcinoma									75		
Benign Nodular Adenosis									25		
Mastopathy								1.2±0.4			

Bit-Volt Relationship for the Actuator

Table 4.7: Data showing the verification results of the set actuation amplitude and displacement reading through Laser Doppler vis-a-vis binary values

Set Amplitude	10 Hz		20 Hz		30 Hz		40Hz		50 Hz		60Hz		70Hz		80Hz	
(mm)	Bits	Disp (um)	Bits	Disp (um)	Bits	Disp (um)	Bits	Disp (um)	Bits	Disp (um)	Bits	Disp (um)	Bits	Disp (um)	Bits	Disp (um)
0.9	10475	1259	10427	899	11110	999	11056	1050	10805	1048	11309	1156	11250	1177	10125	1130
0.8	9504	1148	9442	802	10039	970	10042	985	9890	958	9311	961	9849	1035	10126	1036
0.7	8720	997	8673	725	8426	685	8510	832	8420	840	8515	881	8743	926	8624	960
0.6	7399	842	7315	609	7189	588	7275	746	7273	734	7295	765	7106	770	7440	827
0.5	5997	680	5886	490	6228	500	5930	632	6012	630	5950	687	6006	660	5799	680
0.4	4995	580	4867	404	4845	395	4965	420	5065	533	4990	520	4835	548	4752	565
0.3	3560	400	3474	301	3674	296	3592	300	3433	300	3470	411	3530	410	3539	414
0.2	2483	287	2408	219	2545	204	2345	199	2603	224	2509	264	2293	300	2205	298
0.1	1173	150	1148	112	1185	101	1275	104	1403	120	1104	102	998	97	990	99
Mean	6034	705	5960	507	6137	526	6110	585	6100	598	6050	638	6068	658	5956	668
Bits/um	8.56		11.76		11.66		10.44		10.19		9.48		9.22		8.92	

Table 8.5: Showing Storage Modulus (E', kPa) mean and standard deviation for during dynamic mechanical testing

Freq (Hz)	A	B	C	D	E	F	G	H
4	32.8±6.5	21.1±1.3	9.5±1.4	2.1±0.1	401.8±38.2	59.7±1.6	86.1±21.6	8.9±1.3
6	33.7±5.9	21.1±1.3	9.6±1.3	2.1±0.1	422.2±39.2	61.0±1.9	93.1±19.2	9.4±1.3
8	34.3±5.5	21.3±1.2	9.7±1.3	2.1±0.1	440.6±42.2	61.9±2.3	97.4±19.7	9.8±1.4
10	35.1±4.6	21.4±1.2	9.8±1.4	2.1±0.1	456±46.5	62.6±2.5	101±20.1	10.2±1.4
12	35.5±4.7	21.4±1.2	9.8±1.3	2.1±0.1	469.8±50	63.1±2.6	104.1±20.5	10.4±1.5
14	35.8±4.7	21.5±1.2	9.7±1.3	2±0.1	482.2±54.1	63.4±2.7	107±21	10.6±1.5
16	35.9±4.5	21.4±1.2	9.7±1.3	1.9±0.1	493±57.3	64.2±3	109.6±21.5	10.8±1.5
18	36.1±4.5	21.5±1.2	9.7±1.3	2±0.1	502.6±60.4	64.6±3	111.8±21.5	11.1±1.5
20	36.3±4.4	21.6±1.2	9.8±1.3	2±0.1	510.4±62.3	65±3.1	114±21.8	11.4±1.5
22	36.1±4.4	21.3±1.2	9.6±1.3	1.7±0.1	517±64.4	65.0±3.1	115.9±22	11.3±1.6
24	36.5±4.3	21.6±1.2	9.8±1.3	1.9±0.1	524.2±65.3	65.5±3.1	118.5±22.4	11.7±1.6
26	36.3±4.3	21.4±1.2	9.5±1.3	1.7±0.1	528.4±65.1	65.6±3.1	120.2±22.7	11.7±1.6
28	36.1±4.3	21.1±1.2	9.3±1.3	1.4±0.1	533.2±65.2	65.5±3.2	121.8±22.9	11.6±1.6
30	35.8±4.4	20.8±1.2	9±1.4	1.1±0.2	537.4±65.1	65.4±3.2	123.4±22.7	11.4±1.6
35	36.1±4.4	20.9±1.2	9.2±1.3	1.1±0.1	547.4±64.9	65.9±3.2	128.1±22.5	11.8±1.7
40	36.2±4.3	20.8±1.2	9.1±1.3	1.1±0.1	555.2±63.8	66.5±3.3	132.2±22	12±1.8
50	36.4±4.2	20.4±1.2	8.6±1.2	0.4±0.1	570.6±66.2	66.1±3.5	139.2±20.7	12.2±1.9

Table 8.6: Showing Damping Ratios ($\zeta = \tan \delta$) mean and standard deviation during dynamic mechanical testing

Freq (Hz)	A	B	C	D	E	F	G	H
4	0.06±0.03	0.03±0.01	0.05±0	0.09±0.02	0.19±0.01	0.06±0.02	0.17±0.01	0.2±0.01
6	0.06±0.03	0.03±0.01	0.05±0.01	0.1±0.02	0.2±0.01	0.07±0.01	0.18±0	0.23±0.01
8	0.06±0.03	0.04±0.01	0.06±0.01	0.11±0.02	0.21±0.01	0.07±0.01	0.19±0	0.25±0.01
10	0.07±0.03	0.04±0.01	0.06±0.01	0.13±0.02	0.22±0.01	0.07±0.01	0.2±0	0.27±0.01
12	0.07±0.02	0.04±0.01	0.06±0.01	0.14±0.01	0.23±0.01	0.08±0.01	0.21±0	0.28±0.01
14	0.07±0.02	0.04±0.01	0.07±0.01	0.16±0.01	0.23±0.01	0.08±0.01	0.21±0	0.29±0.01
16	0.07±0.02	0.05±0.01	0.08±0.01	0.23±0.02	0.24±0.01	0.09±0.01	0.22±0	0.32±0.02
18	0.08±0.02	0.06±0.01	0.1±0.01	0.29±0.02	0.24±0.01	0.09±0.01	0.22±0	0.33±0.02
20	0.08±0.02	0.05±0	0.08±0.01	0.22±0.01	0.24±0.01	0.09±0.01	0.23±0	0.32±0.02
22	0.08±0.02	0.07±0.01	0.11±0.01	0.34±0.04	0.25±0.01	0.09±0.01	0.23±0	0.35±0.02
24	0.08±0.02	0.06±0.01	0.09±0.01	0.28±0.01	0.25±0.01	0.09±0.01	0.23±0	0.34±0.02
26	0.08±0.02	0.06±0.01	0.09±0.01	0.27±0.01	0.25±0.01	0.09±0.01	0.23±0	0.35±0.02
28	0.09±0.02	0.06±0	0.1±0.02	0.35±0.02	0.26±0.01	0.1±0.01	0.24±0	0.36±0.02
30	0.09±0.02	0.07±0.01	0.13±0.02	0.61±0.07	0.26±0.01	0.1±0.01	0.24±0	0.39±0.02
35	0.11±0.03	0.09±0.01	0.16±0.02	0.91±0.1	0.27±0.01	0.11±0	0.25±0.01	0.44±0.03
40	0.14±0.03	0.14±0.01	0.28±0.05	1.8±0.25	0.28±0.01	0.13±0	0.26±0.01	0.52±0.04
50	0.15±0.03	0.15±0.01	0.3±0.04	5.1±1.22	0.28±0.01	0.14±0.01	0.27±0.01	0.56±0.05